FUNDAMENTAL STRUCTURE-DIELECTRIC PROPERTY RELATIONSHIPS IN FLUORITE-RELATED CERAMICS

By

LU CAI

A DISSERTATION PRESENTED TO THE GRADUATE SCHOOL
OF THE UNIVERSITY OF FLORIDA IN PARTIAL FULFILLMENT
OF THE REQUIREMENTS FOR THE DEGREE OF
DOCTOR OF PHILOSOPHY

UNIVERSITY OF FLORIDA

2010

With my deepest love to my entire family

ACKNOWLEDGMENTS

First of all, I would like to acknowledge my advisor, Dr. Juan C. Nino, for his support and guidance. His knowledge, care, optimism, diligence and aspirations inspired me to work hard and expand my potential. I would like to express deepest gratitude to my other committee members (Dr. David P. Norton, Dr. Simon R. Phillpot and Dr. Jacob L. Jones, and Dr. Arthur F. Hebard) for their time and guidance.

I would like to acknowledge all the collaborative work which greatly improved my research. Collaborations are listed without a particular order:

Dr. Stanislav Kamba and his students Dmitry Nuzhnyy and Veronica Goian from the Institute of Physics of the Academy of Science of the Czech Republic for their great support and help on the infrared spectroscopy measurement and complex dielectric spectra from the time-domain THz spectrometer.

Brian H. Toby and all other scientists at 11 - BM Advanced Photon Source, Argonne National Lab for their help with the high resolution XRD collection.

Daniel Arenas and Dr. David Tanner from the Physics Department at University of Florida for their help with infrared measurements.

Sava Denev and Dr. Gopalan at Penn State for second harmonic generation measurement.

Clarina R. Dela Cruz, Ovidiu Garlea, and Ashfia Huq at HB-2A of High Flux Isotope Reactor at Oak Ridge National Laboratory for their help on neutron diffraction data collection.

I would like to thank the previous and current group members: Alex Arias, Mohammed Elshennawy, Marta Giachino, Donald Moore, Shobit Omar, Satyajit Phadke,

Wei Qiu, Kevin Tierney, Laurel Wucherer, Peng Xu, Samantha Yates, *etc.*, for providing me excellent research environment and being helpful.

Last but not least, I am deeply indebted to my parents and my husband and their continuous support. Their love has encouraged me to go through the hard times. I cannot imagine myself having any of my progress without my family's strong support behind me.

TABLE OF CONTENTS

page

LIST OF TABLES

LIST OF FIGURES

LIST OF ABBREVIATIONS

ANL	Argonne National Lab
APF	atomic packing factor
APS	Advance Photon Source
CN	coordination number
DI	deionized
EDS	energy dispersive spectroscopy
HFIR	High Flux Isotope Reactor
HT	high temperature
IR	infrared spectroscopy
LT	low temperature
MAIC	Major Analytical Instrumentation Center
ORNL	Oak Ridge National Lab
SEM	scanning electron microscopy
SHG	second harmonic generation
TCC	temperature coefficient of capacitance
$T(\varepsilon_m)$	the temperature where the maximum of the real part of the permittivity occurs
T_m	the temperature where the peak of the imaginary part of the permittivity occurs
SA	stacking angle
SV	stacking vector
RT	room temperature

Abstract of Dissertation Presented to the Graduate School
of the University of Florida in Partial Fulfillment of the
Requirements for the Degree of Doctor of Philosophy

FUNDAMENTAL STRUCTURE-DIELELCTRIC PROPERTY RELATIONSHIPS IN FLUORITE-RELATED CERAMICS

By

Lu Cai
May 2010

Chair: Juan C. Nino
Major: Materials Science and Engineering

Compounds with anion-deficient fluorite-related crystal structure ($A_2B_2O_7$), such as weberite and pyrochlore, have gained attention because their ability to accommodate various cations as well as a large variety of distortions, allowing their properties to be tailored. A comprehensive investigation of the structure-property relationships in a series of fluorite-related compounds $Ln_2(Ln_{0.5}Nb_{0.5})_2O_7$ (or Ln_3NbO_7, Ln = rare earth element) and $Ln_2(Ln'_{0.5}Nb_{0.5})_2O_7$ (where the ionic radius of Ln' is smaller than that of Ln) is the topic of the dissertation.

At room temperature, La_3NbO_7 and Nd_3NbO_7 are orthorhombic weberite-type with space group *Pmcn* (No. 62). The crystal structure of Gd_3NbO_7 is also orthorhombic weberite-type but with a different space group *Cm2m* (No. 38). It was found that La_3NbO_7, Nd_3NbO_7, and Gd_3NbO_7 have a phase transition. Of particular interest is Gd_3NbO_7, which exhibits a centrosymmetric to non-centrosymmetric transition on cooling based on second harmonic generation (SHG) measurement. X-ray measurements were undertaken using synchrotron source. After crystal structure refined using the Rietveld method, the phase transition is mainly due to off-center shifts of Nb^{5+} and one third of Gd^{3+} ions within their corresponding polyhedra. There is net

dipole along [010], which suggests an incipient ferroelectric. As for Nd_3NbO_7 and La_3NbO_7, below the phase transition temperature there are antiparallel shifts of Nb^{5+} and Ln^{3+}, which indicates an antipolar nature.

As for dielectric properties, weberite-type Ln_3NbO_7 and $Ln_2Ln'NbO_7$ exhibit dielectric relaxation but there is no relaxation in defect-fluorite Ln_3NbO_7 (Ln^{3+} = Dy^{3+}, Er^{3+}, Yb^{3+}, and Y^{3+}). Infrared spectroscopy (IR) was used to correlate phase transition with dielectric properties. The infrared spectrum of Gd_3NbO_7 revealed that a peak at about 450 cm^{-1} appears at 340 K and becomes stronger with decreasing temperature, consistent with the phase transition. However, the dielectric contribution from the mode is small, less than 2% of the total permittivity.

As for structure-dielectric property relationship, it was found that the $T(\varepsilon_m)$ and the permittivity increase ($\Delta\varepsilon'_r$) increases with increasing off-center shifts of Ln^{3+} within LnO_8 polyhedra for weberite-type Ln_3NbO_7. As for $Ln_2Ln'NbO_7$, the temperature (T_m) at which the dielectric loss is maximum increase with the ionic radius ratio of cations.

CHAPTER 1
INTRODUCTION

1.1 Statement of Problem and Motivation

The fluorite structure (AO_2) is considered to be one of the most flexible for its ability to construct superstructures or derivatives.[1] Anion-deficient fluorite-related structures ($A_2B_2O_7$), such as pyrochlore and weberite, maintain the closed-packed cation layers as in the fluorite structure. The deficiency of anions enables accommodation of various cations on both *A*-site and *B*-site. Therefore, compounds with fluorite-related structure exhibit various interesting properties, including conductivity (*e.g.*, $Bi_2Ru_2O_7$[2-5]), dielectric properties (*e.g.*, $Bi_{1.5}Zn_{0.92}Nb_{1.5}O_{6.92}$[6-10]), ferroelectric properties (*e.g.*, $Cd_2Nb_2O_7$ and $Ca_2Sb_2O_7$[11-14]), magnetic properties (*e.g.*, $Ln_2(Ln_{0.5}Re_{0.5})_2O_7$ and $Ln_2(Ln_{0.5}Os_{0.5})_2O_7$[15-21], where Ln = rare earth element) as well as photocatalytic activity (La_3NbO_7 and $Ca_2Sb_2O_7$[22-25]).

Compounds with anion-deficient fluorite-related structure ($A_2B_2O_7$) exhibit interesting dielectric properties with intermediate dielectric constants especially in niobates, tantalates and titanates ($\varepsilon_r \sim 30 - 100$).[14] A lot of these materials have been studied for potential electronic applications such as capacitors, filters and resonators. However, due to the large structural flexibility, the huge number of compounds available and diverse nature of the properties, there is a limited comprehension of the fundamental structure-dielectric property relationships inside fluorite-related ceramics. To address this issue, a series of Ln_3NbO_7 and $Ln_2Ln'NbO_7$ compounds have been chosen to achieve a fundamental understanding of structure-dielectric property relationships. The series of compounds are ideal for studying the correlation between ionic polarizability and dielectric permittivity because there is an approximately linear

relationship between the dielectric polarizability and ionic radius of Ln^{3+} (Figure 1-1). The variation in crystal structure within the fluorite family also provides a stage to investigate structure-dielectric property relationships within fluorite-related ceramics.

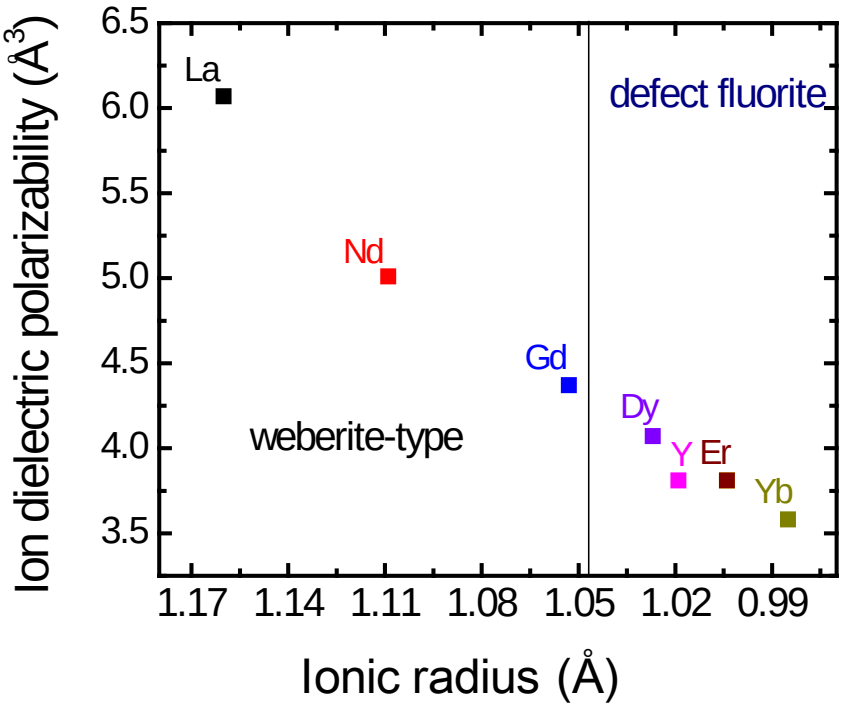

Figure 1-1. Ion polarizability[26] and ionic radius[27] of rare earth elements.

In addition, an interesting phenomenon is that dielectric relaxation is commonly observed in Bi-pyrochlores (Figure 1-2(A)). At first, it was proposed that dielectric relaxation is related to the lone-pair cations. Recently, dielectric relaxation was also observed in a non-Bi pyrochlore, $Ca_{1.47}Ti_{1.47}Nb_{1.04}O_7$ (Figure 1-2 (B)).[28] Therefore, the origin of the dielectric relaxation is definitely not due to the lone-pair since $Ca_{1.47}Ti_{1.47}Nb_{1.04}O_7$ does not have the lone pair but apparently lies in the structural disorder. This study also intends to find the correlation between structure and dielectric relaxation within fluorite-related structures.

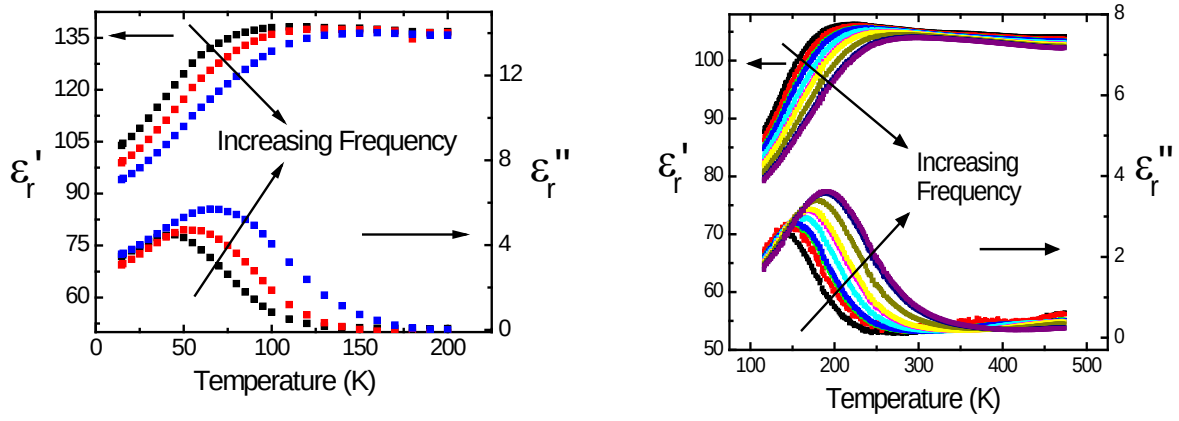

(A) (B)

Figure 1-2. Dielectric relaxation in the pyrochlore compounds (A) $Bi_{1.5}Zn_{0.92}Nb_{1.5}O_{6.92}$[6] (B) $Ca_{1.47}Ti_{1.47}Nb_{1.04}O_7$.[28]

1.2 Scientific Approach

Crystallographic investigations on Ln_3NbO_7 can be found dating as far back as 1964.[29] Since then, there have been considerable discrepancies between various studies on the crystal structure of Ln_3NbO_7 reported in literature. Some investigators referred to Sm_3NbO_7 and Gd_3NbO_7 as having an orthorhombic structure (probably a weberite-type structure) while others determined them to be pyrochlores.[30-35] Rossell[36] first determined the crystal structure of a series of Ln_3NbO_7 compounds. Though the main features of the structures have been captured, the space groups proposed for La_3NbO_7 (*Cmcm*) and Gd_3NbO_7 (*C222₁*) have been questioned by later investigations. Kahnharari *et al.*[37] studied single crystal La_3NbO_7 and proposed the space group (*Pnma*) based on x-ray diffraction. Astafyev[38] measured the second harmonic generation (SHG) and suggested a polar space group for Gd_3NbO_7 rather other *C222₁*. Therefore, the first step of this research is to clarify the crystal structure.

The second step of this work is to characterize dielectric properties at different temperatures and frequencies. For all defect-fluorite samples, the dielectric permittivity

increases slightly with increasing temperature. By contrast, weberite-type Ln_3NbO_7 exhibits dielectric relaxation above room temperature (RT). Efforts were placed to look for the structural origin of dielectric relaxation. The focus on dielectric properties include calculation and analysis of the permittivity (real and imaginary), the temperature coefficient of capacitance (TCC), the temperature ($T(\varepsilon_m)$) where the maximum permittivity occurs, the temperature (T_m) where the peak of the imaginary part of the permittivity happens. Contrast between the dielectric properties/relaxation and structural features such as ionic radius, polarizability, structural openness, phase transition, polyhedra distortion, *etc.* was performed to identify structure-property correlations. It was found out that the off-center shifts of cations within their polyhedra impact the dielectric properties. A series of new $Ln_2(Ln'_{0.5}Nb_{0.5})_2O_7$ compounds (where the ionic radius of Ln' is smaller than Ln) were introduced to expand the study. The $Ln_2Ln'NbO_7$ compounds have higher permittivity with more polarizable Ln^{3+}. The $Ln_2Ln'NbO_7$ (except Gd_2YbNbO_7) also exhibits dielectric relaxation but below 100 K. T_m increases with increasing the ratio of ionic radius and TCC increases with decreasing the average ionic radius of Ln^{3+}.

Based on heat capacity measurements, there is a phase transition in Ln_3NbO_7. Of particular interest is that only Gd_3NbO_7 shows SHG signal. The signal disappears above the phase transition temperature, indicating a non-centrosymmetric to centrosymmetric transition. For all three weberite-type Ln_3NbO_7 compounds, it is proven the origin of the dielectric relaxation is the phase transition because $T(\varepsilon_m)$ is close to the phase transition temperature indicated by the heat capacity data. The next research area focused on the characterization of the crystal structures below and above

the phase transition temperature by synchrotron x-ray diffraction at Advanced Photon Source (APS) of Argonne National Laboratory (ANL) and neutron diffraction at High Flux Isotope Reactor (HFIR) of Oak Ridge National Laboratory (ORNL).

The final step was to correlate the crystal structure, phase transition, and dielectric properties by infrared (IR) spectroscopy and to predict the dielectric properties in the terahertz (THz) frequency range.

These results not only contribute to the comprehension of structure-dielectric property relationships, but also lead towards the possibility to control the dielectric relaxation and develop a paradigm for compositional design of fluorite-related ceramics with optimized dielectric properties.

1.3 Organization of Dissertation

Chapter 2 provides a brief introduction and background information on the weberite structure and the weberite-type Ln_3NbO_7 structure. The correlations between these two structures are discussed. Chapter 2 also introduces the dielectric polarization mechanisms, the concept of the phase transition, the definitions of ferroelectric, antipolar, and antiferroelectric, the basic concept of second harmonic generation (SHG), and the normal mode determination in Raman and IR. Chapter 3 presents the experimental procedures and characterization techniques mainly used in this study.

Chapter 4 reports the crystallographic study by XRD at room temperature. Chapter 5 presents the dielectric properties for all compounds studied in the investigation. The dielectric properties from 1 kHz to 1 MHz were measured as a function of temperature.

Chapter 6 reports the phase transition of weberite-type Gd_3NbO_7. Heat capacity measurement, second harmonic generation measurement, the infrared (IR)

spectroscopy and dielectric properties measurement are all evidence supporting phase transition. Synchrotron x-ray diffractometer was used to study the crystal structure of Gd_3NbO_7 below and above the phase transition temperature. In Chapter 7, different techniques including heat capacity measurement, synchrotron x-ray and neutron diffraction were performed on Nd_3NbO_7 and La_3NbO_7. All results confirmed a phase transition in these compounds. Crystallographic refinements of all phases below and above phase transition point are also presented.

Chapter 8 includes the analysis of infrared (IR) spectroscopy studies in Gd_3NbO_7. The nuclear site group analysis is used to calculate the possible modes in IR. Oscillator model is utilized to fit the spectrum and calculate the real and imaginary permittivity.

Chapter 9 covers correlations between dielectric properties and crystal structure. In weberite-type Ln_3NbO_7, T(ε_m) and normalized permittivity difference ($\Delta\varepsilon_r/\alpha$, α – ion polarizability of Ln^{3+}) increases with increasing the off-center shift of the 8 coordinated $Ln1^{3+}$ ions within their corresponding polyhedra. As for $Ln_2Ln'NbO_7$, the TCC increases with decreasing the average ionic radius of Ln^{3+} ($2/3r_{Ln} + 1/3r_{Ln'}$). The T_m increases with increasing the ratio of the ionic radius of *A* (Ln^{3+}) over *B* (Ln'^{3+} and Nb^{5+}). Finally Chapter 10 presents a summary of the dissertation and discusses the future work in the relevant research areas.

At the end of the thesis, there are five appendices including the study on CaO-TiO_2-Nb_2O_5 film (Appendix A), tolerance factor for pyrochlore (Appendix B), Raman spectroscopy (Appendix C), IR of La_3NbO_7 , Nd_3NbO_7 and Sm_3NbO_7 (Appendix D), and the structure and dielectric properties of Sm_3NbO_7 (Appendix E)

1.4 Contributions to the Field

This work investigates the structure-property relationships in fluorite-related Ln_3NbO_7 and $Ln_2(Ln'_{0.5}Nb_{0.5})_2O_7$ ceramics. The main contributions of this work to the field of materials science and engineering are summarized below:

1. A series of Ln_3NbO_7 (Ln^{3+} = La^{3+}, Nd^{3+}, and Gd^{3+}) compounds were studied to solve the contradictions regarding their crystal structure. Neutron powder diffraction and synchrotron XRD data was collected to solve the space group issue and present the correct structure.

2. The $La_2Ln'NbO_7$ (Ln'^{3+} = Yb^{3+}, Er^{3+} and Dy^{3+}) and Ln_2YbNbO_7 (Ln^{3+} = Nd^{3+}, Sm^{3+}, and Gd^{3+}) were synthesized for the first time. Based on Subramanian's[14] stability field and Isupov's[39] prediction, it was inferred that the crystal structure was likely to be cubic pyrochlore. However, the structural characterization indicates they (except Gd_2YbNbO_7) actually have an orthorhombic lattice. Gd_2YbNbO_7 has a tetragonal lattice. The structure is probably intermediate between orthorhombic weberite-type and cubic defect fluorite.

3. The dielectric properties of defect-fluorite Ln_3NbO_7 (Ln^{3+} = Dy^{3+}, Y^{3+}, Er^{3+}, and Yb^{3+}) were studied first time. The real part of the permittivity increases with increasing temperature. The TCC increases with decreasing the ionic radius of Ln^{3+}.

4. The weberite-type Ln_3NbO_7 (Ln^{3+} = La^{3+}, Nd^{3+}, and Gd^{3+}) exhibits dielectric relaxation above room temperature (RT). It was proven that the origin of the dielectric relaxation is a phase transition. The phase transition was found out to be chiefly mediated by the off-center shifts of both the Nb^{5+} and 8-coordinated $Ln1^{3+}$ ions.

5. Antipolar displacements were found in the low temperature phase of Nd_3NbO_7 and La_3NbO_7, indicating the potential of antiferroelectric.

6. In the LT phase of Gd_3NbO_7, there is a net dipole parallel to [010]. It indicates that Gd_3NbO_7 is an incipient ferroelectric.

7. It was found that the $T(\varepsilon_m)$ and $\Delta\varepsilon_r/\alpha$ increase with increasing the off-center shift of the 8-coordinated Ln^{3+} in weberite-type Ln_3NbO_7.

8. The $La_2Ln'NbO_7$ (Ln'^{3+} = Yb^{3+}, Er^{3+}, and Dy^{3+}) and Ln_2YbNbO_7 (Ln^{3+} = Nd^{3+} and Sm^{3+}) also exhibit dielectric relaxation but below 100 K. There is no phase transition found in these compounds. The T_m increases with increasing the ratio of the ionic radius of *A* (Ln^{3+}) over *B* (Ln'^{3+} and Nb^{5+}). The TCC at RT increases with decreasing the average ionic radius of Ln^{3+}. Only Gd_2YbNbO_7 has positive TCC (~225 MK^{-1}). Nd_2YbNbO_7 and Sm_2YbNbO_7 have the most stable

permittivity as a function of temperature with TCC ~ -40 MK^{-1}. It is possible that a small amount of Gd_2YbNbO_7 secondary phase inside Sm_2YbNbO_7 and Nd_2YbNbO_7 can compensate TCC to zero, which may have potential applications.

CHAPTER 2
BACKGROUND

The core of the first section of this chapter is chiefly based on the journal article (Acta Crystallographica Section B-Structural Science, ***65*** *269-290 (2009)) titled "Complex Ceramic Structures. I. Weberites," by L. Cai, and J.C. Nino.*[40] *It is reprinted with permission from International Union of Crystallography (IUCr).*

The present chapter briefly summarizes some of the theoretical background required for understanding the research work covered in the following chapters.

2.1 The Weberite Structure

The weberite crystal structure (space group: *Imma*, No. 74), with typical stoichiometry $A_2B_2X_7$ (*A* and *B* are cations, *X* is O or F), is a type of anion-deficient fluorite superstructure (AX_2). Possible ionic valences in weberite include $A_2^{1+}B^{2+}B^{3+}F_7$, $A_2^{2+}B_2^{5+}O_7$ and $A_2^{1+}B_2^{6+}O_7$. While several other compounds posses the same stoichiometry (pyrochlores, layered perovskites, *etc.*), weberites are isomorphic compounds with the mineral, Na_2MgAlF_7. This mineral was originally found in Ivigtut in southwestern Greenland and was named after Theobald Weber.[41] In 1944, Byström[42] determined the crystal structure with space group *Imm2*, basing his studies on the pyrochlore structure, which is another fluorite-related superstructure. It was later proven that the correct space group is *Imma*.[43-44] The detailed history of the controversy of the space group has been reviewed by Yakubovich *et al.*[1]

The atomic positions and site symmetry of the weberite structure are given in Table 2-1. The *A* ions sit in the *4a* and *4d* atomic positions with site symmetry 2/*m* and establish a coordination number of 8 with the anions. The *A* ions have two different coordination environments. The *A1* cations (in atomic position 4*d*) lie in a highly

distorted cube (or square prism) where there are two different *A1-X* bond lengths (Figure 2-1 (A) and (B)). The cubes are edge-shared to form a series of chains in the [100] direction (Figure 2-1 (C)). The *A2* cations (in atomic position 4*a*) are located within bi-hexagonal pyramids in which anions are spaced at three different distances from the central cations (Figure 2-2). Each pyramid is corner-shared with other two pyramids and edge-shared with four $A1X_8$ cubes. As presented in Table 2-1, there are three Wyckoff positions for anions (*X*1 at *8h, X*2 at *16j,* and *X*3 at *4e*). *A1* ions only connect to *X*1 and *X*2, while *A2* link to all three types of anions (two *X*1, four *X*2, and two *X*3).

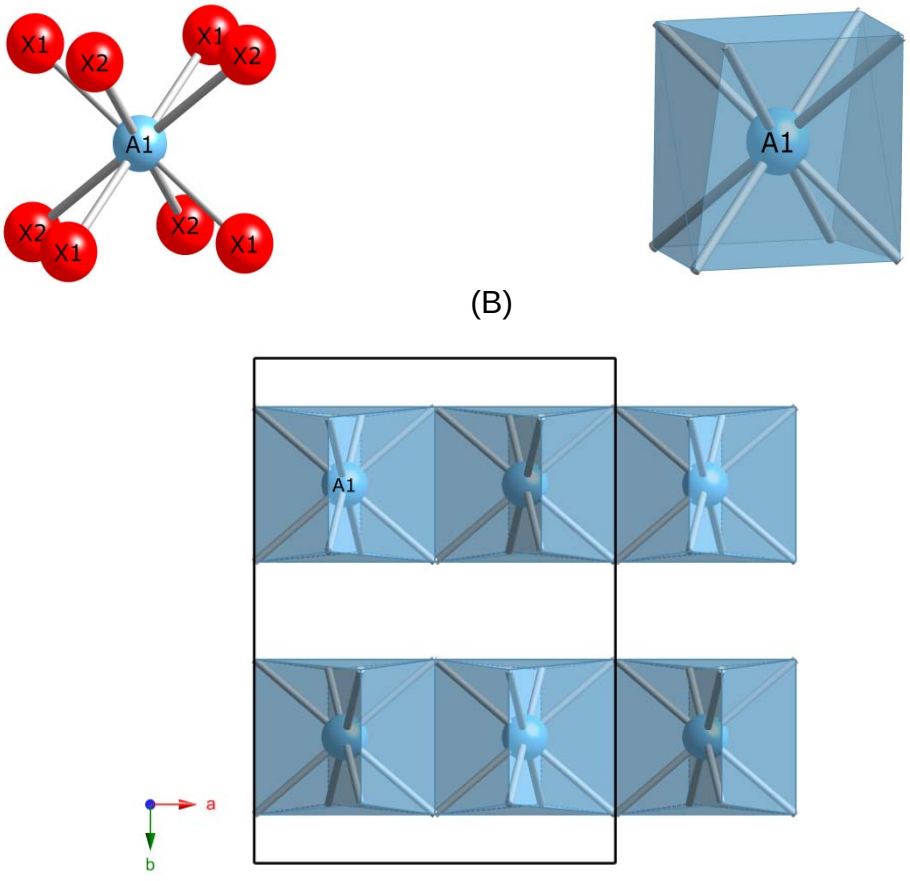

(A) (B)

(C)

Figure 2-1. (A) Ball-stick view of $A1X_8$ (B) Polyhedral view of $A1X_8$ (C) Edge-shared $A1X_8$ polyhedra form chains in [100]. The black lines indicate the unit cell.

(A) (B)

Figure 2-2. (A) Ball-stick view of $A2X_8$ (B) Polyhedral view of $A2X_8$. The shape of the polyhedra is bi-hexagonal pyramid.

Table 2-1. Weberite structure data (origin at *A* cations) with space group of *Imma*.[40]

Atoms	Wyckoff position	Site symmetry	Atomic position		
			x	y	z
A(1)	4*d*	2/m	0.25	0.25	0.75
A(2)	4*a*	2/m	0	0	0
B(1)	4*c*	2/m	0.25	0.25	0.25
B(2)	4*b*	2/m	0	0	0.5
X(1)	8*h*	m	0	y_1	z_1
X(2)	16*j*	1	x_2	y_2	z_2
X(3)	4*e*	mm2	0	0.25	z_3

X(1) is on A_3B interstitial site, *X*(2) is in A_2B_2 tetrahedron, and *X*(3) is inside A_4B_2.

The *B* ions are located in the *4b* and *4c* Wyckoff positions (site symmetry 2/m) and have a coordination number of 6, i.e. $A_2^{VIII}B_2^{VII}X_7$. There are two types of BX_6 octahedra: *B-1* (B^{2+} in the case of $A_2B^{2+}B^{3+}F_7$, *A* = Na^+ or Ag^+) in *4c* Wyckoff positions, and *B-2* (B^{3+} in the case of $A_2B^{2+}B^{3+}F_7$) in *4b* Wyckoff positions. Each of the six vertices of *B-1* octahedra connects to another *B*-octahedron while only four vertices of a *B-2* octahedron link to other *B*-octahedra (see Figure 2-3).

The arrangements of *A* and *B* ions lead to three different cation tetrahedra. Six anions occupy the two A_3B (A_3BX, *X*1) and four A_2B_2 tetrahedral interstices (A_2B_2X, *X*2) and none are located inside the two AB_3 sites ($AB_3[]$, where *[]* represents a vacant site) in a formula unit. The remaining anion (*X*3) maintains four coordination and lies outside the two edge-shared AB_3 tetrahedra, very close to the shared *B-B* edge (see Figure 2-4).

*X*3 can also be considered to sit inside the octahedron (A_4B_2), which shares faces with two adjacent AB_3 tetrahedra, and distort towards the *B-B* edge.[45]

(A) (B)

Figure 2-3. (A) a *B*-1 octahedron in the center and its connection to another six octahedra. (B) a *B*-2 octahedron connecting to 4 *B*-1 octahedra.[40]

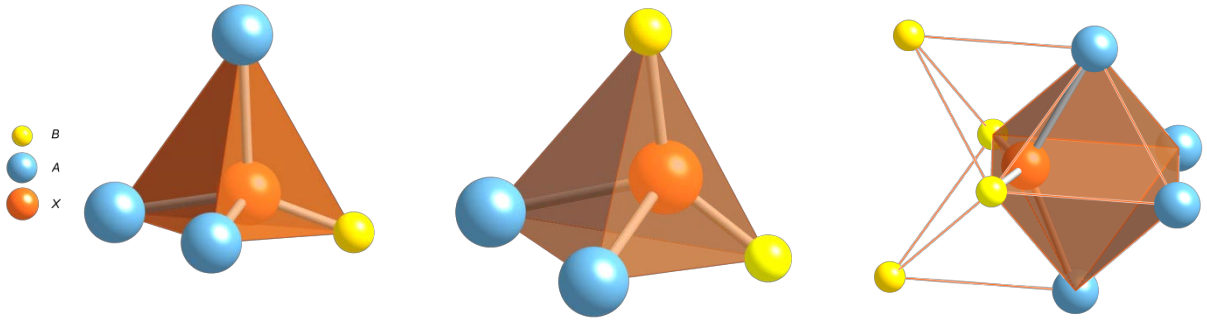

(A) (B) (C)

Figure 2-4. Anion coordination of weberite (A) *X*-1 inside A_2B_2 (B) *X*-2 inside A_3B (C) *X*-3 inside A_4B_2.[40]

2.1.1 Description of the Weberite Structure

A common way to describe the weberite structure is a network of corner-shared BX_6 octahedra with the penetration of *A* cations (see Figure 2-5). The *B-1* octahedra are corner-linked to each other and form *B-1* octahedral chains parallel to the *A1* chains (in the [100] direction). The *B-2* octahedra are isolated from each other and link the *B-1* octahedra chains to form a 3-D octahedral network.

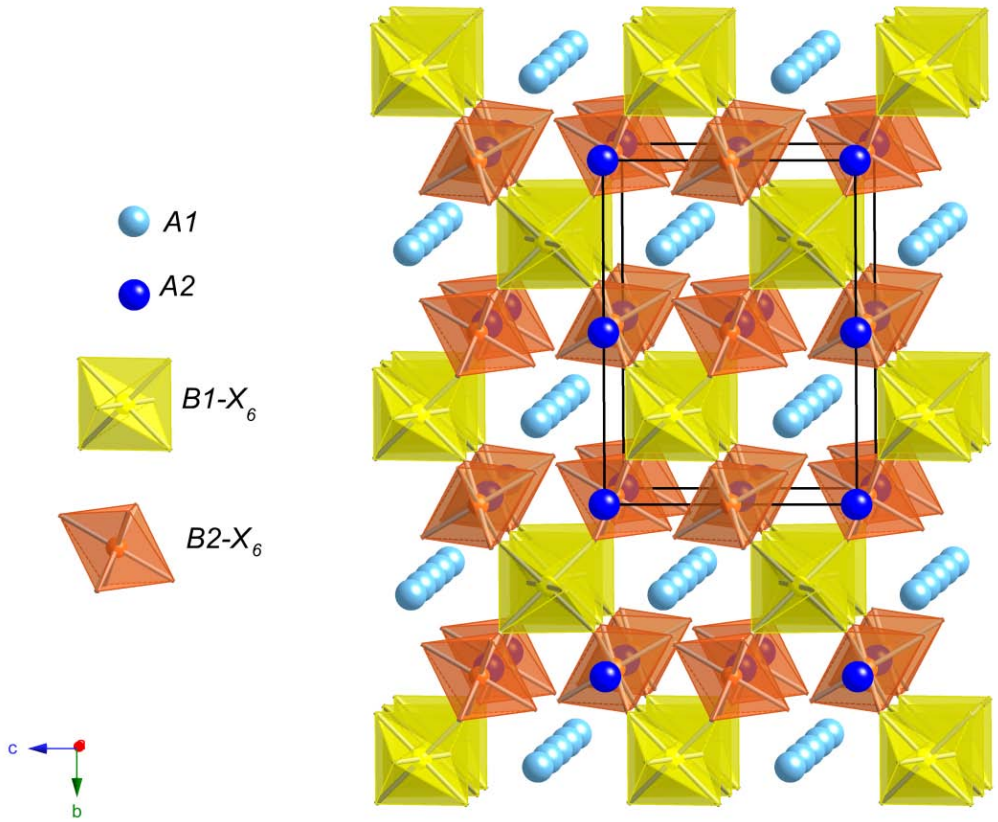

Figure 2-5. *B*-octahedral network and *A* cations in the nearly [100] direction.[40]

The weberite structure can also be considered as a stacking of repeated layers or slabs. The most common way to examine the structure is to view it as stacked, alternating close-packed metal layers A_3B and AB_3 on (011) parallel planes. In A_3B layers, four *A-1* and two *A-2* ions form a hexagonal ring with *B-2* occupying the center. In other words, the *A* cations form Kagomé-type networks [Kagomé in Japanese means a bamboo-basket woven pattern. It is formed by interlaced triangles and each lattice point has 4 equivalent bonds. The "Kagomé" crystallographic concept was introduced by Husimi[46] after he and his co-worker Syôzi found a new antiferromagnetic lattice by star-to-triangle transformation from a honeycomb lattice. Syôzi[47] published the first Kagomé paper in 1951. See Figure 2-6]. In AB_3 layers, the BX_6 octahedron arrangement is nearly identical with the basal plane of the hexagonal tungsten bronze

(HTB) structures and *A-2* cations are in the center of the hexagonal rings. The HTB-like layers can also be simplified by a Kagomé net representation (Figure 2-7). The HTB-like layers are displaced with respect to each other by an interlayer stacking vector (SV) which is defined as the projected distance, viewed down the (pseudo) six-fold axis, between crystallographically similar atoms in adjacent layers. White[48] and Cohelho *et al.*[49] used SV as an alternative description for zirconolite, zirkelite, pyrochlore and polymignyte. Here, SV is used to describe weberite. The stacking vectors in the weberite structure are nearly in the [0-11], [-31-1] and [31-1] directions. They are typically of the order 4 Å. The angle between successive stacking vectors (SA) is approximately 120°. The distance between two neighbouring HTB-like layers along the (pseudo) six-fold axis is approximately 5.8 Å. Figure 2-8 shows the stacking vectors between three sequences of HTB layers.

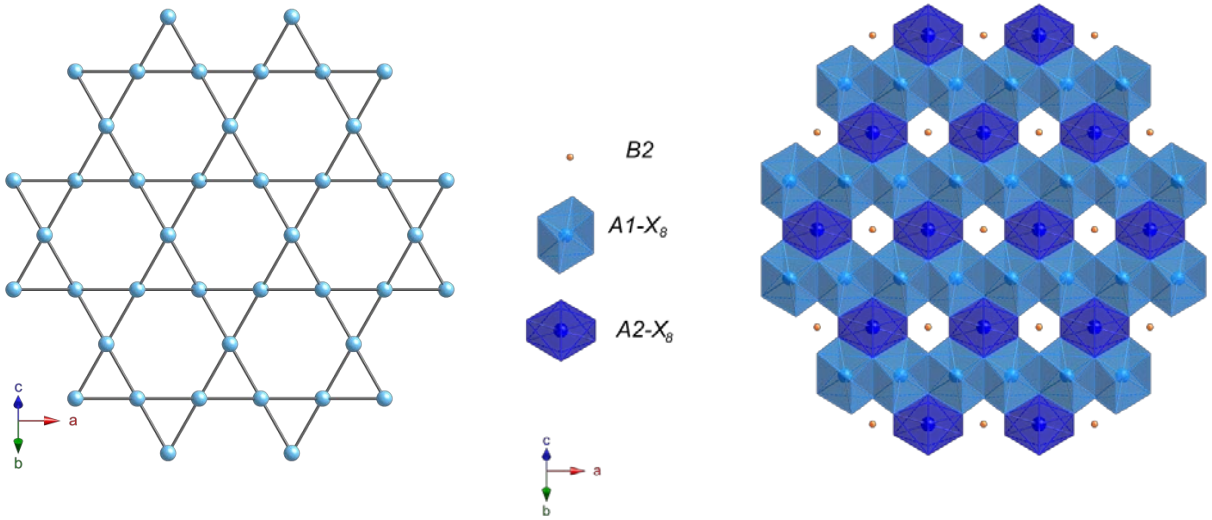

(A) (B)

Figure 2-6. (A) Kagomé net presentation of *A* cations on A_3B layers. (B) AX_8 polyhedral representation of A_3B layers, which are parallel to (011) plane.[40]

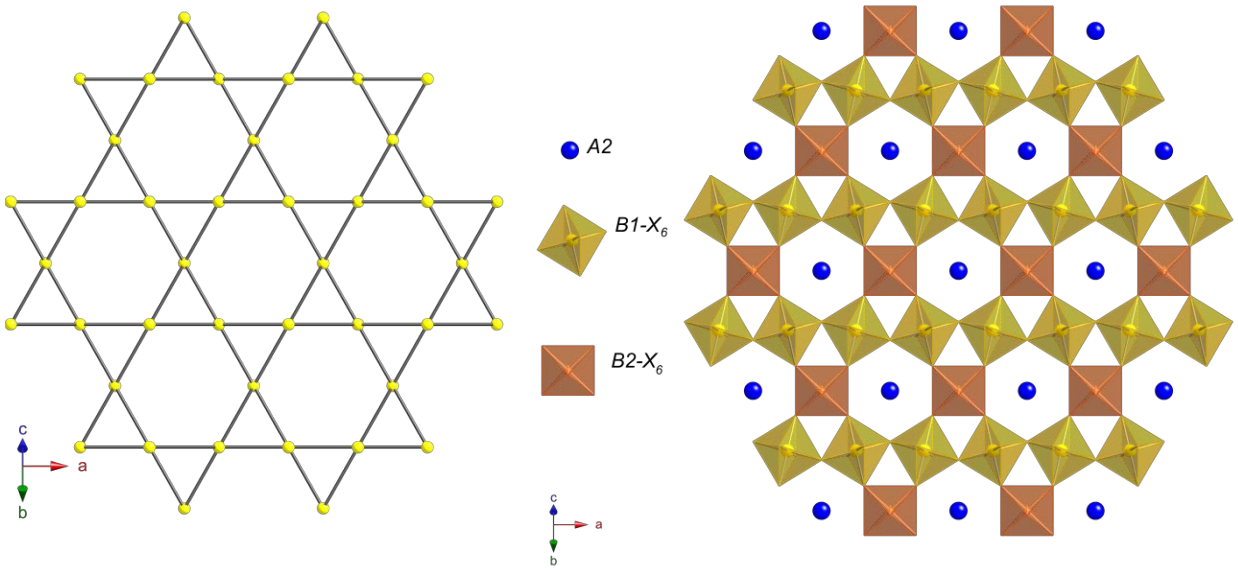

(A) (B)

Figure 2-7. (A) Kagomé net presentation of *B* cations on AB_3 layers. (B) BX_6 polyhedral representation of AB_3 layers, which are parallel to (011) plane.[40]

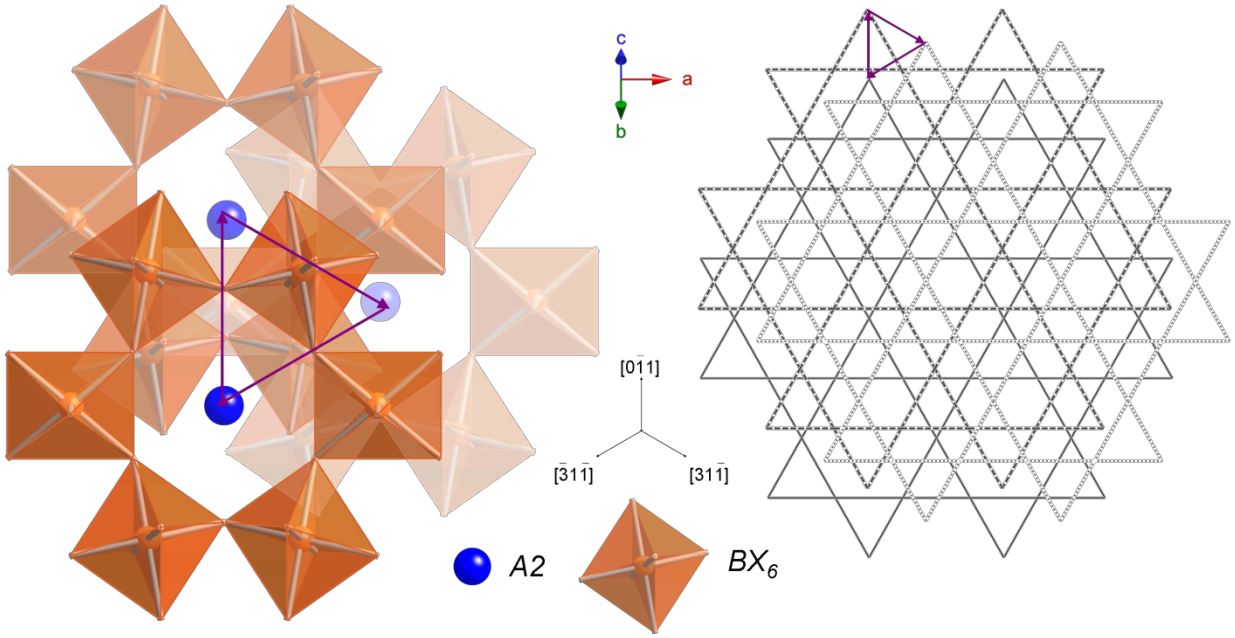

(A) (B)

Figure 2-8. (a) Stacking vectors (black arrows) between three sequence of HTB layers (b) Kagomé nets of three successive HTB layers (purple arrows are stacking vectors).[40]

There is yet another way to consider the weberite repeated layers. The first layer is formed by the alternating *B-1* octahedra chains and *A-1* distorted cube (or square prism) chains, which are in [100] direction for classic orthorhombic weberites. In this layer, the *B-1* octahedra are edge-shared with *A-1* cubes. The second layer is alternating *B-2* octahedra and *A-2* bi-hexagonal pyramids in the [100] direction as in Figure 2-9 and Figure 2-10.[36,50]

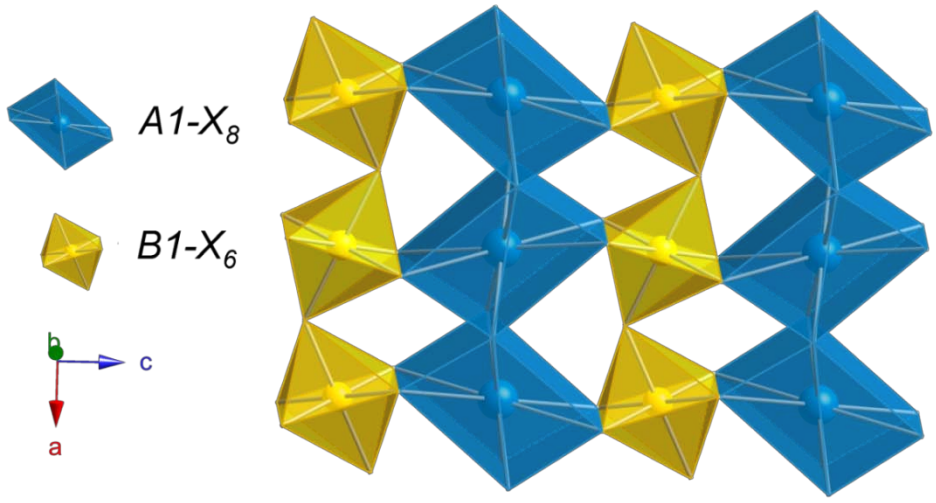

Figure 2-9. The layer of *A*1-X_8 lines and *B*1-X_6 lines, viewing in approximately [010].[40] direction.

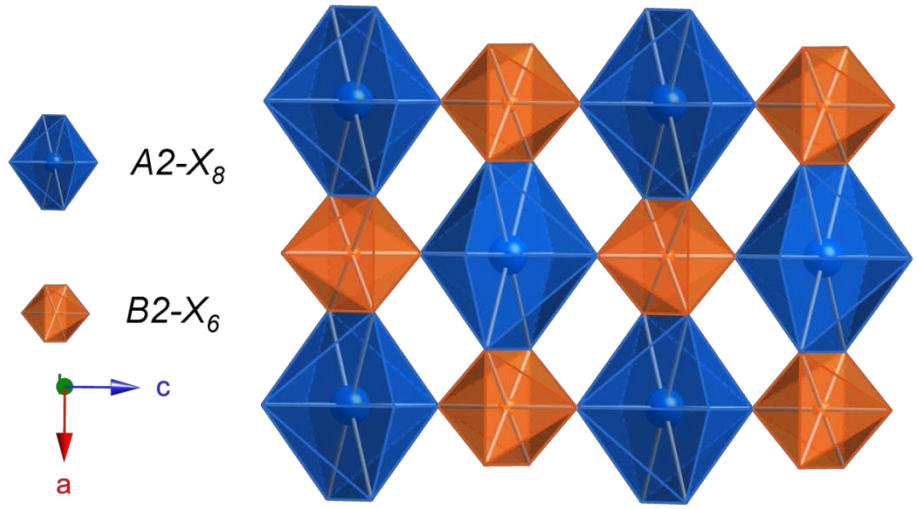

Figure 2-10. The *A*-2 and *B*-2 layers, viewing in approximately [010] direction.[40]

2.1.2 Relationship to Fluorite and Pyrochlore

Weberite and pyrochlore ($A_2B_2X_7$) are both fluorite-related superstructures. The coordination number of *A* and *B* is the same in both structures. These two structures have a similar cationic sublattice, which is arranged by stacking cubic close-packed cation layers, same as the (111) planes in fluorite. These layers alternate between the compositions A_3B and AB_3 and are parallel to (111) planes in pyrochlore and (011) planes in weberite (Figure 2-11). AB_3 layers in pyrochlore can also be described as HTB-like layers. The length of stacking vectors and the value of SA of the pyrochlore structure are almost the same as weberite. However, the difference between the weberite and the pyrochlore structures is the different stacking of two successive AB_3 and A_3B layers, which will be discussed later in this section. The crystallographic relationship between the weberite and the pyrochlore structures is further confirmed by the fact that the space group of weberite (*Imma*) is a subgroup of $Fd\bar{3}m$, the space group of pyrochlore.

If the lattice parameter of pyrochlores is 2*a* with respect to fluorite *a* (*a* ~ 5Å), then the lattice parameters of the classic orthorhombic weberites are approximately $\sqrt{2}\,a$, 2*a* and $\sqrt{2}a$. The rotation of 45° about the *b* axis of the fluorite or the pyrochlore cation sublattice leads to the weberite-like cation sublattice (Figure 2-12). The (111) planes of pyrochlore or fluorite are transformed to the (011) of the new lattice. Standard crystallographic transformations follow the guidelines from the international table for crystallography:[51]

$$(a,b,c)_w = (a,b,c)_f T \qquad (2\text{-}1)$$

where *a*, *b*, and *c* are the basis vectors. The subscript *w* stands for weberite and the subscript *f* indicates fluorite. The transformation matrix *T* implies both the change of

orientation and the length of the basis vectors. The transformation relationship between weberite (W), fluorite (F), and pyrochlore (P) can be written as following,

$$W = F\begin{pmatrix} 1 & 0 & 1 \\ 0 & 2 & 0 \\ -1 & 0 & 1 \end{pmatrix} = P\begin{pmatrix} 0.5 & 0 & 0.5 \\ 0 & 1 & 0 \\ -0.5 & 0 & 0.5 \end{pmatrix} \quad (2\text{-}2)$$

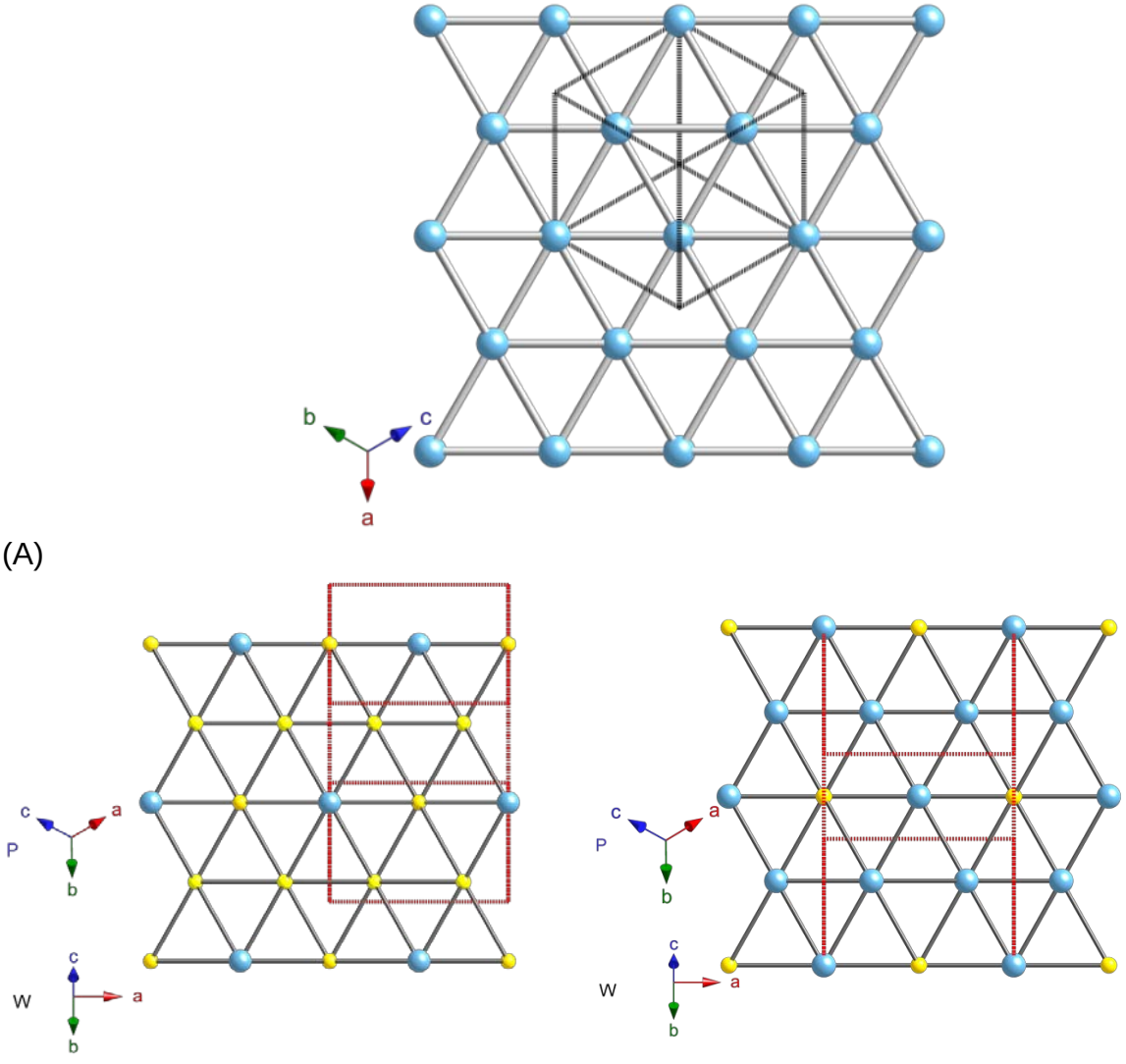

(A)

(B) (C)

Figure 2-11. (A) cationic network on the (111) of fluorite (B) AB_3 layer (C) A_3B layer on (011) of weberite; dash lines are unit cell.[40]

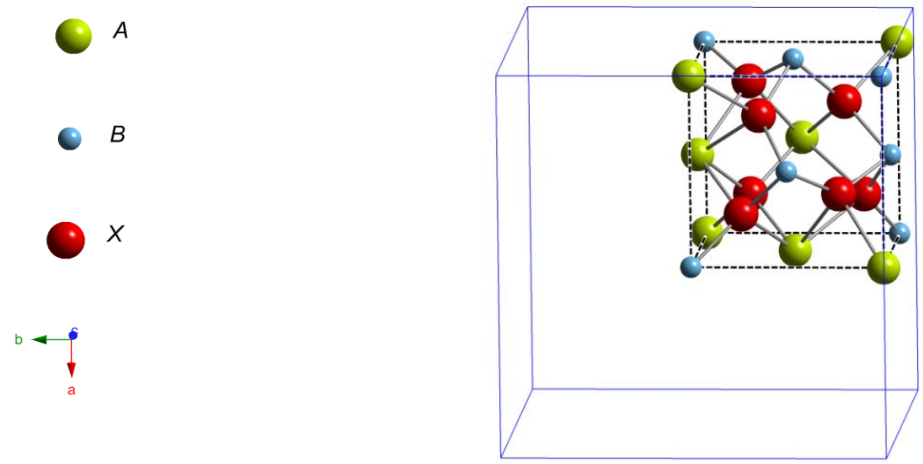

(A)

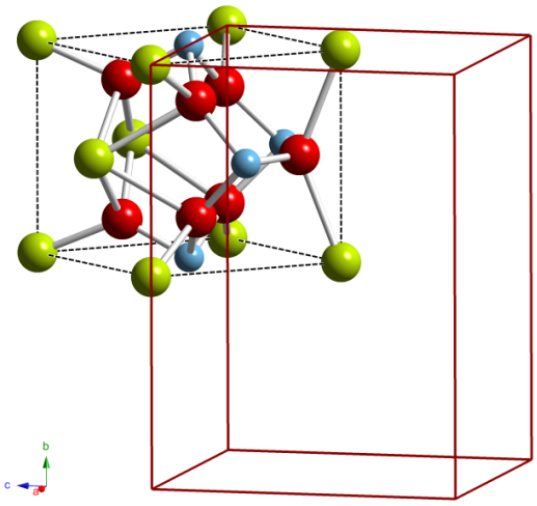

(B)

Figure 2-12. (A) Axial transformation of fluorite to pyrochlore (black dashed lines is a fluorite cell; blue solid lines is a pyrochlore cell). (B) Axial transformation of fluorite to weberite (black dashed lines - a fluorite cell, red solid lines - a weberite cell).

The transformation of pyrochlore leads to the space group *Imcm*, which is a different setting of *Imma*. The *Imma* lattice can be achieved by the 90^{o} rotation of the coordinate system of *Imcm.* The transformation matrix is

$$P_{Imma} = P_{Imcm}\begin{pmatrix} 0 & 1 & 0 \\ 0 & 0 & 1 \\ 1 & 0 & 0 \end{pmatrix} \tag{2-3}$$

The resulting lattice parameters in *Imma* are *2a,* $\sqrt{2}a$ and $\sqrt{2}a$. In order to match the weberite lattice parameters, the space group *Imcm* is preferred when presenting the atomic positions of pyrochlore in the weberite-like orthorhombic lattice (Table 2-2).

Table 2-2. Pyrochlore ($A_2B_2X_6X'$) structure data presented in space group of *Imcm* (origin at *B*).[40]

Atoms	Wyckoff position	Site symmetry	Atomic position		
			x	y	z
A	4b	2/m	0	0.5	0
	4c	2/m	0.25	0.25	0.25
B	4a	2/m	0	0	0
	4d	2/m	0.25	0.75	0.25
X	4e	mm2	0.5	x+0.25	0.25
	4e	mm2	0	x	0.25
	16j	1	x-0.125	0.125	x+0.125
X'	4e	mm2	0.25	0.375	0

The x (0.3125 – 0.375) is the oxygen parameter inside A_2B_2 tetrahedral site.

It is easy to recognize weberite and distinguish the three structures from powder diffraction. As it is well known, in Cu*Kα* radiation until $2\theta \sim 70^o$, the five fluorite characteristic peaks are (111), (200), (220), (311) and (222). The (111) reflection is at $2\theta \sim 30^o$ with the highest intensity. In pyrochlore, owing to the doubling of the lattice parameter with respect to fluorite, the five fluorite peaks become (222), (400), (440), (622) and (444). The appearance of several weak reflections especially the (111) peak at $2\theta \sim 15^o$ is a major difference between the XRD patterns of fluorite and pyrochlore. In orthorhombic weberite, the five fluorite peaks are split, for example, the most intense $(111)_f$ or $(222)_p$ are split into $(022)_w$ and $(220)_w$. There are several more reflections in weberite, which are systematic absences in pyrochlore, for example, $(101)_w$ and $(020)_w$ (corresponding to $(200)_p$). Details on the XRD reflection for fluorite, pyrochlore, and

weberite are listed in Table 2-3. For space reasons, only reflections up to $(222)_f$ are presented.

Table 2-3. XRD reflections for fluorite, pyrochlore and weberite.[40]

XRD reflections			
hkl (Fluorite)	hkl (Pyrochlore)	hkl (Weberite)	Corresponding Pyrochlore plane
	1 1 1	0 1 1	1 1 1
		1 0 1	2 0 0
		0 2 0	0 2 0
	2 2 0	0 0 2	2 0 2
		1 2 1	2 2 0
		2 0 0	2 0 -2
	3 1 1	1 1 2	3 1 1
		2 1 1	3 1 -1
		0 3 1	1 3 1
1 1 1	2 2 2	0 2 2	2 2 2
		2 2 0	2 2 -2
2 0 0	4 0 0	2 0 2	4 0 0
		0 4 0	0 4 0
	3 3 1	0 1 3	3 1 3
		1 3 2	3 3 1
		2 3 1	3 3 -1
		1 0 3	4 0 2
		2 2 2	4 2 0
		3 0 1	4 0 -2
		1 4 1	2 4 0
		1 2 3	4 2 2
		0 4 2	2 4 2
		3 2 1	4 2 -2
		2 4 0	2 4 -2
	3 3 3	0 3 3	3 3 3
		2 1 3	5 1 1
	5 1 1	3 1 2	5 1 -1
		0 5 1	1 5 1
2 2 0	4 4 0	0 0 4	4 0 4
		2 4 2	4 4 0
		4 0 0	4 0 -4

Table 2-3. XRD reflections for fluorite, pyrochlore and weberite (Continued).[40]

XRD reflections			
hkl (Fluorite)	hkl (Pyrochlore)	hkl (Weberite)	Corresponding Pyrochlore plane
	5 3 1	1 1 4	5 1 3
		2 3 3	5 3 1
		1 5 2	3 5 1
		3 3 2	5 3 -1
		2 5 1	3 5 -1
		4 1 1	5 1 -3
	4 4 2	0 2 4	4 2 4
		1 4 3	4 4 2
		3 4 1	4 4 -2
		4 2 0	4 2 -4
		3 0 3	6 0 0
		0 6 0	0 6 0
	6 2 0	2 0 4	6 0 2
		3 2 3	6 2 0
		4 0 2	6 0 -2
		1 6 1	2 6 0
	5 3 3	1 3 4	5 3 3
		0 5 3	3 5 3
		4 3 1	5 3 -3
3 1 1	6 2 2	2 2 4	6 2 2
		0 6 2	2 6 2
		4 2 2	6 2 -2
		2 6 0	2 6 -2
2 2 2	4 4 4	0 4 4	4 4 4
		4 4 0	4 4 -4

It is important to recall that in fluorites, each anion is at the center of the cationic tetrahedra (A_4X). The arrangement of *A* and *B* leads to different cation tetrahedra: AB_3, A_3B and A_2B_2 in weberites and A_4, B_4 and A_2B_2 in pyrochlores. The reason for the formation of different cation tetrahedra is that weberites and pyrochlores are different in their stacking two neighboring AB_3 and A_3B layers, though generally they follow the pattern of cubic close-packed cation layers. The three nearest-neighbor metal atoms in these layers form pseudo equilateral triangles. The distribution of *A* and *B* cations in AB_3 layers will lead to 2 types of triangles: AB_2 and B_3. The cations in the following A_3B layer lie above the centers of these triangles. If an AB_3 layer is a reference, there are

$\sqrt{2}a/2$ along $[100]_w$ or $[10\text{-}1]_P$ displacement in the above A_3B layer between weberite and pyrochlore. As a result, in the A_3B layer, A cations are above the center of AB_2 triangles and B cations are above B_3 triangles in pyrochlore, while in weberite, 2/3 A (*A-1*) and all B cations are above the AB_2 triangles and the remaining A cations (*A-2*) are above B_3 triangles (see Figure 2-13 and Figure 2-14). Therefore, these arrangements lead to two AB_3, two A_3B, and four A_2B_2 in a formula unit of weberite, and in the case of pyrochlore, one A_4, six A_2B_2, and one B_4. In addition, different stacking of two neighboring AB_3 and A_3B layers can explain why the transformation of the pyrochlore cation sublattice into a weberite-like lattice results in a different setting of the space group.

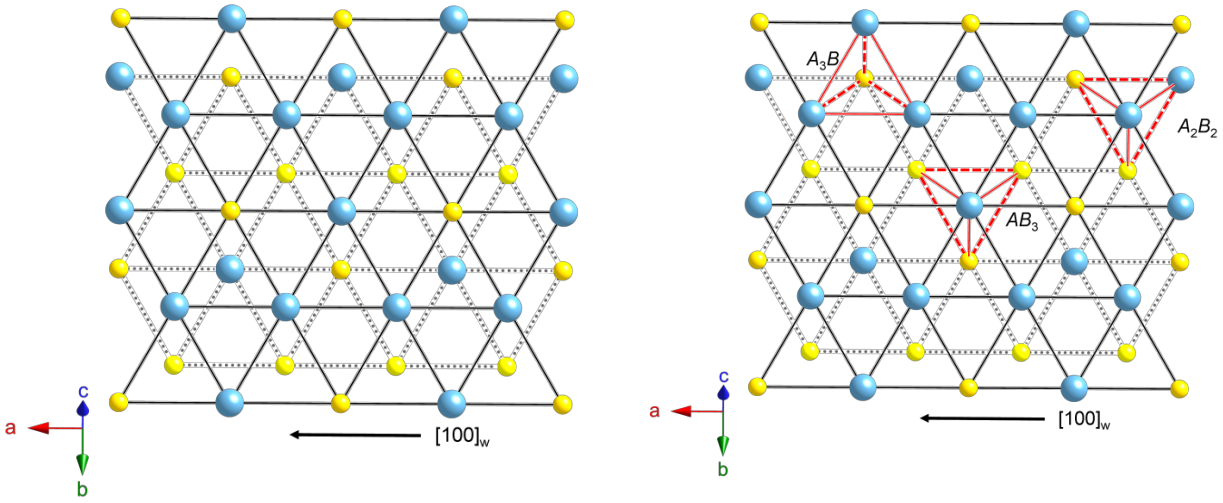

(A) (B)

Figure 2-13. (A) One A_3B and AB_3 slab of weberite. (B) A_3B and AB_3 slab of weberite showing the cationic tetrahedra. Cations connected by dotted lines are on the A_3B layer and by grey lines are on the AB_3 layer. The red lines (or dashed line) show cation tetrahedra.[40]

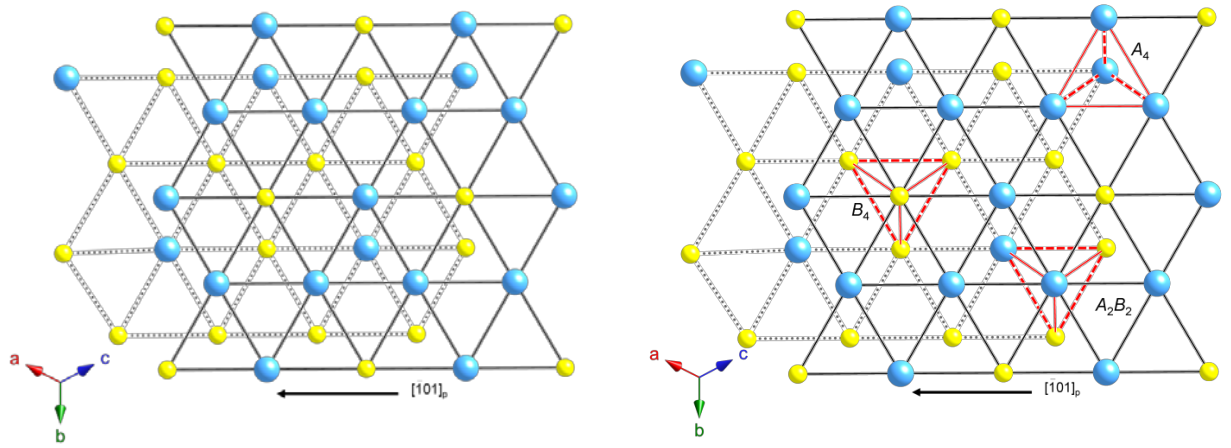

(A) (B)

Figure 2-14. (A) One A_3B and AB_3 slab of pyrochlore. (B) A_3B and AB_3 slab of pyrochlore showing the cationic tetrahedra. Cations connected by dotted lines are on the A_3B layer and by grey lines are on the AB_3 layer. The red lines (or dashed line) show cation tetrahedra.[40]

As stated before, in a formula unit, the *X3* anion of weberite is located outside the cation tetrahedra and leaves two AB_3 tetrahedra with a vacant center. In contrast, all anions in the pyrochlore structure are inside the cation tetrahedra. Therefore, it can be argued that pyrochlore is more closely related to fluorite than weberite since the former preserves all the anions in cation tetrahedral interstices.[1,45] In weberite, it is understandable that the *X*-deficient site is more favorable in *B*-rich tetrahedra (AB_3 than A_2B_2 and A_3B) because *B* ions have less coordination number. However, it raises the question: why there are two AB_3 tetrahedra with a vacant center and the *X3* is not inside the cation tetrahedra? Grey *et al.*[45] argued that in $Ca_2Ta_2O_7$ weberite, the sum of valence ($\sum v/CN$, CN is the coordination number, v is the oxidation states for each ions) in $CaTa_3$ tetrahedra is so highly over-saturated that $CaTa_3$ cannot accommodate *X3*. An ionic structure will be stable if the sum of valence of the cations equals the charge on the anion that the cations bonded to. Actually, the highly over-saturated AB_3 tetrahedra occur in all weberite compounds: $A_2^{1+}B^{2+}B^{3+}F_7$, $A_2^{2+}B_2^{5+}O_7$ and $A_2^{1+}B_2^{6+}O_7$.

The nominal sum of valence in the center of AB_3 is 1.46 for $A_2^{1+}B^{2+}B^{3+}F_7$, 2.75 for $A_2^{2+}B_2^{5+}O_7$, 3.13 for $A_2^{1+}B_2^{6+}O_7$. Thus, anions should distort largely towards *A* cations to meet the required valence, which would then result in a shorter *A-X* distance than a *B-X* distance. However, *A* ions are larger and have more CN than *B* ions and so the *A-X* bond length should be larger than the *B-X* bond length. The end result is that anions cannot move towards *A* cations and the required valence cannot be achieved. By contrast, the sum of valence in the center of AB_3 is under-saturated, being 0.875 for $A_2^{1+}B^{2+}B^{3+}F_7$, 1.58 for $A_2^{2+}B_2^{5+}O_7$ and 1.375 for $A_2^{1+}B_2^{6+}O_7$. Anions are required to move towards *B* cations, which is favored by the bond length argument above. As for A_2B_2 tetrahedra, the sum of valence is 1.08 for $A_2^{1+}B^{2+}B^{3+}F_7$, 2.17 for $A_2^{2+}B_2^{5+}O_7$, and 2.25 for $A_2^{1+}B_2^{6+}O_7$. In this case, the sum of valence is close to the anion oxidation state.

In order to check the stability of the *X3*, the empirical equation by Brese and O'Keeffe[52] is used to calculate the valence of the *X3*:

$$V_i = \sum v_{ij} = \sum \exp((R_{ij} - r_{ij})/b) \qquad (2\text{-}4)$$

where R_{ij} is the bond-valence parameter, r_{ij} is the bond distance and *b* is a constant. Three representative compounds were chosen for detailed analysis: $Na^{1+}{}_2Mg^{2+}Al^{3+}F_7$, $Sr^{2+}{}_2Sb^{5+}{}_2O_7$ and $Ag^{1+}{}_2Te^{6+}{}_2O_7$. There is few, if any reported bond length data for $Ag_2B_2F_7$. Na_2MgAlF_7 was chosen since it is the aristotype of the weberite compounds. The r_{ij} of $Na^{1+}{}_2Mg^{2+}Al^{3+}F_7$ is from Knop *et al.*[53] based on single crystal XRD. $Sr^{2+}{}_2Sb^{5+}{}_2O_7$ was chosen because it is a stable weberite even under high pressure and neutron diffraction data is available.[54-55] As for $A_2^{1+}B_2^{6+}O_7$ compounds, only $Ag_2Te_2O_7$ crystal structure has been reported.[56] Table 2-4 lists the detailed valence information including all three anion types as well as cations by the empirical equation above using

the bond-valence parameters[52,57] and the bond lengths (r_{ij}) from literature. The valence of *X3* is close to its oxidation state in these compounds.

Table 2-4. Examples of bond valence sum for anions and cations by Brese and O'Keeffe (r_{ij} is the bond distance, v_{ij} is the bond valence.)

Na_2MgAlF_7

X(1) in A_3B tetrahedra				X(2) in A_2B_2 tetrahedra				X(3) outside the AB_3 tetrahedra			
bonds	r_{ij} (Å)	v_{ij}	$\sum v_{ij}$	bonds	r_{ij} (Å)	v_{ij}	$\sum v_{ij}$	bonds	r_{ij} (Å)	v_{ij}	$\sum v_{ij}$
Al-F	1.825	0.469	0.972	Mg-F	1.960	0.360	1.022	Mg-F	1.951	0.368	0.866
Na2-F	2.211	0.236		Al-F	1.793	0.512		Mg-F	1.951	0.368	
Na1-F	2.423	0.133		Na2-F	2.549	0.095		Na2-F	2.689	0.065	
Na1-F	2.423	0.133		Na1-F	2.749	0.055		Na2-F	2.689	0.065	

$Na(1)^{1+}$: $\sum v_{ij}$ =0.779; $Na(2)^{1+}$: $\sum v_{ij}$ = 0.981; Mg^{2+}: $\sum v_{ij}$ = 2.17; Al^{3+}: $\sum v_{ij}$ = 2.89

$Sr_2Sb_2O_7$

X(1) in A_3B tetrahedra				X(2) in A_2B_2 tetrahedra				X(3) outside the AB_3 tetrahedra			
bonds	r_{ij} (Å)	v_{ij}	$\sum v_{ij}$	bonds	r_{ij} (Å)	v_{ij}	$\sum v_{ij}$	bonds	r_{ij} (Å)	v_{ij}	$\sum v_{ij}$
Sb2-O	1.922	1.056	2.280	Sb1-O	1.971	0.926	2.151	Sb1-F	2.005	0.843	1.963
Sr2-O	2.363	0.515		Sb2-O	2.202	0.512		Sb1-F	2.005	0.843	
Sr1-O	2.502	0.354		Sr1-O	2.833	0.145		Sr2-F	2.850	0.138	
Sr1-O	2.502	0.354		Sr2-O	2.599	0.273		Sr2-F	2.850	0.138	

$Sr(1)^{2+}$: $\sum v_{ij}$ =1.996; $Sr(2)^{2+}$: $\sum v_{ij}$ = 2.40; $Sb(1)^{5+}$: $\sum v_{ij}$ = 5.39; $Sb(2)^{5+}$: $\sum v_{ij}$ = 5.34

$Ag_2Te_2O_7$

X(1) in A_3B tetrahedra				X(2) in A_2B_2 tetrahedra				X(3) outside the AB_3 tetrahedra			
bonds	r_{ij} (Å)	v_{ij}	$\sum v_{ij}$	bonds	r_{ij} (Å)	v_{ij}	$\sum v_{ij}$	bonds	r_{ij} (Å)	v_{ij}	$\sum v_{ij}$
Te2-O	1.825	1.281	1.864	Ag1-O	2.806	0.067	2.041	Ag2-O	2.806	0.067	1.983
Ag2-O	2.388	0.207		Ag2-O	2.549	0.134		Ag2-O	2.806	0.067	
Ag1-O	2.465	0.168		Te1-O	1.997	0.806		Te1-O	1.946	0.925	
Ag1-O	2.465	0.168		Te2-O	1.905	1.034		Te1-O	1.946	0.925	

$Ag(1)^{1+}$: $\sum v_{ij}$ = 0.939; $Ag(2)^{1+}$: $\sum v_{ij}$ = 1.084; $Te(1)^{6+}$: $\sum v_{ij}$ = 5.785; $Te(2)^{6+}$: $\sum v_{ij}$ = 5.983.

Another significant difference is the formation of BX_6 networks. All of the anions in weberites participate in the formation of BX_6 octahedra but only 6/7 of the anions in pyrochlores do so. The BX_6 octahedral network in both structures is fairly rigid. Therefore, in order to maintain the octahedral network, it is difficult for the weberite to form vacancies at anion sites. By contrast, the pyrochlore structure tolerates *X* deficiency or paired *A* and *X* deficiencies relatively easily. Examples of such pyrochlore oxides are $Bi_{1.5}Zn_{0.92}Nb_{1.5}O_{6.92}$ and $Tl_2B_2O_6$ (*B* = Nb, Ta and U), $Tl_2Os_2O_{7-x}$ and

$Pb_2Os_2O_{7-x}$.[6,14,58] In addition, the substitution of small amounts of oxygen by F^- may prevent the formation of weberites. For example, $Ca_2Sb_2O_7$ pyrochlore transforms into weberite irreversibly above 973 K but $CaNaSb_2O_6F$ and $Ca_{1.56}Sb_2O_{6.37}F_{0.44}$ pyrochlores are stable.[59-60]

2.1.3 Weberite-like Structures

The weberite structures show a wide variety of different modifications including monoclinic and trigonal variants. Grey *et al.*[45] proposed the use of the nomenclature of the International Mineralogical Association Commission New Minerals and Mineral Names (IMA-CNMMN), which was initially approved for zirconolite $CaZrTi_2O_7$.[61] As discussed above, the basic building unit is a slab formed by one A_3B and one AB_3 layers. The differences between weberites are the crystal system and the number of slabs (*N*) in a unit cell. A notation which combines *N* and the first letter crystal system is used to indicate different weberites. For example, the notation of the classic orthorhombic weberite is *2O* because it has two slabs in a unit cell. The reported weberites include *2O*, *2M*, *3T*, *4M*, *5M*, *6M*, *6T*, *7M* and *8O*. $(NaCu)Cu_2F_7$ (or $NaCu_3F_7$, space group *C2/c*) and $(Ca_{0.5}Ln_{1.5})(Ca_{0.5}Sb_{1.5})O_7$ (or $CaLn_{1.5}Sb_{1.5}O_7$, space group *I2/m11*, Ln^{3+} = La^{3+}, Pr^{3+}, Nd^{3+}, and Y^{3+}) are special *2M* weberites and more like pseudo-*2O* weberites for they maintain the structural feature of *2O* rather than *2M*. $Ca_2Ta_2O_7$-based compounds are important in weberite family since for $N > 4$, only $Ca_2Ta_2O_7$-based compounds have been reported. Grey and co-workers[45,62-64] have shown that $Ca_2Ta_2O_7$ compounds can crystallize into *3T*, *4M*, *5M*, *6T*, *6M* and *7M* by different doping or synthesis methods and later Ebbinghaus *et al.*[65] also synthesized an *8O* $Ca_2Ta_2O_7$ single crystal using the optical floating zone method.

A significant difference between *2O* and non-*2O* weberites is that the AB_3 and A_3B layers are parallel to the (011) planes for *2O* and parallel to the (001) planes for other weberites except for $NaCu_3F_7$ and $CaLn_{1.5}Sb_{1.5}O_7$ (Ln^{3+} = La^{3+}, Pr^{3+}, Nd^{3+}, and Y^{3+}). The formula unit (Z) of $NaCu_3F_7$ and $CaLn_{1.5}Sb_{1.5}O_7$ is also consistent with *2O* weberites, 4 rather than 8, the latter the formula unit for other *2M* weberites. As in section 2.1.2, the lattice parameters of *2O* weberites are approximately $\sqrt{2}a$, $2a$ and $\sqrt{2}a$ (a ~ 5Å, the lattice parameter for fluorite). The lattice parameters of *2M* weberites are nearly $\sqrt{6}a$, $\sqrt{2}a$ and $\sqrt{6}a$. The [0-11], [100] and [011] vectors of *2O* become [100], [010] and [001] of *2M*. The lattice parameter difference between *2M*, *4M*, *5M*, *6M* and *7M* is mainly on the *c*-axis. The lattice parameters for *nM* (n = 2, 4, 5 and 7) are approximately $\sqrt{6}\ a$, $\sqrt{2}\ a$ and $(n\sqrt{6}/2)\ a$ and they are nearly $\sqrt{2}\ a$, $\sqrt{6}\ a$ and $3\sqrt{6}/\ a$ for *6M*.[45,62-64] The *8O* weberite is closely related to monoclinic variant rather than *2O* in both the orientation of AB_3 and A_3B layers and the lattice parameters. The lattice parameters are nearly $\sqrt{2}a$, $\sqrt{6}a$ and $4\sqrt{6}/a$. As for *3T*, the [100], [-0.5,-0.5, 0.5] and [012] vectors in *2O* are transformed into the basal vectors. The resulting lattice parameters are approximately $\sqrt{2}\,a$, $\sqrt{2}a$ and $2\sqrt{3}a$. The relationship of *2O*, *2M* and *3T* weberites is shown in Figure 2-15. Meanwhile, the lattice parameters of *6T* are approximately $\sqrt{2}\,a$, $\sqrt{2}a$ and $4\sqrt{3}a$, just double the length of the basal vector in *c*-axis.

For *2O* weberites, there are two special types in which the body-center symmetry is lost. The first case is when Cu^{2+} is introduced into $Na_2B^{2+}B^{3+}F_7$ at *B-1* sites such as Na_2CuCrF_7 and Na_2CuInF_7.[66-67] The CuF_6 octahedra are elongated perpendicular to the *B*-1 chains, which leads to the lowering of symmetry while maintaining the orthorhombic lattice. The space group is reduced to *Pmnb*, a subgroup of *Imma*.[1]

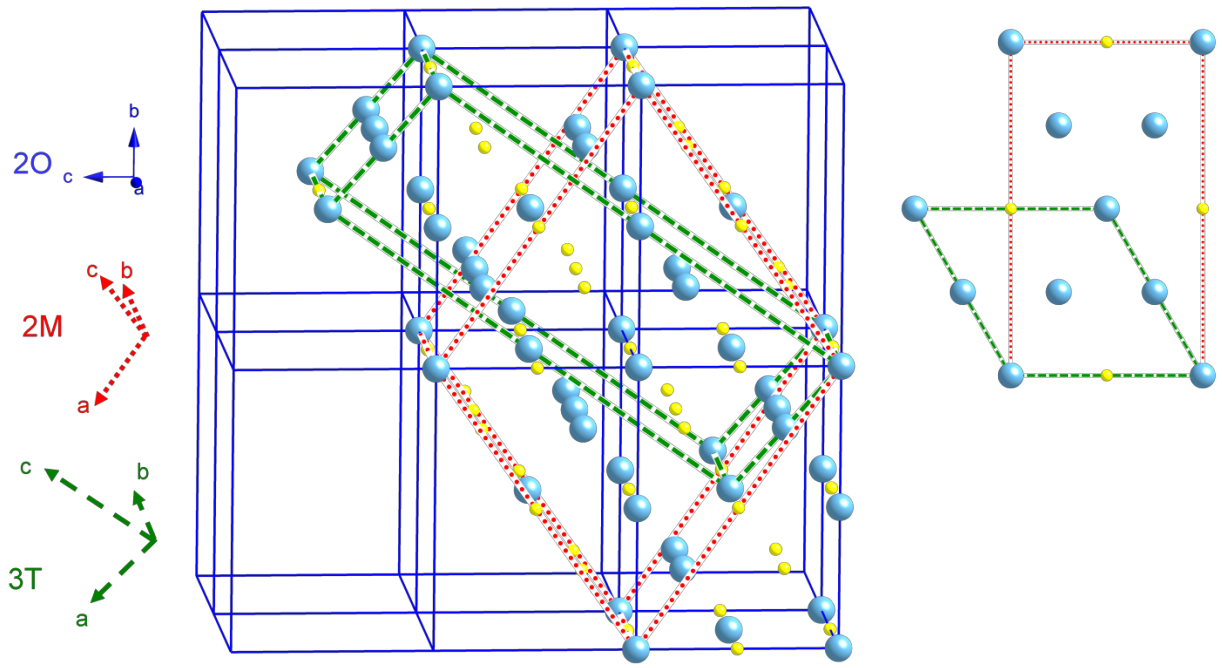

(A) (B)

Figure 2-15. (A) Relationship between *2O*, *2M*, and 3T weberites (origin at *A2* site); large spheres are *A* ions and small spheres are *B* ions; blue solid lines are the multiple unit cells of *2O*, red dotted lines are the unit cell of *2M* and green dashed lines are the unit cell of *3T*. (B) (001) plane of *3T* (green dashed lines) and *2M* (red dotted lines, also indicating (011) of *2O*).

Another case of losing *I*-centring symmetry happens when the ionic radius of *B*-2 is larger than that of *B*-1. In a classic *2O* weberite structure, the ionic radius of *B*-2 is equal or smaller than that of *B*-1. When a larger *B*-2 ion appears in a weberite compound, the anions, which are shared by two *B*-1 octahedra neighbours distort toward *B*-2 ions. As a result, the *A*-2 ions cannot hold 8-coordination and change to 7-coordination. The *B*-2 ion keeps octahedral coordination with a seventh anion relatively close to it. As in the case of Na_2NiInF_7, the distance between the distorted anion and B-2 (In^{3+}) is only 1.3 times larger than the shortest In-F bond length in *B*-2 octahedra.[68] In a *2O* weberite structure, the ratio of the two distances is higher, such as 1.97 in Na_2MgAlF_7 or 1.83 in $Ca_2Os_2O_7$.[58,69] The distortion of anion excludes the *I*-centering of

the structure and results in the space group *Pnmb*.[1] The extreme of the second case is $Ln_2(B,Ln)O_7$ (or Ln_3BO_7, where Ln^{3+} is a rare earth element, and *B* is Os^{5+}, Re^{5+}, Ru^{5+}, Re^{5+}, Mo^{5+}, Ir^{5+}, Sb^{5+}, Nb^{5+} or Ta^{5+}), which is covered in detail in section 2.2.

2.1.4 Stability Field

Both pyrochlores and weberites have BX_6 octahedral networks. Due to the fact that *B-2* octahedra have two unpaired vertices, the BX_6 octahedral network in weberite is typically less compact. Therefore, weberite has more potential to permit larger radius of *A* ions. Figure 2-16 shows R_A vs. R_B diagram for 159 pyrochlore oxides and 131 weberite compounds (83 weberite fluorides and 48 weberite oxides, see Table 2-5 and Table 2-6, which are listed at the end of the chapter). The 159 pyrochlore oxides are taken from two reviews.[14,39] Figure 2-16 indicates that the majority of pyrochlores have R_A ranging from 0.97 Å to 1.13 Å while most weberites have R_A value from 1.10 Å to 1.30 Å. Weberite $Ba_2U_2O_7$ has the highest R_A - 1.42 Å.[27,70] This clearly shows that larger R_A prefers the formation of the weberite.[71] The ratio of R_A/R_B for the weberite is between 1.5 and 2. The two end members are $Cd_2Sb_2O_7$ and $Ag_2Te_2O_7$. However, the range of R_A/R_B for weberite greatly overlaps with the stability field for pyrochlore, 1.46 ~ 1.8 for $A_2^{3+}B_2^{4+}O_7$ and 1.4 ~ 2.2 for $A_2^{2+}B_2^{5+}O_7$.[14] Therefore, ionic radius ratio is not the only determining factor in the structural stability.

Electronegativity (χ) is another important factor in the field of existence, because the formation of weberites is closely related to the covalent character of the bonds.[72-75] Weller *et al.*[74] used only χ_A and χ_B to picture the stability field of the weberite, but their study only included a limited number of compounds. Lopatin *et al.*[73,76] successfully utilized χ_A and R_A/R_B to distinguish pyrochlores and weberites and χ_B and R_A/R_B to

determine the different regions of the weberite and the layered perovskite. They chose Allred-Rochow[77] electronegativities (which were completed by Little and Jones[78]) because Allred-Rochow electronegativities are more precise when measuring the degree of covalent character of the bonds. Sych *et al.*[72] introduced R_A/R_B *versus* relative ionicity of *A-O* bond, which is a ratio of the ionicity of *A-O* bond to the sum of ionicity of *A-O* and *B-O* bonds. The ionicity of *A-O* bond is calculated as

$$I_{A\text{-}O} = 1 - \exp[-0.25(\chi_A - \chi_O)^2] \quad (2\text{-}5)$$

They used the electronegativities for the crystalline state calculated by Batanov.[79] The advantage of relative ionicity is that it contains the information for both *A-O* and *B-O* bonds. Therefore, relative ionicity of *A-O* vs. R_A/R_B is used to determine the stability field in this study, as shown in Figure 2-17 and Figure 2-18. Here, Allred-Rochow[77] and Little-Jones[78] electronegativities are used in calculating the ionicity.

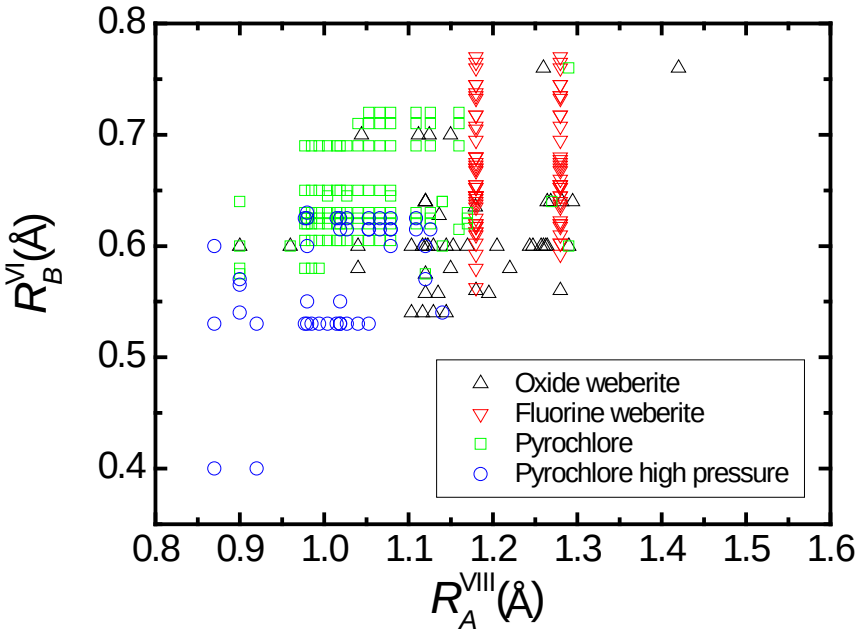

Figure 2-16. Summary of R_A vs. R_B for weberites (including oxide and fluorine) and pyrochlore oxides.

In Figure 2-17, there is no obvious separation between weberites and pyrochlores. The reason for this may be that both $A_2^{2+}B_2^{5+}O_7$ and $A_2^{3+}B_2^{4+}O_7$ pyrochlore compounds are plotted. There are very few, if any, $A_2^{3+}B_2^{4+}O_7$ weberites reported. Most weberites are $A_2^{2+}B_2^{5+}O_7$ or $(A,A')_2^{2+}(B, B')_2^{5+}O_7$ and several $A_2^{1+}B_2^{6+}O_7$ ($Na_2Te_2O_7$ and $Ag_2Te_2O_7$). The inclusion of $A_2^{3+}B_2^{4+}O_7$, particularly high pressure phases, complicates the stability field, therefore, Figure 2-18 only contains $A_2^{2+}B_2^{5+}O_7$, $(A,A')_2^{2+}(B,B')_2^{5+}O_7$ compounds, $Na_2Te_2O_7$ and $Ag_2Te_2O_7$. Observing the plotted data in Figure 2-18, there is a clear separation between weberites and pyrochlores. The dashed line is for visual effect -- above the line, it is the weberite region. Weberites prefer higher ratio of $I_{A\text{-}O}/(I_{A\text{-}O}+I_{B\text{-}O})$ and higher ratio of R_A/R_B than pyrochlores.

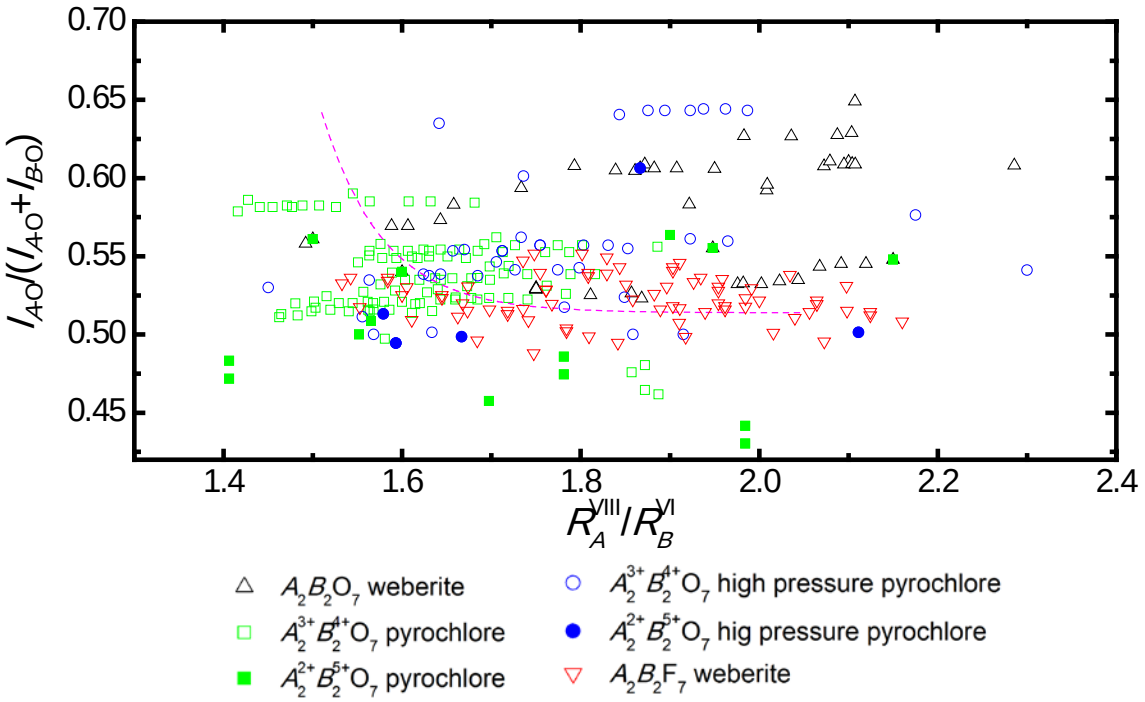

Figure 2-17. Relative ionicity *vs*. the ratio of R_A/R_B for weberite oxides, weberite fluorides and pyrochlore oxides.

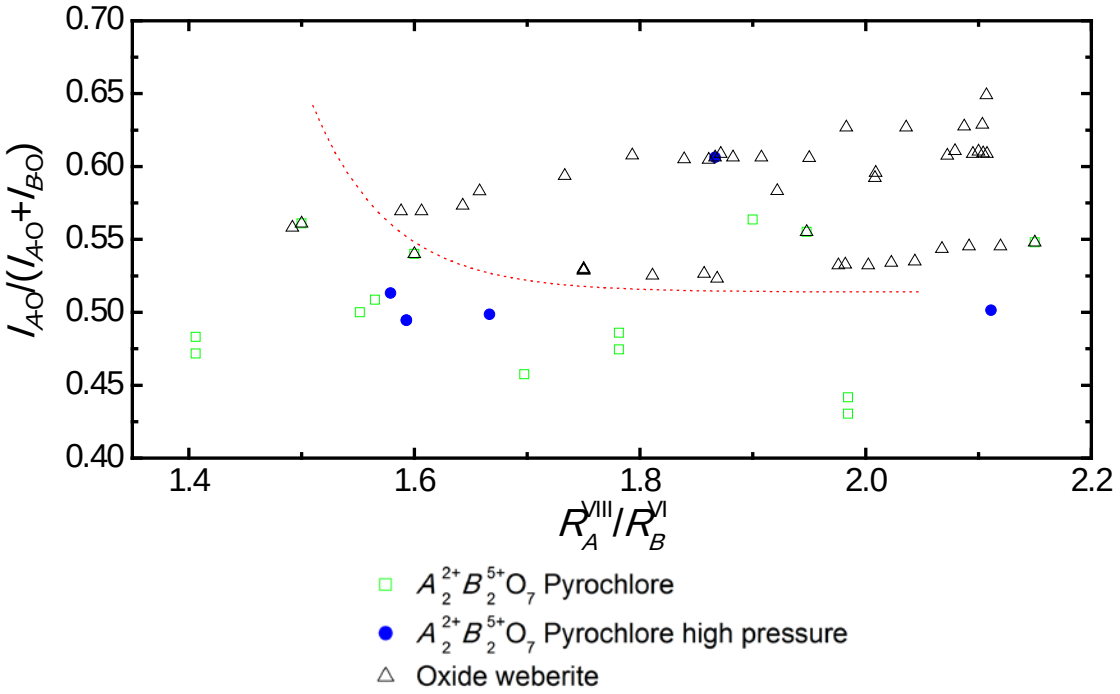

Figure 2-18. Stability field for the weberite oxides.

It is worth mentioning four specific compounds: $Cd_2Sb_2O_7$ (R_{Cd}^{2+} = 0.9 Å) in the pyrochlore region, and $Ca_2Sb_2O_7$, $Ca_2Os_2O_7$ (R_{ca}^{2+} = 1.12 Å), and $Pb_2Sb_2O_7$ (R_{Pb}^{2+} = 1.29 Å) in the weberite region.[27] A high pressure study has been performed on first three compounds to investigate the transformation of pyrochlore and weberite phases. $Cd_2Sb_2O_7$ can form a metastable phase of weberite, which can be fully converted to pyrochlore under high pressure. $Ca_2Sb_2O_7$ weberite is more stable. The same high pressure condition only results in mixed phases of $Ca_2Sb_2O_7$ pyrochlore and weberite.[54] Pyrochlore $Ca_2Sb_2O_7$ is metastable with respect to temperature and requires mild reaction condition for synthesis.[71] Meanwhile, $Ca_2Os_2O_7$ weberite is stable and the synthesis of pyrochlore $Ca_2Os_2O_7$ under pressure leads to calcium-deficient $Ca_{1.7}Os_2O_7$.[58,74] The reported crystal structure of $Pb_2Sb_2O_7$ also strongly depends on the synthesis conditions. Low temperature firing or wet chemical synthesis resulted in a

cubic pyrochlore phase. The cubic phase was metastable and readily transformed into weberite or rhombohedrally distorted pyrochlore.[12,71] Although these four compounds can form a metastable phase depending on the processing, they are presented here in the regions of their stable phases in the stability field. It is worth noting that though ionic radii ratio and bond ionicity are two major factors, there may be some additional crystallochemical characteristics or parameters that play a role in determining the prevalence of weberite over pyrochlore or *vice versa*.

2.2 Weberite-type Ln_3NbO_7

As mentioned above, there are two types of BO_6 octahedra: corner-linked $B1O_6$ and self-isolated $B2O_6$ (Figure 2-5). The chains of $B1O_6$ octahedra are oriented in an anti-phase motif (Figure 2-19 (A)). In this case, the ionic radius of *B*2 is equal or smaller than that of *B*1. When a larger *B*2 ion appears in a weberite compound, the anions, which are shared by two *B*1 octahedra neighbors, distort toward the *B*2 ions. As a result, the *A*2 ions cannot hold 8-coordination and change to 7-coordination. The *B*2 ion keeps octahedral coordination with a seventh anion relatively close to it as in the case of Na_2NiInF_7 (Figure 2-19 (B)).[68]

One extreme case of Na_2NiInF_7 is $Ln_2(B_{0.5}Ln_{0.5})_2O_7$ (or Ln_3BO_7, where *B* is Os^{5+}, Re^{5+}, Ru^{5+}, Re^{5+}, Mo^{5+}, Ir^{5+}, Sb^{5+}, Nb^{5+}, or Ta^{5+}).[15-19,21-22,37,80-101] In the above case, *B*-2 ions are the same as *A* ions. As a result, the *B-2* sites and *A-2* sites are indistinguishable. The adjacent BO_6 chains are in phase and the Ln^{3+} ions between the two chains (account for 2/3 of the total Ln^{3+} ions) result in 7 coordination (Figure 2-19 (C)). Due to the fact that this type of structure does not maintain the 3-D BO_6 octahedral network, it is considered a weberite-type structure rather than the weberite structure. In literature, it is also reported as a La_3NbO_7–type structure.

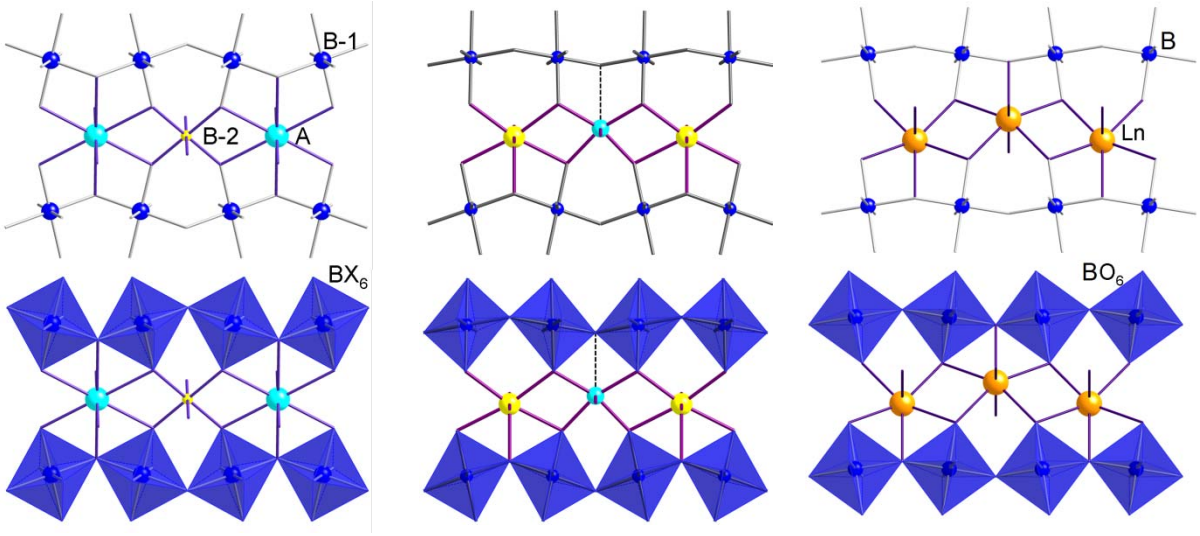

(A) (B) (C)

Figure 2-19. (A)Weberite $A^{VIII}{}_2B^{VI}{}_2O_7$ (B) Na_2NiInF_7 (when ionic radius of *B-1* is smaller than *B-2*), the dashed line represents the distance between the *B*-2 cation and the relatively close seventh anion. (C) Ln_3BO_7.

Ln_3BO_7 compounds maintain similar close-packed cation layers as in weberite and fluorite. However, due to the large ionic radius of Ln2, the cationic sublattice in Ln_3BO_7 is distorted. The first layer is composed of Ln^{3+} ions, half of which are 8-coordinated Ln1 ions and half are 7-coordinated Ln2 ions (Figure 2-20). In the second layer, there is an equivalent number of Ln2 and *B* ions.

(A) (B)

Figure 2-20. Closed-packed cation layers (A) Ln layers (B) Ln_2B_2.

In addition, there is another way to describe the structure in a layered configuration. The structure has an arrangement of BO_6-LnO_8 layers (much like

weberites, see Figure 2-9 (A)), but a different cation configuration with VII coordination between the layers (Figure 2-21). The 7-coordinated Ln^{3+} ions account for 2/3 of the total Ln^{3+} ions.

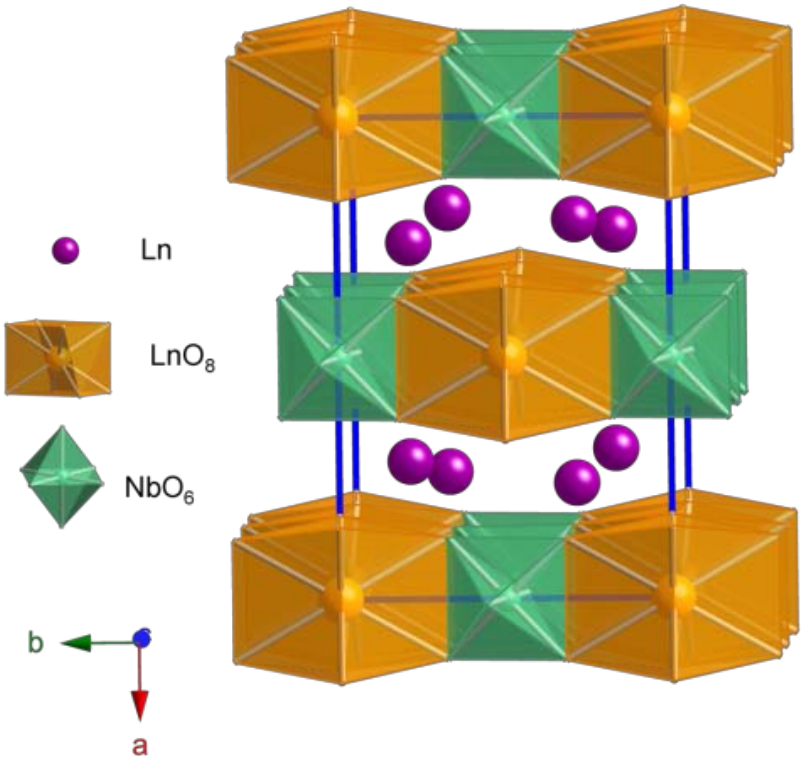

Figure 2-21. Weberite-type Ln_3BO_7, viewing in approximatly [001] direction. The layers, which are composed of parallel LnO_8 lines and BO_6 lines, are parallel to (001) plane. Between the layers are Ln with 7 coordination number.

2.3 Interesting Properties and Potential Applications

For fluorine-based weberites, the magnetic properties attract most of the attention. The triangular network formed by B^{2+} and B^{3+} cations in the HTB-like planes generally support three different magnetically ordered systems:

1. the diamagnetic B^{3+} ions separate linear chains of paramagnetic B^{2+} ions, for example, antiferromagnetic Na_2NiAlF_7, Na_2FeAlF_7 and Na_2NiInF_7;[68,102]

2. both B^{2+} and B^{3+} are paramagnetic ions, like ferromagnetic Na_2NiFeF_7 and antiferromagnetic Na_2NiCrF_7;[44,68,102-103]

3. diamagnetic B^{2+} forming linear chains which isolate the paramagnetic B^{3+} such as antiferromagnetic Na_2MgFeF_7.[104]

As for weberite oxide, various properties have been investigated including the photocatalytic properties,[22-25] the resistivity of $Ca_2Os_2O_7$ weberite,[58] magnetic properties,[21,88,95] ferroelectric properties,[11-12] and dielectric properties.[64,86,105] The interest in the properties is first due to the fact that the weberite structure is considered more favorable for the realization of a ferroelectric state than the pyrochlore structure.[11] The Sb-based compounds are the most investigated weberites for ferroelectric properties. More than ten years ago, Cava *et al.*[105] found out the temperature coefficients of the capacitance (TCC) of $Ca_2Ta_2O_7$ - $Ca_2Nb_2O_7$ system can be close to zero. A series of investigations on $Ca_2Ta_2O_7$-based weberites have followed.[45,62-65] This section is focused on the ferroelectric properties and dielectric properties of weberite oxides.

2.3.1 Ferroelectric Properties

$A_2Sb_2O_7$ (A = Ca^{2+}, Pb^{2+} and Sr^{2+}) are perhaps the most studied weberites due to their ferroelectric properties. Second harmonic generation and heat capacity measurements indicated a possible ferroelectric phase transition in $Pb_2Sb_2O_7$. Dielectric constants showed a thermal hysteresis around the Curie temperature (T_c) in $Pb_2Sb_2O_7$.[11,106] Single crystal X-ray and powder neutron diffraction were performed in detailed crystallographic studies.[11,13] Below T_c, there is a slight distortion from a centrosymmetric structure and ionic displacements cause spontaneous polarization in this structure. The results indicated a non-centrosymmetric (space group *I2cm*) to centrosymmetric (space group *Imam*, another setting of *Imma*) phase transition.[11-13] T_c

depends on the *A*-cation: 510 K for $Pb_2Sb_2O_7$, 110 K for $Ca_2Sb_2O_7$, and 90 K for $Sr_2Sb_2O_7$. The substitution of Ca by Pb in $Ca_2Sb_2O_7$ causes a shift of T_c towards a higher temperature: 200 K for $CaPbSb_2O_7$ weberite. Therefore, the *A*-sublattice seems more likely to be the ferroelectrically active one.

It is worth noting that $Pb_2Sb_2O_7$ can also form rhombohedrally distorted pyrochlore.[71] The pyrochlore phase is paraelectric even at room temperature. Actually, $Pb_2Sb_2O_7$ weberite has a higher T_c than most Pb-based pyrochlores. These facts may serve as evidence that the weberite structure is more suitable for the appearance of ferroelectric state.[11,39] As will discussed in Chapter 6, there is net dipole in weberite-type Gd_3NbO_7 indicating possible ferroelectric behavior.

2.3.2 Dielectric Properties

One of the most interesting dielectric properties of $Ca_2Ta_2O_7$ is that temperature coefficient of the capacitance (TCC) is 0 when mixing with 18 mol% of $Ca_2Nb_2O_7$, meeting the requirement for the application of microwave dielectrics.[105] The $(1-x)Ca_2Ta_2O_7 – xCa_2Nb_2O_7$ system can form solid solution up to x ~ 15mol%. TCC ~ 0 can be easily understood because TCC is negative for $Ca_2Ta_2O_7$ (- 444 MK^{-1} at room temperature (RT)) and positive for $Ca_2Nb_2O_7$ (231 MK^{-1} at RT). As will be discussed in Chapter 9, the TCC of $Ln_2Ln'NbO_7$ changes from negative to positive, depending on the average ionic radius of Ln^{3+}. It may point to the potential avenue controlling TCC.

The dielectric constants of *3T* $Ca_{1.6}Nd_{0.4}Ta_{1.6}Zr_{0.4}O_7$, *5M* $Ca_2Ta_{1.8}Nb_{0.2}O_7$ and *7M* $Ca_2Ta_{1.9}Nb_{0.1}O_7$ are approximately stable (18 ~ 19) from 100 kHz up to 5 GHz and reach maximum (22, 24.5 and 26.1, respectively) at about 8 GHz. The dielectric constant is comparable for some important microwave dielectrics, like $BaMg_{1/3}Ta_{2/3}O_3$ (~

24).[107] However, the problem with these systems is that they have low quality factors (Q ~ 200) for technical applications.[64]

It is also potential to tailor the dielectric properties by structural distortion. The *8O* $Ca_2Ta_2O_7$, which is synthesized by optical floating zone from melting *3T* $Ca_2Ta_2O_7$ powder, have a relative high dielectric constant (~ 60) at room temperature.[65] The high dielectric constant may result from a net dipole created by the off-center Ta^{5+} in the TaO_6 octahedra of the Ca_3Ta layers.

As for Ln_3NbO_7, Gd_3NbO_7 has a "loose" structure and may be a polar substance.[38,108] The dielectric properties of Gd_3NbO_7 at 1 kHz were investigated and a dielectric relaxation was observed.[38] As will be discussed in details in the following chapters, La_3NbO_7 and Nd_3NbO_7 compounds also exhibit dielectric relaxation. The off-center shifts of Ln^{3+} and Nb^{5+} within their corresponding polyhedra play an important role in the dielectric relaxation behavior of Ln_3NbO_7.

2.4 Polarization Mechanisms

When an external electric field is applied to insulators and dielectric materials, there is short-range movement or a limited rearrangement of charge carriers, namely polarization. The polarization (P) is determined by the dipole moments (μ):

$$P = N\mu = Nq\delta \tag{2-6}$$

where N is the number of the dipole moments per unit volume, q is the charge, and δ is the charges separating distance. High polarization results in a large dielectric permittivity (ε_r'):

$$\varepsilon_r' - 1 = \frac{P}{\varepsilon_0 E_{loc}} \tag{2-7}$$

where E_{loc} is the local electric field. In a solid, E_{loc} is different from the external field because polarization of the surrounding can affect E_{loc}.

Another important parameter, α, the polarizability of an atom or ion is defined by

$$\alpha = \frac{P}{NE_{loc}} \tag{2-8}$$

In a solid with a cubic lattice, E_{loc} can be calculated by

$$E_{loc} = \frac{E}{3}(\varepsilon_r' + 2) \tag{2-9}$$

Then, the permittivity can be calculated using α by the Clausius-Mossotti equation:

$$\varepsilon_r' - 1 = \frac{N\alpha / \varepsilon_0}{1 - N\alpha/(3\varepsilon_0)} \tag{2-10}$$

where ε_0 is the permittivity of free space. The importance of the Clausius-Mossotti equation is that it links the macroscopic ε_r' and the microscopic polarization phenomena, *i.e.* α.

There are four main polarization mechanisms (only considering linear dielectrics): space charge polarization, dipolar polarization, ionic polarization, and electronic polarization (see Figure 2-22). Space charge polarization, which can respond up to about 10^6 Hz, is a spatial distribution of charge centers over the microstructure because charge carriers are obstructed at a potential barrier such as a grain boundary or phase boundary after limited transport. Dipolar polarization is the preferential occupation of equilibrium positions with a probability depending on an external field. In other words, randomly oriented dipoles are rotated and aligned under an external field, giving rise to a net dipole. It can respond to frequencies up to ~10^8 to 10^{11} Hz. Ionic polarization involves relative displacement of the cation and anion sublattices. It causes shifts of both the center of negative charge and the center of positive charge, resulting in ionic dipoles. It is active up to ~10^{13} Hz. Electronic polarization (or atomic polarization) occurs when the electron clouds become displaced by the external field relative to the

nucleus. It can respond to very high frequencies ~10^{15} Hz. The sum of the contributions is shown in Figure 2-23.

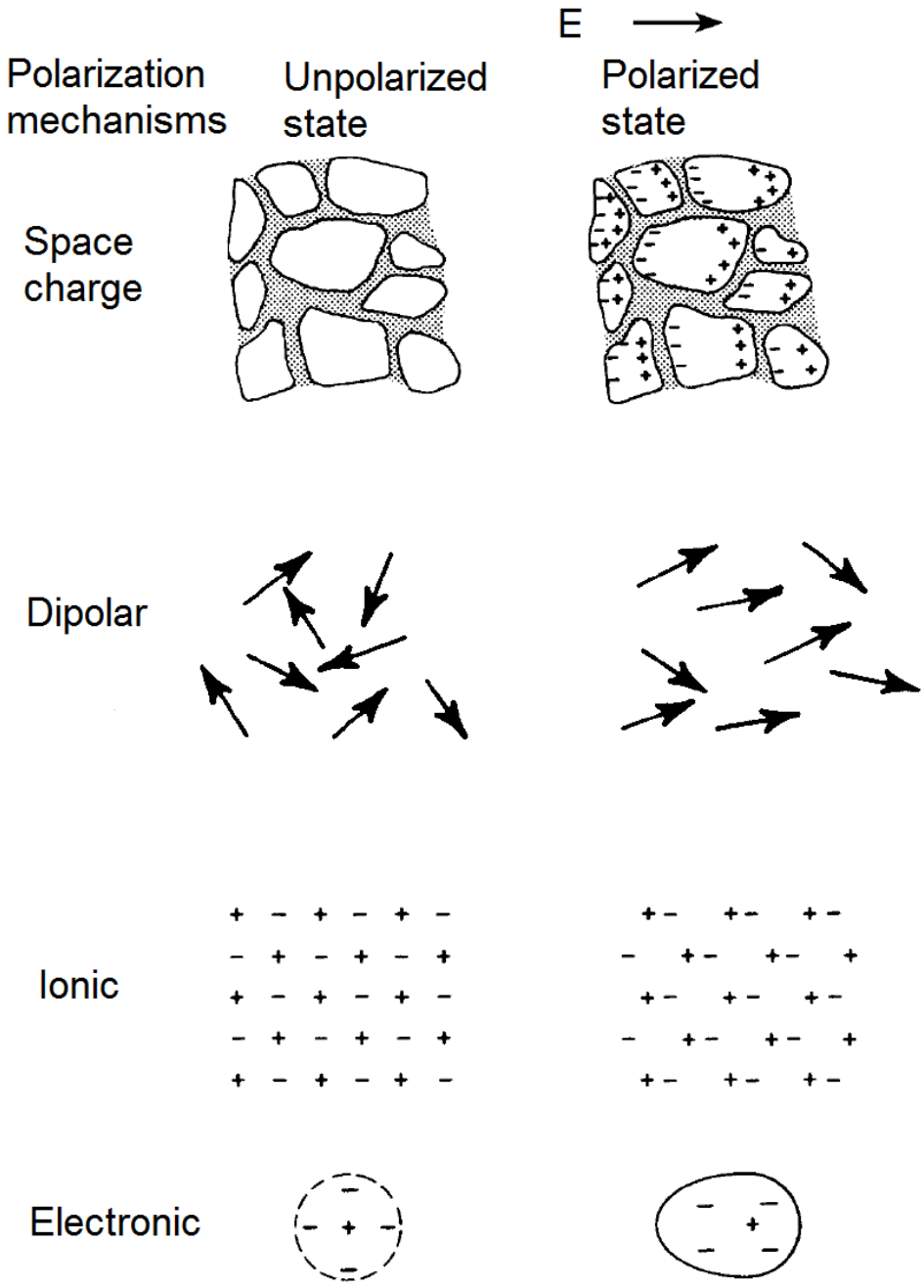

Figure 2-22. Four main polarization mechanisms. Left is unpolarized state and right is polarized state. (Diagram from Moulson and Herbert[109]).

Both electronic polarization and ionic polarization can be simulated by a spring model in which the displaced charge is bound elastically to an equilibrium position. When the frequency of the applied external field (ω_a) is close to or at ω_0 (~10^{13} Hz for ionic polarization and ~10^{15} for electronic polarization), the vibrational system is at resonance (Figure 2-23). [110]

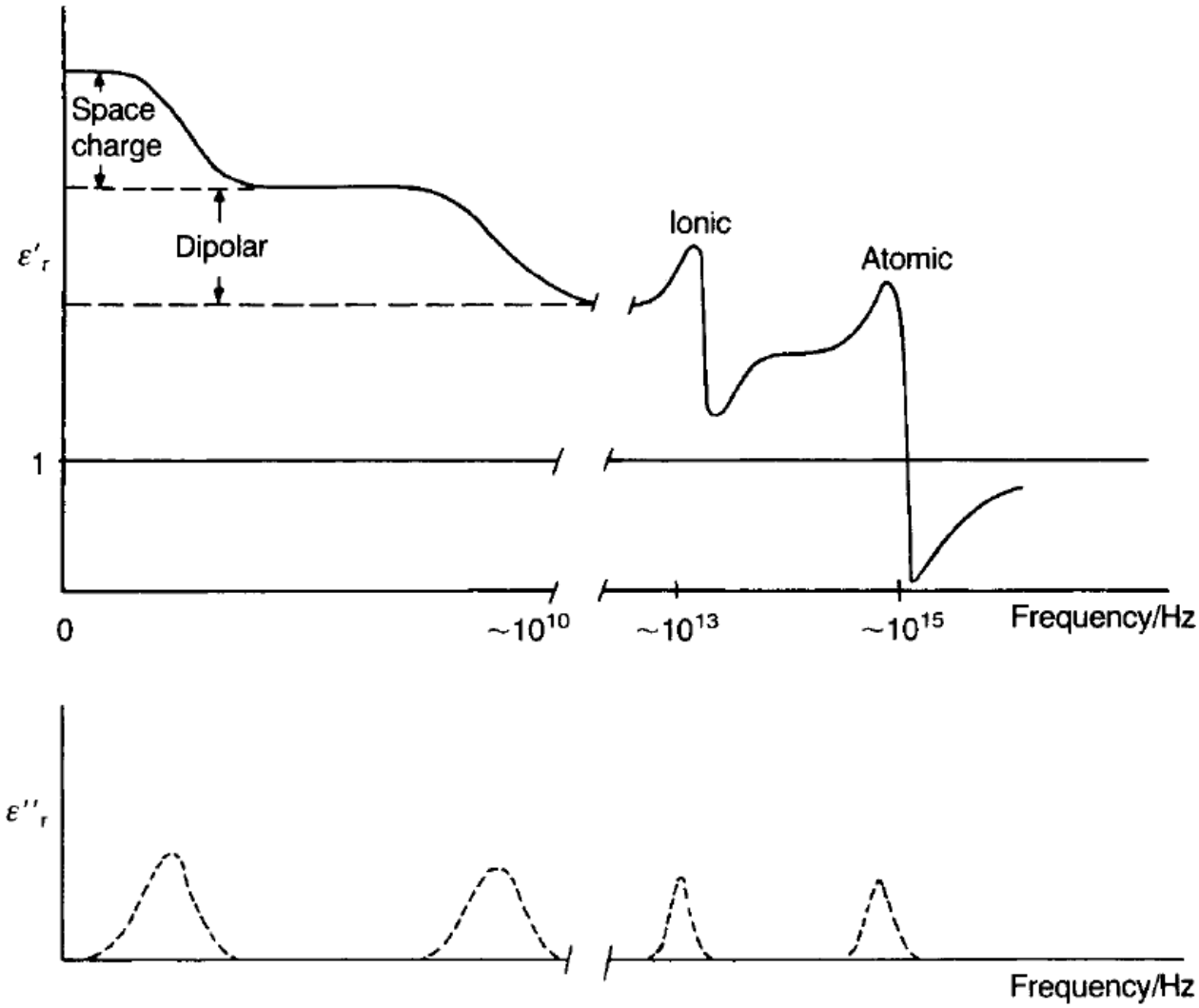

Figure 2-23. Real and imaginary parts of permittivity as a function of frequency, showing the contribution from the four mechanisms. Space charge and dipolar polarizations are relaxation processes while the rest are resonance processes. (Diagram from Moulson and Herbert[109]).

The dipolar polarization mechanism is different from electronic and ionic polarization since the former relates to the occupational probability of several equilibrium sites. The probability (p) of an ion making a jump is dependent on the depth of the energy well (ΔH_m) and temperature (T in Kelvin):

$$p = K \exp(-\frac{\Delta H_m}{kT}) \tag{2-11}$$

where K is a constant, k is the Boltzmann's constant. Without an external electric field, the energy of both sites are equivalent, resulting in an equal occupational probability. Under the applied field (E), the energy well of one position (named A) is ΔH_m-μ_{dip}E and the energy well of the second position (named B) becomes ΔH_m+μ_{dip}E, where μ_{dip} is the dipole moment. Then, the jump probability from A to B differs from the probability from B to A. The contribution of the dipolar mechanism to dielectric permittivity under static field is

$$\varepsilon_r^{'} - 1 = \frac{(ze)^2 N_{dip} \lambda_s^2}{4kT\varepsilon_0} \tag{2-12}$$

where N is the number of dipoles, λ_s is the distance between the two sites. It is important to note that dielectric permittivity from the dipolar mechanism decreases with increasing temperature due to thermal randomization.

It is worth noting that due to the ion jumping (or dipole reorientation), dipolar polarization takes a longer time to reach its static value P_s when compared to electronic and ionic polarization. Then dielectric relaxation occurs, which is delayed response to an external field. The average residence time (τ) of an atom or ion at any given site (or the relaxation time), is temperature-dependent:

$$\tau = \frac{1}{\omega_0} \exp(\frac{E_a}{kT}) \tag{2-13}$$

where ω_0 is the attempt jump frequency and E_a is the activation energy. Therefore, the ε_r' increases with temperature because of the lowering of τ. When the temperature is high enough, ε_r' begins to decrease with increasing temperature due to thermal randomization. The imaginary part of the permittivity (ε_r") undergoes a peak near the temperature (T(ε_m)) where ε_r' reaches the maximum. The temperature (T_m) at which the peak occurs is related to the frequency of the applied electric field through the Arrhenius relationship:

$$v = v_0 \exp(-\frac{E_a}{kT_m}) \quad (2\text{-}14)$$

where v is the frequency of the applied field and v_0 is the attempt jump frequency. The above equation will be used in Chapter 5 to calculate v_0 and the activation energy for dielectric relaxation.

2.5 Definitions of Ferroelectric and Antiferroelectric

Ferroelectricity is the occurrence of spontaneous polarization that can be re-oriented (or reversed) by a realizable electric field. In ferroelectric, the directions of spontaneous polarization are parallel to each other in a domain. By contrast, anti-polar crystals have antiparallel orientation to lower the dipole-dipole interaction energy.[111] They can be considered as being composed of two sublattices polarized spontaneously in antiparallel directions. If a ferroelectric phase can be induced by an external field, the antipolar phases are called antiferroelectric. The free energy of the antipolar dipole arrangement is comparable to that of ferroelectric.[112] Figure 2-24 shows the schematic representation of ferroelectric, antipolar, and antiferroelectric phases below the Curie temperature (T_c) with or without an external field.

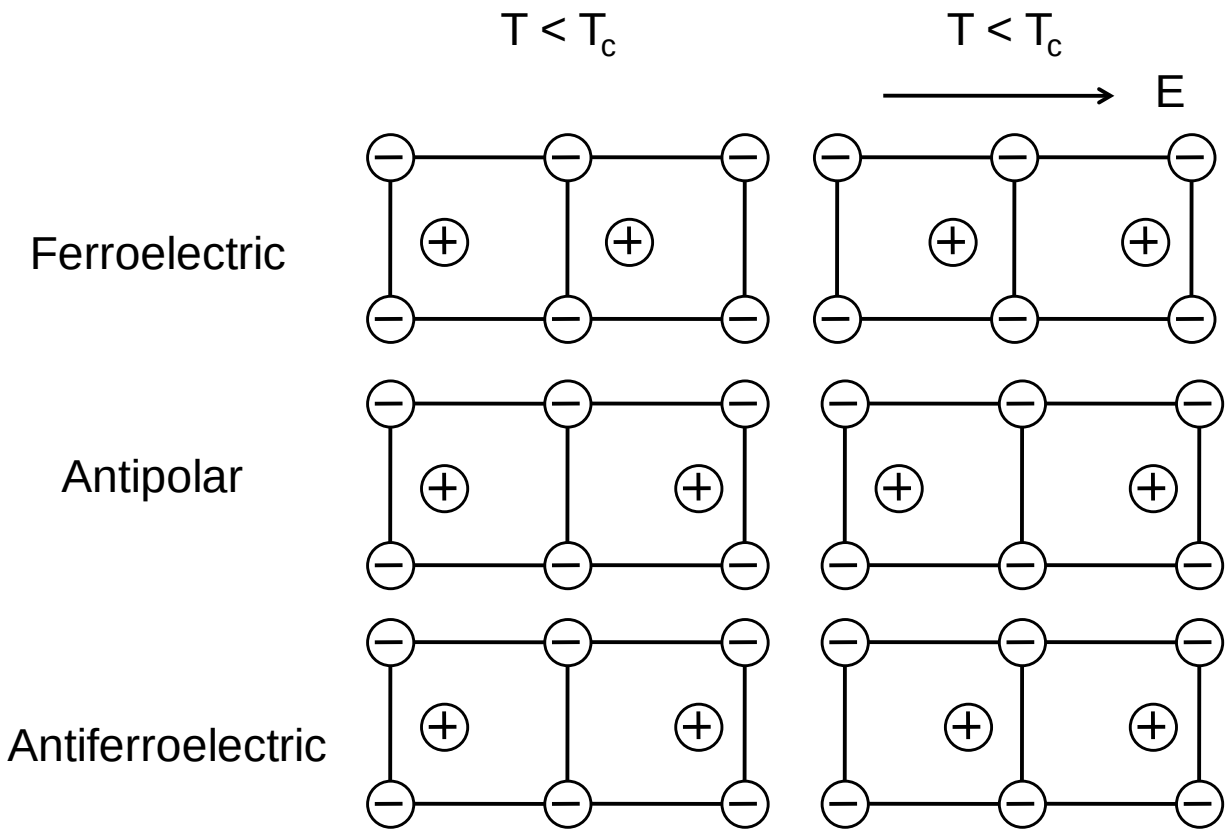

Figure 2-24. A schematic representation of ferroelectric, antipolar, and antiferroelectric, and their responses under an external field. T_c is the Curie temperature.[113]

2.6 Phase Transitions

A phase transition can occur when there is an external stress such as a change in temperature or pressure. It is defined as an event "which entails a discontinuous (sudden) change of at least one property of a material",[114] such as dielectric properties, which will be discussed extensively in this thesis. Commonly, structural changes are involved in the phase transition. A first-order transition happens when the first derivatives (entropy S and volume V) of the free enthalpy (G = U + pV - TS) experiences discontinuous change, *i.e.* $\Delta S \neq 0$ or $\Delta V \neq 0$. In a second phase transition, one of the second derivatives of G experiences a discontinuity but S and V are continuous. The second derivatives are the specific heat at constant pressure divided

by temperature ($-C_p/T$) and the multiplication of the volume and the compressibility at constant temperature (-Vk). The main difference is that the first-order transition involves the latent heat and the second-order is absent of the latent heat. The reciprocal of dielectric susceptibility behaves differently near a first-order ferroelectric transition and a second-order one (Figure 2-25). Also, near a second-order phase transition, there tends to be a λ-shape anomaly in the heat capacity vs. temperature plot.

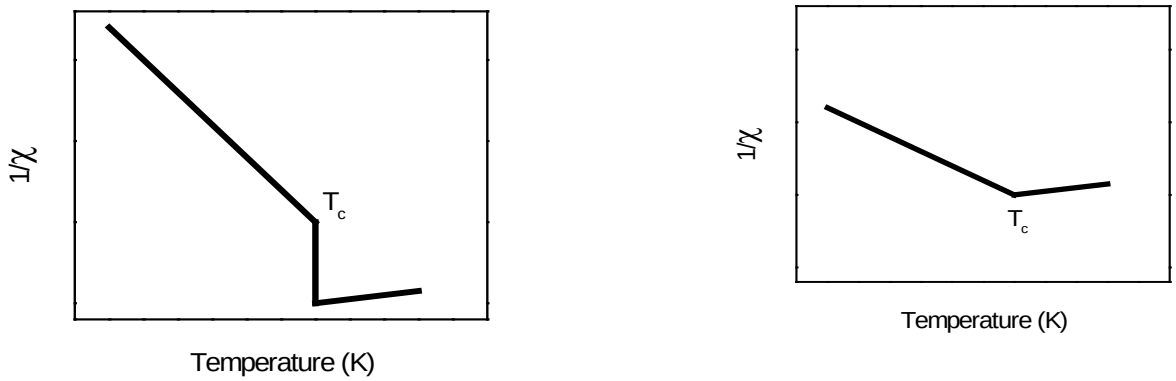

(A) (B)

Figure 2-25. For ferroelectric materials (A) the reciprocal susceptibility near a first-order ferroelectric transition; (B) the reciprocal susceptibility near a second-order transition.[113]

Solid state phase transitions can be categorized into three types: reconstructive phase transitions, displacive phase transitions, and order-disorder transitions. Reconstructive phase transitions are always first-order transitions. They involve the broken and reforming chemical bonds and considerable atomic movements. Order-disorder transitions are usually second-order. Order-disorder transitions happen when the atoms that are perfectly ordered on crystallographically non-equivalent sites become statistically distributed on an crystallographically equivalent site. Displacive phase transitions implicate limited atomic shifts and no primary chemical bond broken. The transitions have only straightforward changes in symmetry: *e.g.* symmetry operations

are gained or lost.[114] For example, the transitions in $BaTO_3$ from orthorhombic to tetragonal and to cubic are displacive phase transitions.

2.7 Second Harmonic Generation

When an electromagnetic wave propagates in a material, its electric field causes electric polarization. Materials with a non-centrosymmetric crystal structure can have a nonlinear susceptibility $\chi^{(2)}$:

$$P = \varepsilon_0\left(\chi^{(1)}E + \chi^{(2)}E^2 + ...\right) \quad (2\text{-}14)$$

where P is the polarization and E is the electric field of the wave. If E is a sinusoidal function, then

$$P = \varepsilon_0\left(\chi^{(1)}E_0\sin(\omega t) + \chi^{(2)}E_0^2\sin^2(\omega t) + ...\right) \quad (2\text{-}15)$$

Since $\sin^2(\omega t) = 1-\cos(2\omega t)$, the polarization has a component at twice of the frequency of E as shown below:

$$P = \varepsilon_0\left(\chi^{(1)}E_0\sin(\omega t) + \frac{1}{2}\chi^{(2)}E_0^2\left[1-\cos(2\omega t)\right] + ...\right) \quad (2\text{-}16)$$

This process is called second-harmonic generation (SHG) or frequency doubling, where an input wave generates another wave with twice the optical frequency in the medium.[115-116] The nonlinearity $\chi^{(2)}$ can only occur in non-centrosymmetric material. In Chapter 6 and 7, the SHG measurements were used to test whether the material is centrosymmetric or not.

2.8 Normal Mode Determination

The nuclear site group analysis allows the determination of the infrared (IR) and Raman active modes of each symmetry without detailed analysis of the symmetry elements in the unit cell. For crystals, the only information needed is the space group and the Wyckoff position of each atom in the unit cell. The table A, table B, and table E provided by Rosseau *et al.*[117] have sufficient information to determine the selection

rules. Table 2-7 presents a simple example of the mode determination in CeO_2. CeO_2 has a fluorite structure with space group $Fm\bar{3}m$ with Ce at 4*a* site and O at 8*c* site. The table A provides the site symmetries based on the space group and the Wyckoff position. From the table 32A (32 is the point group number), the site symmetry of Ce and O is O_h and T_d. The table B specifies lattice modes for each symmetry and the table E presents the selection rule of each mode. From the table 32B, the representation of the symmetry O_h is F_{1u} and that of T_d is F_{1u} + F_{2g}. The table 32E indicates F_{1u} is IR active and acoustic mode and F_{2g} is Raman active. The irreducible representation Γ is calculated by the sum of Raman active modes and IR active modes minus the acoustic modes, in case of CeO_2, Γ = 1 F_{1u} (IR) + 1 F_{2g} (R). The normal determination is more complex for Ln_3NbO_7 and will present in Chapter 8 and Appendix B.

Table 2-5. List of $A_2B_2F_7$ weberites.

‘		Space group	Z	Lattice parameters			R_A (Å)	R_B (Å)	Properties investigated
				a (Å)	b (Å)	c (Å)			
2O	Na_2MgCrF_7 [117]	Imma	4	7.39	7.15	10.20	1.18	0.67	
2O	Na_2MgGaF_7 [117]	Imma	4	7.42	7.16	10.16	1.18	0.67	
2O	Na_2MgScF_7 [117]	Imma	4	7.55	7.34	10.43	1.18	0.73	
2O	Na_2MgVF_7 [117]	Imma	4	7.45	7.24	10.30	1.18	0.68	
2O	Na_2NiFeF_7 [43,102,118]	Imma	4	7.2338 (3)	10.3050 (3)	7.4529 (3)	1.18	0.62	Magnetic
2O	Na_2NiAlF_7 [101,119]	Imma	4	7.31 (2)	7.07 (2)	10.04 (2)	1.18	0.60	Magnetic
2O	Na_2NiCoF_7 [118-119]	Imma	4	7.40 (2)	7.20 (2)	10.24 (2)	1.18	0.62	Magnetic

Table 2-5. List of $A_2B_2F_7$ weberites (Continued).

‘		Space group	Z	Lattice parameters			R_A (Å)	R_B (Å)	Properties investigated
				a (Å)	b (Å)	c (Å)			
2O	Na_2NiCrF_7 [120-121]	Imma	4	7.183(1)	10.224(1)	7.414(1)	1.18	0.65	Magnetic
2O	Na_2CoGaF_7 [122]	Imma	4	7.3011(6)	10.5436(9)	7.3845(7)	1.18	0.65	
2O	Na_2CoInF_7 [122]	Imma	4	7.4032(6)	10.3892(8)	7.5302(9)	1.18	0.75	
2O	Na_2CoScF_7 [122]	Imma	4	7.431(1)	10.546(1)	7.544(1)	1.18	0.72	
2O	Na_2MnTlF_7 [122]	Imma	4	7.371(1)	10.369(3)	7.603(1)	1.18	0.67	
2O	Na_2NiGaF_7 [122-123]	Imma	4	7.1805 (7)	10.2433 (9)	7.4256 (7)	1.18	0.66	
2O	Na_2NiInF_7 [122]	Imma	4	7.3632 (5)	10.3490 (7)	7.5274 (6)	1.18	0.75	
2O	Na_2NiScF_7 [122]	Imma	4	7.3116 (7)	10.3278 (9)	7.4779 (7)	1.18	0.72	
2O	Na_2MgTlF_7 [122]	Imma	4	7.3756 (8)	10.418 (1)	7.5496 (8)	1.18	0.70	
2O	Na_2ZnFeF_7 [122]	Imma	4	7.281(1)	10.446(2)	7.459(1)	1.18	0.65	
	Na_2ZnGaF_7 [122]	Imma	4	7.2494 (7)	10.3283 (8)	7.3582 (6)	1.18	0.68	
2O	Na_2ZnInF_7 [122]	Imma	4	7.4077(6)	10.4759(9)	7.5732(6)	1.18	0.77	
2O	Na_2ZnTlF_7 [122]	Imma	4	7.338(1)	10.300(2)	7.539(1)	1.18	0.71	
2O	Na_2MgFeF_7 [103,117]	Imma	4	7.49	7.25	10.26	1.18	0.64	Magnetic
2O	Na_2MgAlF_7 [41,52]	Imma	4	7.501(1)	9.968(2)	7.285(1)	1.18	0.62	
2O	Na_2ZnAlF_7 [124]	Imma	4	7.092(1)	10.092(1)	7.337(1)	1.18	0.64	
2O	Ag_2CuMnF_7 [122]	Imma	4	7.5006(9)	10.5025(9)	7.6452(8)	1.28	0.66	
2O	Ag_2CoAlF_7 [125]	Imma	4	7.252	10.16	7.601	1.28	0.60	
2O	Ag_2CoGaF_7 [125]	Imma	4	7.313	10.35	7.678	1.28	0.66	
2O	Ag_2CoInF_7 [125]	Imma	4	7.544	10.72	7.851	1.28	0.75	
2O	Ag_2CoScF_7 [125]	Imma	4	7.497	10.64	7.789	1.28	0.72	
2O	Ag_2MnAlF_7 [125]	Imma	4	7.360	10.32	7.601	1.28	0.60	
2O	Ag_2MnGaF_7 [125]	Imma	4	7.465	10.62	7.787	1.28	0.65	
2O	Ag_2MnScF_7 [125]	Imma	4	7.634	10.78	7.802	1.28	0.71	
2O	Ag_2NiGaF_7 [125]	Imma	4	7.255	10.28	7.650	1.28	0.66	
2O	Ag_2NiScF_7 [125]	Imma	4	7.463	10.54	7.771	1.28	0.72	
2O	Ag_2MgAlF_7 [125]	Imma	4	7.197	10.01	7.571	1.28	0.62	
2O	Ag_2MgGaF_7 [125]	Imma	4	7.257	10.21	7.664	1.28	0.67	
2O	Ag2MgInF7 125	Imma	4	7.495	10.62	7.832	1.28	0.76	

Table 2-5. List of $A_2B_2F_7$ weberites (Continued).

		Space group	Z	Lattice parameters			R_A (Å)	R_B (Å)	Properties investigated
				a (Å)	b (Å)	c (Å)			
2O	Ag_2MgScF_7 [125]	Imma	4	7.427	10.52	7.782	1.28	0.73	
2O	Ag_2CuAlF_7 [125]	Imma	4	7.109	10.22	7.684	1.28	0.62	
2O	Ag_2CuGaF_7 [125]	Imma	4	7.200	10.34	7.755	1.28	0.68	
2O	Ag_2ZnAlF_7 [125]	Imma	4	7.237	10.14	7.590	1.28	0.64	
2O	Ag_2ZnGaF_7 [125]	Imma	4	7.303	10.32	7.688	1.28	0.68	
2O	Ag_2ZnInF_7 [125]	Imma	4	7.531	10.71	7.841	1.28	0.77	
2O	Ag_2CoCrF_7 [122]	Imma	4	7.349(1)	10.376(1)	7.683(1)	1.28	0.65	
2O	Ag_2CoFeF_7 [122]	Imma	4	7.3711(8)	10.437(1)	7.7145(8)	1.28	0.62	
2O	Ag_2MnFeF_7 [122]	Imma	4	7.490(1)	10.612(2)	7.731(1)	1.28	0.61	
2O	Ag_2MnInF_7 [122]	Imma	4	7.6747(8)	10.856(1)	7.8641(7)	1.28	0.74	
2O	Ag_2MgCrF_7 [122]	Imma	4	7.2746(6)	10.3128 (9)	7.7060(7)	1.28	0.67	
2O	Ag_2MgFeF_7 [122]	Imma	4	7.3100(7)	10.335(1)	7.6972(9)	1.28	0.64	
2O	Ag_2MgTlF_7 [122]	Imma	4	7.2506(9)	10.362(2)	7.497(1)	1.28	0.70	
2O	Ag_2CuCrF_7 [122]	Imma	4	7.2103(6)	10.454(1)	7.7871(8)	1.28	0.67	
2O	Ag_2CuFeF_7 [122]	Imma	4	7.2435(9)	10.474(2)	7.769(1)	1.28	0.64	
2O	Ag_2CuInF_7 [122]	Imma	4	7.3461(6)	10.7501(9)	7.9098(6)	1.28	0.77	
2O	Ag_2ZnCrF_7 [122]	Imma	4	7.3165(7)	10.362(1)	7.6877(8)	1.28	0.68	
2O	Ag_2ZnFeF_7 [122]	Imma	4	7.359(1)	10.409(2)	7.706(1)	1.28	0.65	
2O	Ag_2ZnMnF_7 [122]	Imma	4	7.408(1)	10.503(1)	7.6972(9)	1.28	0.66	
2O	Ag_2NiAlF_7 [126]	Imma	4	7.564(6)	7.210(6)	10.139(15)	1.28	0.60	Magnetic
2O	Ag_2NiCrF_7 [126]	Imma	4	7.673(6)	7.305(6)	10.285(9)	1.28	0.65	Magnetic
2O	Ag_2NiFeF_7 [126]	Imma	4	7.692(6)	7.345(6)	10.345(9)	1.28	0.62	Magnetic
2O	Ag_2NiInF_7 [126]	Imma	4	7.822(6)	7.499(6)	10.622(9)	1.28	0.75	Magnetic
2O-II	Na_2CuInF_7 [66]	Pmnb	4	7.318	10.602	7.712	1.18	0.77	Magnetic
2O-II	Na_2CuCrF_7 [65,127]	Pmnb	4	7.100(1)	10.338(1)	7.518(1)	1.18	0.67	
2O-II	Na_2CuScF_7 [124]	Pmnb	4	7.260(1)	10.534(1)	7.658(1)	1.18	0.74	
2O-III	Na_2NiInF_7 [67]	Pmnb	4	7.356	10.334	7.523	1.18	0.75	Magnetic
2O-III	Na_2MgInF_7 [128]	Pnma	4	10.435(1)	7.345(1)	7.533(1)	1.18	0.76	Magnetic

Table 2-5. List of $A_2B_2F_7$ weberites (Continued).

		Space group	Z	Lattice parameters				R_A (Å)	R_B (Å)	Properties investigated
				a (Å)	b (Å)	c (Å)	β (°)			
2M	Na_2CuGaF_7 [66]	C2/c	8	12.325 (5)	7.318 (1)	12.780 (5)	109.29 (2)	1.18	0.68	Magnetic
2M & 4M	Na_2CuFeF_7 [65,129-130]	C2/c	8	12.46 (1)	7.363 (8)	12.93 (1)	109.36 (7)	1.18	0.64	
		C2/c	16	12.444 (2)	7.343 (1)	24.672 (5)	99.27 (3)			
3T	Na_2MnAlF_7 [122]		6	7.2854(4)		17.844(1)		1.18	0.59	
3T	Na_2MnInF_7 [122]		6	7.6006(3)		18.617(1)		1.18	0.74	
3T	Na_2MnScF_7 [122]		6	7.5442(4)		18.479(1)		1.18	0.71	
3T	Na_2MnGaF_7 [131]	$P3_121$	6	7.421(3)		18.166(6)		1.18	0.65	
3T	Na_2MnCrF_7 [131]	$P3_121$	6	7.401(1)		18.091(2)		1.18	0.64	
3T	Na_2MnVF_7 [132]	$P3_121$	6	7.467		18.216		1.18	0.65	
3T	Na_2MnFeF_7 [118,133-134]	$P3_121$	6	7.488(2)		18.257(6)		1.18	0.61	Magnetic
3T	Ag_2MnInF_7 [122]		6	7.751(1)		18.838(4)		1.28	0.74	
4M	Na_2CoAlF_7 [134-135]	C2/c	16	12.378 (4)	7.210 (3)	24.019(9)	99.67 (2)	1.18	0.61	Magnetic
4M	Na_2ZnGaF_7 [123]	C2/c	16	12.519	7.303	24.353	99.74	1.18	0.68	
4M	Na_2ZnFeF_7 [123]	C2/c	16	12.610	7.359	24.538	99.70	1.18	0.65	
4M	Na_2FeVF_7 [136]	C2/c	16	12.710 (3)	7.429 (1)	24.716 (5)	100.03 (3)	1.18	0.63	
4M	Na_2CoVF_7 [136]	C2/c	16	12.703 (5)	7.391 (3)	24.651 (5)	100.02 (3)	1.18	0.65	
4M	Na_2FeCrF_7 [136]	C2/c	16	12.625 (3)	7.391 (1)	24.695 (5)	99.93 (3)	1.18	0.61	
4M	Na_2FeFeF_7 [1,118-119]	C2/2	16	12.676 (3)	7.422 (1)	24.710 (5)	99.97 (3)	1.18	0.58	Magnetic
4M	Na_2CoFeF_7 [118-119,129,134]*	C2/c	16	12.622 (10)	7.360 (4)	24.516 (20)	99.71 (5)	1.18	0.62	Magnetic
4M	Na_2CoCrF_7 [134,136]	C2/c	16	12.578 (3)	7.335 (1)	24.415 (5)	99.64 (3)	1.18	0.65	Magnetic
4M	Na_2FeAlF_7 [119,123]	C2/c	16	12.426	7.278	24.206	99.99	1.18	0.56	Magnetic

Table 2-6. List of weberite oxides with the R_A/R_B and relative ionicity of *A-O* bond.

Type		Lattice Parameters			R_A (Å)	R_B (Å)	Properties investigated
		a (Å)	b (Å)	c (Å)			
2O	$Cd_2Sb_2O_7$ [70,137]	7.21	7.33	10.14	0.9	0.6	

Table 2-6. List of weberite oxides with the R_A/R_B and relative ionicity of *A-O* bond (Continued).

		Lattice Parameters			R_A (Å)	R_B (Å)	Properties investigated
		a (Å)	b (Å)	c (Å)			
2O	$Ca_2Sb_2O_7$ [12,24-25,137]	7.28	7.44	10.18	1.12	0.6	Ferroelectric & photocatalytic
		7.3060	7.4627	10.2263			
		7.2900	10.2000	7.4500			
2O	$Sr_2Sb_2O_7$ [24-25,53-54]	7.452	7.687	10.381	1.26	0.6	Ferroelectric & photocatalytic
		7.4557(2)	10.3708(3)	7.6860(1)			
		7.4557	10.3708	7.6860			
2O	$Pb_2Sb_2O_7$ [12-13]	7.484(1)	7.857(1)	10.426(2)	1.29	0.6	Ferroelectric
		7.4774	7.8549	10.4250			
2O	$Ca_2Os_2O_7$ [57,73]	7.2104(2)	10.1211(3)	7.3813(2)	1.12	0.575	Electronic
2O	$Sr_2Bi_2O_7$ [53]	7.70	7.91	10.58	1.26	0.76	
2O	$Ba_2U_2O_7$ [69]	8.1665(15)	11.3081(21)	8.1943(16)	1.42	0.76	
2O	$Na_2Te_2O_7$ [138]	7.233(5)	10.104(7)	7.454(5)	1.18	0.56	
2O	$Ag2Te_2O_7$ [55]	7.266(2)	10.1430(9)	7.6021 (17)	1.28	0.56	
2O	$CaPbSb_2O_7$ [12]	7.3577	7.5362	10.3521	1.205	0.6	Ferroelectric
2O	$DyNaSb_2O_7$ [139]	7.26(6)	7.41(5)	10.20(6)	1.1035	0.6	
2O	$GdNaSb_2O_7$ [139]	7.29(1)	7.47(0)	10.20(7)	1.1165	0.6	
2O	$EuNaSb_2O_7$ [139]	7.30(0)	7.47(2)	10.21(4)	1.123	0.6	
2O	$SmNaSb_2O_7$ [139]	7.30(8)	7.45(7)	10.22(7)	1.1295	0.6	
2O	$NdNaSb_2O_7$ [139]	7.32(7)	7.49(2)	10.24(2)	1.1445	0.6	
2O	$PrNaSb_2O_7$ [139]	7.33(7)	7.50(6)	10.25(5)	1.153	0.6	
2O	$LaNaSb_2O_7$ [139]	7.37(8)	7.50(1)	10.28(8)	1.17	0.6	
2O	$KLuSb_2O_7$ [55,71,140]	7.23	10.23	7.39	1.2435	0.6	
2O	$KYbSb_2O_7$ [55,71,140]	7.24	10.25	7.40	1.2475	0.6	
2O	$KErSb_2O_7$ [55,71,140]	7.26	10.25	7.41	1.257	0.6	
2O	$KHoSb_2O_7$ [55,71,140]	7.26	10.25	7.42	1.2625	0.6	
2O	$KYSb_2O_7$ [55,71,140]	7.26	10.25	7.43	1.2645	0.6	
2O	$KYTa_2O_7$ [141]	7.78	10.82	7.50	1.2645	0.64	
2O	$KDyTa_2O_7$ [141]	7.80	10.88	7.70	1.2685	0.64	
2O	$KGdTa_2O_7$ [141]	7.84	10.86	7.72	1.2815	0.64	
2O	$KSmTa_2O_7$ [141]	7.86	10.82	7.76	1.2945	0.64	
2O	$NaDyV_2O_7$ [141]	7.53	10.94	7.44	1.1035	0.54	
2O	$NaGdV_2O_7$ [141]	7.56	10.88	7.46	1.1165	0.54	
2O	$NaSmV_2O_7$ [141]	7.58	10.86	7.48	1.1295	0.54	
2O	$NaNdV_2O_7$ [141]	7.62	10.82	7.50	1.1445	0.54	
2O	$NaSrSbTeO_7$ [74]	Not reported			1.22	0.58	
2O	$NaCdSbTeO_7$ [74]	Not reported			1.04	0.58	
2O	$NdCaSbTeO_7$ [74]	Not reported			1.15	0.58	

Table 2-6. List of weberite oxides with the R_A/R_B and relative ionicity of *A-O* bond (Continued).

		Lattice Parameters				R_A (Å)	R_B (Å)	Properties investigated
		a (Å)	b (Å)	c (Å)	β (°)			
2O	$Na_{0.5}Cd_{1.5}(Fe_{0.5}Te_{1.5})O_7$ [74]	7.131	7.317	10.183		1.12	0.56	
2O	$Na_{0.5}Ca_{1.5}(Fe_{0.5}Te_{1.5})O_7$ [74]	Not reported				1.14	0.56	
2O	$Ba_{0.5}Ca_{1.5}(Fe_{0.5}Te_{1.5})O_7$ [74]	7.176	7.464	10.140		1.20	0.57	
2M	$CaLa_{1.5}Sb_{1.5}O_7$ [142]	7.5753(3)	10.6870(5)	7.5482(3)	90.346(3)	1.15	0.7	
2M	$CaPr_{1.5}Sb_{1.5}O_7$ [142]	7.5188(3)	10.611194)	7.4952(2)	90.315(2)	1.12	0.7	
2M	$CaNd_{1.5}Sb_{1.5}O_7$ [142]	7.5019(2)	10.5890(3)	7.4770(2)	90.298(2)	1.11	0.7	
2M	$CaY_{1.5}Sb_{1.5}O_7$ [142]	7.3905(1)	10.4563(2)	7.3894(1)	90.049(1)	1.04	0.7	
3T	$Ca_{1.5}Mn_{0.5}Sb_2O_7$ [143]	7.282(2)		17.604(4)		1.04	0.6	
3T	$Mn_2Sb_2O_7$ [144]	7.191		17.402		0.96	0.6	
3T	$Ca_{1.92}Ta_{1.92}Nd_{0.08}Zr_{0.08}O_7$ [44]	7.356(1)		18.116(1)		1.12	0.66	
3T	$Ca_2Ta_2O_7$ [62,104]	7.355 (1)		18.09(1)		1.12	0.64	Dielectric
4M	$Ca_{1.92}Ta_{1.92}Nd_{0.08}Zr_{0.08}O_7$ [44]	12.761(1)	7.358(1)	24.565(1)	100.17	1.12	0.64	
5M	$Ca_{1.8}Ta_{1.8}Sm_{0.24}Ti_{0.17}O_7$ [61]	12.763(1)	7.130(1)	30.190(1)	94.09(1)	1.14	0.63	
5M	$Ca_2Ta_{1.8}Nb_{0.2}O_7$ [63]	12.749(1)	7.347(1)	30.23(1)	94.23(1)	1.12	0.64	Dielectric
6M	$Ca_2Ta_2O_7$ [62]	7.348(3)	12.727(3)	36.44(5)	95.9(1)	1.12	0.64	
6T	$Ca_{1.89}Ta_{1.86}Sm_{0.16}Ti_{0.1}O_7$ [61]	7.353(1)		36.264(1)		1.18	0.64	
7M	$Ca_2Ta_{1.9}Nb_{0.1}O_7$ [63]	12.714(1)	7.370(1)	42.45(1)	95.75(1)	1.12	0.64	Dielectric
8O	$Ca_2Ta_2O_7$ [64]	7.3690(2)	12.7296(3)	48.263(1)		1.12	0.64	Dielectric & Optical

Table 2-7. An example of normal mode determination (the fluorite CeO_2)

	Wyckoff position	(table A) Site Symmetry	(table B) F_{1u}	F_{2g}
Ce	4a	O_h	1	0
O	8c	T_d	1	1
Acoustic Modes (table E)			1	0
Lattice Modes			1	1
Selectrion Rules (table E)			IR	Raman

CHAPTER 3
EXPERIMENTAL PROCEDURES AND PROCESSING

3.1 Sample Preparation

3.1.1 Powder Preparation

Polycrystalline specimens were prepared by solid state processing. The starting materials were Dy_2O_3 (Alfa, 99.99%), Er_2O_3 (Alfa, 99.99%), Y_2O_3 (ACROS, 99.99%), Nd_2O_3 (Alfa, 99.9%), La_2O_3 (CERAC, 99.99%), Yb_2O_3 (Alfa, 99.9%), and Nb_2O_5 (Alfa, 99.9985%). The powders of Ln_2O_3 and Nb_2O_5 with molar ratio of 3:1 were mixed with 70 ml deionized water and 2 ml ammonium polyacrylate dispersant (Darvan 821 A). The milling media contained 60 g of YSZ spheres with diameter 10 mm and 110 g of YSZ spheres with diameter 3 mm. The slurry was ball-milled for 24 hours at 85 rpm. The slurry was then poured onto a Teflon sheet, covered with aluminum foil, and subsequently dried in the oven at 393 K for 16 hours followed by grinding with a corundum mortar and pestle and sieving through a 212 μm mesh. The powders were then placed in an alumina crucible and calcined in air with 400 K/h heating and cooling rate. The calcination temperature was in the range of 1573 K - 1773 K. For the defect fluorite compounds, the pure phase was formed when Dy_3NbO_7 was calcined at 1573 K for 8 h and Er_3NbO_7, Y_3NbO_7, and Yb_3NbO_7 were calcined at 1673 K for 8 h. The pure phase of Gd_3NbO_7 was formed after calcination at 1673 K for 8 h. Any impurity phase of Nd_3NbO_7 cannot be detected by CuKα XRD when calcined at 1673 K for 8 h. As for La_3NbO_7, multiple calcinations with intermediate grinding were needed to eliminate the $LaNbO_4$ phase. La_3NbO_7 had to be calcined at 1773 K for at least 48 h in total.

$Ln_2Ln'NbO_7$ was synthesized in the same manner as to Ln_3NbO_7. Multiple and long time calcinations with intermediate grinding were also necessary to reach the equilibrium phase.

3.1.2 Pellet Formation

After the pure phase was formed, 1wt%-3wt% of PVA binder (Celvol 103) was added to assist in pellet formation. The binder contained 20vol% PVA and 80vol% deionized water. An additional 3wt% of binder was needed in pellet forming for the powders with defect-fluorite crystal structure. The binder and the powders were mixed with the mortar and pestle and sieved through 212 μm mesh. The mixed powders were then dried in oven at 373 K for 5 min to evaporate water. After that, the powders were uniaxially pressed at 150 MPa into cylindrical pellets with a diameter of 13 mm or 7 mm or 3 mm and a thickness of approximately 1 mm. A geometric green density was calculated, and the pellets with a density greater than 50% of the theoretical value were sintered at 1923 K for 4 hours for the defect-fluorite pellets and 1873 K for 4 hours for all other pellets following a binder burn-out step at 723 K for 2 hours. The heating and the cooling rate was 200 K/h. The sintered pellets were first checked for surface finish. The weight and the dimension of the pellets without surface cracks were measured, and then the geometric density was determined. If the geometric density of the pellet was above 92% of the theoretical value, Archimedes' method, which does not account for the open pores, was used to measure the density of the pellet. The process has also been summarized in Figure 3-1.

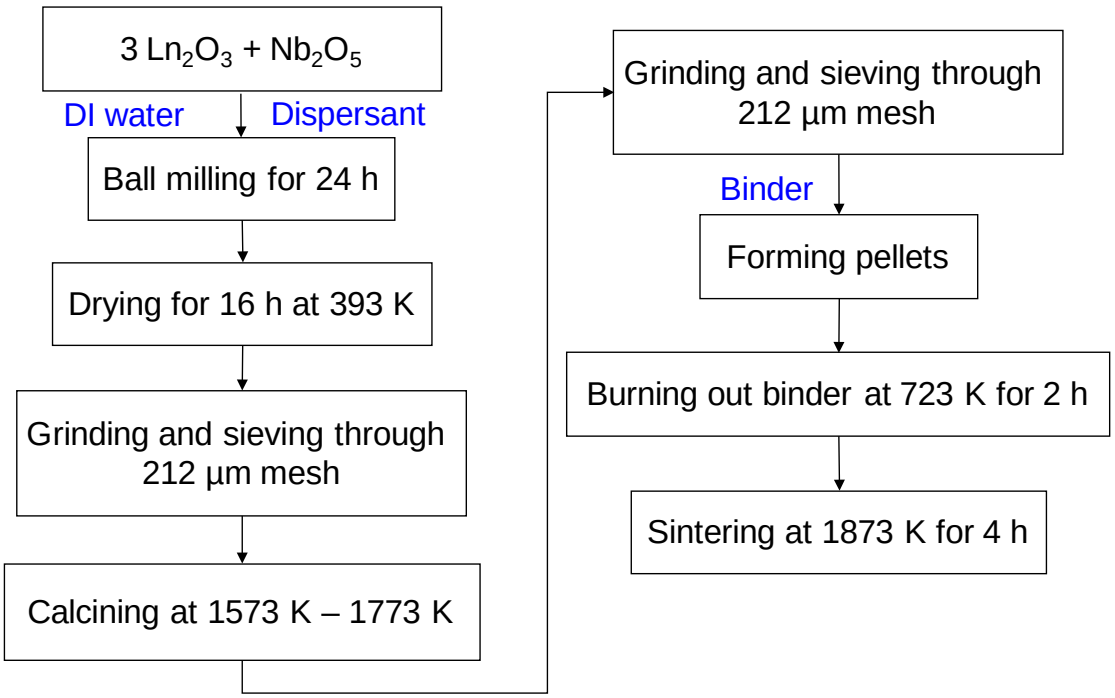

Figure 3-1. Flow chart of ceramic powder and pellet synthesis process for Ln_3NbO_7.

3.2 Characterization

3.2.1 Structural Characterization

Philips APD 3720 and Inel CPS x-ray diffractometers were used for structural characterization. The XRD was conducted using CuKα radiation with the operation conditions 40 kV and 20 mA for APD and 30 kV and 30 mA for CPS. Figure 3-2 shows an example of XRD collected during the solid state processing. Before calcination, XRD was performed on powder mixtures to assure the right starting materials as well as that no impurity was introduced. As in case of La_3NbO_7 in Figure 3-2, the powder after ball milling showed two phases Nb_2O_5 and $La(OH)_3$, which is reasonable since deionized water was used during ball milling process. After every calcination process, XRD was used to check the phase purity after the powders were grounded by mortar and pestle. After the pellets were sintered, XRD was used again to check phase purity and to

ensure that the phase of the pellets is consistent with the powders and no secondary phase was produced.

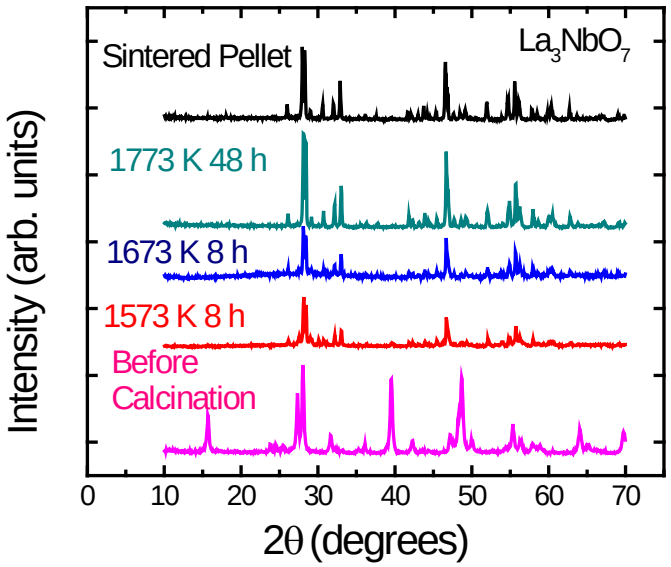

Figure 3-2. XRD of La_3NbO_7 during the solid state processing.

In addition to the above, the 11-BM high resolution powder diffractometer[118] in the Advanced Photon Source, Argonne National Laboratory and the HB-2A neutron powder diffractometer in High Flux Isotope Reactor at Oak Ridge National Laboratory were used at different temperatures for crystal structure and phase transition characterization.

3.2.2 Particle size measurement

The particle size and size distribution of ceramic powders was characterized using laser scattering (Beckman Coulter LS 13320). The powders were suspended in deionized water and placed in an ultrasonic bath for at least 30 seconds before analysis. Figure 3-3 shows a typical particle size distribution (Gd_3NbO_7).

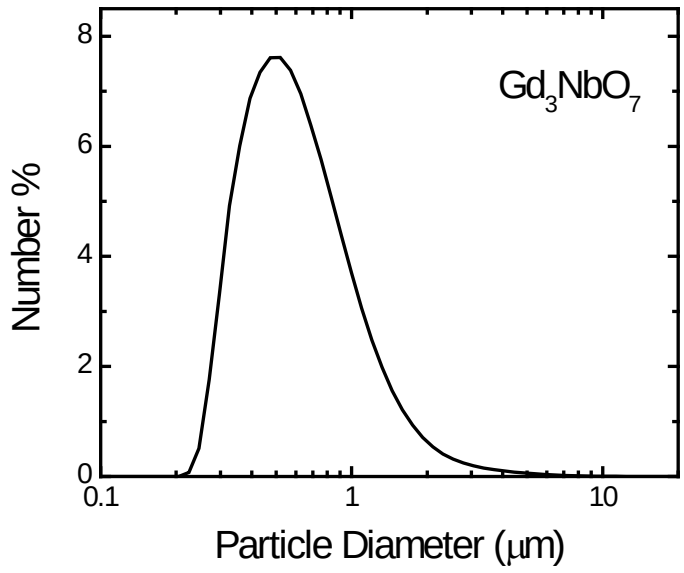

Figure 3-3. Particle size distribution of Gd_3NbO_7.

3.2.3 Heat Capacity Measurement

Heat capacity measurement on pellets was conducted using differential scanning calorimeter (DSC, Seiko Instrument, Inc.) following ASTM E 1269-05.[119] The measurement was done in a nitrogen atmosphere using a synthetic sapphire disk as a standard from 170 K to 673 K.

3.2.4 Scanning Electron Microscopy

The microstructure of the sintered ceramic pellets was characterized using scanning electron microscopy (SEM, JEOL 6335F). The SEM was operated under the condition of an accelerating voltage of 15 kV, a probe current of 8 μA, and a working distance of approximately 15 mm. To prepare SEM samples, the sintered ceramic pellets were first mechanically polished to a near-mirror finish using sandpapers with different grit sizes followed by diamond lapping films. After polishing, the pellets were

sonicated in deionized water for 5 min. Then the pellets were heated at the rate of 400 K/h to 100 K below the sintering temperature for 1 hour to thermally etch the surface. In some cases ceramic pellets were fractured using a pestle to examine fracture surfaces. All samples were then sputter coated with approximately 20 nm carbon film. Figure 3-4, Figure 3-5, and Figure 3-6 show the typical microstructure of Ln_3NbO_7 and $Ln_2Ln'NbO_7$ samples. Limited closed porosity is observed at the grain boundaries. As mentioned before, the overall porosity in all of the synthesized pellets is below 8%.

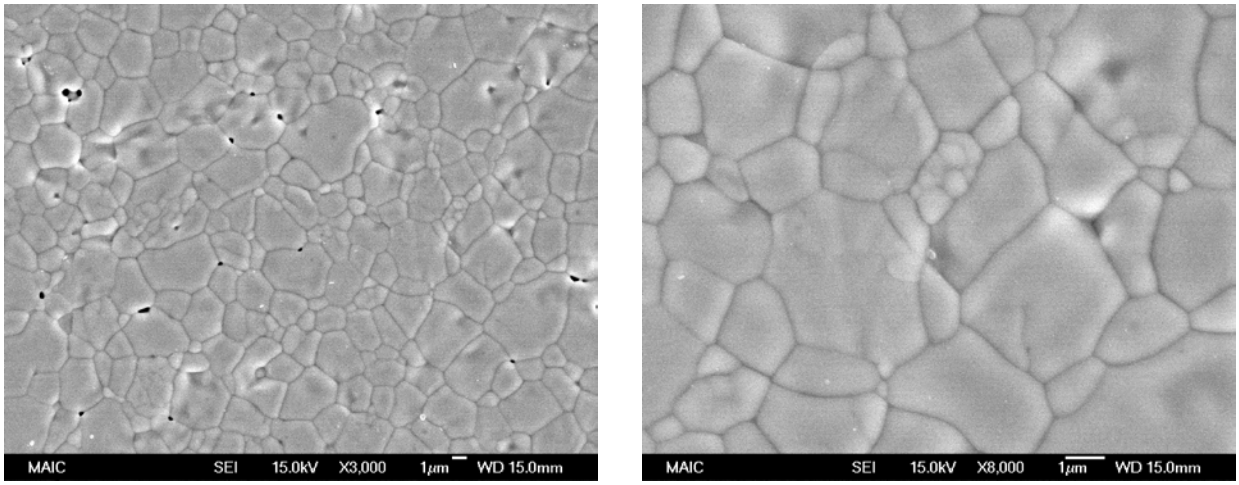

(A) (B)

Figure 3-4. (A) SEM picture of Yb_3NbO_7 with 3000 X magnification. (B) SEM picture of Yb_3NbO_7 with 8000 X magnification.

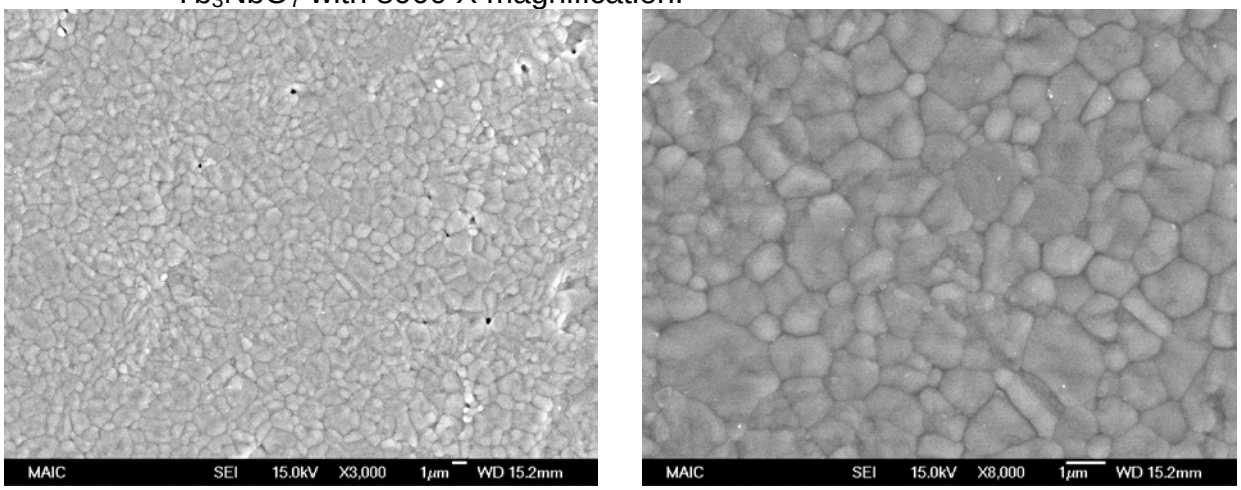

(A) (B)

Figure 3-5. (A) SEM picture of Gd_3NbO_7 with 3000 X magnification. (B) SEM picture of Gd_3NbO_7 with 8000 X magnification.

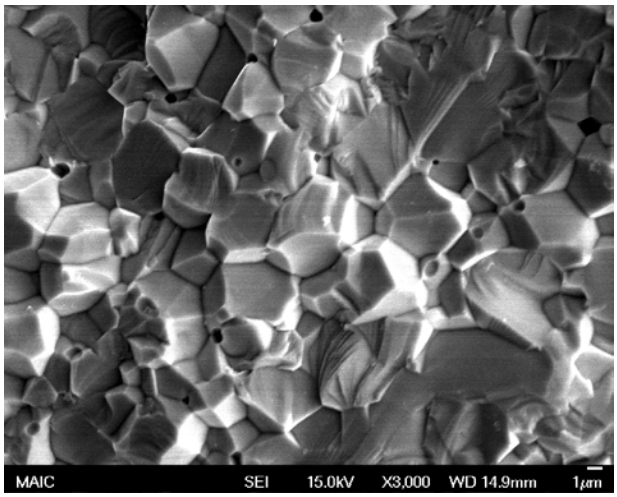

(A)

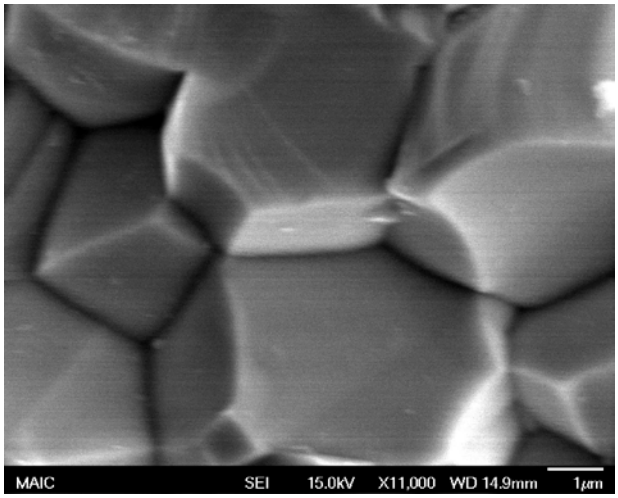

(B)

Figure 3-6. (A) SEM picture of Nd_2YbNbO_7 fracture surface with 3000 X magnification. (B) SEM picture of Nd_2YbNbO_7 cross sectionwith 11000 X magnification.

3.2.5 Second Harmonic Generation Measurement

The second harmonic generation (SHG) signal was measured by D. Sava and Professor V. Gopalan at Penn State University. The sintered pellets were polished progressively with smaller sizes of alumina powder and finally submicron size colloidal silica. The laser source was an amplified Ti:sapphire laser with 1 kHz repetition rate, 800 nm wavelength and 130 fs pulse width. The signal was collected using photomultiplier tube and lock-in amplifier to reduce noise. The laser was incident at 45 degrees to the sample surface.

3.2.6 Dielectric Characterization

To prepare parallel plate capacitors, Au/Pd or Au electrodes were sputtered on both sides of the polished pellets followed by a painted coat of air-dried Ag-paste (Figure 3-7 (A)). Dielectric properties were measured using an Agilent 4284A or 4980A LCR meter over a frequency range of 1 kHz – 1 MHz. The measurements were computer controlled with samples inside Delta 9023 (Figure 3-7 (B)) oven from 113 K to

500 K (liquid nitrogen cooled) or in a closed cycle cryogenic workstation (see Figure 3-7 (C), CTI- Cryogenics, Model 22) in the temperature range of 20 K to 295 K. The measurements were conducted both during the cooling and heating cycle. The real parts of permittivity were compensated for porosity as follows:

$$\varepsilon_r^{'} = \frac{\varepsilon_m}{1-\frac{3V_f}{2}} \tag{3-1}$$

where ε_m is measured permittivity and V_f is the volume fraction of pores. V_f is determined by the percentage of theoretical density of the pellet using Archimedes' method. The equation is reduced from James Maxwell's derivation based on 3-0 composite system.[109]

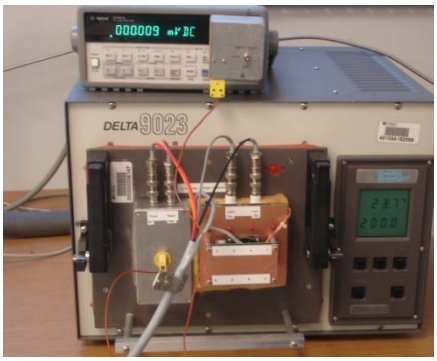

(A) (B) (C)

Figure 3-7. (A) Different sizes of pellets with electrodes. (B) Delta oven for dielectric measurement from 113 K to 500 K. The digital multimeter above the oven is connected to the thermocouple inside the oven. (C) Cryogenic workstation for dielectric measurement from 20 K to 350 K.

CHAPTER 4
PRELIMINARY CRYSTALLOGRAPHY OF THE Ln_3NbO_7 (Ln = La^{3+}, Nd^{3+}, Gd^{3+}, Dy^{3+}, Er^{3+}, Y^{3+}, and Yb^{3+}) and $Ln_2Ln'NbO_7$ (Ln = La^{3+} and Nd^{3+}; Ln'$^{3+}$ = Dy^{3+}, Er^{3+}, and Yb^{3+})

4.1 Introduction

The core of this chapter is chiefly based on three articles: 1. the journal article (Journal of the European Ceramic Society, ***27*** *(13-15) 3971-3976 (2007)) titled "Structure and Dielectric Properties of Ln_3NbO_7 (Ln = Nd, Gd, Dy, Er, Yb, and Y)," by L. Cai and J.C. Nino;*[86] *2. the journal article (Journal of the European Ceramic Society,* ***30*** *(2) 307-313 (2010)) titled "Phase Formation and Dielectric Properties of $Ln_2(Ln'_{0.5}Nb_{0.5})_2O_7$ (Ln = rare earth element)," by L. Cai and J.C. Nino;*[120] *3. the proceedings article (Solid State of Inorganic Materials VI (Materials Research Society Symposium Proceeding),* ***998E*** *0988-qq01-04 (2007)) titled "Phase Formation and Dielectric Properties of Ln_3NbO_7 (Ln = rare earth elements)," by L. Cai, J. Guzman, L. Perez, and J.C. Nino.*[85] *They are reprinted with permission from Elsevier and MRS E-Proceedings.*

It has been proved that the crystal structure of Ln_3NbO_7 shifts from orthorhombic weberite-type structures to a cubic defect fluorite structure with decreasing Ln^{3+} ionic radius.[15,22-23,29,36,80,108,121-122]

The crystal structure of La_3NbO_7 and Nd_3NbO_7 is an orthorhombic weberite-type. Additionally, Gd_3NbO_7 has also been reported as an orthorhombic lattice, however, with another weberite-type structure. Meanwhile, others have reported Gd_3NbO_7 as a pyrochlore.[22-23,29,123]

A cubic defect-fluorite structure has been reported for Ln_3NbO_7, in which the ionic radius of Ln^{3+} cation is equal to or less than that of Dy^{3+} (1.027 Å).[22-23,27,29,80,124] Unlike

pyrochlore ($A_2B_2O_7$) in which *A*, *B* cations, and the oxygen vacant sites have ordered arrangements, the defect-fluorite structure has both disordered cations as well as disordered oxygen deficiency sites. It is important to note that some investigations indicated that Ln_3NbO_7 compounds have a pyrochlore-type structure.[29,108,121,125] In fact, there is some evidence showing that these compounds may have local ordering. This evidence includes six pyrochlore-characteristic Raman active vibrations found in Y_3NbO_7,[121] along with the appearance of weak reflections, which are not associated with the fluorite structure, in the electron diffraction pattern.[80] However, the evidence does not seem to strongly relate these compounds to the pyrochlore structure. The five less intensive Raman active vibrations seem too broad and too vague to be claimed as peaks.[121] The Raman spectra of Y_3TaO_7, an isomorphic compound to Y_3NbO_7, confirmed a fluorite structure.[22] The weak reflections in the electron diffraction patterns of Ho_3TaO_7, Y_3NbO_7, Er_3TaO_7, and Er_3NbO_7 were not clearly defined, but were determined to not be related to the pyrochlore or the orthorhombic weberite-type phases.[80]

The crystal structure of a series of $Ln_2Ln'NbO_7$ (where the ionic radius of Ln'^{3+} is smaller than that of Ln^{3+}) was also investigated. The $Ln_2(Ln'_{0.5}Nb_{0.5})_2O_7$ compounds lie in or close to the pyrochlore stability area where $1.46 < r_A/r_B < 1.80$ for $A_2^{3+}B_2^{4+}O_7$ by Subramanian *et al.*[14] as shown in Figure 4-1. Meanwhile, these compounds are in the pyrochlore range of the stability field proposed by *Cai et al.*[40] shown in Figure 4-2, which was also covered in Chapter 2. As also suggested by Isupov,[125] $Ln_2(Ln'_{0.5}Nb_{0.5})_2O_7$ are expected to crystallize in the pyrochlore structure. Therefore, to test this prediction and

further understand fluorite-related superstructures, the structure of three compounds, $La_2(Yb_{0.5}Nb_{0.5})_2O_7$, $La_2(Er_{0.5}Nb_{0.5})_2O_7$, and $La_2(Dy_{0.5}Nb_{0.5})O_7$ were studied here.

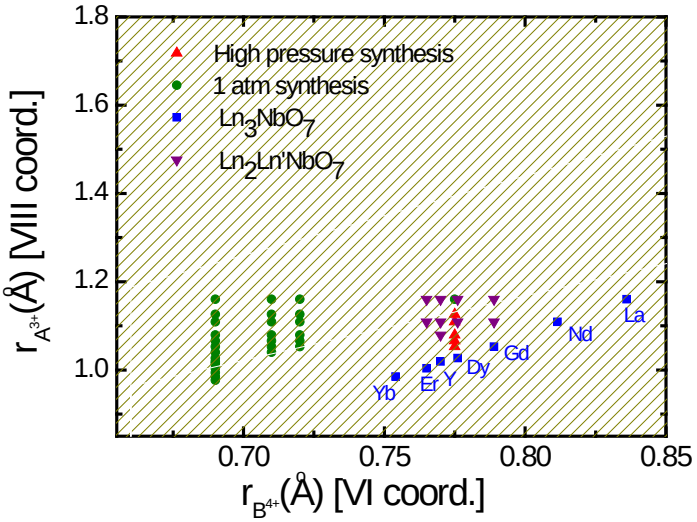

Figure 4-1. The pyrochlore stability field based on the ratio of ionic radius of *A* over that of *B* after Subramanian *et al.*[14] The stability field is where the r_A/r_B is between 1.46 and 1.8 for $A_2B_2O_7$ pyrochlore. The points other than Ln_3NbO_7 and $Ln_2Ln'NbO_7$ are from Subramanian *et al.*[14] The ionic radius are after Shannon.[27]

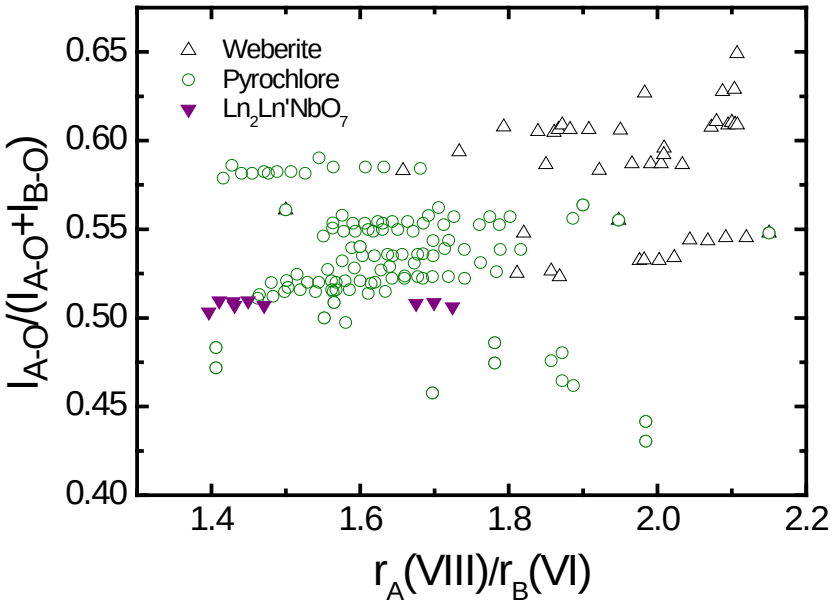

Figure 4-2. The pyrochlore and the weberite stability fields based on the ionic ratio of *A* over *B* and the relative A-O bond ionicity.[40]

In this chapter, structural characterization of Ln_3NbO_7 (Ln^{3+} = La^{3+}, Nd^{3+}, Gd^{3+}, Dy^{3+}, Er^{3+}, Y^{3+}, and Yb^{3+}) and $Ln_2Ln'NbO_7$ was based on XRD at room temperature.

4.2 Crystal Structure of Ln_3NbO_7 (Ln = Dy^{3+}, Er^{3+}, Y^{3+}, and Yb^{3+})

Pure fluorite phase of Dy_3NbO_7 powders was formed when calcined at 1573 K (Figure 4-3). The XRD pattern shows no reflections associated with the pyrochlore structure or any other related superstructures. To ensure the equilibrium state, the powders were then calcined at 1673 K and 1773 K with intermediate grinding. All XRD profiles for Dy_3NbO_7 were found to be consistent with the cubic fluorite structure, and showed no evidence of the pyrochlore phase.

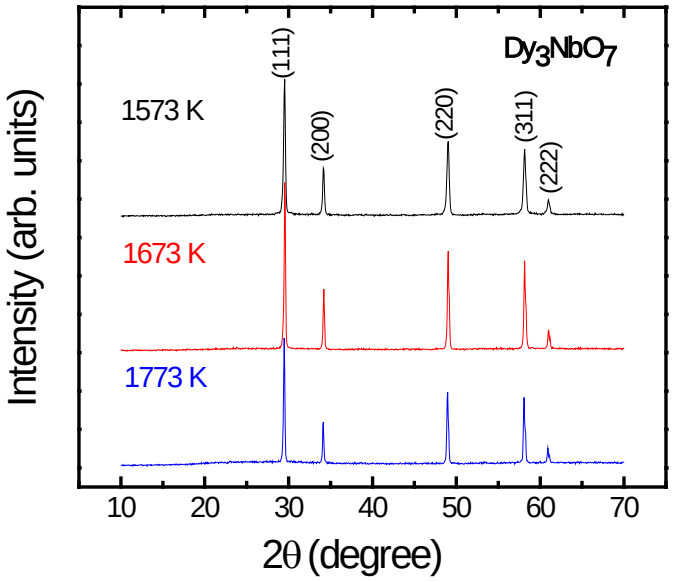

Figure 4-3. XRD of Dy_3NbO_7 at different calcination temperatures.

The XRD patterns of Ln_3NbO_7 (Ln^{3+} = Y^{3+}, Er^{3+}, and Yb^{3+}) is also consistent with a cubic fluorite structure and shows no reflections associated with the pyrochlore structure (Figure 4-4). As expected, there are shifts in 2θ, indicating changes in the lattice parameters. The lattice parameters are calculated by the Nelson-Riley function:

$$a = a_0 - a_0 k\left(\frac{\cos^2\theta}{\sin\theta} + \frac{\cos^2\theta}{\theta}\right) \quad (4\text{-}1)$$

where a is the apparent lattice parameter, a_0 is the lattice parameter, and k is a constant. The Nelson-Riley function is used to correct for the sample displacement error. Table 2-1 lists an example of the $\cos^2\theta/\sin\theta + \cos^2\theta/\theta$ parameter and the apparent lattice based on a single reflection. Figure 4-5 indicates the apparent lattice parameter *a vs.* $\cos^2\theta/\sin\theta + \cos^2\theta/\theta$ and the resulting a_0. The lattice parameters have a linear relationship with the ionic radius of Ln^{3+} as shown in Figure 4-6.

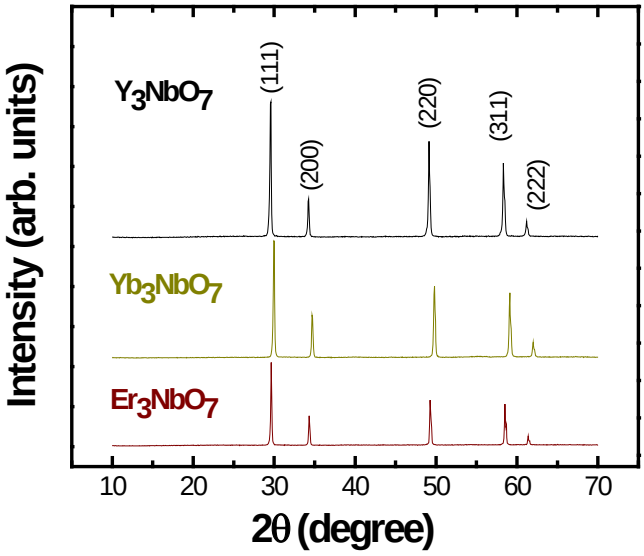

Figure 4-4. XRD patterns of Y_3NbO_7, Yb_3NbO_7, and Er_3NbO_7.

Table 4-1. The 2θ positions, the corresponding (hkl), the $\cos^2\theta/\sin\theta + \cos^2\theta/\theta$ parameter, and the apparent lattice parameter of Dy_3NbO_7.

2θ (degrees)	hkl	cos2θ/sinθ + cos2θ/θ	a (Å)
29.52	111	7.300	5.2367
34.19	200	6.1699	5.2408
49.02	220	3.9310	5.2517
58.17	311	3.0759	5.2559
61.005	222	2.857	5.2570

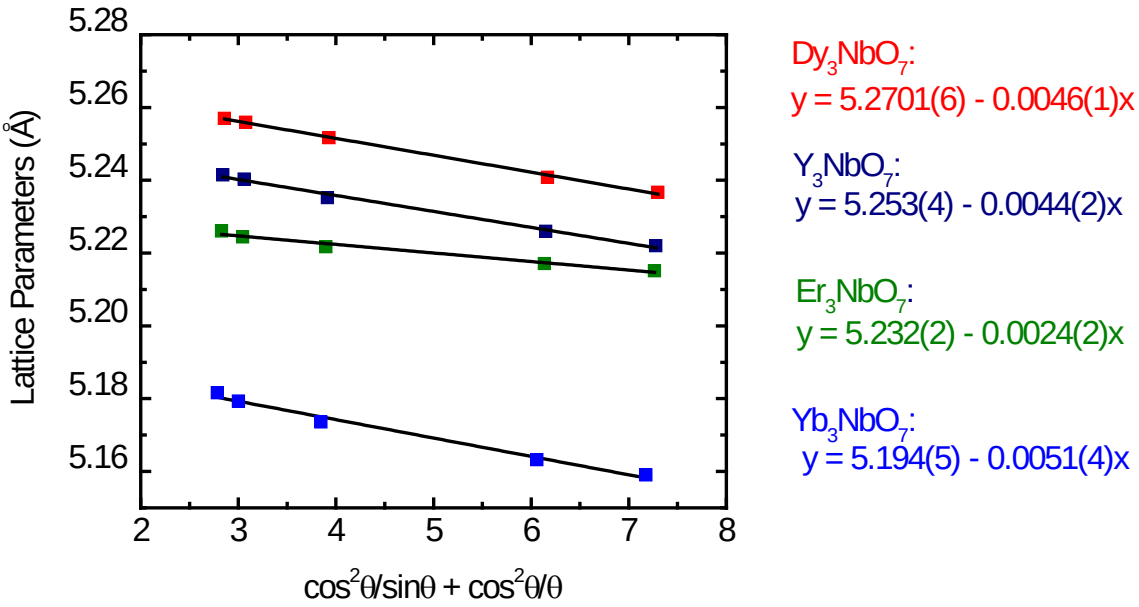

Figure 4-5. Nelson-Riley function for the lattice parameter calculations of Dy_3NbO_7, Y_3NbO_7, Er_3NbO_7, and Yb_3NbO_7.

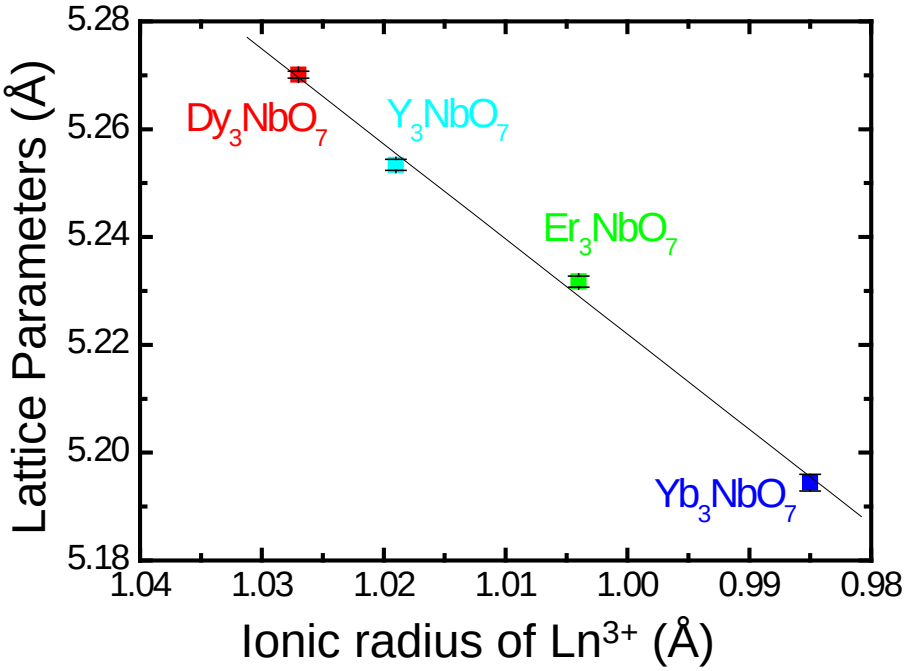

Figure 4-6. Lattice parameters (with error) of defect-fluorite Ln_3NbO_7 as a function of Ln^{3+} ionic radius. The solid line is the linear fitting.

4.3 Crystal Structure of Ln_3NbO_7 ($Ln = La^{3+}$, Nd^{3+}, and Gd^{3+})

Two space groups have been used to describe the crystal structure of La_3NbO_7. One space group, used by Rossell[36], was *Cmcm* (No. 63), with the lattice parameters being 11.167 Å, 7.517 Å, and 7.624 Å. On the other hand, Kahnharari *et al.*[37] used the space group *Pmcn* (No. 62) with the lattice parameters being 11.149 Å, 7.611 Å, and 7.747 Å (in Kahnharari's original paper, the space group *Pnma*, which is another setting of *Pmcn*, with the lattice parameters 7.747 Å, 11.149 Å, 7.611 Å was used.[51] Here, the author transformed the space group to *Pmcn* to match with the axes for a better comparison). Figure 4-7 shows the comparison between the experimental XRD pattern and simulated XRD profiles after Rossell and Kahnharari. All 53 observed peaks are associated with the La_3NbO_7 structure and the peaks with relative intensities less than 8% are indicated by diamond symbols. However, the experimental diffraction pattern seems to be in agreement with both simulated profiles, therefore making it impossible to determine which space group is correct. There are 152 calculated reflections with 2θ ranging from 10 to 70 degrees (CuKα x-ray) based on the description of the La_3NbO_7 structure with space group *Pmcn*, while there are only 85 calculated reflections for that of *Cmcm*. Based on the simulation from PowderCell, the 67 extra reflections from *Pmcn* are so weak and close to their neighboring peaks that they are easily buried in the background or overlapped with their neighboring peaks.[126] The highest relative intensity among the 67 peaks is only 1.08%, being (121) at $2\theta \sim 27.2^{o}$. The (121) reflection is only about 0.7^{o} away from the strongest reflection (220). Therefore, there is a possibility that the (121) reflection is buried in the tail of the (220) reflection or the background noise. As a result, it is clear that La_3NbO_7 crystallizes into a weberite-type structure; however a CuKα XRD cannot resolve the space group issue. A more detailed

discussion about the space group and the crystal structure of La_3NbO_7 will be presented in Chapter 7 based on neutron diffraction.

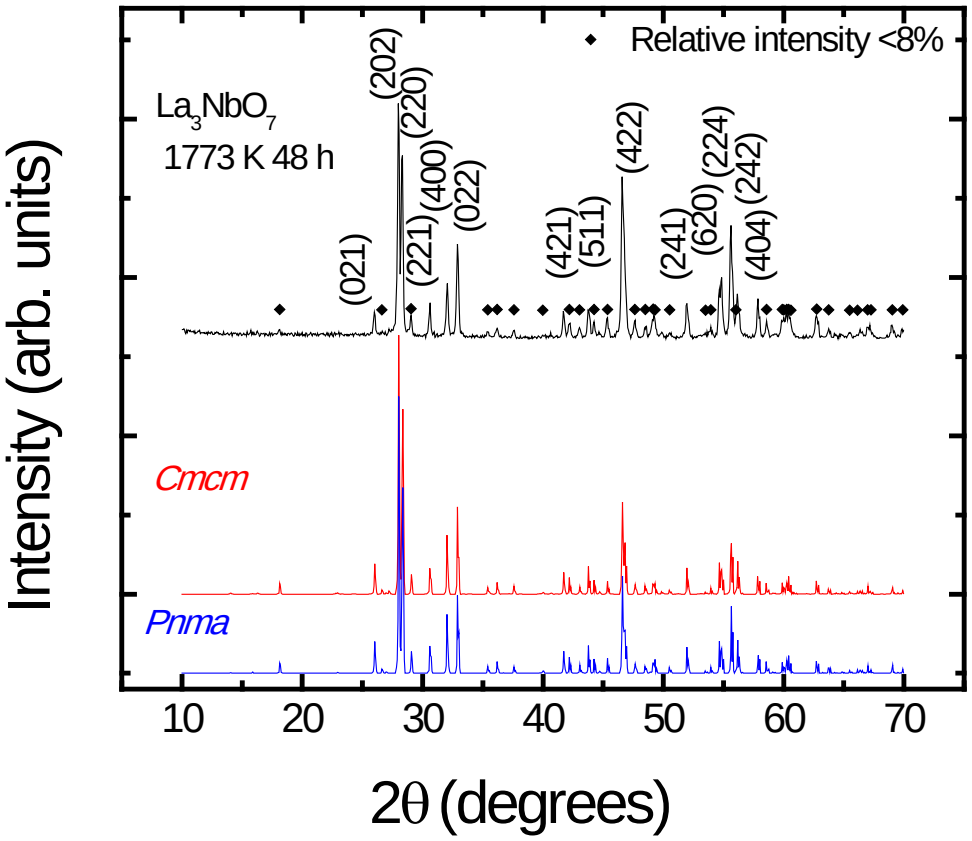

Figure 4-7. Comparison of experimental XRD of La_3NbO_7 with theoretical XRD after Rossell[36] (space group *Cmcm*) and Kahnharari[37] (space group *Pnma*).

The XRD profile of Nd_3NbO_7 is shown in Figure 4-8. The experimental pattern of Nd_3NbO_7 is in reasonably good agreement with the theoretical XRD pattern based on the atomic positions after Rossell (space group *Cmcm*).[36] While all of the experimentally observed peaks are part of the Nd_3NbO_7 crystal structure, only the peaks with relative intensities larger than 8% are indexed in Figure 4-8. The least intense peaks are indicated by diamond symbols. It is important to note that although there are few, if any, published atomic positions for Nd_3NbO_7 with the space group *Pnma,* it was

nonetheless proposed as an acceptable space group of Nd_3NbO_7.[127-128] Similar to La_3NbO_7, it is difficult to figure out the correct space group of Nd_3NbO_7 by CuKα XRD. Therefore, both synchrotron x-ray and neutron powder diffraction were performed on Nd_3NbO_7 and will be discussed in Chapter 7.

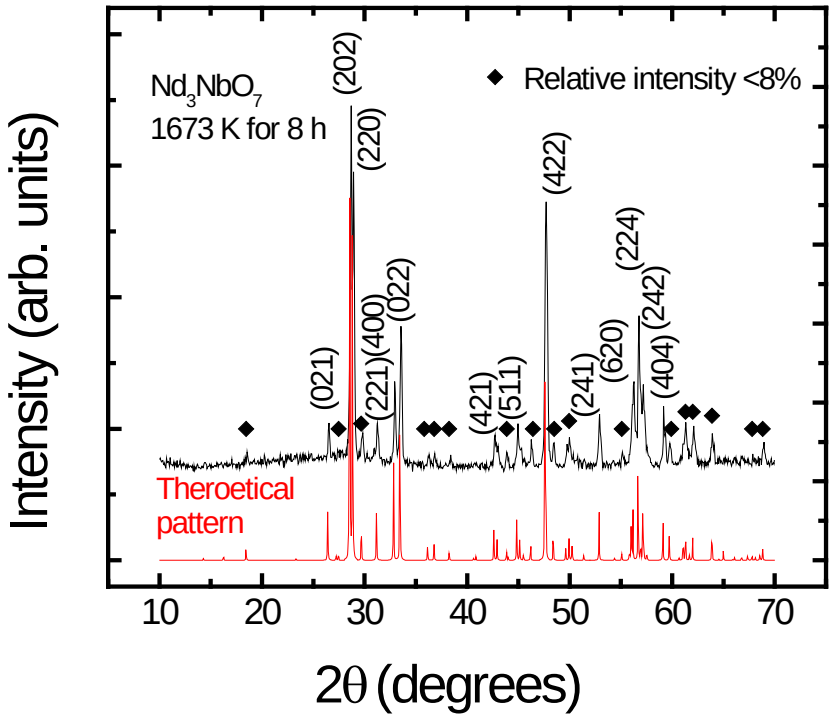

Figure 4-8. Experimental and theoretical XRD of Nd_3NbO_7.[36,86]

The XRD pattern for Gd_3NbO_7 is shown in Figure 4-9. At first glance, it matches well with a cubic fluorite profile. However, the Gd_3NbO_7 pattern contains more minor peaks with intensities below 1% of the relative intensity. These minor peaks have been identified in the past as superlattice lines typically associated with the pyrochlore structure by Abe *et al.*[23] However, Abe's claim was not based on any detailed XRD analysis. Based on the Gd_3NbO_7 XRD profile collected here, some of the peaks cannot be attributed to the pyrochlore structure. These peaks are indexed as the planes with

mixed odd and even *h*, *k*, *l* values, and they violate the reflection conditions for pyrochlore, where *h*, *k*, *l* values should be either all odd or all even. By contrast, all of the peaks can be correctly indexed on the basis of the Gd_3TaO_7 compound (JCPDS 38-1409, Gd_3TaO_7 is a similar compound to Gd_3NbO_7), which according to Yokogawa *et al.*[129] is a weberite-type structure with the space group $C222_1$.

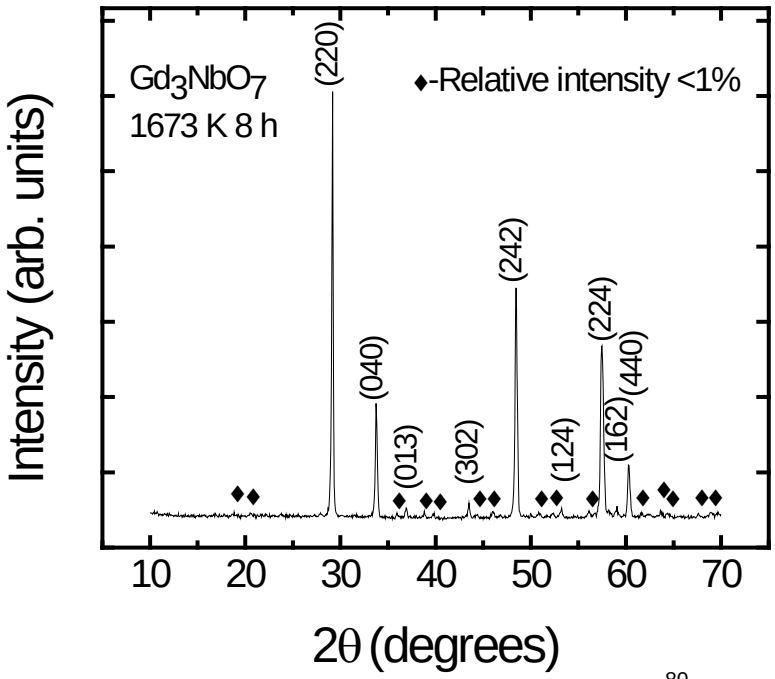

Figure 4-9. Experimental and theoretical XRD of Gd_3NbO_7.[80]

Although the space group $C222_1$ was initially proposed for Gd_3NbO_7 by Allpress *et al.*[80], it was later questioned by Astafyev *et al.*[38] due to the fact that Gd_3NbO_7 exhibited second harmonic generation (SHG) signals at room temperature. Astafyev then proposed the space group *Cmm2* without proof. Therefore, in this work, Le Bail structureless whole pattern fitting by PowderCell[126] was performed using the space groups $C222_1$ and *Cmm2* to see which one was a better fit. However, the fitting for both of these space groups gave a good match with the experimental data since every

observed peak can be indexed in these two space groups. At this stage, although it is proven that Gd_3NbO_7 crystallizes into a weberite-type structure, the correct space group is still in question. Synchrotron x-ray diffraction is therefore necessary for further investigation, as will be discussed in Chapter 6.

4.4 Crystal Structure of $Ln_2(Ln'_{0.5}Nb_{0.5})_2O_7$

The XRD profiles of $La_2(Yb_{0.5}Nb_{0.5})_2O_7$ at different calcination temperatures and the stoichiometric mixture of the La_2O_3, Yb_2O_3 and Nb_2O_5 are shown in Figure 4-10 (A). After initial calcination at 1673 K for 8 h, the resulting pattern showed a mixture phase of $La_2(Yb_{0.5}Nb_{0.5})_2O_7$, Yb_3NbO_7, and La_2O_3. After the subsequent calcination at 1773 K for 24 h, there was no obvious La_2O_3 phase and Yb_3NbO_7 phase is greatly depressed, which relative intensity of the strongest peak decreased from 42% to 7%. After the third calcination at 1773 K for 24 h, it was clearly shown that there are no unreacted La_2O_3, Yb_2O_3 Nb_2O_5 or Yb_3NbO_7 in the $La_2(Yb_{0.5}Nb_{0.5})_2O_7$ pattern. The XRD profile remained the same after additional calcination at 1773 K for 12 h. Therefore, equilibrium was presumed after the third calcination. The pattern is very similar to the cubic fluorite profile. Upon further inspection, some of the intense peaks are in fact split into two peak reflections. When compared with the fluorite, the peak splits occur at the 2θ position of (111), (220), (113) and (222). The splitting may be due to the formation of two phases. However, the existence of two phases should also cause the splitting of (002) peaks at a 2θ around 33^o, which is not obvious in the XRD pattern. It could be possible that the (002) peaks are greatly overlapped and hard to be distinguished. However, in the two phase case, the splitting increases with increasing 2θ, which means the splitting at (002) should be larger than the splitting at (111). Therefore, since

this is not the case, it is concluded that the peak splitting is not due to the formation two phases.

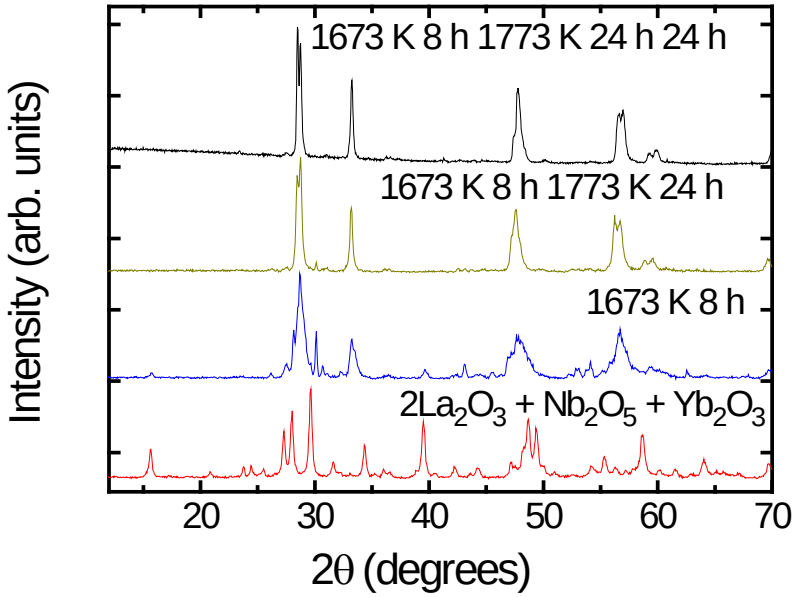

(A)

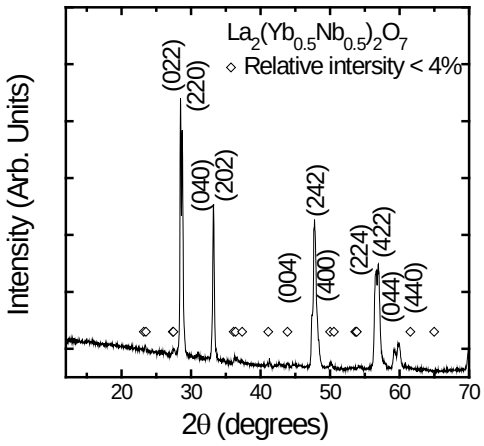

(B)

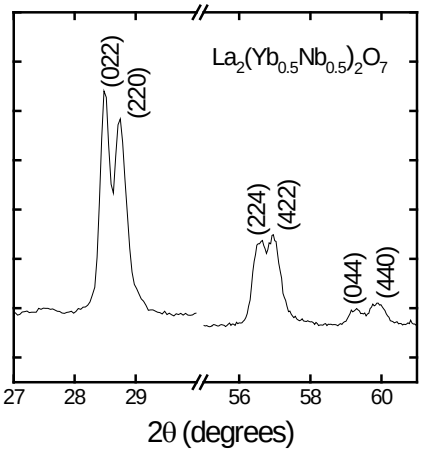

(C)

Figure 4-10. (A) XRD patterns $La_2(Yb_{0.5}Nb_{0.5})_2O_7$ at different calcination temperatures and time, and the mixture of La_2O_3, Nb_2O_5 and Yb_2O_3 (B) Indexed XRD profile of $La_2(Yb_{0.5}Nb_{0.5})_2O_7$ after calcinations at 1673 K for 8h and 1773 K for 24 h and 24 h (c) details of the peak splitting in $La_2(Yb_{0.5}Nb_{0.5})_2O_7$.[120]

By contrast, the peak splitting observed is consistent with an orthorhombic distortion of the cubic fluorite structure. If the lattice parameter of the cubic fluorite is *a* (where *a* ~ 5Å), then the lattice parameters of the orthorhombic structure are approximately $\sqrt{2}a$, $2a$ and $\sqrt{2}a$. The transformation relationship from the cubic to the orthorhombic structure can be written as following:

$$\text{Orthorhombic} = \text{Cubic}\begin{pmatrix} 1 & 0 & 1 \\ 0 & 2 & 0 \\ -1 & 0 & 1 \end{pmatrix} \quad (4\text{-}2)$$

Therefore, the (111) plane in the cubic structure corresponds to (220) and (022) planes in the orthorhombic structure in the XRD pattern and the $(222)_c$ (the subscript "c" means cubic) is transformed into $(440)_o$ and $(044)_o$ (the subscript "o" means orthorhombic) as in Table 2-3. The $(220)_c$ splits into $(400)_o$, $(004)_o$ and $(242)_o$ while the $(113)_c$ converts to $(422)_o$ and $(224)_o$.

Meanwhile, the pattern contains several weak peaks with intensities below 5% relative intensity. These weak reflections may suggest the formation of a fluorite superstructure. The lattice parameters are initially given by the TREOR program in Crysfire and refined in Maud program.[130-131] The sample displacement is also refined. The Debye-Scherrer geometry is used for the pattern collected from the inel CPS diffractometer. The obtained lattice parameters are 7.5623(13) Å, 10.7666(23) Å, 7.6619(13) Å. The lattice parameters are in the range of orthorhombic fluorite-related compounds such as pyrochlore $Cd_2Nb_2O_7$ (7.3295 Å, 10.3655 Å, 7.3295 Å), weberite $Ca_2Sb_2O_7$ (7.3060 Å, 10.2263 Å, 7.4627 Å) and weberite $Ba_2U_2O_7$ (8.1665 Å, 11.3081 Å and 8.1943 Å).[12,70,132] It is worth noting that the peak at $2\theta \sim 33^o$ ($(002)_c$) should also split into $(202)_o$ and $(040)_o$. The difference in 2θ position between (202) and (040) is only 0.059^o based on the calculated lattice parameters (The difference in 2θ position

between (022) and (220) is 0.260^{o} shown in Figure 4-10 (C)). The step size of the XRD detector is about 0.038^{o}. Therefore, it is safe to assume that the (022) and (040) peaks are overlapped and the splitting cannot be detected.

The XRD pattern of $La_2(Yb_{0.5}Nb_{0.5})_2O_7$ is similar to the XRD profile of orthorhombic pyrochlore $Cd_2Nb_2O_7$ (space group *Ima2*), which also have some additional minor peaks compared to the fluorite structure and peak splitting at characteristic fluorite peaks. Therefore, the initial guess of the structure is based on $Cd_2Nb_2O_7$. The Powdercell program was used to refine the experimental XRD profile.[133] All the peaks but one with 2% relative intensity at 2θ ~ 31^{o} were fitted with the proposed structure. For clarify, the peaks with relative intensities larger than 4% are indexed and the other below 4% relative intensities are indicated by diamond symbols in Figure 4-10 (B).

The XRD profiles of $La_2(Dy_{0.5}Nb_{0.5})_2O_7$ and $La_2(Er_{0.5}Nb_{0.5})_2O_7$ are shown in Figure 4-11. The 5 characteristic fluorite peaks are all split into two or more peak reflections. The patterns contain more weak peaks than in the case of $La_2(Yb_{0.5}Nb_{0.5})_2O_7$. The minor peaks at 2θ ~ 26^{o}, 29.5^{o} and 31^{o} violate the reflection condition for the orthorhombic pyrochlore in which the value of h + k + l should be even. The XRD profiles of $La_2(Dy_{0.5}Nb_{0.5})_2O_7$ and $La_2(Er_{0.5}Nb_{0.5})_2O_7$ were compared with the XRD of fluorite-related structures including orthorhombic weberite, weberite-type La_3NbO_7 (or Nd_3NbO_7), weberite-type Gd_3NbO_7, orthorhombic ZrO_2, monoclinic ZrO_2, Zirkelite and Zirconolite. The XRD patterns were found similar to the weberite-type La_3NbO_7 and Nd_3NbO_7. Le Bail fitting was performed to confirm that all peaks can be fitted based on the weberite-type structure using Powdercell program.[133] The peaks

with relative intensities larger than 8% are indexed and the other less intense peaks are indicated by diamond symbols in Figure 4-11.

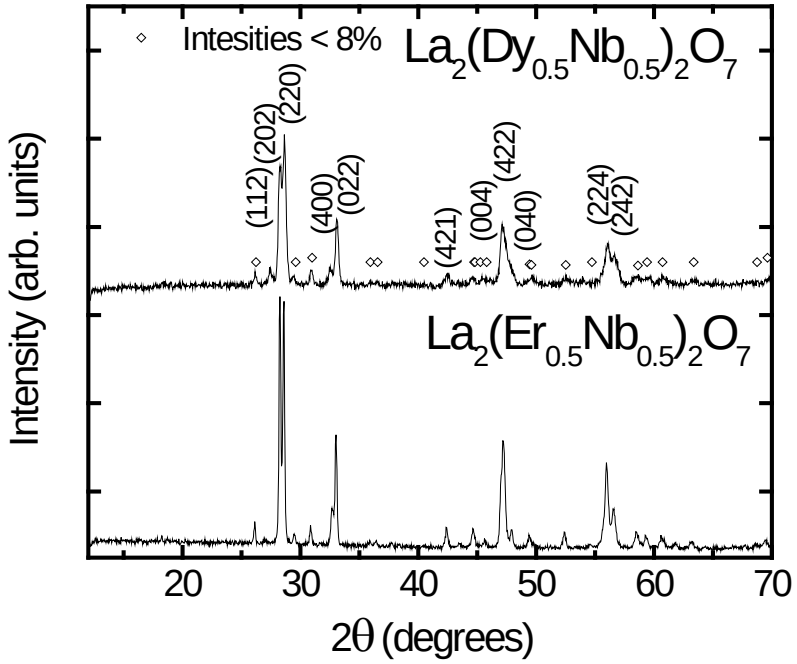

Figure 4-11. XRD patterns of $La_2(Dy_{0.5}Nb_{0.5})_2O_7$ and $La_2(Er_{0.5}Nb_{0.5})_2O_7$.[120]

The reason why $La_2(Yb_{0.5}Nb_{0.5})_2O_7$ is pyrochlore-related, and $La_2(Er_{0.5}Nb_{0.5})_2O_7$ and $La_2(Dy_{0.5}Nb_{0.5})_2O_7$ are weberite-type, is probably that $La_2(Yb_{0.5}Nb_{0.5})_2O_7$ has a higher r_A/r_B ratio. The R_A/R_B ratio of $La_2(Er_{0.5}Nb_{0.5})_2O_7$ (r_A/r_B = 1.50) and $La_2(Dy_{0.5}Nb_{0.5})_2O_7$ (r_A/r_B = 1.49) is closer to the edge of the pyrochlore stability field (1.46 - 1.8) than $La_2(Yb_{0.5}Nb_{0.5})_2O_7$ (r_A/r_B = 1.51); thus the first two compounds are less likely to form a pyrochlore phase. The lattice parameters of $La_2(Dy_{0.5}Nb_{0.5})_2O_7$ are 10.9220(8) Å, 7.5646(12) Å, and 7.7060(13) Å. The lattice parameters of $La_2(Er_{0.5}Nb_{0.5})_2O_7$ are 10.9220(8) Å, 7.5915(12) Å and 7.7189(5) Å.

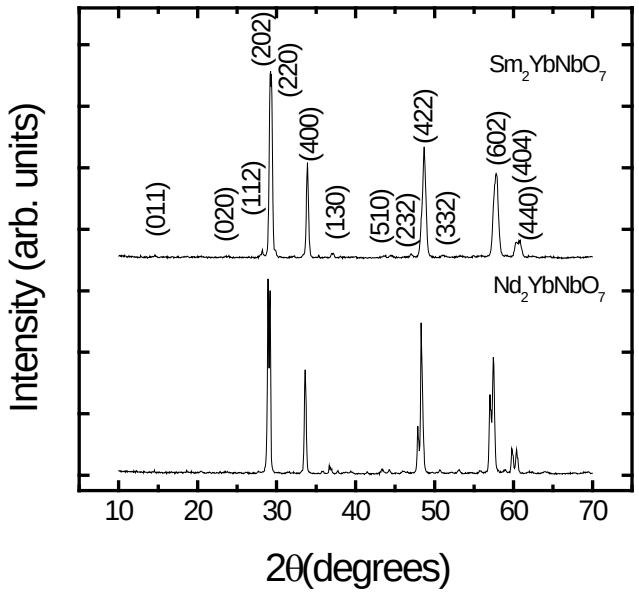

Figure 4-12. XRD patterns of Sm_2YbNbO_7 and Nd_2ErNbO_7.[120]

The XRD profiles of Sm_2YbNbO_7 and Nd_2YbNbO_7 are shown in Figure 4-12. The XRD patterns can be indexed using an orthorhombic lattice. The lattice parameters of Sm_2YbNbO_7 are 10.566(8) Å, 7.443(5) Å and 7.528(8) Å. The lattice parameters of Nd_2YbNbO_7 are 10.624(4) Å, 7.482(4) Å and 7.582(3) Å. The summary of lattice parameters of all investigated compounds will be presented in Chapter 9.

4.5 Conclusion

Structural characterization of Ln_3NbO_7 (Ln = La^{3+}, Nd^{3+}, Gd^{3+}, Dy^{3+}, Er^{3+}, Y^{3+}, and Yb^{3+}) and $La_2Ln'NbO_7$ was presented here. It was found that if the ionic radius of Ln^{3+} is equal to or smaller than Dy^{3+} (1.027 Å), then the crystal structure of Ln_3NbO_7 is confirmed by XRD analysis to be a defect fluorite structure, with the lattice parameter increasing linearly with increasing ionic radius of Ln^{3+}. Additionally, it can be noted that La_3NbO_7 and Nd_3NbO_7 crystallize into a weberite-type structure. However, it is difficult to determine the correct space group (*Pnma* or *Cmcm*) with CuKα XRD. Also, Gd_3NbO_7

was found to have another weberite-type structure, similar to that of Gd_3TaO_7. Again, the correct space group for the Gd_3NbO_7 structure is still in question. As for $La_2Ln'NbO_7$, these compounds have an orthorhombic fluorite-related structure. $La_2(Yb_{0.5}Nb_{0.5})_2O_7$ is orthorhombic pyrochlore, and $La_2(Er_{0.5}Nb_{0.5})_2O_7$ and $La_2(Dy_{0.5}Nb_{0.5})_2O_7$ are weberite-type. Due to the limitation of CuKα XRD, synchrotron x-ray and neutron powder diffraction were also performed on the weberite-type Ln_3NbO_7 compounds as will be discussed in Chapter 6 and Chapter 7.

CHAPTER 5
DIELECTRIC PROPERTIES OF Ln_3NbO_7 and $Ln_2(Ln'_{0.5}Nb_{0.5})_2O_7$

5.1 Introduction

The core of this chapter is chiefly based on three articles: 1. the journal article (Journal of the European Ceramic Society, ***27*** *(13-15) 3971-3976 (2007)) titled "Structure and Dielectric Properties of* Ln_3NbO_7 *(Ln = Nd, Gd, Dy, Er, Yb, and Y)," by L. Cai and J.C. Nino;*[86] *2. the journal article (Journal of the European Ceramic Society,* ***30*** *(2) 307-313 (2010)) titled "Phase Formation and Dielectric Properties of* $Ln_2(Ln'_{0.5}Nb_{0.5})_2O_7$ *(Ln = rare earth element)," by L. Cai and J.C. Nino;*[120] *3. the proceedings article (Solid State of Inorganic Materials VI (Materials Research Society Symposium Proceeding),* ***998E*** *0988-qq01-04 (2007)) titled "Phase Formation and Dielectric Properties of* Ln_3NbO_7 *(Ln = rare earth elements)," by L. Cai, J. Guzman, L. Perez, and J.C. Nino.*[85] *They are reprinted with permission from Elsevier and MRS E-Proceedings.*

There are a few scattered investigations on the dielectric properties of Ln_3NbO_7. Chincholkar[134] first reported the dielectric properties of x Sm_3NbO_7 + (1-x) La_3NbO_7 system (x is from 0 to 1). The reported room temperature dielectric permittivity of pure La_3NbO_7 was high, 800 at 1 kHz. Since the study was limited to 1 kHz, the high permittivity may mainly contribute from space charge polarization mechanism. The results were not convincing as well because of lack of description of experimental procedures. Astaf'ev *et al.*[38] investigated the dielectric properties of Gd_3NbO_7 at 1 kHz from 200 K to 380 K. The dielectric permittivity increases with increasing temperature until 330 K and decreases above 330K, accompanied by a dielectric loss peak at about 300 K. As for defect-fluorite Ln_3NbO_7, literature review shows there are no

investigations on the dielectric properties of these compounds. To explore the fundamental structure-dielectric properties relationships, in the present work, research was conducted on the dielectric properties of Ln_3NbO_7 (Ln^{3+} = La^{3+}, Nd^{3+}, Gd^{3+}, Dy^{3+}, Er^{3+}, Y^{3+}, and Yb^{3+}) and $Ln_2(Ln'_{0.5}Nb_{0.5})_2O_7$ over a broad range of frequency and temperature.

5.2 Dielectric Properties of Defect Fluorite Ln_3NbO_7

The sample preparation was described in Chapter 3. The dielectric properties between 1 kHz and 1 MHz from 113 K to 473 K for Dy_3NbO_7 are shown in Figure 5-1. The real part of permittivity increases from 35 to 39 with increasing temperature, and increases slightly with decreasing frequency. The positive temperature coefficient of capacitance shows two slope variations (inflection points) with associated changes in the imaginary part with a peculiar cross-over at approximately 350 K. The imaginary part of permittivity is on the order of 10^{-1} at 1 MHz from 113 K to 473 K.

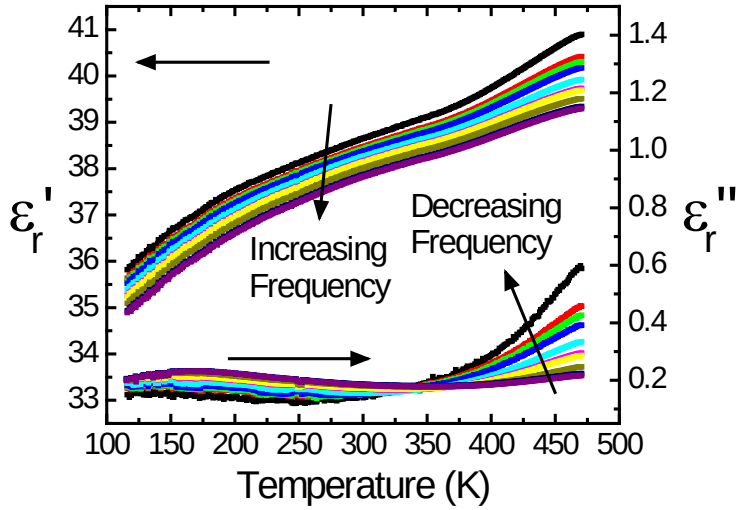

Figure 5-1. Dielectric properties of Dy_3NbO_7 at 1 kHz, 3 kHz, 8 kHz, 10 kHz, 30 kHz, 80 kHz, 100 kHz, 300 kHz, 800 kHz, and 1 MHz.

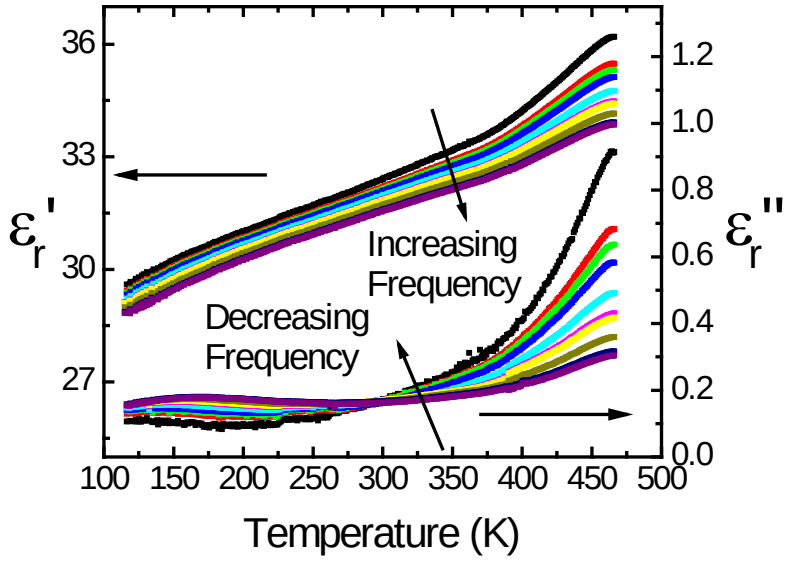

Figure 5-2. Dielectric properties of Yb_3NbO_7 from 1 kHz to 1 MHz.

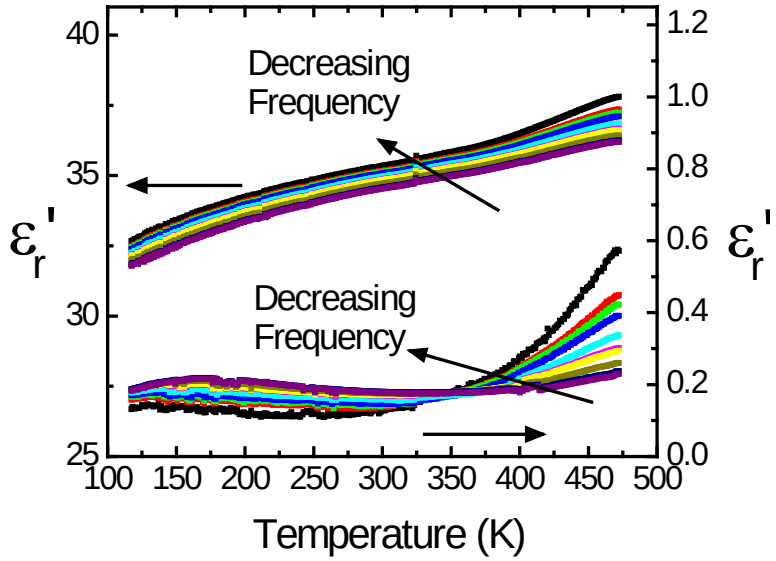

Figure 5-3. Dielectric properties of Y_3NbO_7 from 1 kHz to 1 MHz.

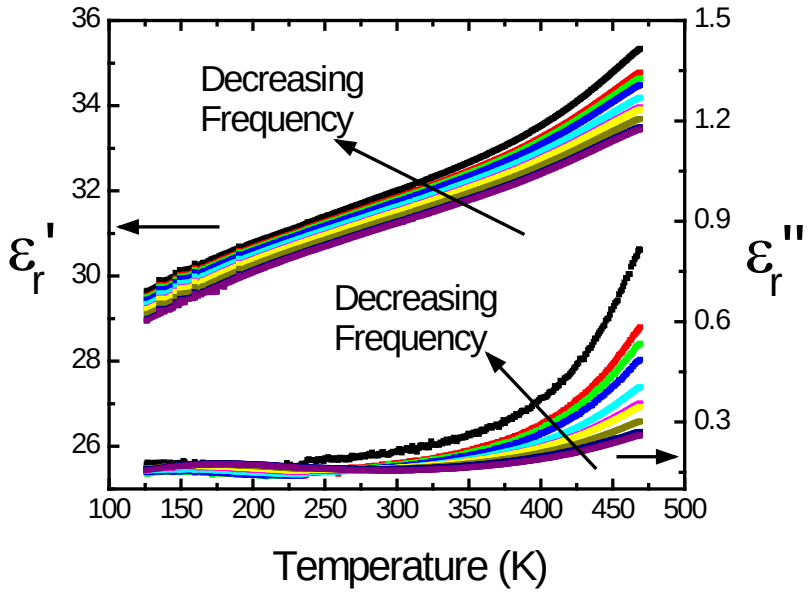

Figure 5-4. Dielectric properties of Er_3NbO_7 from 1 kHz to 1 MHz.

The dielectric properties of Yb_3NbO_7 (Figure 5-2), Y_3NbO_7 (Figure 5-3), and Er_3NbO_7 (Figure 5-4), and show the same trend as Dy_3NbO_7. The room temperature real part of permittivity is 34.7, 31.4, and 31.2, for Y_3NbO_7, Er_3NbO_7, and Yb_3NbO_7 respectively. The imaginary part is on the order of 10^{-1} from 113 K to 473 K at 1 MHz. The real part of permittivity of these four compounds increases with increasing temperature. The temperature coefficient of capacitance (TCC) was calculated from 218 K to 350 K,

$$TCC = \frac{1}{C_{RT}} \frac{\Delta C}{\Delta T} \qquad (5\text{-}1)$$

ΔC is the difference between the capacitance at 350 K and at 218 K. C_{RT} is the capacitance at room temperature. ΔT is 312 K in this case. The units of TCC is MK^{-1} (parts per million per K). As shown in Figure 5-5, TCC increases with increasing ionic radius of Ln^{3+}. As stated in the introduction of Chapter 4, other study indicated that the

defect-fluorite may have local ordering.[80] It is reasonable to expect that the local ordering increase with the increasing difference between ionic radius of $Nb^{5+}$and Ln^{3+}. Therefore, it implies that TCC may increase with the structural disorder. The TCC values are also listed in Table 5-1.

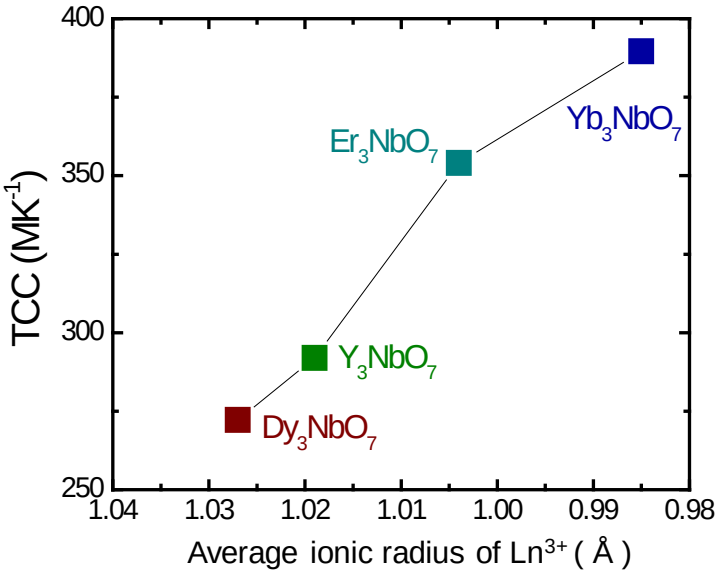

Figure 5-5. TCC of defect-fluorite Ln_3NbO_7 from 218 K to 350 K.

When the observed dielectric constant for these compounds is compared with the predicted values using the Clausius-Mosotti equation, the calculated values only account for 50% of the experimentally observed dielectric constant (Table 5-1). It is important to note that the Clausius-Mosotti equation is derived under the assumption that ions of one type are symmetrically arranged around ions of another type.[135] As such, the equation is used to estimate the dielectric constants contributed by electronic and ionic mechanism with the calculated values agreeing well for the majority of non-polar inorganic oxides.[26] The large deviation of ε'_{cal} from ε'_{mea} indicates that the assumption may not hold for defect-fluorite structures because of unoccupied oxygen

sites and the disorder of the lanthanide and niobium ions. It may also suggest that there exists a weak dipolar contribution contributing to the permittivity in these compounds.

Table 5-1. Summary of ionic radius (r_{Ln}) of rare earth ions, lattice parameters of Ln_3NbO_7, polarizablity (α_{Ln}), experimental (room temperature) and calculated dielectric constants of Ln_3NbO_7 (Ln^{3+} = Y^{3+}, Yb^{3+}, Er^{3+}, and Dy^{3+}), and the temperature coefficient of capacitance (TCC).

	r_{Ln} (Å)[27]	a (Å)	α_{Ln} (Å^3)[26]	ε_r' (measured)	ε_r' (calculated)	TCC (MK^{-1})
Dy_3NbO_7	1.027	5.2700(6)	4.07	37.75	20.31	272.24
Y_3NbO_7	1.019	5.2533(10)	3.81	34.38	18.17	291.94
Er_3NbO_7	1.004	5.2317(10)	3.81	31.47	19.73	354.05
Yb_3NbO_7	0.985	5.194(2)	3.58	31.18	19.43	389.58

5.3 Dielectric Properties of Weberite-type Ln_3NbO_7 (Ln = La^{3+}, Nd^{3+}, and Gd^{3+})

5.3.1 La_3NbO_7 and Nd_3NbO_7

La_3NbO_7 exhibits a temperature-dependent dielectric relaxation shown in Figure 5-6. The variation of dielectric permittivity of La_3NbO_7 with frequency between 1 kHz and 1 MHz is negligible from 20 K to 475 K. The room temperature real part of permittivity is approximately 48 at all measured frequencies. The value is reasonable since it is on the same order of the dielectric permittivity for other Ln_3NbO_7.[38,86] The real part of permittivity increases from 32 to 59 with increasing temperature between 20 K and 360 K. The TCC is 2965 MK^{-1} from 218 K to 350 K. Above 370 K, the permittivity decreases with increasing temperature in an approximately linear manner. The TCC is then -733 MK^{-1} from 370 K to 470 K. The imaginary part of permittivity is on the order of 10^{-2} between 8 kHz and 1 MHz, smaller than that of all of the defect-fluorite Ln_3NbO_7 (on the order of 10^{-1}).

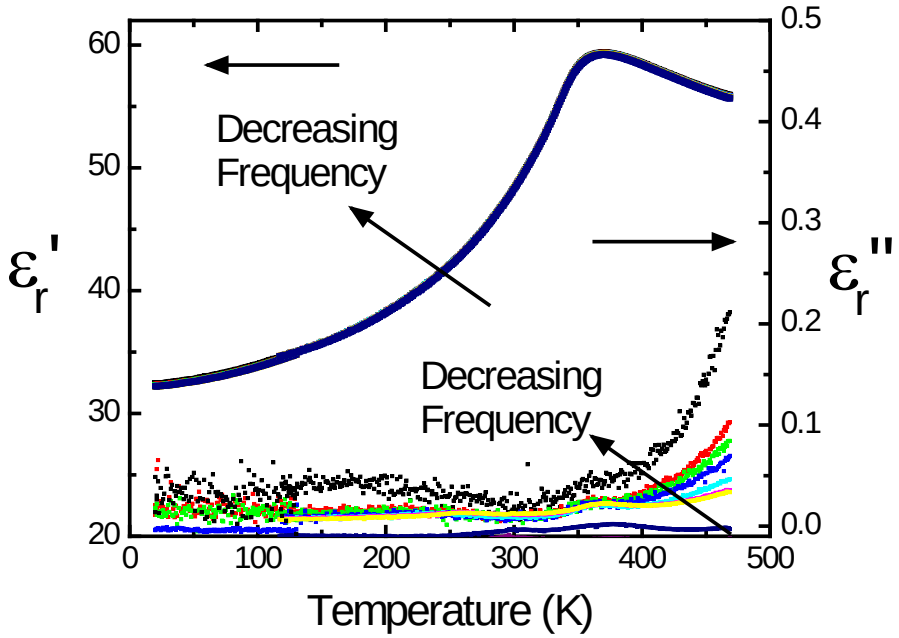

Figure 5-6. Dielectric properties of La_3NbO_7 from the temperature 20 K to 473 K at 1 kHz, 3 kHz, 8 kHz, 10 kHz, 30 kHz, 80 kHz, 100 kHz, 300 kHz, 800 kHz, and 1 MHz.

Figure 5-7 shows the dielectric properties for Nd_3NbO_7 as a function of temperature at different frequencies from1 kHz to 1 MHz. The dielectric behavior of Nd_3NbO_7 resembles that of La_3NbO_7. The variation of the real part of permittivity with frequency is negligible. The real part of permittivity is relative stable between 20 K and 100 K. It increases from 35 to 62 with increasing temperature between 100 K and 450 K. The TCC from 218 K to 350 K is 1718 MK^{-1}. Above 465 K, the variation of the real part of permittivity as a function of temperature is small and with a negative slope (~ -0.02), accompanied by a sharp increase in the imaginary part of dielectric permittivity at 1 kHz (~ 0.9 at 523 K). The TCC from 465 K to 523 K is -443 MK^{-1}.

The dielectric responses of both compounds indicate the dipolar polarization may play a role since the variation of the real part permittivity as a function of temperature

changes from positive to negative. As will be discussed in detail in Chapter 7, the dielectric relaxation is related to phase transition in both compounds.

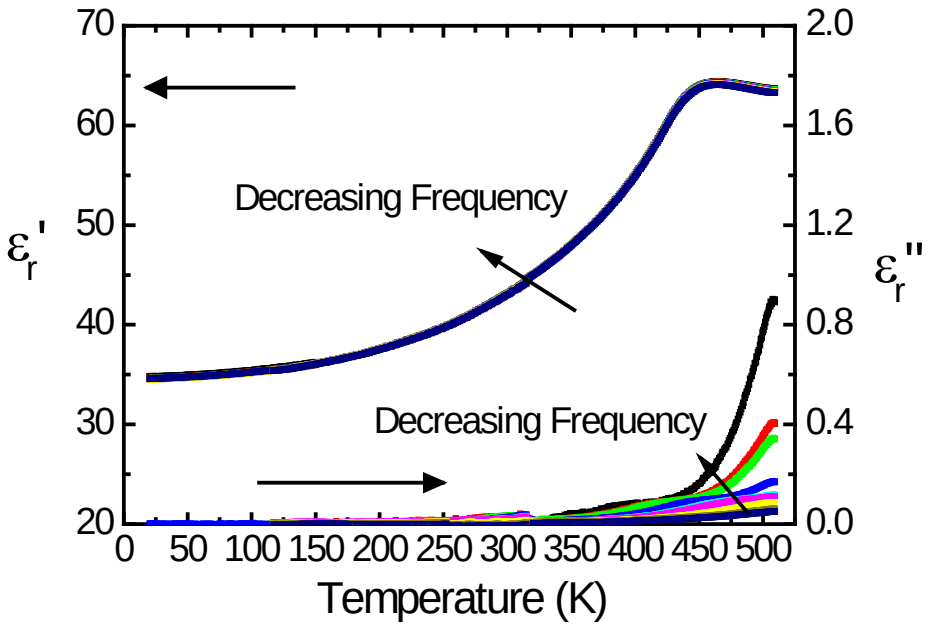

Figure 5-7. Dielectric properties of Nd_3NbO_7 between 1 kHz and 1 MHz from the temperature 20 K to 523 K.

5.3.2 Gd_3NbO_7

The dielectric behavior of Gd_3NbO_7 as a function of temperature at frequencies from 1 kHz to 1 MHz is shown in Figure 5-8. The real part of permittivity is between 33 and 48, and the imaginary part of permittivity is on the order of 10^{-4} to 10^{-1} at 1 MHz from 20 K to 475 K. It is observed that the dielectric response undergoes a frequency and temperature dependent dielectric relaxation. The real part of permittivity of Gd_3NbO_7 at different frequencies becomes more dispersive with rising temperature, increasing sharply from 20 K to 330 K where a maximum is reached. The TCC from 218 K to 350 K is 1575 MK^{-1}. At higher temperatures the permittivity decreases slightly

with increasing temperature in an almost linearly manner. The TCC is -90 MK^{-1} from 340 K to 470 K. The temperature, at which the peak of the imaginary part occurs, shifts to higher temperatures with increasing frequency. That being the case, it is unclear why there is no clear shift in the maxima of the real part of the permittivity.

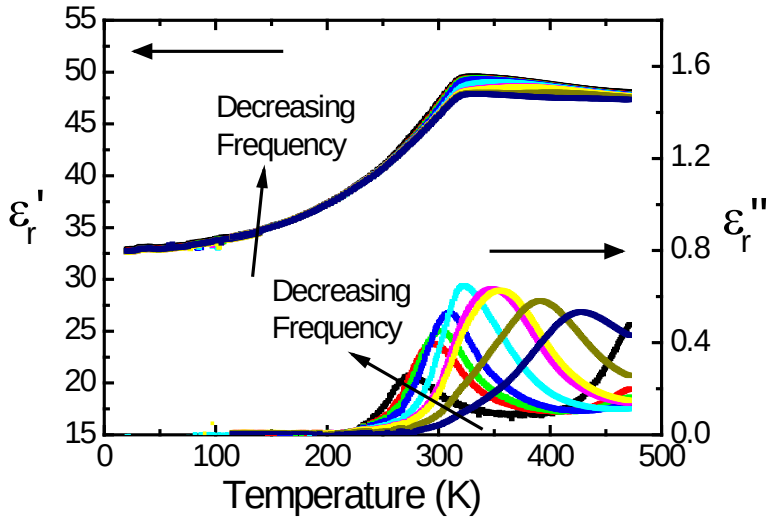

Figure 5-8. Dielectric properties of Gd_3NbO_7 between 1 kHz and 1 MHz from the temperature 20 K to 473 K.

To better understand the phenomena, the Arrhenius function is used to model the relaxation behavior of Gd_3NbO_7:

$$\nu = \nu_0 \exp[-\frac{E_a}{k_B T_m}] \qquad (5\text{-}2)$$

where ν is the measuring frequency, the pre-exponential ν_0 is the attempt jump frequency, E_a is the activation energy, and k_B is Boltzmann's constant. T_m is determined by fitting the peak of the imaginary part of permittivity for each measuring frequency to a Gaussian function. The non-symmetric tails of the peaks are cut off during fitting. The resulting Arrhenius plot is presented in Figure 5-9. From the linear fit,

v_0 = 1.51×10^{11} Hz, and the activation energy E_a is 0.45 eV, which is larger than typical values observed in Nb-based pyrochlores, for example 0.32 eV in Ca-Ti-Nb-O pyrochlore and 0.14 eV in Bi-Zn-Nb-O pyrochlore.[6,28] However, other ionic and dipolar compounds systems have even higher activation energies; for example, 0.53 eV for CaF_2 doped NaF and 1.02 eV for $(Ba_{0.8}Sr_{0.2})(Ti_{1-x}Zr_x)O_3$.[136-137] Thus, the calculated E_a is acceptable.

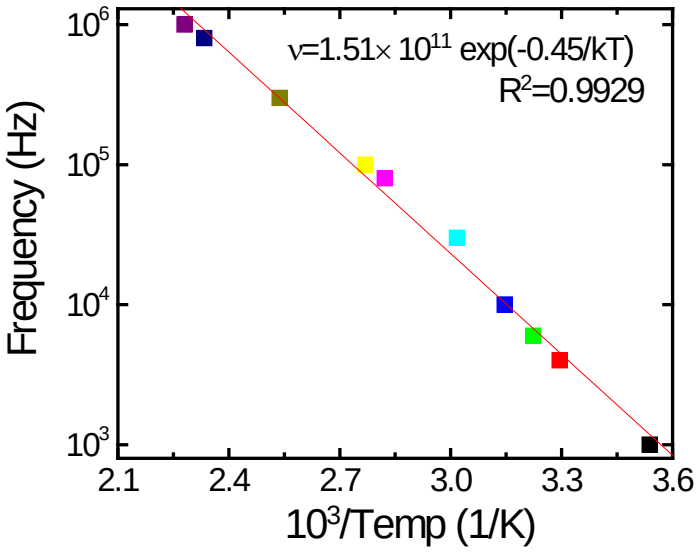

Figure 5-9. Arrhenius plot of temperature at which the maximum peak of imaginary part of permittivity occurs in Gd_3NbO_7.

A summary of the permittivity of Ln_3NbO_7 at room temperature and 1 MHz is shown in Figure 5-10. While it can be expected that the more polarizable Ln^{3+} ions would result in higher permittivity, it is clear that the room temperature permittivity does not follow the trend. Gd_3NbO_7 has higher dielectric permittivity than that of Nd_3NbO_7, even though the polarizability of Gd^{3+} is lower than that of Nd^{3+}. Sirotinkin *et al.*[108] revealed an abnormally loose structure in Ln_3NbO_7 compounds in the middle of the

series (Sm, Eu, and Gd). According to the lattice parameters calculated in this work, Gd_3NbO_7 has the highest ratio of the formula volume to the Ln^{3+} ionic radius (Figure 5-11). The formula volume is determined by the unit cell volume divided by the formula number Z (Z is 4 for weberite-type and 1 for defect fluorite). The formula volume is generally a linear relationship with respect to the ionic radius of Ln^{3+} (the red line is the linear fitting). The formula volume of Gd_3NbO_7 is outside the 95% confidence limit of the linear fitting (the grey lines), which indicate a more open structure. On the other hand, the formula volume of Nd_3NbO_7 is on the lower side of the confidence limit. It is predicted that the structural openness causes an easier polarization of the material.[38] The openness may be also responsible for lower dielectric relaxation temperature. A detailed discussion about structure-dielectric property relationships will be presented in Chapter 9.

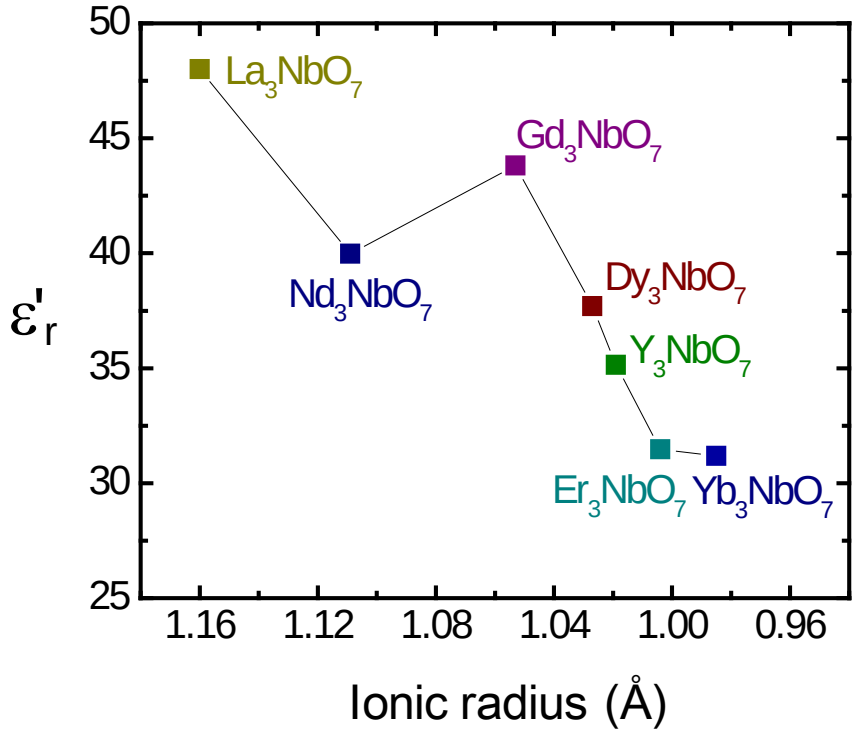

Figure 5-10. Summary of real part of permittivity for all Ln_3NbO_7 compounds.

Figure 5-12 shows the TCC for all investigated Ln_3NbO_7 compounds. Above the dielectric relaxation temperature, the TCC of Ln_3NbO_7 (Ln^{3+} = La^{3+}, Nd^{3+}, and Gd^{3+}) is negative and follows the same trend as defect fluorite Ln_3NbO_7, increasing ionic radius of Ln^{3+}. From 218 K and 350 K, the TCC of Ln_3NbO_7 (Ln^{3+} = La^{3+}, Nd^{3+}, and Gd^{3+}) decreases with decreasing ionic radius of Ln^{3+}. The TCC is large due to rapid change in permittivity the dielectric relaxation temperature. The relative large change of permittivity may contribute from dipole reorientations, which involves activation energy and the jump frequency. Therefore, a simple relationship cannot apply.

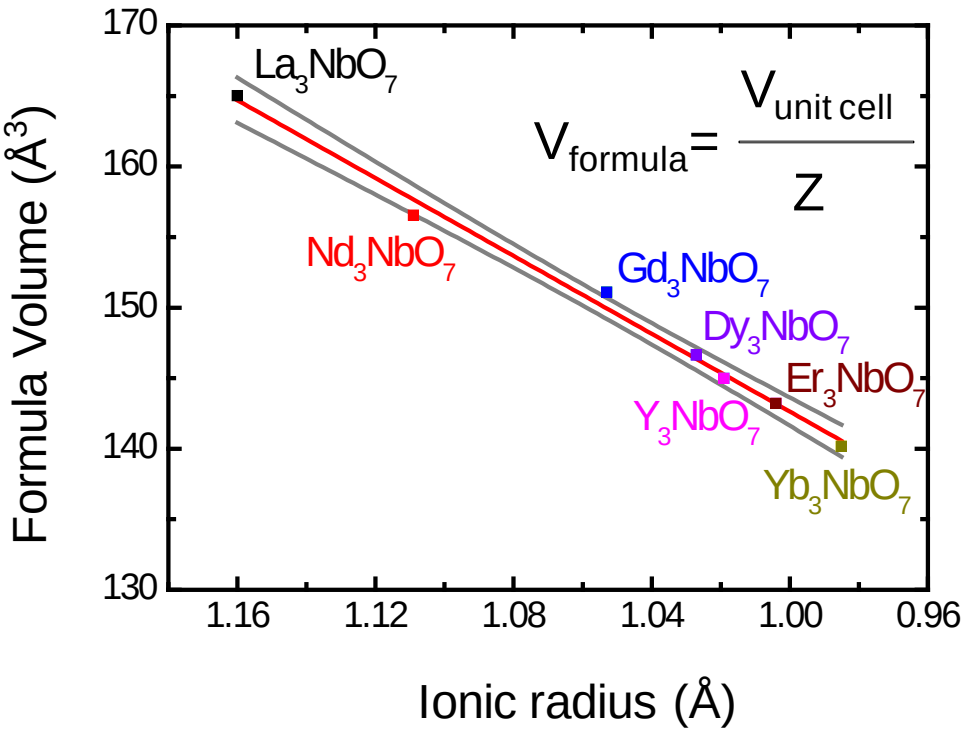

Figure 5-11. The formula volume vs. the ionic radius of Ln^{3+} for Ln_3NbO_7 at room temperature. The red line is the linear fitting and the grey lines show 95% confidence limit of the fitting.

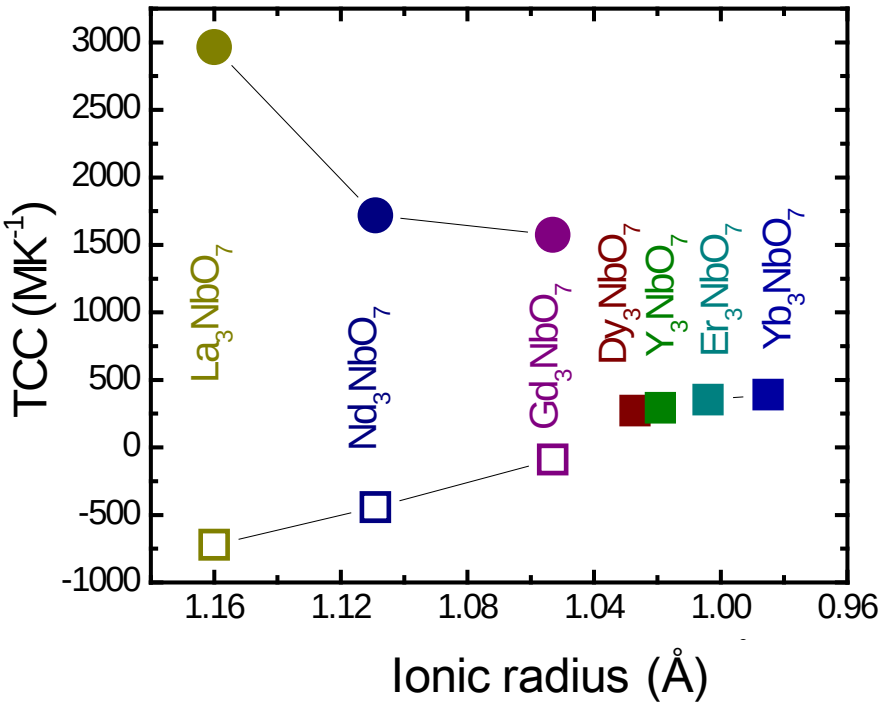

Figure 5-12. Summary of TCC for all Ln_3NbO_7 compounds. The TCC from 218 K to 350 K (circles in the figure) were calculated for La_3NbO_7, Nd_3NbO_7, and Gd_3NbO_7 but their permittivity does not change linearly with temperature. The TCC (open squares) above the dielectric relaxation temperature. The capacitance at RT was also used.

5.4 Dielectric Properties of $Ln_2(Ln'_{0.5}Nb_{0.5})_2O_7$

The dielectric behavior of $La_2(Yb_{0.5}Nb_{0.5})_2O_7$ as a function of temperature at frequencies from 10 kHz to 1 MHz is shown in Figure 5-13. The real part of permittivity is between 43.5 and 44.5 from 20 K to 295 K, and the imaginary part of permittivity is on the order of 10^{-1} at 1 MHz. It is observed that the dielectric behavior undergoes a frequency and temperature dependent dielectric relaxation. The permittivity increases slightly with increasing temperature from 20 K to 140 K where a maximum is reached (~ 44.5 at 1 MHz). The temperature, where the maximum permittivity occurs, and consequently the temperature (T_m), where the peak of the imaginary part of permittivity

is located, both increase with increasing frequency. However, the dielectric relaxation behavior of $La_2(Yb_{0.5}Nb_{0.5})_2O_7$ is different from that observed in weberite-type Gd_3NbO_7.[86] In Gd_3NbO_7, there is no clear shift in the maxima of the dielectric permittivity and a larger variation of T_m as a function of frequency.

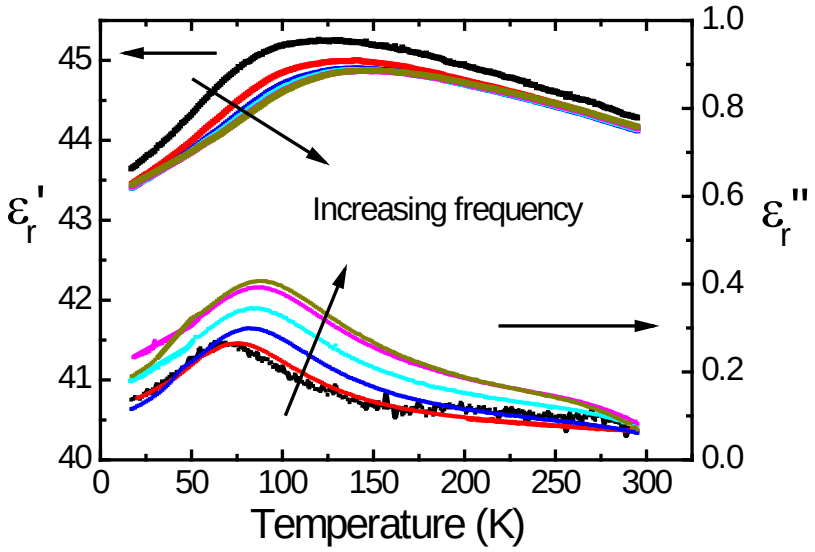

Figure 5-13. Dielectric properties of $La_2(Yb_{0.5}Nb_{0.5})_2O_7$ at 10 kHz, 100 kHz, 300 kHz, 500 kHz, 800 kHz and 1 MHz

To better understand the phenomena, as customarily, the Arrhenius function is used to model the relaxation behavior of $La_2(Yb_{0.5}Nb_{0.5})_2O_7$. The resulting Arrhenius plot is presented in Figure 5-14. From the linear fit, $v_0 = 1.2\times10^{14}$ Hz, and the activation energy E_a is 0.14 eV. The attempt frequency is lower than cubic pyrochlore $CaO\text{-}TiO_2\text{-}Nb_2O_5$ (4.6×10^{14} Hz), but higher than pyrochlore $Bi_{1.5}ZnNb_{1.5}O_7$ (3×10^{12} Hz).[28,138] It is proposed that lighter A site cations result in a higher attempt frequency in pyrochlore because the attempt frequency is related to the O'-A-O' bending phonon modes.[28,139] The calculated attempt frequency of $La_2(Yb_{0.5}Nb_{0.5})_2O_7$ is also acceptable as the mass of A cations (La^{3+}) is intermediate between $Bi_{1.5}ZnNb_{1.5}O_7$ and cubic pyrochlore CaO-

TiO_2-Nb_2O_5. The observed activation energy is smaller than that of weberite-type Gd_3NbO_7, 0.45 eV and close to $B_{1.5}ZnNb_{1.5}O_7$, 0.136 eV.[86,138]

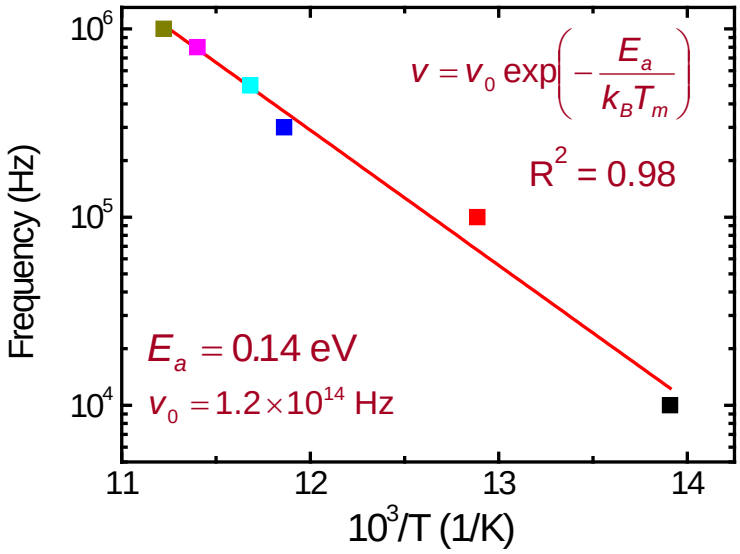

Figure 5-14. Arrhenius plot of temperature at which the maximum of imaginary parts of permittivity occurs for $La_2(Yb_{0.5}Nb_{0.5})_2O_7$

The dielectric properties of $La_2(Dy_{0.5}Nb_{0.5})_2O_7$ are shown in Figure 5-15 The permittivity slightly increases from 54.9 to 55.2 from 25 K to 86 K, and then decreases to 51 at room temperature and 1 MHz. The imaginary part of permittivity is on the order of 10^{-1} at 1 MHz, the same as the $La_2(Yb_{0.5}Nb_{0.5})_2O_7$. This compound also exhibits a dielectric relaxation. The maximum of the permittivity shifts to a higher temperature with increasing frequency. The Arrhenius function is also used to model the relaxation behavior of $La_2(Dy_{0.5}Nb_{0.5})_2O_7$. The resulting Arrhenius plot is presented in Figure 5-16. From the linear fit, $v_0 = 1.9\times10^{13}$ Hz, and the activation energy E_a is 0.12 eV. The attempt frequency of $La_2(Dy_{0.5}Nb_{0.5})_2O_7$ is between $Bi_{1.5}ZnNb_{1.5}O_7$ (3×10^{12} Hz) and the CaO-TiO_2-Nb_2O_5 pyrochlore (4.6×10^{14} Hz).[138] The activation energy is close to that of $La_2(Yb_{0.5}Nb_{0.5})_2O_7$ and $Bi_{1.5}ZnNb_{1.5}O_7$.[6]

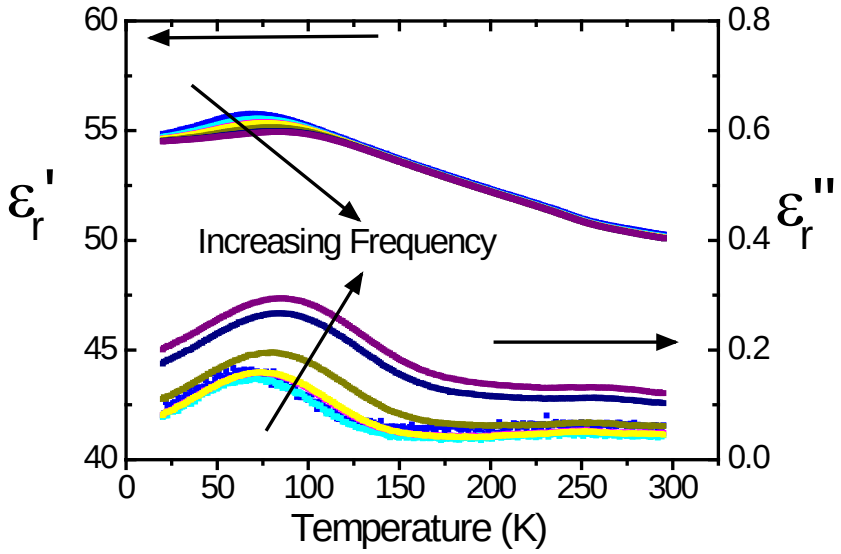

Figure 5-15. Dielectric properties of $La_2(Dy_{0.5}Nb_{0.5})_2O_7$ at 10 kHz, 100 kHz, 300 kHz, 800 kHz and 1 MHz

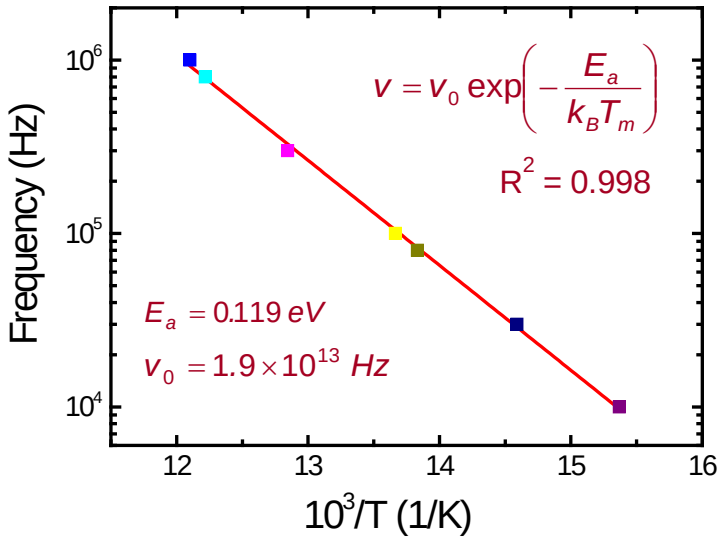

Figure 5-16. Arrhenius plot of temperature at which the maximum of imaginary parts of permittivity occurs for $La_2(Dy_{0.5}Nb_{0.5})_2O_7$

Figure 5-17 shows the dielectric properties for $La_2(Er_{0.5}Nb_{0.5})_2O_7$ as a function of temperature at different frequencies from 10 kHz to 1 MHz. The permittivity is between 48 and 50.4 from 20 K to 295 K, and the imaginary part of permittivity is also on the

order of 10^{-1} at 1 MHz. This compound also exhibits a frequency and temperature dependent dielectric relaxation. The real part of permittivity of $La_2(Er_{0.5}Nb_{0.5})_2O_7$ at different frequencies becomes more dispersive near the relaxation temperature while above 150 K, the variation of permittivity as a function of frequency is negligible. At the same time, the variation of the real part of permittivity as a function of temperature near the relaxation temperature is smaller than that from room temperature to 100 K. There is no clear shift in the maxima of the dielectric permittivity with respect to frequency in $La_2(Er_{0.5}Nb_{0.5})_2O_7$, which is similar to weberite-type Ln_3NbO_7.[86]

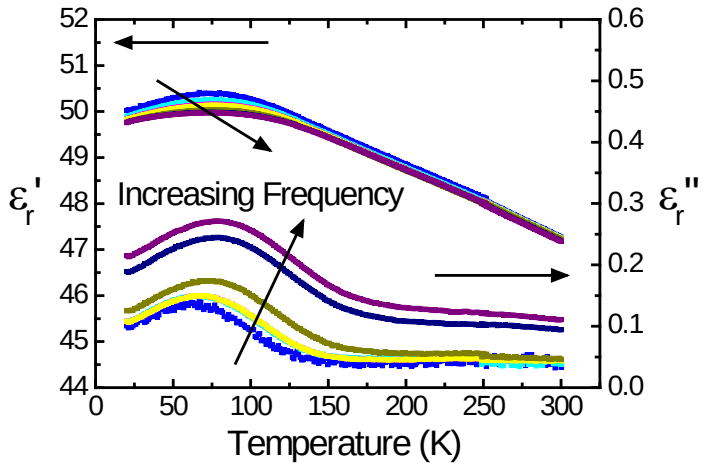

Figure 5-17. Dielectric properties of $La_2(Er_{0.5}Nb_{0.5})_2O_7$ between 10 kHz an d1 MHz

T_m increases with increasing frequency from 10 kHz to 1 MHz. The Arrhenius function is also used to model the relaxation behavior of $La_2(Er_{0.5}Nb_{0.5})_2O_7$ as shown in Figure 5-18. The calculated v_0 is 1.3×10^{12} Hz, and the activation energy E_a is 0.09 eV. While this compound is neither, a dipolar glass or relaxor ferroelectric [A well known example for dipolar glass is 1at% Li^{3+} doped $KTaO_3$ system. In this type of materials, the dipoles freeze with no net polarization in the absence of an external field applied.[140] Relaxaor ferroelectric is one kind of ferroelectric materials. Unlike the other ferroelectric,

the maximum of the real part of the permittivity does not correspond to a transition from non-polar phase to a ferroelectric polar phase. The archetype is $PbMg_{1/3}Nb_{2/3}O_3$.[141-142], it is important to note that similar activation energies have been observed or calculated for those type of materials, and thus the measured activation energy value (0.09 eV) is not unheard of.[143-145]

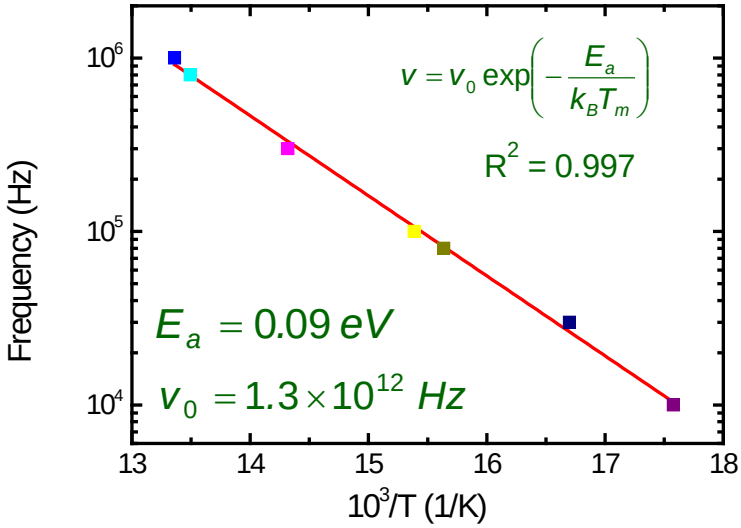

Figure 5-18. Arrhenius plot of temperature at which the maximum of imaginary parts of permittivity occurs for $La_2(Er_{0.5}Nb_{0.5})_2O_7$.

The dielectric properties of $Nd_2(Yb_{0.5}Nb_{0.5})_2O_7$ are shown in Figure 5-19. The real part of permittivity at 1 MHz is between 36 and 37 at measured temperature range. It slightly increases with temperature from 20 K to about 80 K, and decreases with increasing temperature above 80 K. The imaginary part of permittivity is on the order of 10^{-1} at 1 MHz, the same as the above $La_2(Ln_{0.5}Nb_{0.5})_2O_7$. This compound also exhibits a dielectric relaxation. The maximum of the permittivity (both the real part and the imaginary part) shifts to a higher temperature with an increase in frequency. It is interesting to note that the imaginary part of permittivity has narrower peaks than the

above $La_2(Ln'_{0.5}Nb_{0.5})_2O_7$ compounds. The Gaussian function was used to fit the peaks and the Arrhenius function is also used to model the relaxation behavior. The resulting Arrhenius plot is presented in Figure 5-20. From the linear fit, $v_0 = 2.48\times10^{10}$ Hz, and the activation energy E_a is 0.04 eV. The activation energy is on the same order of $La_2(Er_{0.5}Nb_{0.5})_2O_7$ as discussed above.

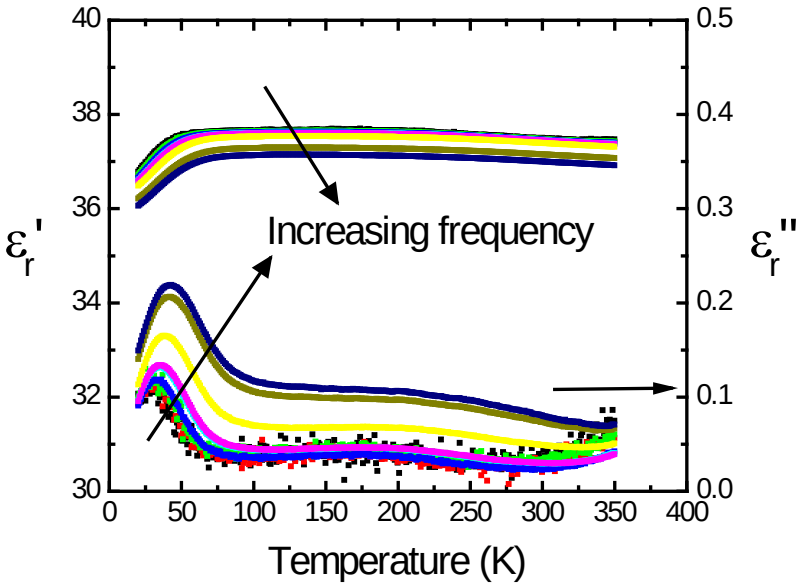

Figure 5-19. Dielectric properties of $Nd_2(Yb_{0.5}Nb_{0.5})_2O_7$ between 10 kHz and 1 MHz

It is interesting to note that all investigated $Ln_2(Ln'_{0.5}Nb_{0.5})_2O_7$ compounds exhibit temperature and frequency dependent dielectric relaxation. The temperature where the maximum permittivity occurs is much lower than that of weberite-type Ln_3NbO_7. It is not clear what causes dielectric relaxation in $Ln_2Ln'NbO_7$. It may be due to a phase transition, similar to weberite Ln_3NbO_7, or cation disorder, similar to pyrochlore (*e.g.*, $Ca_{1.46}Ti_{1.38}Nb_{1.11}O_7$[28]). The understanding of the structural origin that causes the dielectric relaxation may lead to potential avenues towards controlling the dielectric

relaxation observed in fluorite-related materials. The topic of structure-dielectric relaxation relationships will be discussed in more detail in Chapter 9.

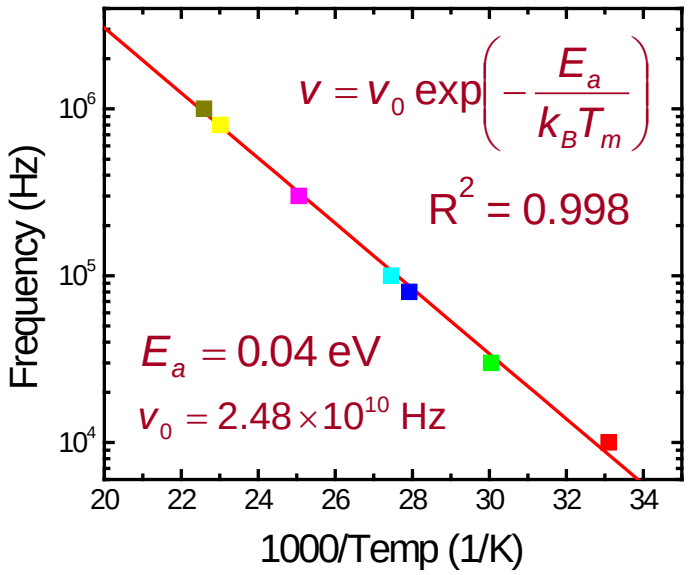

Figure 5-20. Arrhenius plot of T_m for $Nd_2(Yb_{0.5}Nb_{0.5})_2O_7$

5.5 Conclusion

The experimentally determined room temperature dielectric permittivity for rare earth niobates ranges between 29 and 45, at 1 MHz. Gd_3NbO_7 has a higher room temperature permittivity than Nd_3NbO_7, probably because the former has a more open structure. The different structures show different dielectric property behaviors as a function of temperature. The dielectric permittivity of Ln_3NbO_7 (Ln^{3+} = Dy^{3+}, Er^{3+}, Yb^{3+}, and Y^{3+}) increases with increasing temperature from 115 K to 475 K. Weberite-type Ln_3NbO_7 and $Ln_2(Ln'_{0.5}Nb_{0.5})_2O_7$ exhibit dielectric relaxation. There are three main differences in dielectric behavior between Ln_3NbO_7 and $Ln_2(Ln'_{0.5}Nb_{0.5})_2O_7$:

The temperature, where maximum of permittivity occurs, in weberite-type Ln_3NbO_7 is a much higher than in $Ln_2(Ln'_{0.5}Nb_{0.5})_2O_7$;

In Gd_3NbO_7, there is no clear shift in the maxima of the real part of permittivity. On the other hand, the maxima of the real part of permittivity increases with an increase in frequency for $Ln_2(Ln'_{0.5}Nb_{0.5})_2O_7$;

Gd_3NbO_7 has a larger variation of T_m as a function of frequency.

The Arrhenius function was used to model the relaxation behavior for Gd_3NbO_7 and $Ln_2(Ln'_{0.5}Nb_{0.5})_2O_7$. Gd_3NbO_7 has the highest calculated activation energy, 0.45 eV. By contrast, $Nd_2(Yb_{0.5}Nb_{0.5})_2O_7$ has the lowest activation energy, 0.04 eV. A more detailed discussion about the correlation between structure and dielectric relaxation will be the topic of Chapter 9.

CHAPTER 6
PHASE TRANSITION IN WEBERITE-TYPE Gd_3NbO_7

6.1 Introduction

*The core of this chapter is chiefly based on the journal article (Journal of the American Ceramic Society **93**(3) 875-880 (2010)) titled "Phase Transition in Weberite-type Gd_3NbO_7," by L. Cai, D. Sava, V. Gopolan, and J.C. Nino.*[146] *It is reprinted with permission from Wiley-Blackwell.*

It was discussed previously in Chapter 4 that the correct space group of Gd_3NbO_7 cannot be determined by CuKα X-ray diffraction. Furthermore, in Chapter 5, it reported that the Gd_3NbO_7 exhibits dielectric relaxation. The current chapter attempts to solve the space group issue and present the possible structural origin of the dielectric relaxation.

A review of the literature shows the crystal structure of Gd_3NbO_7 was first determined by Rossell.[36,80] Rossell assigned the space group $C222_1$ to Gd_3NbO_7 at room temperature. However, the non-polar space group $C222_1$ was later questioned by Astafyev *et al.*[38] as Gd_3NbO_7 exhibits second harmonic generation (SHG) signal at room temperature. The SHG signal disappears above 330 K, consistent with a non-centrosymmetric to centrosymmetric transition. It was suggested then that the transition was between *Cmm2* and *Cmmm* without proof. The existence of a transition was further confirmed by heat capacity measurement by Astafyev *et al.*[38] and Klimenko *et al.*[147] and Raman spectroscopy by Kovyazina *et al.*[121] In addition, as stated in Chapter 5, Gd_3NbO_7 exhibits a dielectric relaxation and the relaxation temperature where maximum permittivity occurs is close to the transition temperature.[85-86]

It is important to note that a phase transition is commonly observed in Ln_3BO_7 family and there has been considerable study especially in crystallographic aspects on Ln_3IrO_7,[91] Ln_3MoO_7,[81-82,87,148] Ln_3OsO_7,[149] and Ln_3RuO_7.[150-151] Here, high resolution XRD was collected on Gd_3NbO_7 powder before and after the reported phase transition to solve the space group issue and for the first time determine an unequivocal space group and crystal structure that is consistent with all the experimental data available (dielectric property, infrared spectroscopy, heat capacity, SHG, XRD, etc.). In addition, heat capacity and SHG measurements were also conducted on Gd_3NbO_7 samples in this study as the experimental procedures were not well stated by Astafyev *et al.*[38] It indicated using the same method with Sirotinkin's.[108] However, two methods were used by Sirotinkin *et al.*[108], furnace cooled (calcined from 1473 K to 1673 K) and quenched from 1593 K. It is not clear which experimental method was used for preparing the SHG sample.[38] To avoid possible discrepancy, all measurements in this study were conducted on Gd_3NbO_7 samples within the same batch.

6.2 SHG and Heat Capacity Measurements

The SHG of Gd_3NbO_7 was measured twice, the second time with higher power yielding higher intensity and it is shown in Figure 6-1. Both measurements confirmed that the SHG signal disappears at about 340 K. Figure 6-1 also shows the real part of permittivity and the reciprocal of dielectric susceptibility at 1 MHz.[86] It clearly indicates that the dielectric relaxation temperature, at which the maximum of the dielectric constant occurs, matches well with the temperature, at which the SHG signal disappears. When comparing with typical ferroelectric behavior on first and second order transition, the susceptibility plot resembles that of a 2nd order. Before the transition, Gd_3NbO_7 should have a polar space group. There are only three point

groups corresponding to an orthorhombic lattice: *222*, *mm2*, and *mmm*; and the only polar group is *mm2*. It is thus fairly evident that the transition has to be between *mm2* and *mmm;* further validation comes from the fact that *mmm* is a supergroup of *mm2*.

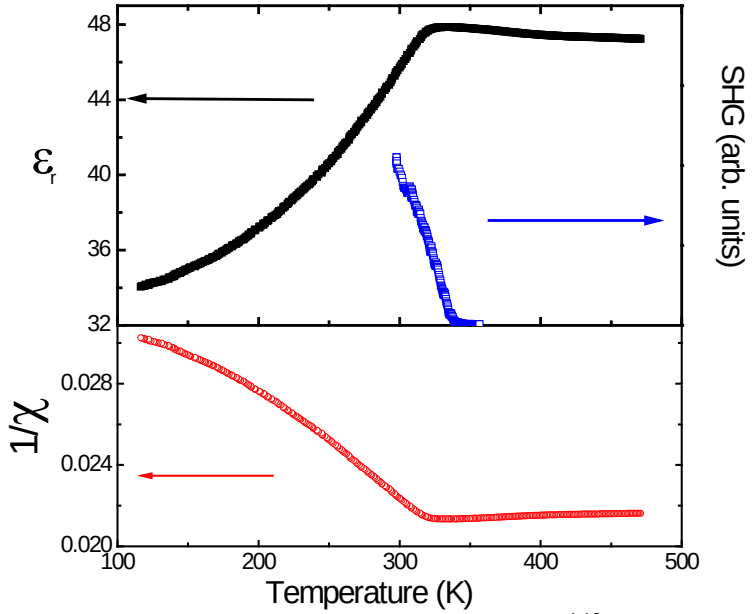

Figure 6-1. Dielectric constant and SHG of Gd_3NbO_7.[146]

The heat capacity of Gd_3NbO_7 was re-measured in this study and the measuring temperature was extended down to 160 K as presented in Figure 6-2. It shows a phase transition between 310 K and 340 K. This result matches previous studies.[38,147] The heat capacity was fitted combining the Debye and Einstein models for photonic specific heat:

$$C_p(T) = 3R \times (m \times D(\theta_D / T) + n \times E(\theta_E / T)) + A \times T + B \times T^2 \quad (6\text{-}1)$$

where R is the gas constant, $D(\theta_D/T)$ and $E(\theta_E/T)$ are Debye and Einstein functions, respectively.[152-153] There are in total six fitting parameters, m, θ_D, n, θ_E, A, B. Because Debye and Einstein functions are for isochoric molar heat capacities, the terms A and B account for the difference between isochoric and isobaric molar heat capacities. The difference between experimental and fitted data shows the specific heat associated with

phase transition. Near 273 K, heat capacity data becomes noisy, probably due to the solidification of moisture. Approaching the structural phase transition, there is a diverging of the specific heat, resembling a lambda shape. Both of the reciprocal of susceptibility and the lambda-shape specific heat suggest a 2nd order nature of the phase transition (Figure 6-2).

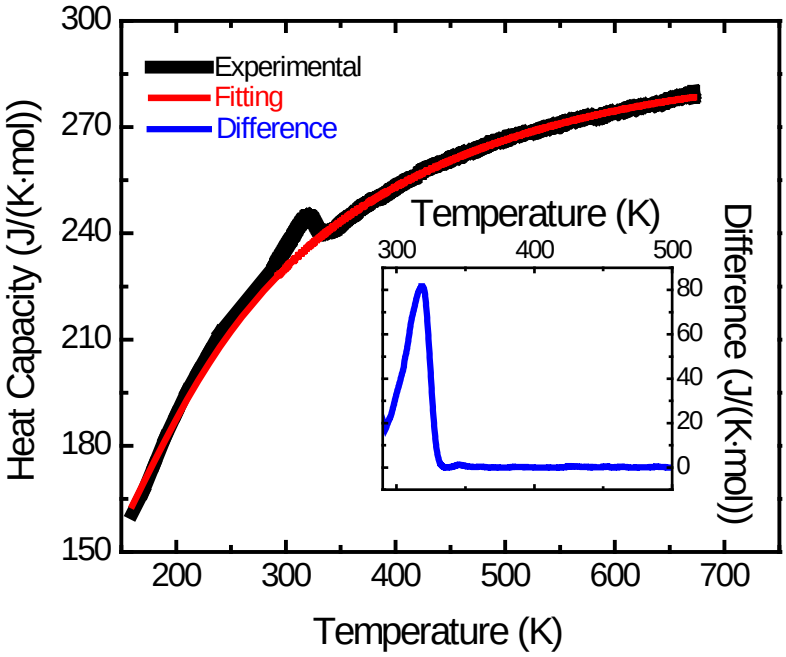

Figure 6-2. Heat capacity of Gd_3NbO_7.[146]

6.3 Infrared Spectroscopy

Two independent experiments were performed to measure the IR of Gd_3NbO_7 by Daniel Arenas in Professor Tanner's lab at University of Florida and Veronica Goian in Professor Kamba's lab at Institute of Physics of the ASCR, Czech Republic. Observable vibrational modes match well with each other. A peak at about 450 cm^{-1} disappears above the phase transition temperature (Figure 6-3 (A)). In Figure 6-3 (B), it can be clearly seen that with increasing temperature there is a decrease in the intensity

of the peak, which disappears above the phase transition temperature (~ 340 K). This is strong evidence supporting the phase transition. Detailed IR analysis will be presented in Chapter 8.

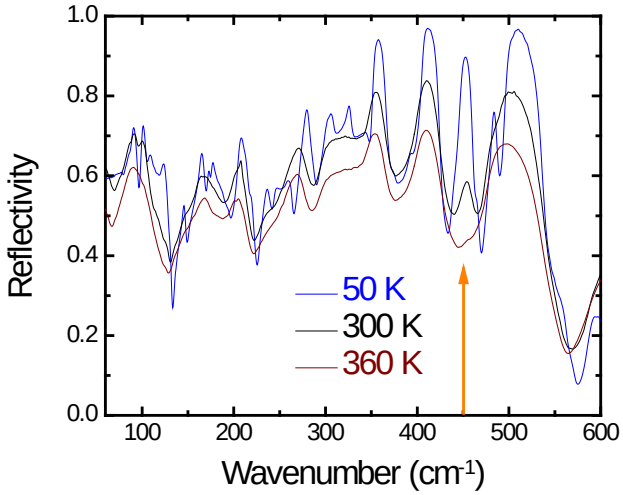

(A)

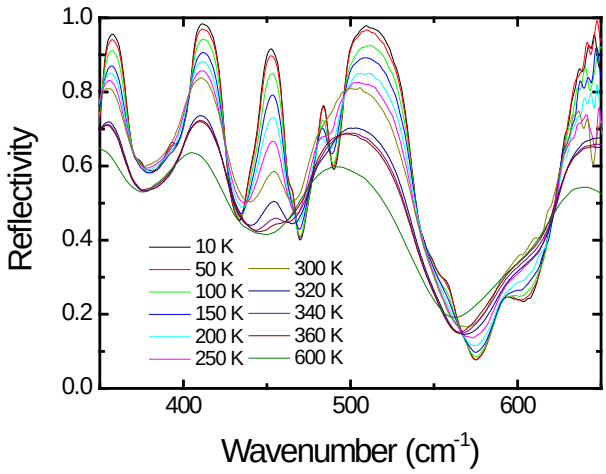

(B)

Figure 6-3. (A) Infrared Spectroscopy of Gd_3NbO_7 at 50 K, 300 K, and 360 K. The arrow indicates the mode disappearing above the transition temperature. (B) More detailed view of the mode at 450 cm^{-1}.

6.4 High Resolution XRD

Synchrotron XRD (11-BM, Advanced Photon Source of Argonne National Laboratory) at 100 K, 295 K, 345 K, and 400 K was collected on Gd_3NbO_7 as shown in Figure 6-4 (A). The diffraction has high sensitivity that allows weak reflections to be distinguished from the background. The instrumental resolution is smaller than 2×10^{-4} ($\Delta Q/Q$), with a typical 2θ resolution of $< 0.01^{o}$ at 30 keV. The monchromator is Si(111) double crystal. There are 12 independent analyzer sets with 2θ separation of about 2 degrees.[118] The wavelength used was 0.4009 Å for the pattern at 100 K and 0.4142 Å for all higher temperatures. For better visual comparison, the 2θ at 100 K is converted using the wavelength 0.4142 Å in Figure 6-4. Diamond symbols indicate low intensity peaks, all of which are associated with the structure determined below. It is seen that with increasing temperature from 100 K to 345 K, there is increased peak splitting of the first two strongest reflections (220) and (022) as shown in Figure 6-4 (B). Using Gaussian peak fitting, at 100 K the splitting is negligible, at 295 K the peaks split by 0.010^{o}, and at 345 K by 0.016^{o}. There is no obvious change in peak splitting between 345 K and 400 K. A similar splitting trend is observed for the (440) and (044) peaks; increasing from 100 K to 345 K and no obvious increase between 345 K and 400 K. This is consistent with anisotropic lattice expansion. By contrast, it is also interesting to note that both (022) and (044) peaks shift to the right from 295 K to 345 K, which indicates contraction across those planes as a function of temperature.

Figure 6-5 (A) shows a summary of lattice parameters at the four different temperatures. While lattice parameters *b* and *c* increase with increasing temperature, lattice parameter *a* exhibits an anomalous decrease from 100 K to 345 K, which is also indicative of a possible phase transition. This type of lattice parameter shrinkage also

happens near the phase transition temperature in Gd_3RuO_7, which also has a weberite-type structure.[151]

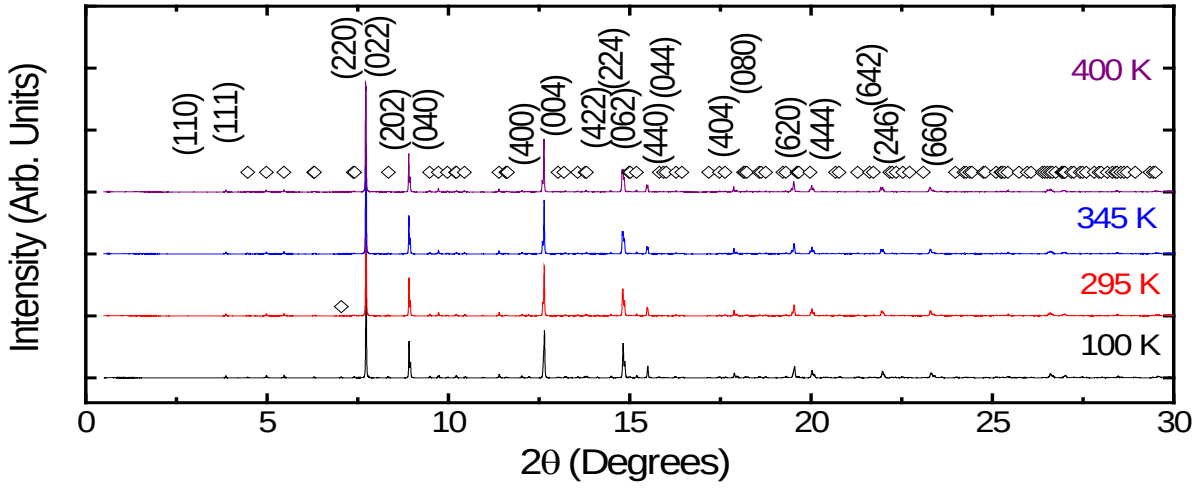

(A)

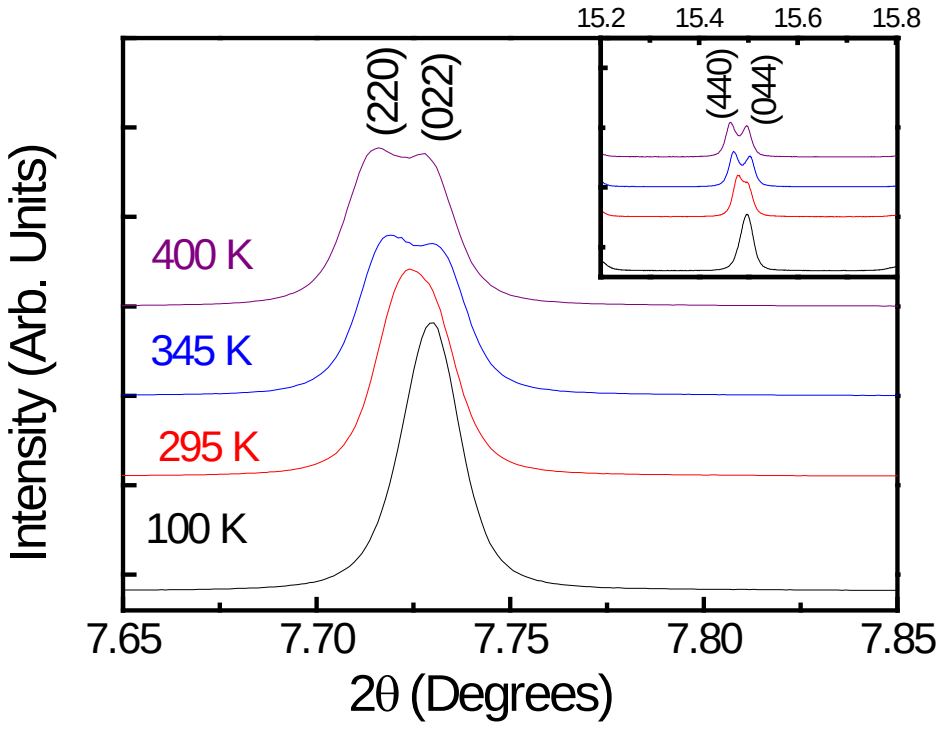

(B)

Figure 6-4. (A) High resolution XRD of Gd_3NbO_7, λ = 0.414201 Å. (B) High resolution XRD showing details about the increasing peak split of (220) and (022), and (044) (440).

It is worth remembering that the weberite-type structure is a superstructure of fluorite, and the lattice parameters of the weberite-type can be viewed as $\sqrt{2}\,a_f$, $2a_f$ and $\sqrt{2}a_f$ (a_f is the lattice parameter of fluorite, ~ 5 Å). Figure 6-5 (B) shows a_f calculated from lattice parameters *a*, *b*, *c*, and the unit cell volume at four different temperatures. It clearly shows that although *a* exhibits anomalous lattice contraction from 100 K to 345 K, the overall effect is still volumetric expansion.

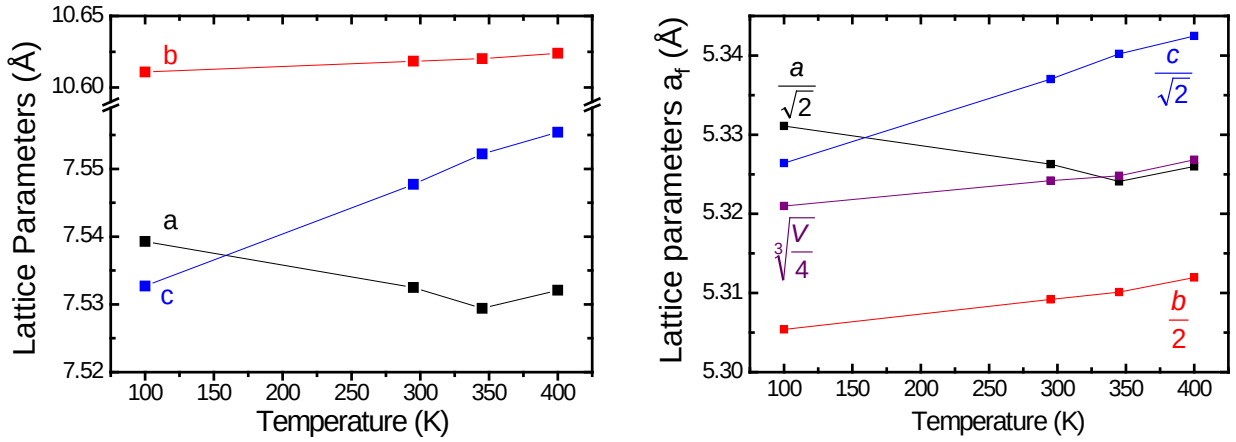

(A) (B)

Figure 6-5. (A) Lattice parameters of Gd_3NbO_7 at different temperatures (B) Lattice parameters of a_f.

Upon detailed inspection of the XRD patterns, perhaps the strongest evidence of phase transition is revealed in that the (201) reflection appears at $2\theta \sim 7^o$ at 100 K and 295 K but does not above 345 K (Figure 6-6). The disappearance of (201) reflection adds an extra reflection condition above 345 K: both *h* and *l* are 2*n* (*n* is an integer) for (*h*0*l*). At all measured temperatures, the reflection conditions also have to satisfy $h + k = 2n$ for (*hkl*) and $l = 2n$ for (00*l*). The software Checkcell was used to search the space groups that can be consistent with these observations.[154] The initial search resulted in 8 space groups with *mm2* point group for the low temperature (LT) phase and 3 space

groups with *mmm* point group for the high temperature (HT) phase. The similarity of XRD patterns suggests that the transition is displacive with only straightforward changes in symmetry: *e.g.* symmetry operations are gained or lost. Therefore, it is safe to assume that the space groups of the LT phase and the HT phase should have a sub-group and super-group relationship. Previously, Astafyev *et al.*[38] proposed that the transition is between *Cmm2* and its super-group *Cmmm*. However, (201) reflection is allowed in the *Cmmm* space group. Among the 8 candidate space groups for the LT phase and 3 for the HT phase, only space group *Cm2m* (No.38) and *Cmcm* (No.63) have a sub-group and super-group relationship. In light of the above information, *Cm2m* and *Cmcm* were selected for the LT structure and the HT structure, respectively and utilized as the basis for the pattern refinement described below.

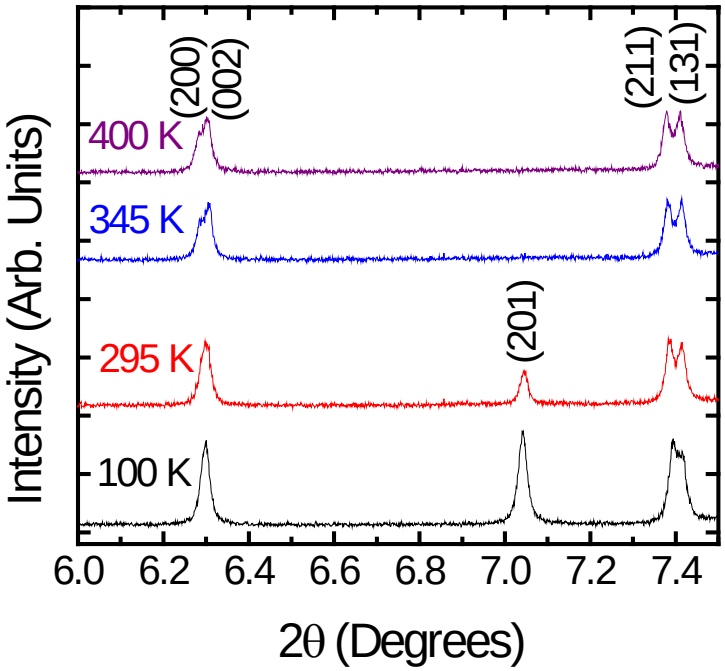

Figure 6-6. High resolution XRD showing details about the (201) reflection.

The initial structural model was based on Na_2NiInF_7 as Ln_3MO_7 are extreme cases of Na_2NiInF_7 in the weberite family as discussed in Chapter 2.[40] The space group of Na_2NiInF_7 is *Pnma*.[68] A space group transformation between *Pnma* and *Cm2m* was applied using Powdercell[126] through their common subgroup $Pmc2_1$ to get the initial atomic positions of Gd_3NbO_7 in a C-centered unit cell. The powder diffraction patterns were refined with GSAS software.[155-156] Table 6-1 shows a summary of refinement parameters. There are a total of 71 refined parameters for low temperature and 54 parameters for high temperature phases including crystal structure (lattice, atomic positions, and isotropic atomic displacement), diffractometer constants (zero shift and polarization), scale factor, background, and profile function. The observed intensities, calculated intensities, and their difference at 100 K are shown in Figure 6-7.

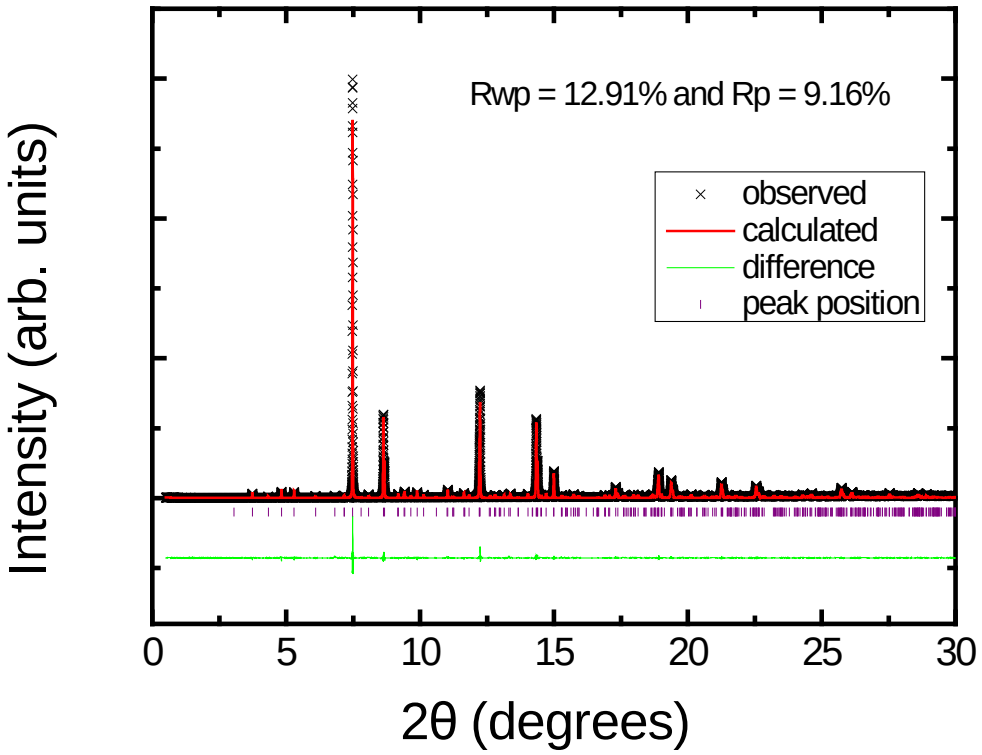

Figure 6-7. Observed and calculated high resolution powder X-ray diffraction.

Table 6-1. Crystal data and refinement parameters.

Temperature	100 K	295 K	345 K	400 K
Lattice	7.5393(3) Å, 10.6108(3) Å, 7.5327(3) Å	7.5324(1) Å, 10.6185(2) Å, 7.5476(1) Å	7.5294(2) Å, 10.6202(2) Å, 7.5522(1) Å	7.5321(2) Å, 10.6239(2) Å, 7.5554(2) Å
Z	4	4	4	4
Space group	*Cm2m*	*Cm2m*	*Cmcm*	*Cmcm*
λ (Å)	0.400919	0.414201	0.414201	0.414201
Refined 2θ range (deg)	0.5 ~ 29.999	0.5 ~ 29.999	0.5 ~ 29.999	0.5 ~ 29.999
Total no. reflections	29501	29501	29501	29501
No. peaks	432	404	371	373
No. Parameters refined	71	71	54	54
R_{wp}	12.91%	10.39%	10.28%	11.06%
R_p	9.16%	7.93%	8.10%	8.69%
GOF (χ^2)	8.100	5.169	4.989	5.808

Table 6-2 and Table 6-3 list atomic positions and isotropic atomic displacement parameters of Gd_3NbO_7 at 400 K, 345 K, 295 K, and 100 K after Rietveld refinement. It is important to note that due to the limitations of X-ray, the atomic displacement of oxygen ions may not be accurate. Usually, neutron diffraction is more suitable for refining the atomic positions and displacement parameters of oxygen. However, since Gd absorbs thermal neutrons, neutron diffraction cannot be used on Gd_3NbO_7.

Table 6-2. Lattice parameters and atomic positions at 345 K and 400 K (space group *Cmcm*)

	345 K				400 K			
Site and Wyckoff	x	y	z	U_{iso} (×100)	x	y	z	U_{iso} (×100)
Gd1 *4b*	0	0.5	0	2.05(1)	0	0.5	0	2.61(1)
Gd2 *8g*	0.7337(3)	0.7330(2)	0.25	1.303(5)	0.7341(3)	0.73335(3)	0.25	1.871(6)
Nb *4a*	0	0	0	0.67(1)	0	0	0	1.15(2)
O1 *4c*	0	0.0648(5)	0.25	1.8(2)	0	0.0648(6)	0.25	2.5(2)
O2 *4c*	0	0.6288(5)	0.25	0.6(1)	0	0.6289(6)	0.25	1.2(1)
O3 4*c*	0	0.3640(5)	0.25	0.8(1)	0	0.3642(6)	0.25	1.5(1)
O4 *16h*	0.1918(3)	0.8794(3)	0.0317(3)	2.02(9)	0.1922(4)	0.8794(3)	0.0319(4)	2.8(1)

The Gd_3NbO_7 structure has an arrangement of NbO_6-$Gd1O_8$ layers and VII coordinated Gd2 between layers. It is seen that the Gd2 (Wyckoff position *8g*) splits into two Wyckoff positions, *4e* (Gd2(1)) and *4d* (Gd2(2)). Also, the four oxygen atomic positions in *Cmcm* split into eight types in *Cm2m*.

Table 6-3. Lattice parameters and atomic positions at 100 K and 295 K (space group *Cm2m*)

		100 K				295 K			
Site and Wyckoff		x	y	z	U_{iso} (×100)	x	y	z	U_{iso} (×100)
Gd1	*4c*	0	0.5060(4)	0.2440(1)	2.91(1)	0	0.4943(5)	0.2546(2)	2.91(1)
Gd2(1)	*4e*	0.7734(2)	0.2327(4)	0.5	4.55(2)	0.7681(2)	0.2275(5)	0.5	3.48(2)
Gd2(2)	*4d*	0.2661(1)	0.2678(4)	0	0.242(5)	0.2664(1)	0.2618(5)	0	0.733(6)
Nb	*4c*	0	0.9996(4)	0.7353(3)	1.48(2)	0	0.9993(5)	0.7551(2)	1.20(1)
O1(1)	*2a*	0	0.952(1)	0	0.03(24)	0	0.932(2)	0	3.0(3)
O1(2)	*2b*	0	0.070(1)	0.5	3.7(4)	0	0.060(2)	0.5	3.3(3)
O2(1)	*2a*	0	0.623(1)	0	0.17(22)	0	0.616(1)	0	1.2(2)
O2(2)	*2b*	0	0.348(3)	0.5	2.9(4)	0	0.340(1)	0.5	1.7(3)
O3(1)	*2a*	0	0.377(1)	0	2.4(3)	0	0.379(1)	0	0.4(2)
O3(2)	*2b*	0	0.634(2)	0.5	3.8(4)	0	0.6387(9)	0.5	0.4(2)
O4(1)	*8f*	0.2144(8)	0.8754(8)	0.7304(8)	1.1(1)	0.203(1)	0.878(1)	0.7285(9)	1.8(1)
O4(2)	*8f*	0.669(1)	0.6168(8)	0.2132(9)	3.2(2)	0.680(1)	0.6184(9)	0.2103(9)	2.4(1)

At 345 K and 400 K, Nb^{5+} ions occupy Wyckoff position 4*a* with site symmetry 2/*m* in the center of NbO_6 polyhedra (distorted octahedra). Each Nb^{5+} ion is bonded to two O1 and four O4 with O1 being corner-shared by neighboring NbO_6 polyhedra. The bond angle of O1-Nb-O1 is 180^o. The NbO_6 polyhedra align in a zigzag manner along [001] and the Nb^{5+} ions are separated along [001] with constant distance (*c*/2, *c* being the lattice parameter). When cooling down to the transition temperature, Nb^{5+} ions shift slightly away from the 2-fold axis parallel to the [100] direction but still in the mirror plane which is perpendicular to [100].(Figure 6-8). Therefore, there is no Nb^{5+} displacement projected on the *a* axis. The shift of the Nb^{5+} ions from the 2/*m* site projected on the *c* axis (δ_c) is opposite with their two nearest Nb^{5+} neighbors along [001] (Figure 6-9 and Figure 6-10). The distances between two neighboring Nb^{5+} ions

become alternatively $c/2 + 2\delta_c$ or $c/2 - 2\delta_c$. By contrast, the shift of the Nb^{5+} from the 2/*m* site projected on the *b* axis (δ_b) is in the same direction with each other (Figure 6-11).

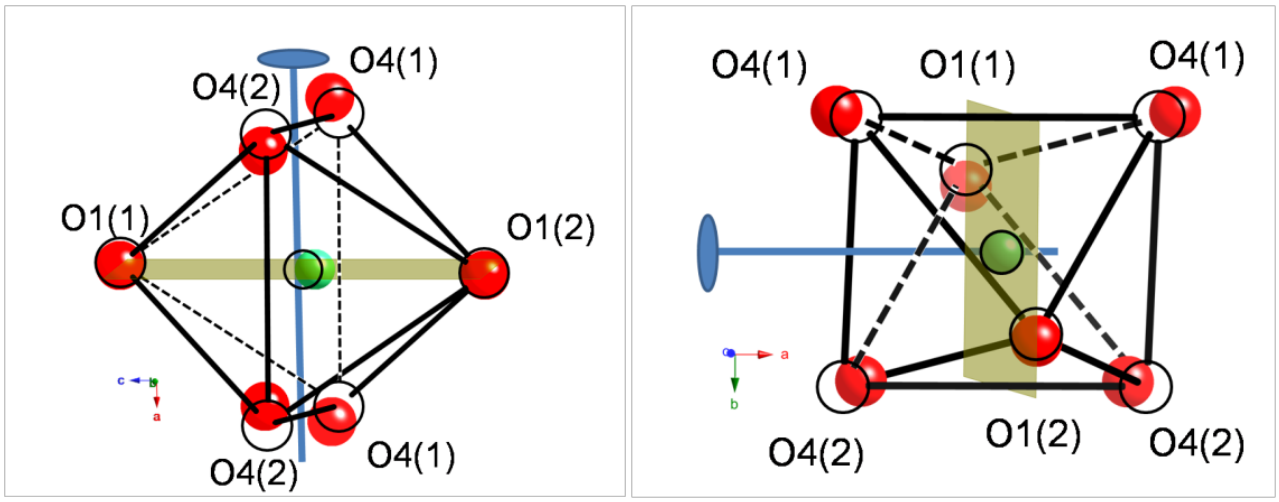

(A) (B)

Figure 6-8. (A) Approximately [010] view of NbO_6 octahedron at the high and low temperature phases. At the high temperature phase, the position of the centered Nb (black circle) has both 2-fold (line and ellipse) and mirror (translucent plane) symmetry. At low temperature phase, Nb displaces away from 2-fold axe but still in the mirror plane. (B) Approximately [100] view of NbO_6 octahedron at the high and low temperature phases.

In the anion sublattice, due to the loss of the 2-fold symmetry, the O1 position (multiplicity: 4) splits into O1(1) (multiplicity:2) and O1(2) (multiplicity:2). The neighboring NbO_6 octahedra are corner-shared alternatively through the O1(1) or the O1(2) ions along the [001] direction. The bond angle of O1(1)-Nb-O1(2) is 177.4^o at 295 K and 171.4^o at 100 K. Same as the O1, the O4 position (16*h*) splits into O4(1) (8*f*) and O4(2) (8*f*). The NbO_6 polyhedra are more distorted from a regular octahedron due to the loss of symmetry. The geometrical center also shifts. Accounting both the shifts of the Nb^{5+} ions and the geometric center, the net displacement of the Nb^{5+} ions from the geometrical center of NbO_6 polyhedra is 0.02 Å at 295 K and 0.15 Å at 100 K.

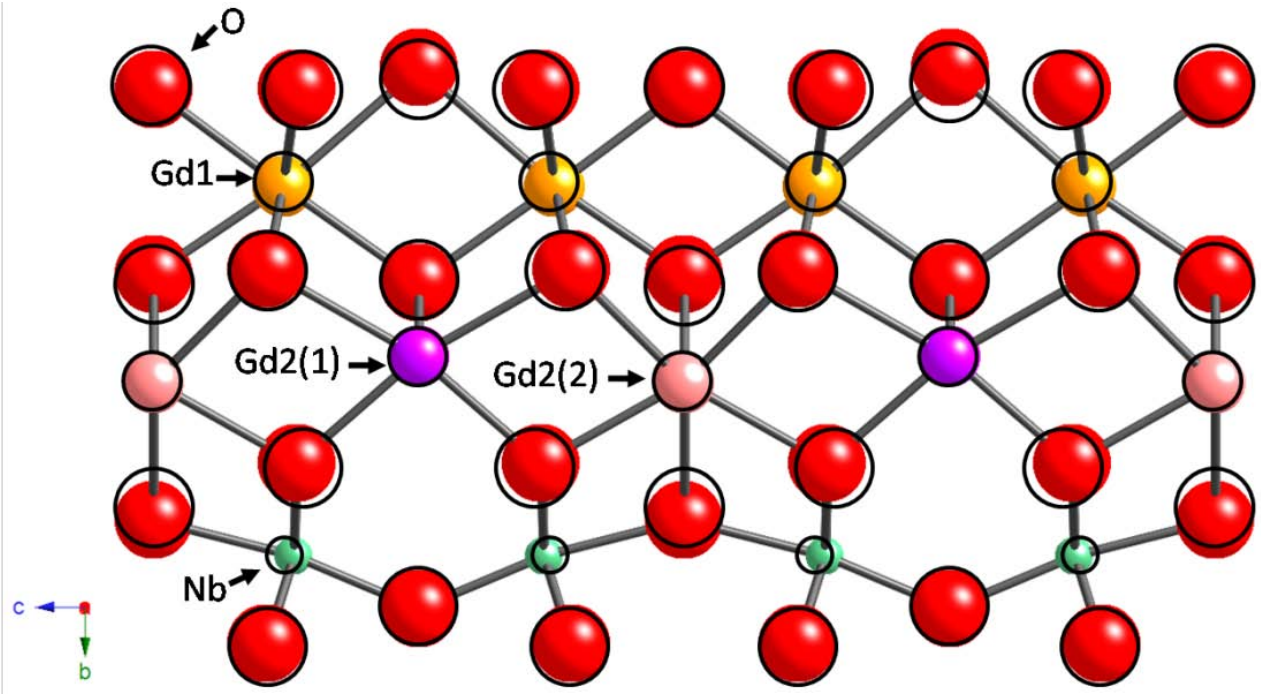

Figure 6-9. [100] view of Gd_3NbO_7, rendered spheres indicate atomic positions at high temperature phase; black circles show atomic positions at low temperature phase.

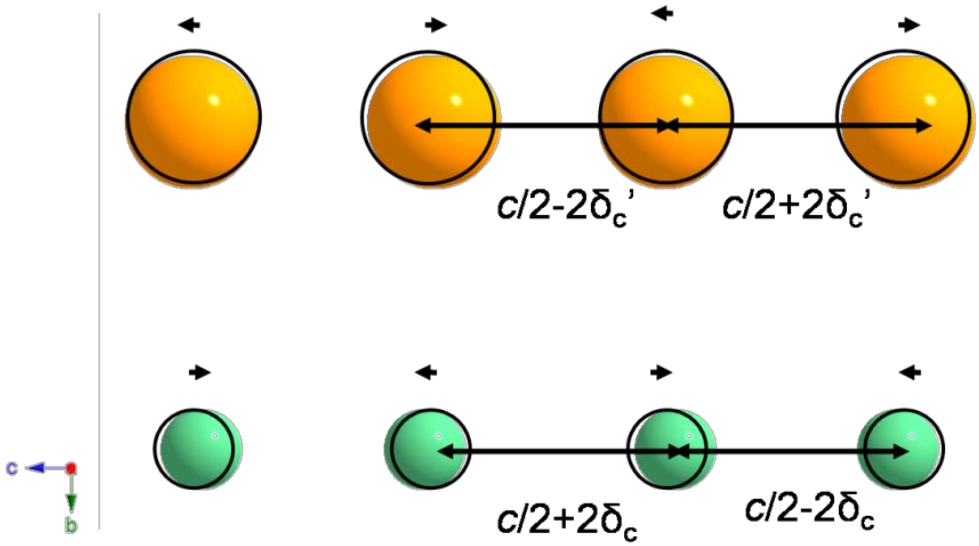

Figure 6-10. [100] view of spacing filling Nb and Gd-1 chains parallel to the [001] direction, black circles show the center positions at high temperature phase, the spacing of which is *c*/2. The black arrows above the atoms indicate the displacement orientation along [001] from the center positions. The δ_c is the shifting distance of the Nb^{5+} ions projected on the *c* axis and the δ_c' stands for the shift of the Gd^{3+} ions projected on the *c* axis.

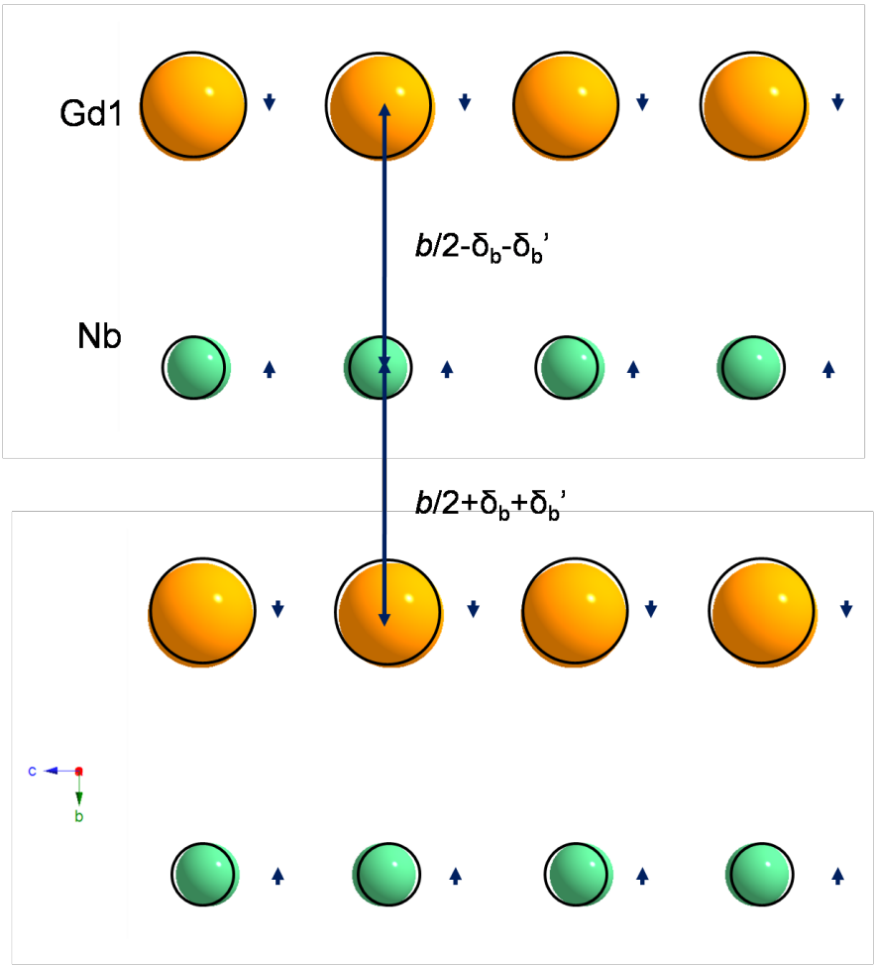

Figure 6-11. [100] view of spacing filling Nb and Gd-1. Black circles show the center positions at high temperature phase. The arrows indicate the displacement along [010]. The δ_b is the shifting distance of the Nb^{5+} ions projected on the *b* axis and the δ_b' stands for the shift of the Gd^{3+} ions projected on the *b* axis.

Focusing on the rare earth ions, in the HT phase, one third of the Gd^{3+} ions ($Gd1^{3+}$) occupy a position with symmetry 2/*m* in the center of LnO_8 polyhedra. However, in the LT phase, they shift slightly away from the 2-fold axis which is parallel to [100] to occupy an off-center site within the mirror plane similar to the Nb^{5+} ions (Figure 6-12). The mirror plane is perpendicular to [100], and hence there is no shift of Gd^{3+} along [100]. Edge-sharing $Gd1O_8$ polyhedra align along the [001] direction in both the HT and the LT phases. The distance along [001] between neighboring $Gd1^{3+}$ ions is constant

and equal to *c*/2 at HT. However, at LT, the distance is alternatively *c*/2 + $2\delta_c$' or *c*/2 - $2\delta_c$' (δ_c' is the projected shifting distance of Gd^{3+} from the 2/*m* site along [001]). The Gd^{3+} ions shift in the same direction along [010], which is the opposite shifting direction of Nb^{5+} (Figure 6-11). At HT, the distance between two neighboring Gd^{3+} and Nb^{5+} ions is *b*/2 (*b* being lattice parameter in [010]). By contrast, at LT, the distance becomes alternatively *b*/2 + δ_b + δ_b' and *b*/2 - δ_b - δ_b' (δ_b and δ_b' is the projected shift of Nb^{5+} and Gd^{3+} along [010], respectively). $Gd1^{3+}$ ions are displaced by 0.07 Å at 295 K and by 0.11 Å at 100 K from the geometrical center of the GdO_8 polyhedra. It is therefore clear that the phase transition in Gd_3NbO_7 is chiefly concurrent by the off-center shift of both Nb^{5+} and $Gd1^{3+}$ ions in their corresponding polyhedra.

The net dipole per unit cell at 100 K and 295 K was calculated based on the atomic positions. The Gd1 position was chosen to be the reference when calculating the net dipole. The net displacements of all other ions from Gd1 are in [010] direction. It confirms the polar axis [010] in space group *Cm2m*. As discussed above, there is no displacement of the Nb^{5+} along [100]. Because of Gd1 is on the mirror plane perpendicular to [100], the net displacements of O^{2-} and $Gd2^{3+}$ from the Gd1 are compensated and zeroed out by symmetry. Along [001], the $Gd2^{3+}$ ions do not shift. The shifts of Nb^{5+} ions as well as O^{2-} are antiparallel, respectively, resulting in zero net displacements along [001]. Therefore, there is no net dipole along [100] and [001]. As shown in Figure 6-11, the displacement of the Nb^{5+} are in the same direction but opposite to those of Gd^{3+}. Since the respective shift distances and net charges of Nb^{5+} and Gd^{3+} are different, there is net dipole in the [010] direction. The details of the calculation are shown in Table 6-4. The net dipole per unit cell at 100 K is 0.0503 C/m^2

in [010] and at 295 K 0.0045 C/m^2 in [0-10]. These values are much lower than the calculated net dipole for tetragonal $BaTiO_3$ (0.16 C/m^2), which is reasonable since the permittivity of $BaTiO_3$ is almost two orders of magnitude higher.[110]

Table 6-4. The net dipole calculation.

			100 K		295 K	
	Q (1.6×10^{-19} C)	# in the unit cell	d_y (Å)	μ (C × Å)	d_y (Å)	μ (C × Å)
Gd1	+3	4	0	0	0	0
Gd2(1)	+3	4	-0.0233	-2.97	-0.0168	-2.14
Gd2(2)	+3	4	0.0118	1.50	0.0175	2.23
Nb	+5	4	-0.0064	-1.36	0.005	1.06
O1(1)	-2	2	0.279	-11.86	0.271	-11.50
O1(2)	-2	2	-0.269	11.43	-0.268	11.34
O2(1)	-2	2	-0.0497	2.11	-0.0450	1.91
O2(2)	-2	2	0.0087	-0.37	0.0124	-0.525
O3(1)	-2	2	0.0377	-1.60	0.0514	-2.18
O3(2)	-2	2	-0.0387	1.64	-0.0223	0.94
O4(1)	-2	8	0.119	-20.27	0.134	-22.70
O4(2)	-2	8	-0.139	23.63	-0.126	21.37
Net dipole (C/m^2)			0.0503		-0.0045	

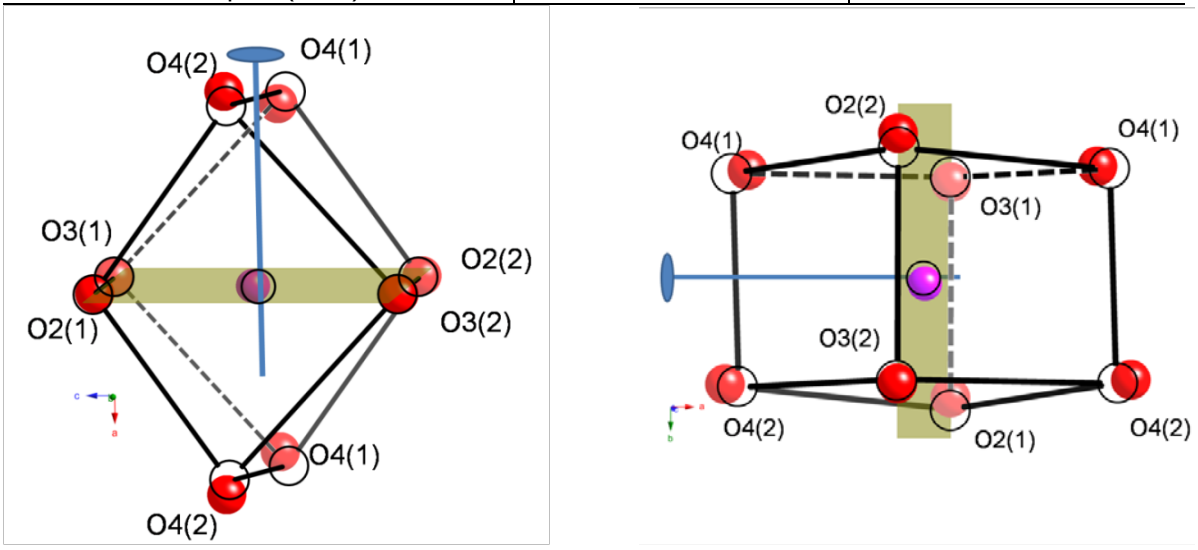

(A) (B)

Figure 6-12. (A) Approximately [010] view of $Gd1O_8$ polyhedron at high and low temperature phases. At low temperature phase, Gd1 (rendered sphere in the center of the polyhedral) moves away from 2-fold axe (line and ellipse) within the mirror plane (translucent plane). (B) Approximately [100] view of Gd1O8 octahedron at the high and low temperature phases.

Finally, it is quite interesting that in the LT phase the off-center distance of both Nb^{5+} and $Gd1^{3+}$ ions increases with decreasing temperature, and that the relative displacement the Nb^{5+} and $Gd1^{3+}$ ions is antiparallel but generates net dipole along [010] (see Figure 6-11). This suggests the possibility of ferroelectric behavior (incipient ferroelectric), and while our preliminary tests (piezoelectric activity and polarization hysteresis) have not yielded significant insight in this respect, further investigation is warranted.

6.5 Conclusion

Second harmonic generation (SHG), heat capacity measurements and IR indicated a phase transition in Gd_3NbO_7 at about 340 K. The lambda-shape specific heat near the phase transition temperature suggests a 2^{nd} order nature of the phase transition. High resolution X-ray diffraction was conducted at 100 K, 295 K, 345 K, and 400 K. The appearance of (201) reflection upon cooling confirmed the phase transition. Rietveld refinement was performed on the XRD patterns at four above mentioned temperatures and resolved the controversy regarding the space group of the low (*Cm2m*) and high temperature (*Cmcm*) phases. It was also concluded that the phase transition upon cooling is mainly due to the off-center shifts of Nb^{5+} and one third of the Gd^{3+} ions within their corresponding polyhedra. The net dipole per unit cell is 0.0503 C/m^2 at 100 K and 0.0045 C/m^2 at 295 K along [010]. It suggests the possibility of ferroelectric behavior (incipient ferroelectric) and deserves a further investigation.

CHAPTER 7
PHASE TRANSITION IN La_3NbO_7 and Nd_3NbO_7

7.1 Introduction

The space group *Pnma* (No. 62) was first assigned to La_3NbO_7 and Nd_3NbO_7.[127-128] However, when the crystal structure was first reported by Rossell[36], the space group *Cmcm* (No. 63) was used. Rossell's description of the crystal structure as well as the space group *Cmcm* was then the prototype widely accepted for Ln_3BO_7-type compounds including Ln_3RuO_7 (Ln^{3+} = La^{3+}, Pr^{3+}, Nd^{3+}, and Sm^{3+}),[16,83,90,92,94-95,97-100,157] Ln_3TaO_7 (Ln^{3+} = La^{3+}, Pr^{3+}, and Nd^{3+}),[15,88,158] Ln_3IrO_7 (Ln^{3+} = Pr^{3+}, Nd^{3+}, Sm^{3+}, and Eu^{3+}),[18,89,91] and Ln_3ReO_7 (Ln^{3+} = Pr^{3+}, Nd^{3+}, Sm^{3+}, Gd^{3+}, Tb^{3+}, and Dy^{3+}).[17,21,93,96] However, Rossell *et al.*[36,80] also commented on the unexpected very weak *h*0*l* reflections with odd *l* in Nd_3NbO_7, which are forbidden in *Cmcm*. Kahnharari *et al.*[37] claimed the very weak forbidden reflections cannot be neglected and therefore assigned the space group *Pnma* to La_3NbO_7 based on single crystal diffraction. Actually, *Cmcm* is related to *Pnma* since *Pmcn* (another setting of *Pnma*) is the subgroup of *Cmcm.*[51] The *h*0*l* reflections with odd *l* are forbidden in *Cmcm* but allowed in *Pnma*.[51] As stated in Chapter 4, it is difficult to determine the right space group by CuKα XRD. Therefore, in this study, synchrotron XRD and neutron powder diffraction have been performed on the two powders to clarify the appearance of the *h*0*l* reflections with odd *l*.

An interesting phase transition was observed in these two compounds based on heat capacity measurements. It was claimed that the phase transition is due to the displacement of atoms with no change in crystal system and no "appreciable" change in lattice parameters based on XRD.[147] In fact, phase transition is commonly observed in Ln_3BO_7 family. Consequently, there have been considerable amounts study, especially

in crystallographic aspects, on Ln_3IrO_7,[91] Ln_3MoO_7,[81-82,87,148] Ln_3OsO_7,[149] Ln_3RuO_7,[150-151] and Gd_3NbO_7[159] (which is also the topic of Chapter 6). The phase transition in Sm_3OsO_7, Eu_3OsO_7, and Gd_3OsO_7 changes from space group $P2_1nb$ (No. 33) to *Cmcm* on heating, maintaining an orthorhombic lattice.[149] Nd_3RuO_7 undergoes a phase transition from monoclinic ($P2_1/m$, No. 11) with $\beta = 90.008^o$ to orthorhombic (*Cmcm*).[97] Therefore, it is reasonable to assume that above the phase transition temperature the space group of La_3NbO_7 and Nd_3NbO_7 is *Cmcm*, which has the highest symmetry among all space groups reported for Ln_3BO_7 compounds. Neutron powder diffraction is used to investigate the crystal structure (including space group) of Nd_3NbO_7 and La_3NbO_7 before and after the phase transition.

7.2 Heat Capacity and SHG Measurements

Klimenko *et al.*[147] first measured the heat capacity of Nd_3NbO_7 and La_3NbO_7 from 295 K to 1100 K. In this study, the heat capacity was re-measured. The measuring temperature was extended down to 170 K as shown in Figure 7-1. The heat capacity plot showed an anomalous divergence between 340 K and 370 K for La_3NbO_7 and between 430 K and 470 K for Nd_3NbO_7. The results confirmed a phase transition, similar to the results of Klimenko's study.[147] Figure 7-2 shows the real part of permittivity of La_3NbO_7 and Nd_3NbO_7 at 1 MHz. The temperature where the maximum of permittivity occurs is close to the phase transition temperature for both compounds. Therefore, the origin of the dielectric relaxation correlates to the phase transition.

SHG measurements were also performed on La_3NbO_7 and Nd_3NbO_7. Figure 7-3 shows the SHG signal of La_3NbO_7 as well as the SHG signal of Gd_3NbO_7 for comparison. The laser power applied in measuring the SHG signals of La_3NbO_7 sample

was 20 times higher than that used in measuring Gd_3NbO_7 sample. Only noise or white light generated by the laser was detected for La_3NbO_7. The same response was observed for Nd_3NbO_7 that is, no SHG signal was detected. Therefore, from these results, it can be inferred that La_3NbO_7 and Nd_3NbO_7 have centrosymmetric structures throughout the measured temperature range.

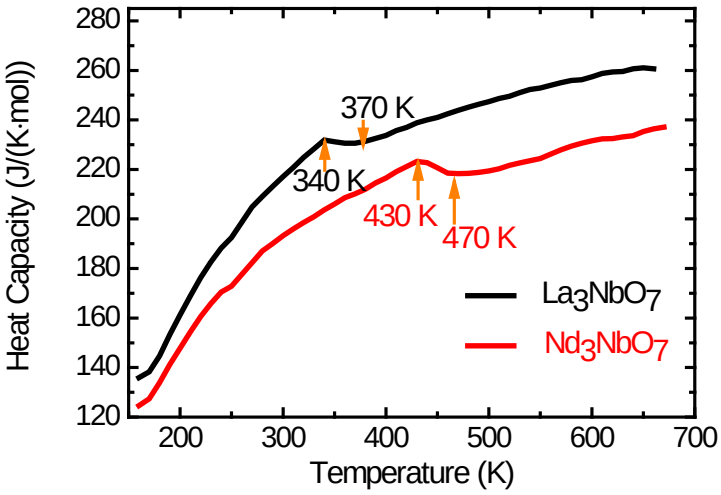

Figure 7-1. Heat capacity of La_3NbO_7 and Nd_3NbO_7.

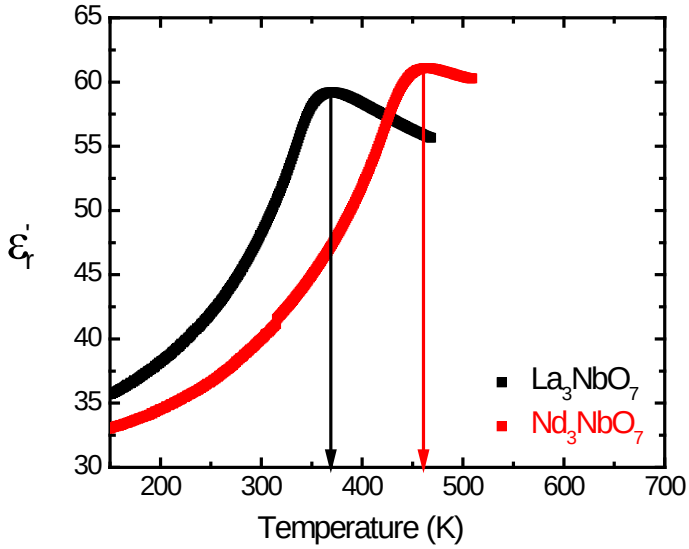

Figure 7-2. The real part of permittivity of La_3NbO_7 and Nd_3NbO_7. The arrows point to the temperature where the maximum permittivity occurs.

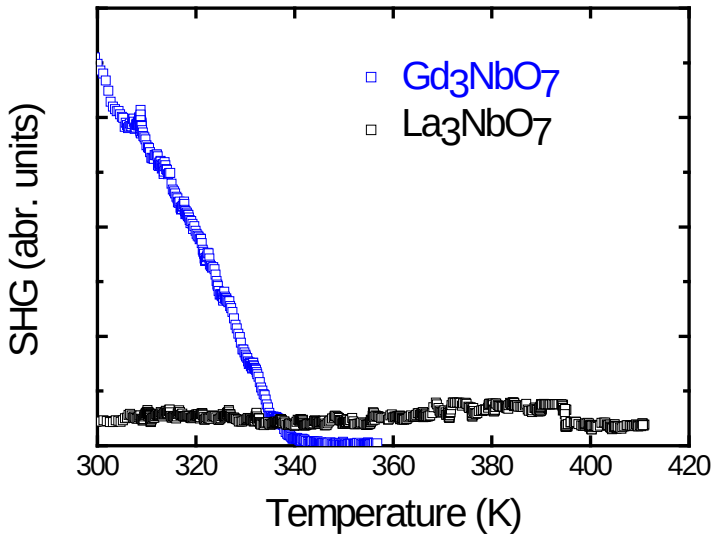

Figure 7-3. SHG of La_3NbO_7 and Gd_3NbO_7.

7.3 Crystal Structure and Phase Transition of Nd_3NbO_7 and La_3NbO_7

7.3.1 Nd_3NbO_7

High resolution XRD at 100 K and room temperature was performed on Nd_3NbO_7. The wavelength used was 0.40092 Å. The general reflection conditions for *Cmcm* are $h + k = 2n$ (n stands for integer) for (hkl) reflection and h, $l = 2n$ for ($h0l$). There are 9 minor peaks that violate the reflection conditions for *Cmcm* as shown in Figure 7-4 and Table 7-1. By contrast, all the reflections are allowed for the general reflection conditions of *Pmcn*, which are $h + k = 2n$ for ($hk0$) and $l = 2n$ for ($00l$). Therefore, it is clear that the correct space group of Nd_3NbO_7 below the phase transition temperature is *Pmcn*.

The Rietveld method was used to refine the high resolution XRD pattern with GSAS software.[155-156] There are a total of 62 refined parameters as shown in Table 7-2 including crystal structure (lattice, atomic positions, and isotropic atomic displacement), diffractometer constants, scale factor, background, and profile function. Figure 7-4

shows the observed intensities, calculated intensities, and their differences for the extra 9 reflections and Figure 7-5 shows observed intensities, calculated intensities, and their differences of the whole pattern at room temperature. The resulting atomic positions and isotropic atomic displacements are listed in Table 7-3.

Table 7-1. List of reflections which are forbidden by *Cmcm* but allowed in *Pmcn*.

h k l	2θ (degrees)	d (Å)	I/Imax (×100)
0 1 1	4.288	5.358	1.0
1 2 1	7.077	3.248	0.9
0 3 1	9.646	2.384	0.4
2 1 3	10.440	2.203	0.3
2 3 1	10.531	2.184	1.3
1 4 1	12.771	1.802	1.5
4 3 1	12.827	1.795	0.9
2 5 1	16.163	1.426	0.8
3 4 3	16.504	1.397	0.7

Table 7-2. Crystal data and refinement parameters.

Temperature	100 K	295 K
Lattice	10.8930(2) Å, 7.5238(2) Å, 7.6179(2) Å	10.9043(1) Å, 7.5295(1) Å, 7.6271(8) Å
Z	4	4
Space group	Pmcn	Pmcn
λ (Å)	0.400919	0.400919
Refined 2θ range (deg)	0.5 ~ 29.999	0.5 ~ 29.999
Total no. reflections	29501	29501
No. peaks	759	765
No. Parameters refined	62	62
Rwp	15.31%,	8.68%
Rp	15.31%,	6.59%
GOF (χ^2)	9.398	3.348

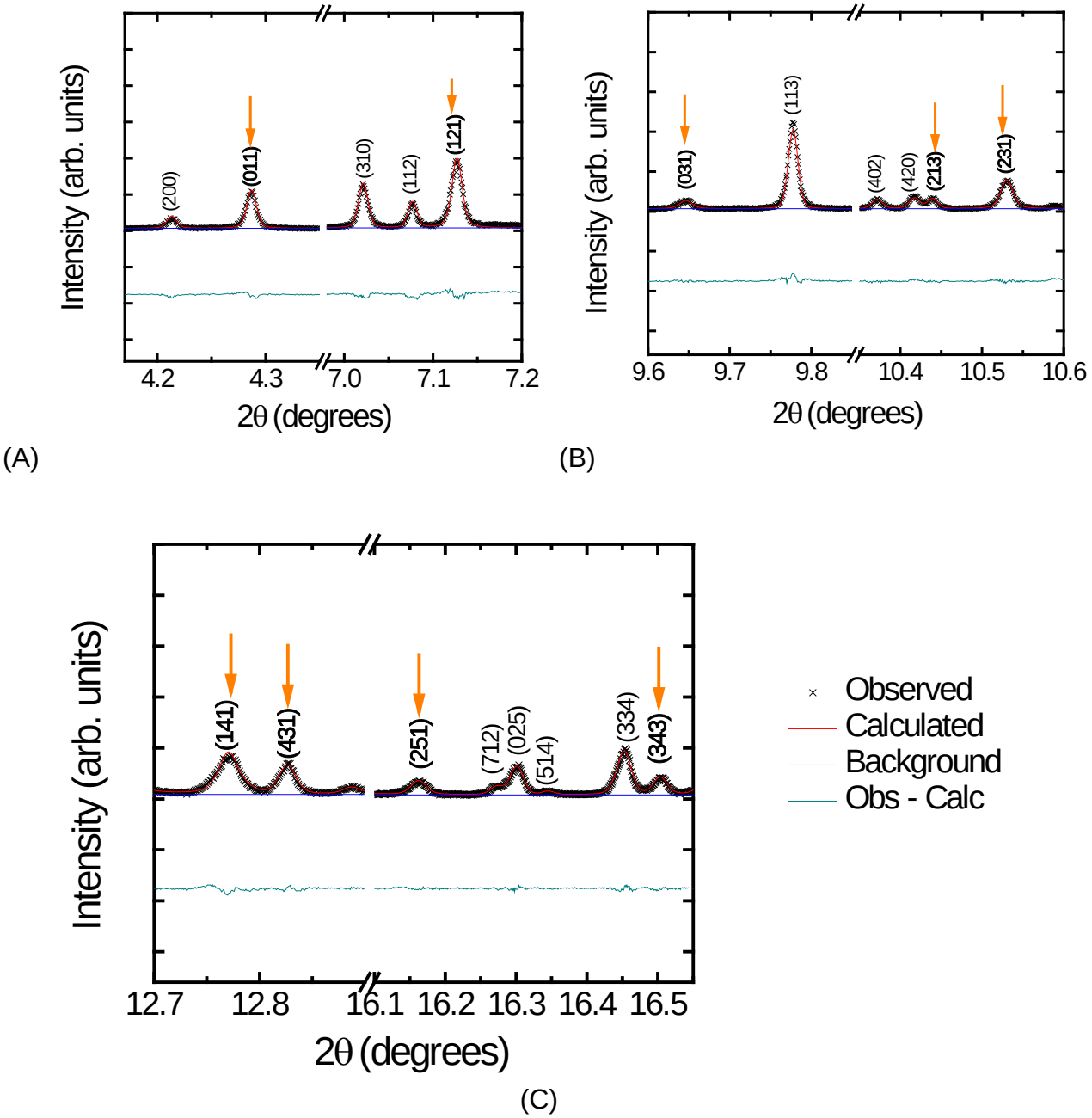

Figure 7-4. Details of the forbidden peaks by *Cmcm*. They are pointed to by the arrows. The red lines and the blue lines are the calculated pattern and the background using the Rietveld method.

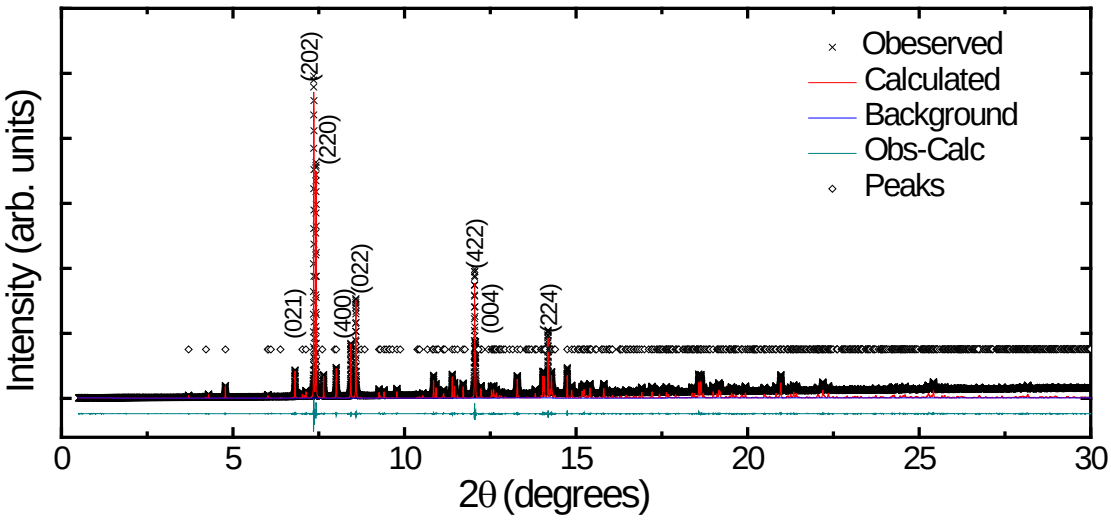

Figure 7-5. High resolution XRD of Nd_3NbO_7 at room temperature (λ = 0.40092Å). Diamond symbols indicate the less intense peaks which are associate with the Nd_3NbO_7 structure but not indexed. The Rietveld method was used to refine the pattern as shown in the red lines.

Neutron powder diffraction (HB2A in HFIR of ORNL) was also performed on Nd_3NbO_7 at different temperatures. The monochromators are vertically focusing Ge (115). The resolution is 2×10^{-3} Δd/d. Below the phase transition temperature (~ 450 K), the appearance of reflections (141) and (431) supports the space group *Pmcn* (Figure 7-6). By contrast, 9 minor reflections in high resolution XRD were found to be associated with the space group *Pmcn* as shown in Table 7-1. The reason why there are two observable extra reflections in neutron diffraction is that the remaining 7 minor reflections are easier to be overlapped or buried in the neighboring peaks in neutron diffraction patterns. For example, the (121) reflection (at $2\theta = 27.388^o$) is overlapped with the (112) reflection (at $2\theta = 27.330^o$) to a great extent since the 2θ difference is approximately equal to the step size (0.05^o) for the neutron diffraction. However, the

step size for high resolution XRD is 0.001°, which is 10 times of the 2θ difference for the (121) (at 2θ = 7.077°) and (112) (at 2θ = 7.067°) reflections.

Table 7-3. Atomic positions of Nd3NbO7 at 100 K, and 295 K, from high resolution XRD.

		100 K			
	Wyckoff	x	y	z	Uiso
Nb	4c	0.25	0.2526(1)	0.0043(3)	0.0020(2)
Nd1	4c	0.25	0.7794(1)	0.0082(1)	0.0022(1)
Nd2	8d	0.47689(3)	0.45359(5)	0.25164(9)	0.00132(7)
O1’	8d	0.8722(5)	0.9475(6)	0.9653(8)	0.005(1)
O1”	8d	0.3828(5)	0.4128(6)	0.9626(8)	0.012(1)
O2	8d	0.3821(4)	0.7264(6)	0.2529(11)	0.0007(10)
O3	4c	0.25	0.3227(8)	0.2472(13)	0.003(2)
		295 K			
	Wyckoff	x	y	z	Uiso
Nb	4c	0.25	0.2530(1)	0.0032(1)	0.0027(1)
Nd1	4c	0.25	0.77569(5)	0.00725(8)	0.0110(1)
Nd2	8d	0.47712(2)	0.45425(3)	0.25140(6)	0.00725(5)
O1’	8d	0.8732(3)	-0.0529(4)	0.9640(5)	0.0037(8)
O1”	8d	0.3830(3)	0.4187(4)	0.9626(5)	0.017(1)
O2	8d	0.3817(2)	0.7273(3)	0.2542(6)	0.0049(7)
O3	4c	0.25	0.3226(5)	0.2484(8)	0.0069(10)

The disappearance of (141) and (431) reflections above 450 K confirms the phase transition as shown in Figure 7-6. The intensities of the (141) and (431) reflections are comparable at 5 K, 295 K, and 310 K and significantly decrease from 310 K to 390 K. These two peaks totally disappear at 450 K, 470 K, and 500 K. Therefore, Nd_3NbO_7 undergoes a phase transition on heating from the space group *Pmcn* to *Cmcm*. The Rietveld refinement method was used to analyze all the neutron diffraction patterns with GSAS software.[155-156] Table 7-4 and Table 7-5 list the lattice parameters and a summary of refined parameters for the low temperature phase and the high temperature phase, respectively. Figure 7-7 shows the observed intensities, calculated

intensities, and their difference at 500 K. Figure 7-8 shows the detailed fitting on the (143) and (431) peaks at 295 K, and the comparison from 2θ 48.5° to 54.5° between 295 K and 500 K. The refined atomic positions are listed in Table 7-6 for the low temperature phase and Table 7-7 for the high temperature phase.

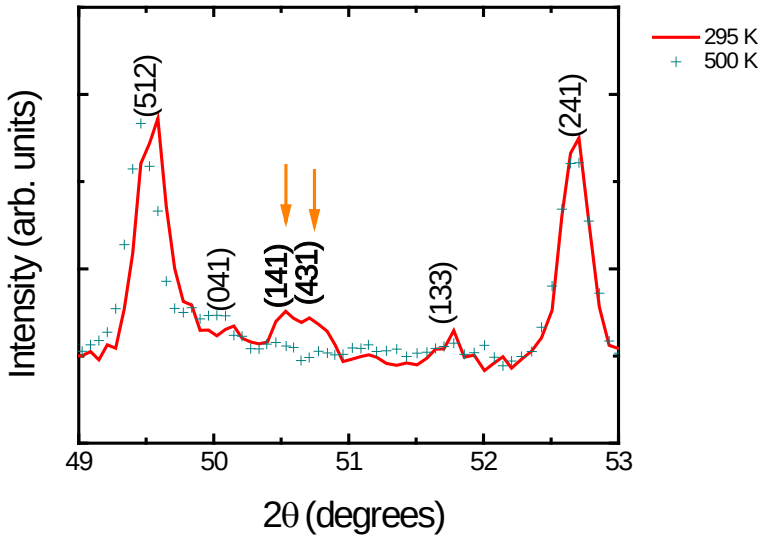

(A)

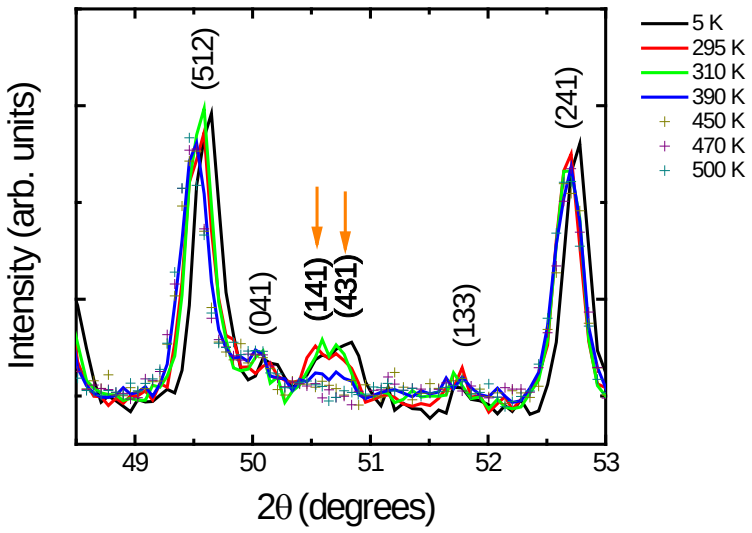

(B)

Figure 7-6. Neutron diffraction patterns (λ = 1.5378 Å) (A) at 295 K and 500 K, (B) at 5 K, 295 K, 310 K, 390 K, 450 K, 470 K, and 500 K. The lines are the patterns below the phase transition and the scattered points are the patterns above the phase transition temperature. Two extra reflections at the low temperature phase are pointed by the arrows.

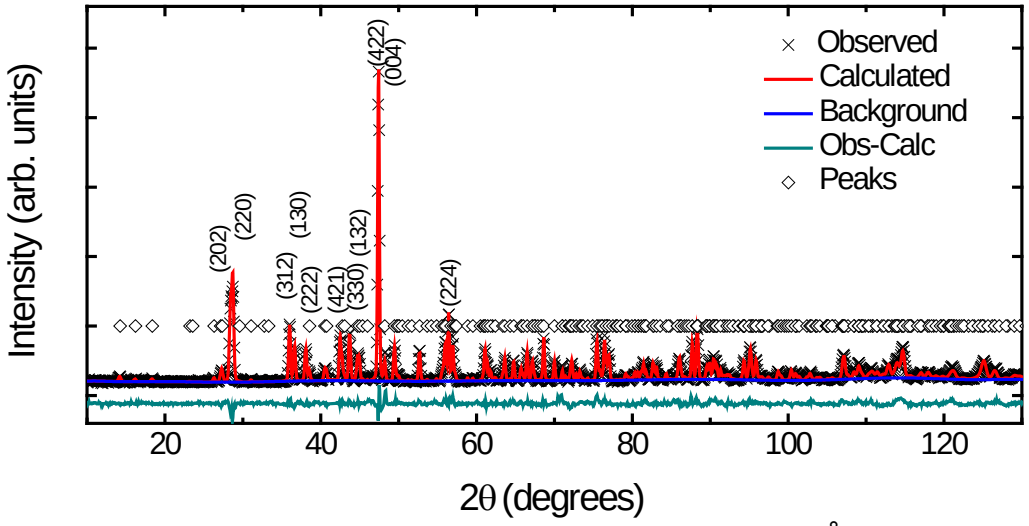

Figure 7-7. Neutron diffraction of Nd_3NbO_7 at 500 K (λ = 1.5378 Å).

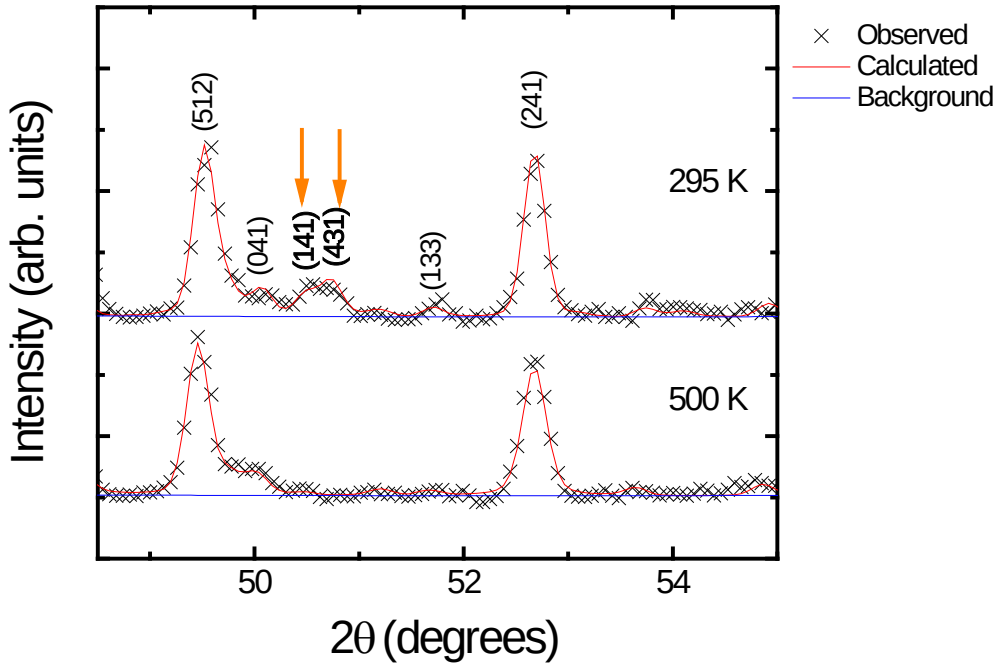

Figure 7-8. Detailed fitting from 2θ 48.5° to 54.5° between 500 K and 295 K. The arrows point to the extra reflections at low temperature

Table 7-4. Crystal data for the low temperature phase and refinement parameters for neutron diffraction

Temperature	5 K	295 K	310 K	390 K
Lattice	10.8815(2) Å, 7.5208(2) Å, 7.6162(1) Å	10.8988(3) Å, 7.5285(2) Å, 7.6270(2) Å	10.8971(3) Å, 7.5292(2) Å, 7.6257(2) Å	10.9048(3) Å, 7.5262(2) Å, 7.6342(2) Å
Z	4	4	4	4
Space group	*Pmcn*	*Pmcn*	*Pmcn*	*Pmcn*
λ (Å)	1.5378	1.5378	1.5378	1.5378
Refined 2θ range (deg)	10 ~ 130	10 ~ 130	10 ~ 130	10 ~ 130
Total no. reflections	1832	1832	1832	1832
No. peaks	574	573	573	573
No. Parameters refined	64	64	64	64
Rwp	8.06%	7.94%	8.14%	8.96%
Rp	6.12%	6.01%	6.29%	6.80%
GOF (χ^2)	2.872	2.845	2.933	7.129

Table 7-5. Crystal data for the high temperature phase and refinement parameters for neutron diffraction.

Temperature	450 K	470 K	500 K
Lattice	10.9075(3) Å, 7.5240(2) Å, 7.6397(2)Å	10.9083(3) Å, 7.5250(2) Å, 7.6405(2)Å	10.9100(3) Å, 7.5272(2) Å, 7.6421(2)Å
Z	4	4	4
Space group	Cmcm	Cmcm	Cmcm
λ (Å)	1.5378	1.5378	1.5378
Refined 2θ range (deg)	10 ~ 130	10 ~ 130	10 ~ 130
Total no. reflections	1832	1832	1832
No. peaks	312	312	312
No. Parameters refined	53	53	53
Rwp	7.39%	6.71%	7.22%
Rp	5.68%	4.91%	5.5%
GOF (χ^2)	2.435	4.054	4.393

Table 7-6. Atomic positions and isotropic atomic displacement of Nd_3NbO_7 at 5 K, 295 K, 310 K, and 390 K from neutron diffraction.

		5 K			
	Wyckoff	x	y	z	U_{iso}
Nb	4c	0.25	0.2550(10)	0.0015(15)	0.0063(10)
Nd1	4c	0.25	0.7783(8)	0.0104(10)	0.0096(12)
Nd2	8d	0.4775(2)	0.4538(4)	0.2500(9)	0.0041(5)
O1’	8d	0.8717(5)	0.9504(6)	0.9652(7)	0.0066(10)
O1”	8d	0.3844(7)	0.4163(8)	0.9590(10)	0.0230(17)
O2	8d	0.3817(4)	0.7267(5)	0.2563(12)	0.0119(9)
O3	4c	0.25	0.3256(7)	0.252(2)	0.0131(12)
		295 K			
	Wyckoff	x	y	z	U_{iso}
Nb	4c	0.25	0.2542(11)	-0.0029(11)	0.006(1)
Nd1	4c	0.25	0.7734(8)	0.0092(10)	0.0093(11)
Nd2	8d	0.4779(3)	0.4551(4)	0.2522(10)	0.0072(6)
O1’	8d	0.8718(6)	0.9502(7)	0.9680(8)	0.013(1)
O1”	8d	0.3826(7)	0.4208(9)	0.9561(9)	0.019(1)
O2	8d	0.3823(4)	0.7267(5)	0.2462(13)	0.0087(10)
O3	4c	0.25	0.3236(8)	0.252(2)	0.0115(12)
		310 K			
	Wyckoff	x	y	z	U_{iso}
Nb	4c	0.25	0.2539(12)	0.005(2)	0.012(1)
Nd1	4c	0.25	0.7747(10)	0.0085(12)	0.016(1)
Nd2	8d	0.4782(3)	0.4542(4)	0.2506(12)	0.0111(8)
O1’	8d	0.8727(7)	0.9493(8)	0.9633(10)	0.011(1)
O1”	8d	0.3829(8)	0.4193(9)	0.9538(13)	0.034(2)
O2	8d	0.3827(4)	0.7261(6)	0.255(2)	0.014(1)
O3	4c	0.25	0.3245(8)	0.255(2)	0.018(1)
		390 K			
	Wyckoff	x	y	z	U_{iso}
Nb	4c	0.25	0.2501(15)	0.003(2)	0.017(1)
Nd1	4c	0.25	0.7658(14)	0.009(2)	0.0238(17)
Nd2	8d	0.4781(3)	0.4535(5)	0.2532(14)	0.0153(7)
O1’	8d	0.8720(8)	0.9498(9)	0.9650(13)	0.019(2)
O1”	8d	0.3834(11)	0.4204(12)	0.9610(17)	0.041(3)
O2	8d	0.3828(5)	0.7268(7)	0.250(2)	0.020(2)
O3	4c	0.25	0.3218(9)	0.249(3)	0.026(2)

Figure 7-9 indicates the lattice parameters after the refinements from both high resolution XRD and neutron diffraction. At room temperature, the lattice parameters

calculated from high resolution XRD matches well with those from neutron diffraction. There is an anomalous decrease of the lattice parameter *c* from 310 K to 450 K, which may be evidence for the phase transition. As discussed in Chapter 6, Gd_3NbO_7 also exhibits a decrease in one lattice parameter from room temperature to the phase transition temperature. A summary of the unit cell volume at different temperatures is shown in Figure 7-10. At room temperature, the difference between the volume from the neutron diffraction and from the high resolution XRD is about 0.6%, which is considered a reasonable match. The unit cell volume at 295 K and 310 K are comparable, only less than 0.2% difference. In general, the unit cell volume increase with increasing temperature though there is anomalous decrease in the lattice parameter *c*.

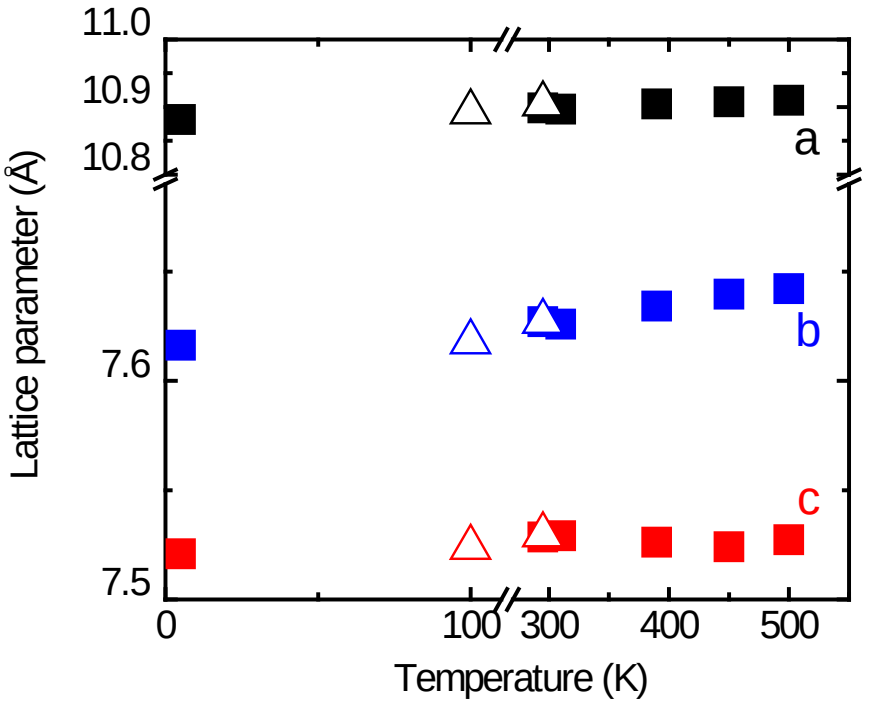

Figure 7-9. Lattice parameters (with errors) of Nd_3NbO_7 at different temperatures. The solid square symbols indicate the lattice parameters from neutron diffraction. The open triangle symbols are from high resolution XRD.

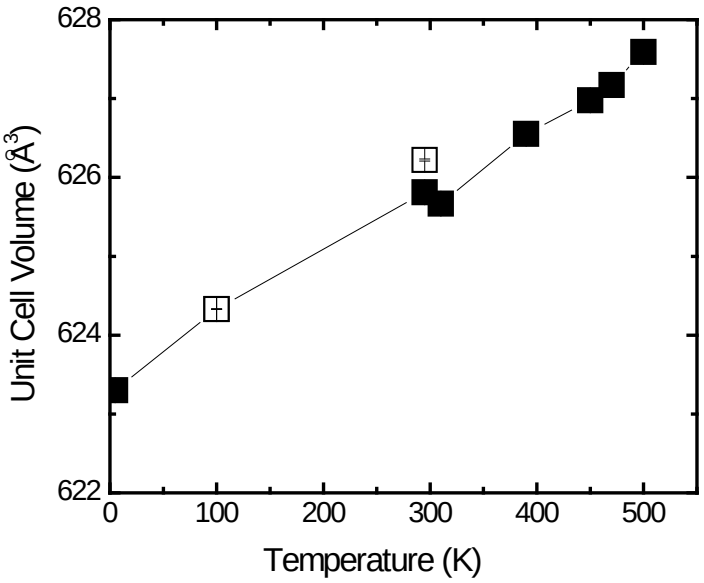

Figure 7-10. Unit cell volume (with errors) of Nd_3NbO_7 at different temperatures. The solid square symbols are calculated from neutron diffraction. The open square symbols are from high resolution XRD.

Above 450 K, Nb^{5+} ions occupy Wyckoff position *4b* with site symmetry 2/*m* in the center of NbO_6 polyhedra (distorted octahedra). Each Nb^{5+} ion is bonded to four O1 (site symmetry *1*) and two O3 (site symmetry *m2m*) with O3 being corner-shared by neighboring NbO_6 polyhedra. The bond angle of O3-Nb-O3 is 180^o (Figure 7-11). The NbO_6 polyhedra align in a zigzag manner along [001] and the Nb^{5+} ions are separated with constant distance (*c*/2, *c* being the lattice parameter).

When cooling down to the transition temperature, the Nb^{5+} ions shift away from the center of the NbO_6 as well as the 2-fold axis, which is parallel to the [100] direction. The shifts of ions are confined in the mirror plane, which is parallel to (100) and occupy a site with only mirror symmetry (Figure 7-12). The off-center displacement of Nb^{3+} decreases as the increasing temperature as shown in Figure 7-13.

Table 7-7. Lattice parameters and atomic positions of Nd_3NbO_7 at 450 K, 470 K, and 500 K from neutron diffraction.

		450 K			
	Wyckoff	x	y	z	Uiso
Nb	4b	0	0.5	0	0.011(1)
Nd1	4a	0	0	0	0.016(1)
Nd2	8g	0.2287(3)	0.2949(4)	0.25	0.0067(6)
O1	16h	0.1265(3)	0.3118(5)	0.9633(4)	0.0229(8)
O2	8g	0.1332(4)	0.0239(6)	0.25	0.0079(9)
O3	4c	0	0.4282(8)	0.25	0.018(1)
		470 K			
	Wyckoff	x	y	z	Uiso
Nb	4b	0	0.5	0	0.012(1)
Nd1	4a	0	0	0	0.0182(10)
Nd2	8g	0.2287(3)	0.2949(4)	0.25	0.0090(6)
O1	16h	0.1263(3)	0.3119(4)	0.9635(4)	0.0250(7)
O2	8g	0.1328(4)	0.0237(5)	0.25	0.0104(9)
O3	4c	0	0.4284(8)	0.25	0.020(1)
		500 K			
	Wyckoff	x	y	z	Uiso
Nb	4b	0	0.5	0	0.016(1)
Nd1	4a	0	0	0	0.019(1)
Nd2	8g	0.2288(3)	0.2956(4)	0.25	0.016(6)
O1	16h	0.1264(3)	0.3116(5)	0.9639(4)	0.0274(8)
O2	8g	0.1331(4)	0.0236(6)	0.25	0.014(1)
O3	4c	0	0.4288(8)	0.25	0.023(1)

The vectors between two neighboring Nb^{5+} ions are alternatively [0, 2δ, -0.5] and [0, -2δ, -0.5] (δ is the shifting distance along [010] of Nb^{5+} ions). The shift of the Nb^{5+} ions away from the 2-fold axis also gives more freedom to the O^{2-} ions. As a result, the O3 ions shift away from the 2-fold axis parallel to [010] and the mirror plane parallel to (001) resulting in a site on the mirror plane parallel to (100). The O1 ions at the site symmetry *1* (Wyckoff position *16h*) split into two unequal *8d* with site symmetry *1* indicated as O1' and O1". Therefore, the NbO_6 polyhedra are more distorted since the O^{2-} ions have more degrees of freedom. The bond angle of O3-Nb-O3 cannot maintain 180^o.

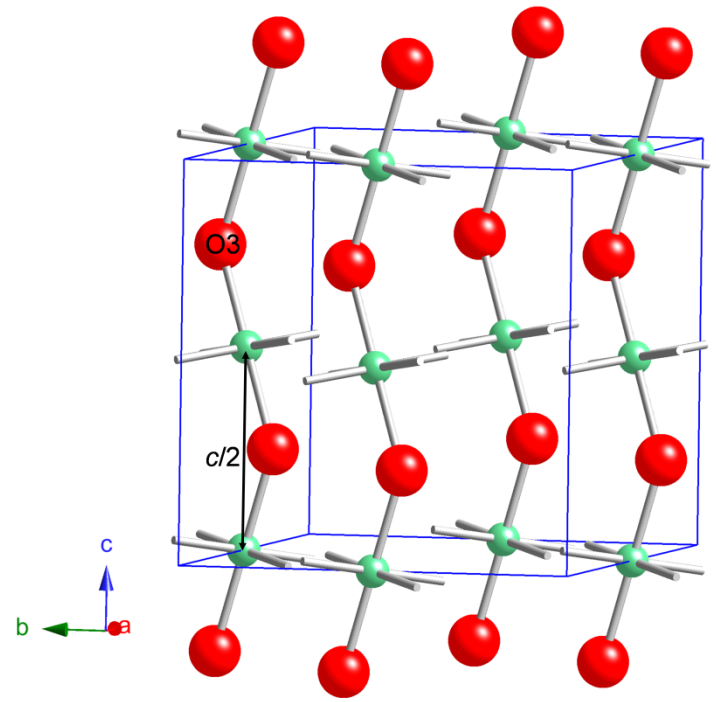

(A)

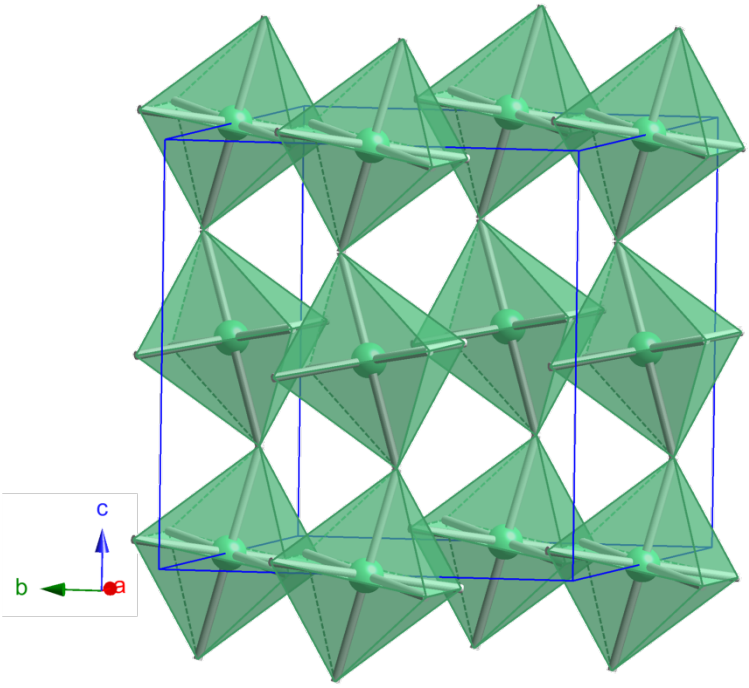

(B)

Figure 7-11. (A) The Nb^{5+} ions align along [001]. The separate between two neighboring Nb5+ along the [001] direction is *c*/2. The O3 ions are shared by two neighboring Nb^{5+} ions (B) Polyhedra view of the NbO_6 octahedra. The NbO_6 octahedra align in a zigzag manner along [001].

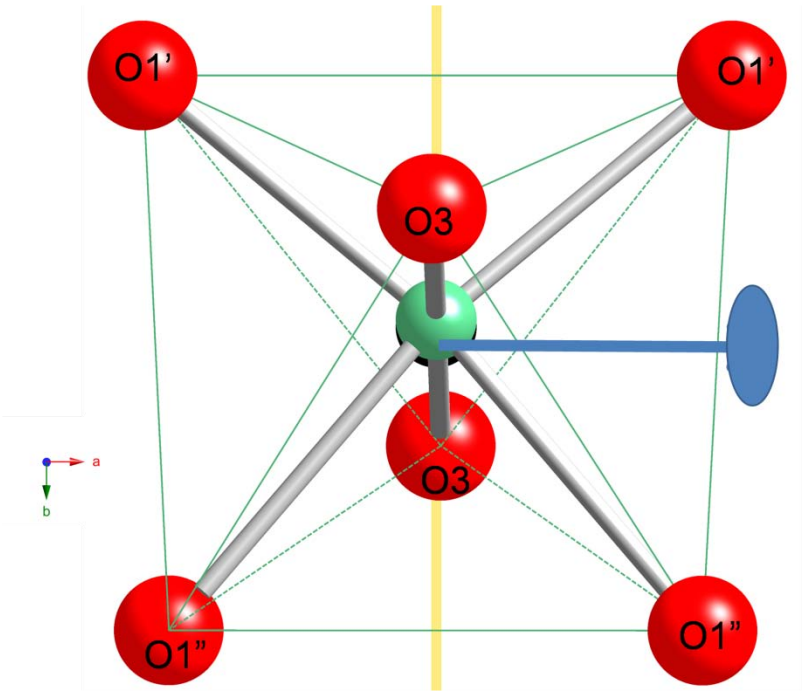

(A)

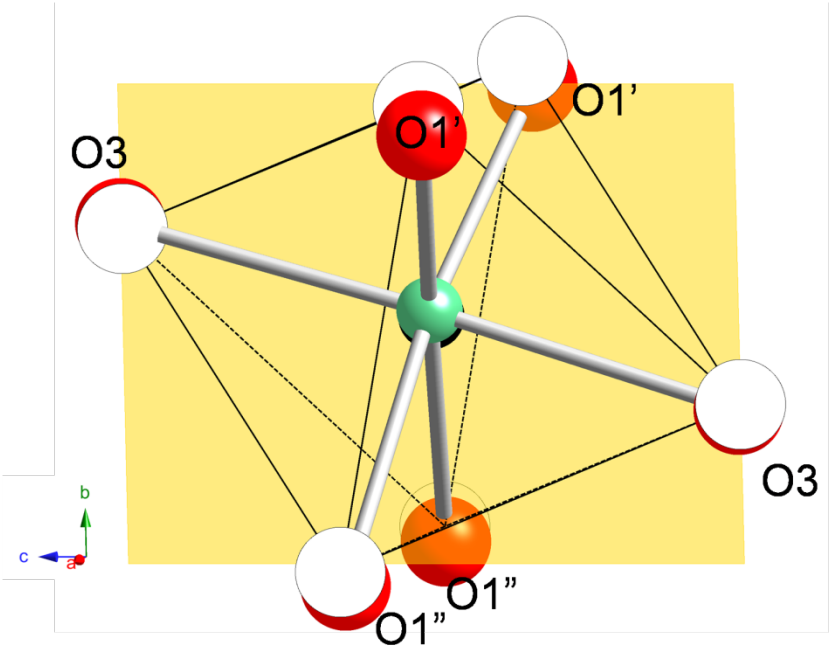

(B)

Figure 7-12. (A) Approximately [001] view of NbO_6 octahedra. At the high temperature phase, the position of the centered Nb (black sphere) has both 2-fold (line and ellipse) and mirror (translucent plane) symmetry. At low temperature phase, Nb displaces away from 2-fold axe but still in the mirror plane. (B) Approximately [301] view of NbO_6 octahedra. The black circles show the oxygen positions at high temperature

Similar to Nb^{5+}, for the high temperature phase, the $Nd1^{3+}$ ions are in the center of $Nd1O_8$ polyhedra with site symmetry *2/m* and connected to four O1 ions and four O2 ions. Below the phase transition temperature, the $Nd1^{3+}$ ions shift away from the 2-fold axis, which is parallel to the [100] direction. The shifts of the ions are confined to the mirror plane, which is parallel to (100). The $Nd1^{3+}$ ions are no longer at the center of the $Nd1O_8$ polyhedra (Figure 7-14). The off-center displacement of $Nd1^{3+}$ is shown in Figure 7-13 as a function of temperature. It is worth mentioning that due to the limitation of XRD, the atomic positions of oxygen ions may not be accurate. This is probably the reason why the calculated off-center displacement at 100 K from high resolution XRD is higher than that at 5 K from neutron diffraction.

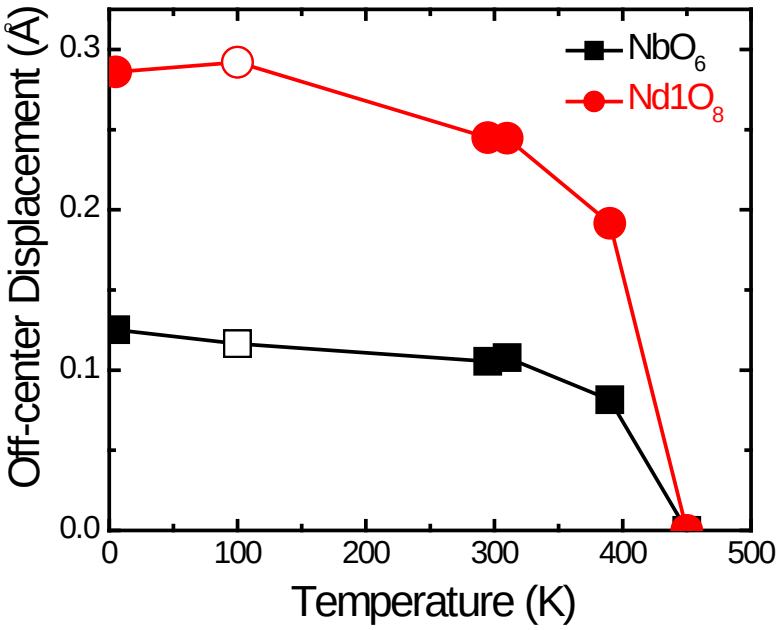

Figure 7-13. Off-center displacements of Nb^{5+} inside NbO_6 and $Nd1^{3+}$ inside $Nd1O_8$ at different temperatures. The solid symbols are calculated from neutron diffraction and the open symbols are from high resolution XRD.

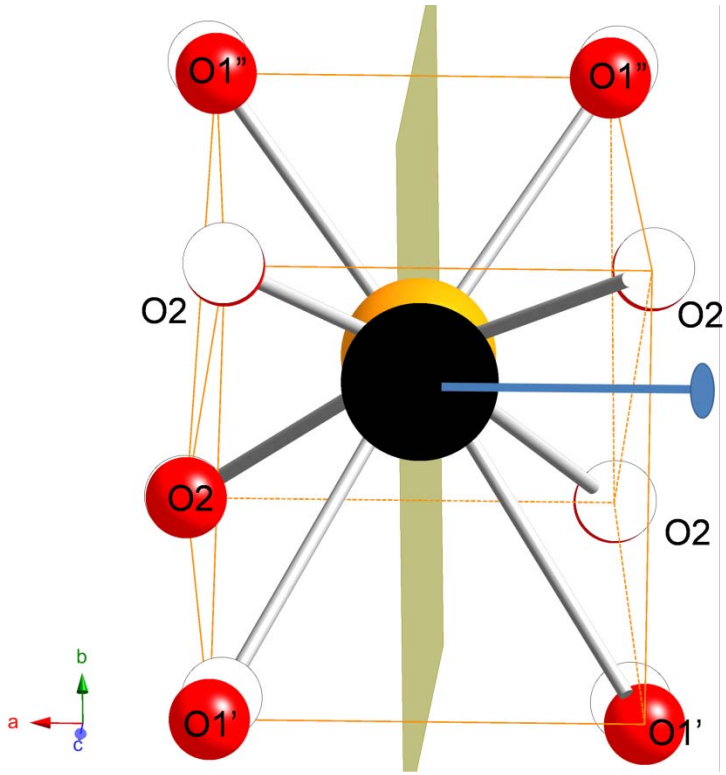

Figure 7-14. $Nd1O_8$ polyhedra. At the high temperature phase, the position of the centered Nd (black sphere) has both 2-fold (line and ellipse) and mirror (translucent plane) symmetry. At low temperature phase, Nb displaces away from 2-fold axe but still in the mirror plane.

As a result of losing 2-fold symmetry of $Nd1^{3+}$, the connected O^{2-} ions have more degrees of freedom. As discussed above, the O1 ions split into O1’ and O1”. The O2 ions move away from the mirror plane parallel to [001], resulting in *8d* of *Pmcn* with site symmetry *1*. Accordingly, the $Nd1O_8$ polyhedra are more distorted.

Figure 7-15 shows the [001] view of the $Nd1^{3+}$ and Nb^{5+} ions both above and below the phase transition temperature. In the high temperature phase, the $Nd1^{3+}$ ions as well as the Nb^{5+} ions align perfectly along the [001] direction. In the low temperature phase, the neighboring $Nd1^{3+}$ ions in the [001] direction shifts alternatively in [010] and [0-10]. The neighboring Nb^{5+} ions in the [001] direction also moves away from the 2-

folder axis alternatively in [010] and [0-10]. There is no displacement along [100] for both types of the ions.

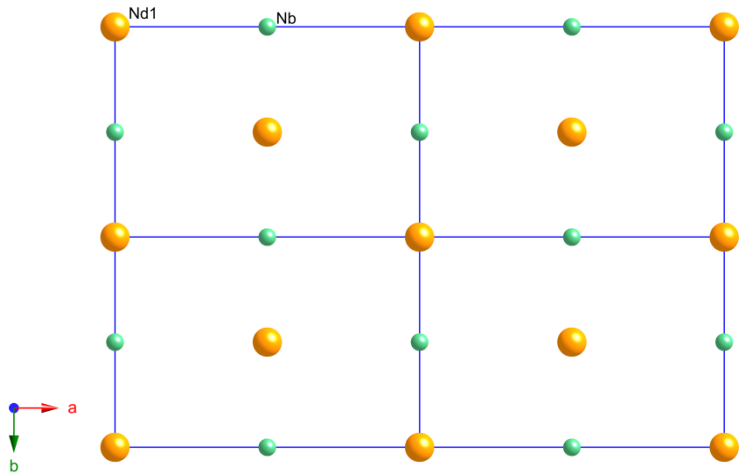

(A)

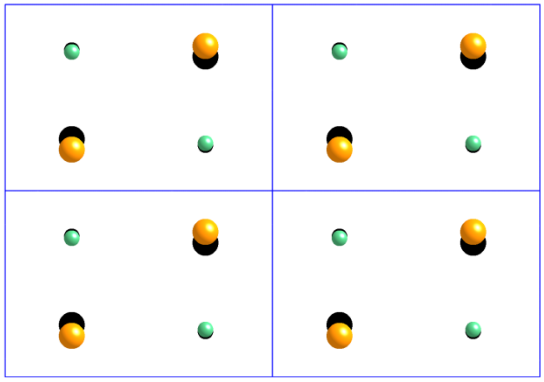

(B)

Figure 7-15. The [001] view of the $Nd1^{3+}$ and Nb^{5+} ions for (A) the high temperature phase (B) the low temperature phase. The blue lines stand for unit cell. The origin of the high temperature phase is (0.25, -0.25, 0) different from the low temperature phase. The ions in the second layer of (B) are indicated as solid black circle for better visual comparison.

A more detailed comparison between the high temperature and low temperature phases is shown in Figure 7-16. The high temperature phase indicated as the black circles are overlapped with the low temperature phase shown as the rendered spheres. It is clear that two neighboring Nb^{5+} ions or two adjacent $Nd1^{3+}$ ions along [001] displace

in an antiparallel manner parallel to [010]. Because of the antiparallel manner, the net dipoles produced by the off-center displacement are compensated to zero. The neighboring Nb^{5+} and $Nd1^{3+}$ ions along [010] displace in the same direction, either in [010] or [0-10].

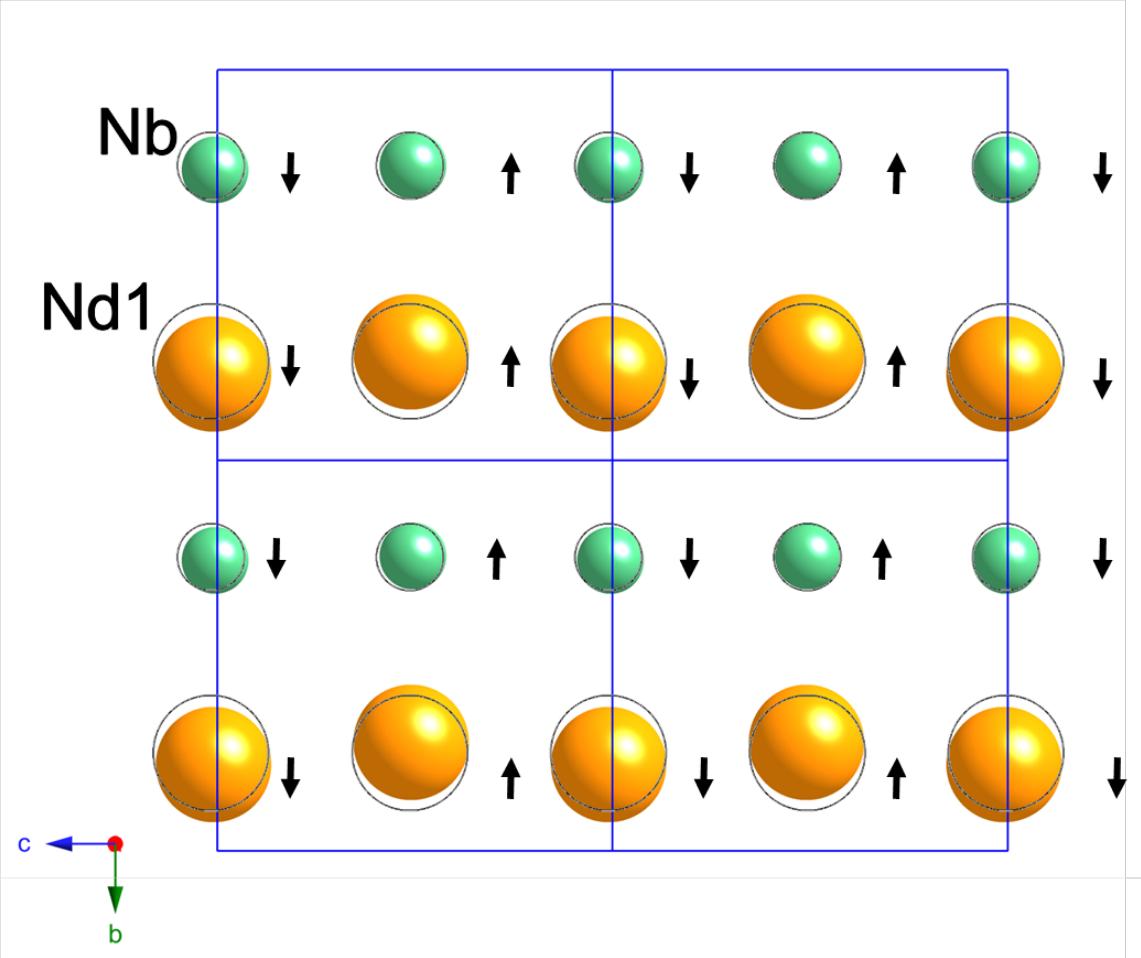

Figure 7-16. [100] view of space filling Nb and Nd1 chains parallel to the [001] direction, black circles show the center positions at high temperature phase. The black arrows above the atoms indicate the displacement orientation from the center positions along [010].

It is worth mentioning that there is one extra peak at d = 2.17 Å which cannot be indexed based on the orthorhombic lattice. This peak appears above and below the phase transition temperature. The relative intensity is about 7% for neutron diffraction

and below 0.15% for high resolution XRD (the peak cannot be detected by CuKα XRD). The theoretical diffraction patterns of possible compounds like Nd_2O_3, $Nd(OH)_3$, $NdNbO_4$, $LaNb_5O_{14}$ (given the similarity of possible $NdNb_5O_{14}$), and $PrNb_3O_9$ (given the similarity of possible $NdNb_3O_9$) were compared with the un-indentified peak, but no clear match was obtained. The structure of Nd_3RuO_7 with a monoclinic lattice was also used as an initial crystal structure for Rietveld refinement.[97] However, it resulted in a poor refinement because the calculated pattern did not have a corresponding reflection for the un-indentified peak and also had several strong extra reflections which did not exist in the observed pattern. Therefore, it is reasonable to assume the un-identified peak comes from an unreported neodymium niobate.

7.3.2 La_3NbO_7

The same phase transition occurring in Nd_3NbO_7 has also been found in La_3NbO_7. Figure 7-17 shows that the two extra reflections (141) and (431) appear below the phase transition temperature and disappear above the temperature. It is strong evidence for the occurrence of a phase transition. The phase transition is between the space group *Cmcm* and *Pmcn* as in Nd_3NbO_7.

The Rietveld refinement method was also used to analyze the neutron diffraction patterns. Figure 7-18 shows an example of refinement including the observed pattern, the calculated pattern by refinement, the background, the difference between the observed pattern and the calculated one. All reflections associated with La_3NbO_7 are indexed by diamond symbols. It is worth mentioning that traces of $LaNbO_4$ and La_2O_3 were also found in the neutron diffraction pattern. The lattice parameters and refinement parameter are listed in Table 7-8 for the low temperature phase and Table 7-

9 for the high temperature phase, respectively. The atomic positions and isotropic atomic displacement are list in Table 7-10 for the low temperature phase and Table 7-11 for the high temperature phase.

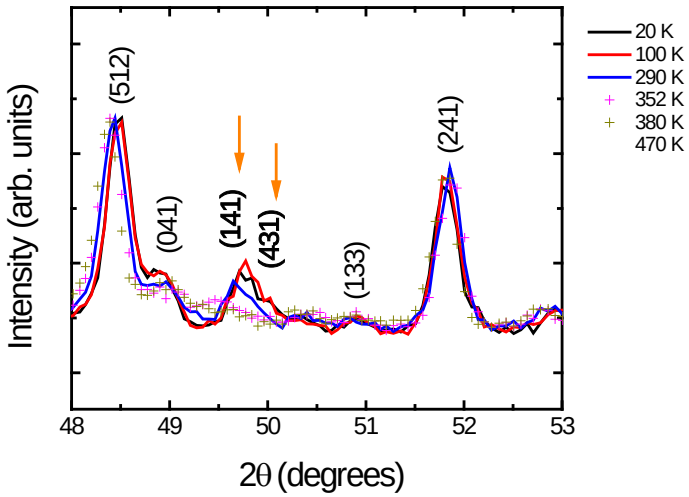

Figure 7-17. Neutron diffraction patterns of La_3NbO_7 at different temperatures (λ = 1.5378 Å). The patterns below the phase transition temperature are plotted in lines. The patterns above the phase transition temperature are plotted in scattered points. Two extra reflections at the low temperature phase are pointed by the arrows.

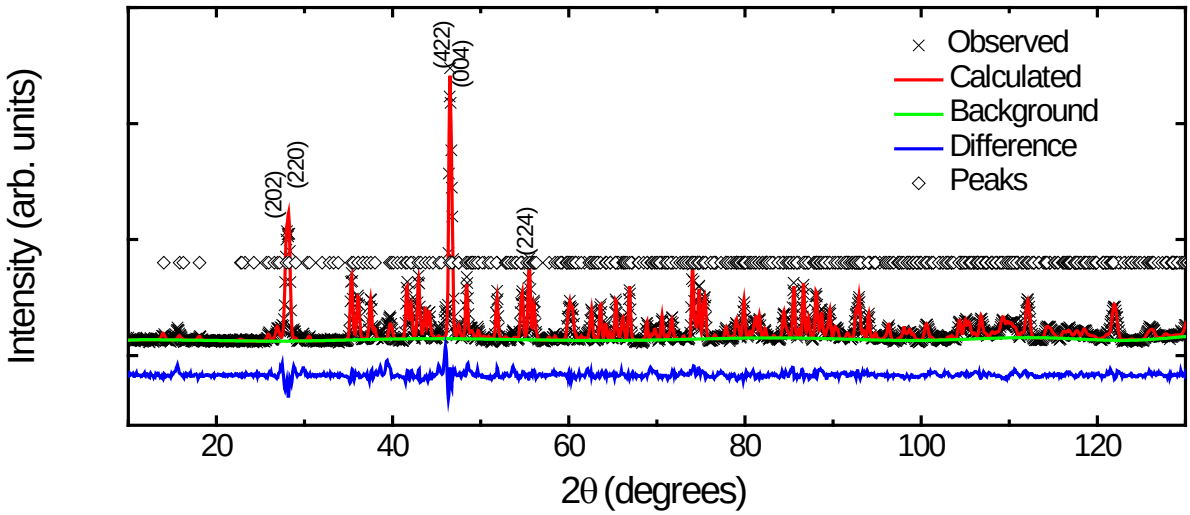

Figure 7-18. Neutron diffraction of La_3NbO_7 at 290 K (λ = 1.5378 Å).

Table 7-8. Crystal data for the high temperature phase and refinement parameters for neutron diffraction.

Temperature	20 K	100 K	295 K
Lattice	11.1478(3) Å, 7.6413(3) Å, 7.7407(2)Å	11.1487(3) Å, 7.6398(3) Å, 7.7407(2) Å	11.1593(4) Å, 7.6309(3) Å, 7.7522(2) Å
Z	4	4	4
Space group	Pmcn	Pmcn	Pmcn
λ (Å)	1.5378	1.5378	1.5378
Refined 2θ range (deg)	10 ~ 130	10 ~ 130	10 ~ 130
Total no. reflections	1832	1832	1832
No. peaks	608	608	608
No. Parameters refined	64	64	64
R_{wp}	10.80%	11.21%	10.19%
R_p	8.07%	8.2%	7.36%
GOF (χ^2)	7.240	7.806	6.566

Table 7-9. Crystal data for the high temperature phase and refinement parameters for neutron diffraction.

Temperature	380 K	470 K
Lattice	11.1667(4) Å, 7.6275(3) Å, 7.7588(2)Å	11.1726(4) Å, 7.6336(3) Å, 7.7636(3) Å
Z	4	4
Space group	Cmcm	Cmcm
λ (Å)	1.5378	1.5378
Refined 2θ range (deg)	10 ~ 130	10 ~ 130
Total no. reflections	1832	1832
No. peaks	330	330
No. Parameters refined	53	53
R_{wp}	9.74%	10.24%
R_p	7.02%	7.61%
GOF (χ^2)	5.968	6.642

Table 7-10. Lattice parameters and atomic positions of La_3NbO_7 at 20 K, 100 K, 295 K, and 390 K from neutron diffraction.

		20 K			
	Wyckoff	x	y	z	U_{iso}
Nb	4c	0.25	0.2584(15)	0.0067(19)	0.008(1)
La1	4c	0.25	0.7762(9)	0.0073(12)	0.0079(15)
La2	8d	0.4748(3)	0.4498(5)	0.2528(13)	0.0063(7)
O1’	8d	0.1296(8)	0.4462(9)	0.5247(10)	0.010(2)
O1”	8d	0.3805(7)	0.4147(9)	0.9619(9)	0.0031(14)
O2	8d	0.3806(5)	0.7252(7)	0.253(2)	0.0074(11)
O3	4c	0.25	0.3206(9)	0.255(3)	0.0052(17)
		100 K			
	Wyckoff	x	y	z	U_{iso}
Nb	4c	0.25	0.2601(16)	0.005(2)	0.0126(14)
La1	4c	0.25	0.7751(11)	0.0066(14)	0.018(2)
La2	8d	0.4750(4)	0.4487(5)	0.2515(15)	0.0157(8)
O1’	8d	0.8698(8)	0.9465(10)	0.9650(12)	0.020 (2)
O1”	8d	0.3806(8)	0.4156(9)	0.9621(11)	0.0126(17)
O2	8d	0.3807(5)	0.7258(7)	0.252(2)	0.0140(12)
O3	4c	0.25	0.3211(10)	0.253(3)	0.0143(18)
		295 K			
	Wyckoff	x	y	z	U_{iso}
Nb	4c	0.25	0.2614(19)	0.001(2)	0.0132(15)
La1	4c	0.25	0.7696(14)	0.0086(17)	0.0179(18)
La2	8d	0.4754(4)	0.4492(5)	0.2512(18)	0.0169(9)
O1’	8d	0.8681(9)	0.9439(11)	0.9661(13)	0.021 (2)
O1”	8d	0.3797(8)	0.4196(10)	0.9615(13)	0.014(2)
O2	8d	0.3803(5)	0.7259(8)	0.250(3)	0.0150(13)
O3	4c	0.25	0.3196(10)	0.254(3)	0.0129(19)

A summary of lattice parameters at different temperatures are shown in Figure 7-19. The lattice parameter *c* shows anomalous extraction for the low temperature phase, the same as Nd_3NbO_7 and Gd_3NbO_7. After the phase transition temperature, the lattice parameter increases with increasing temperature. A summary of the unit cell volume at different temperatures are also plotted in Figure 7-20. Due to the anomalous decrease with increasing temperature in *c*, the unit cell volume at 20 K is slightly larger than that

at 100 K. However, it is clear that the general trend of the unit cell volume is increasing with temperature.

Table 7-11. Lattice parameters and atomic positions of La_3NbO_7 at 380K and 470 K from neutron diffraction.

		450 K			
	Wyckoff	x	y	z	U_{iso}
Nb	4b	0	0.5	0	0.0132(14)
La1	4a	0	0	0	0.0211(14)
La2	8g	0.2258(3)	0.3012(5)	0.25	0.0125(8)
O1	16h	0.1233(4)	0.3175(6)	0.9645(5)	0.0186(9)
O2	8g	0.1308(5)	0.0262(7)	0.25	0.0103(12)
O3	4c	0.25	0.4327(10)	0.25	0.0052(17)
		470 K			
	Wyckoff	x	y	z	U_{iso}
Nb	4b	0	0.5	0	0.0171(17)
La1	4a	0	0	0	0.0241(17)
La2	8g	0.2262(4)	0.3009(5)	0.25	0.0163(9)
O1	16h	0.1233(4)	0.3177(6)	0.9652(6)	0.0245(11)
O2	8g	0.3699(6)	0.5267(8)	0.25	0.0149(14)
O3	4c	0	0.4336(11)	0.25	0.02(2)

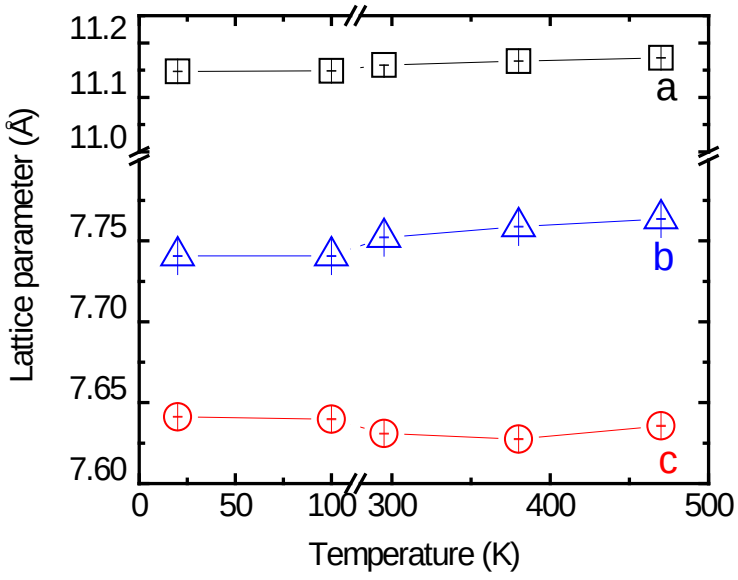

Figure 7-19. Lattice parameters (with errors) of La_3NbO_7 at different temperatures.

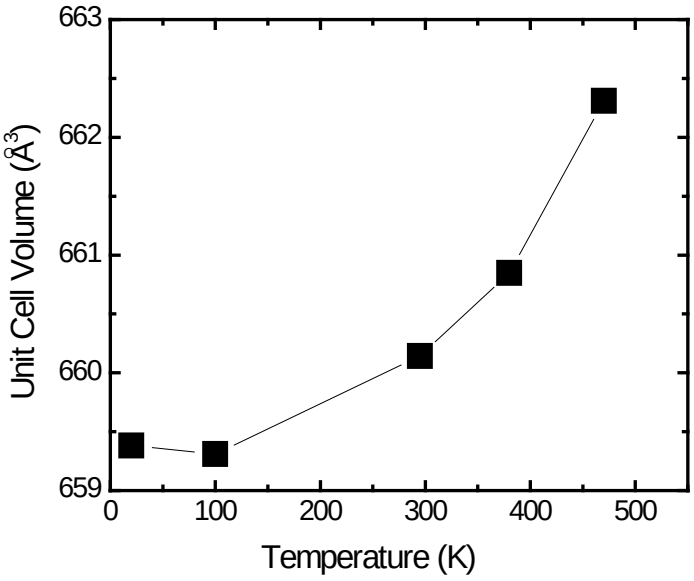

Figure 7-20. Unit cell volume of La_3NbO_7 at different temperatures.

Similar to Nd_3NbO_7, for the high temperature phase, both Nb^{5+} ions and 8 coordinated $La1^{3+}$ (account for 1/3 of total La^{3+}) are in the center of their corresponding polyhedra with site symmetry *2/m*. Below the phase transition temperature, both ions shift away from the 2-fold axis, which is parallel to the [100] direction. The shifts of ions are confined in the mirror plane, which is parallel to (100). The site symmetry of $La1^{3+}$ and Nb^{5+} results in *m* for the low temperature phase. The $La1^{3+}$ and Nb^{5+} ions are no longer at the center of their corresponding polyhedra. The off-center shifts are shown in Figure 7-21. The off-center displacement of $Nd1^{3+}$ decreases with increasing temperature

As mentioned before, phase transition is commonly observed in Ln_3BO_7 compounds. The phase transition temperatures for Ln_3BO_7 are summarized in Figure 7-22. It is based on the summary by Nishimine *et al.*[91] The phase transition temperatures for La_3NbO_7 and Nd_3NbO_7 are also added to Figure 7-22.

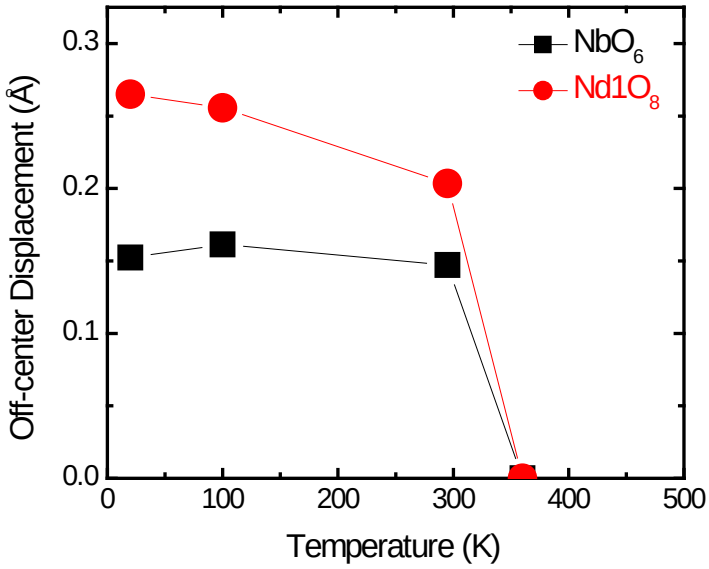

Figure 7-21. Off-center displacements of Nb^{5+} inside NbO_6 and $La1^{3+}$ inside $La1O_8$ at different temperatures.

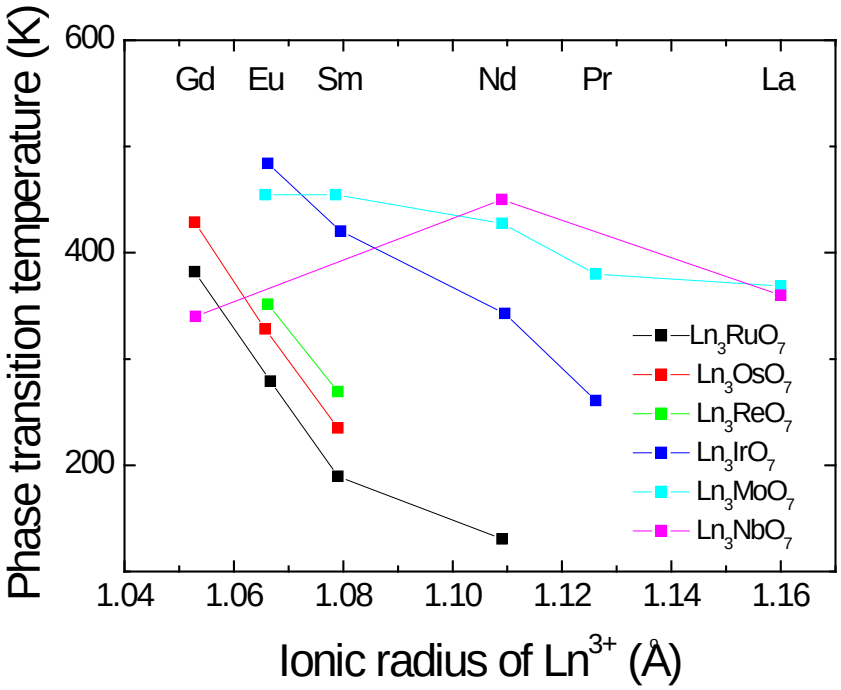

Figure 7-22. Phase transition temperature for Ln_3BO_7. The figure is based on the summary by Nishimine *et al.*[91] and adds Ln_3NbO_7 points based on this work. The phase transition temperature of Ln_3RuO_7 and Ln_3OsO_7 is after Gemmill *et al.*[149,157], Ln_3MoO_7 and Ln_3IrO_7 after Nishimine *et al.*[18,91], Ln_3ReO_7 after Hinatsu *et al.*[96]

It is clearly seen that the phase transition temperature is related to the ionic radius of Ln^{3+}. Within the same B^{5+} ion, the phase transition temperature decreases with increasing the ionic radius of Ln^{3+}. It is worth mentioning that the phase transition in Gd_3NbO_7 occurs at 340 K, which does not follow the general trend. It is because Gd_3NbO_7 belongs to another weberite-type structure. In addition, all the phase transitions in Figure 7-22 except Gd_3NbO_7 are from a *P*-type lattice to the orthorhombic lattice with space group *Cmcm*. The phase transition in Gd_3NbO_7 is from *Cm2m* (No. 38) to *Cmcm*.

7.4 Conclusion

Heat capacity measurements and neutron diffraction confirmed a phase transition in Nd_3NbO_7 at about 450 K as well as in La_3NbO_7 at about 360 K. SHG measurements indicate that Nd_3NbO_7 and La_3NbO_7 have a centrosymmetric structure both below and above the phase transition temperature. Based on high resolution X-ray diffraction and neutron diffraction of Nd_3NbO_7 and La_3NbO_7 at room temperature, the correct space group below the phase transition temperature was determined to be *Pmcn* as there are some minor peaks that violate the reflection conditions for *Cmcm*. The disappearance of (141) and (413) reflections above the phase transition temperature confirmed the phase transition from *Pmcn* to *Cmcm*. The Rietveld refinement method was performed on the XRD patterns and neutron diffraction at different temperatures. It was also concluded that the phase transition upon cooling is mainly due to the off-center shifts of Nb^{5+} and one third of the La^{3+} and Nd^{3+} ions within their corresponding polyhedra. As a result, two neighboring Nb^{5+} ions or two adjacent $Nd1^{3+}$ ions along [001] displace in an antiparallel manner parallel to [010]. Because of

the antiparallel manner, the net dipoles produced by the off-center displacement are compensated to zero since the space group is centrosymmetric.

CHAPTER 8
INFRARED SPECTROSCOPY OF Gd_3NbO_7

8.1 Introduction

Infrared spectroscopy (IR) is a powerful tool for providing information like phonon modes, bonding, orientation of dipoles, *etc*. As already shown in Chapter 6, IR confirms the phase transition in Gd_3NbO_7 as the mode at 450 cm^{-1} disappears above the phase transition temperature. A vibrational mode will absorb IR electromagnetic radiation only if the natural frequency of vibration is the same as the frequency of the radiation and the stimulated vibration produces a change in the dipole moment. The normal vibrational modes can be determined by nuclear site group analysis. In this method, the number of allowed modes of a specific structure is derived based on the symmetry of each atomic site composing the crystal as introduced in Chapter 2.[117] The first part of the study was to determine the IR active modes by the above method below and above the phase transition temperature of Gd_3NbO_7.

It is important to note that only one article about IR spectrum of Gd_3NbO_7 has been published and that study was mainly focused on the crystallographic aspects.[123] In this study, the IR spectra of Gd_3NbO_7 were collected at various temperatures using a Fourier transform spectrometer (Bruker IFS 113v) covering the frequency range between 20 cm^{-1} and 650 cm^{-1} (0.6 THz to 19 THz). A custom made time-domain terahertz transmission spectrometer was used to obtain the complex dielectric response in the range from 12 cm^{-1} to 40 cm^{-1} (0.36 THz to 1.2 THz). This spectrometer uses a femtosecond Ti : sapphire laser and a biased large-aperture antenna from a low-temperature grown GaAs as a THz emitter, and an electro-optic sampling detection technique.[160-161] The collected data was analyzed using dispersion analysis to elucidate

the different contribution of the phonon modes to the reflectivity, which is normalized by the experimental THz data. From these results, the dielectric properties at phonon frequencies were calculated. The chapter represents the collaborative work with Professor Stanislav Kamba's group and Professor David Tanner's group on the subject of IR. The infrared spectra between 10 K and 600 K and dielectric properties at THz were collected in Professor Kamba's lab. The infrared spectra at 50 K, 300 K, and 360 K were also collected in Professor Tanner's lab independently for comparison. The comparison of the IR spectra from the two independent experiments will be in Appendix B.

8.2 Normal Mode Determination

In Chapter 6, the atomic positions of Gd_3NbO_7 at different temperatures were determined by the phase refinements. Based on the symmetry of atomic site from Chapter 6, normal mode determination tables at the low temperature phase and the high temperature phase are presented in Table 8-1 and Table 8-2.

Based on the site symmetry, there are in total 20 A_1, 10 A_2, 18 B_1, and 18 B_2 modes. The acoustic modes are $1A_1 + 1B_1 + 1B_2$. The A_2 is Raman active, and the A_1, B_1, and B_2 are both Raman and IR active. Therefore, the irreducible representation for the low temperature phase can be written as

$$\Gamma = 19A_1(R,IR) + 10A_2(R) + 17B_1(R,IR) + 17B_2(R,IR) \quad (8\text{-}1)$$

As for the high temperature phase, the irreducible representation is

$$\Gamma = 8A_g(R) + 6A_u(-) + 8B_{1g}(R) + 10B_{1u}(IR) + 4B_{2g}(R) + 11B_{2u}(IR) + 7B_{3g}(R) + 9B_{3u}(IR) \quad (8\text{-}2)$$

where (R), (-), (IR), (R,IR) stand for the Raman active, silent, infrared active, and both the Raman and IR active modes, respectively. In summary, there are 53 IR active

modes in the low temperature phase and 30 IR active modes in the high temperature phase.

Table 8-1. Normal mode determination for the low temperature phase of Gd_3NbO_7 with space group *Cm2m*.

	Site Symmetry	A_1	A_2	B_1	B_2
Gd1	C_s^{xz} (4*c*)	2	1	2	1
Gd2(1)	C_s^{yz} (4*e*)	2	1	1	2
Gd2(2)	C_s^{yz} (4*d*)	2	1	1	2
Nb	C_s^{xz} (4*c*)	2	1	2	1
O1(1)	C_{2v} (2*a*)	1	0	1	1
O1(2)	C_{2v} (2*b*)	1	0	1	1
O2(1)	C_{2v} (2*a*)	1	0	1	1
O2(2)	C_{2v} (2*b*)	1	0	1	1
O3(1)	C_{2v} (2*a*)	1	0	1	1
O3(2)	C_{2v} (2*b*)	1	0	1	1
O4(1)	C_1 (8*f*)	3	3	3	3
O4(2)	C_1 (8*f*)	3	3	3	3
Acoustic Modes		1	0	1	1
Lattice Modes		19	10	17	17
Selectrion Rules		Raman **IR**	Raman	Raman **IR**	Raman **IR**

Table 8-2. Normal mode determination for the high temperature phase of Gd_3NbO_7 with space group *Cmcm*.

	Site Symmetry	A_g	A_u	B_{1g}	B_{1u}	B_{2g}	B_{2u}	B_{3g}	B_{3u}
Gd1	C_{2h}^{x} (4*b*)	0	1	0	2	0	2	0	1
Gd2	C_s^{xy} (8*g*)	2	1	2	1	1	2	1	2
Nb	C_{2h}^{x} (4*a*)	0	1	0	2	0	2	0	1
O1	C_{2v}^{y} (4*c*)	1	0	1	1	0	1	1	1
O2	C_{2v}^{y} (4*c*)	1	0	1	1	0	1	1	1
O3	C_{2v}^{y} (4*c*)	1	0	1	1	0	1	1	1
O4	C_1 (16*h*)	3	3	3	3	3	3	3	3
Acoustic Modes		0	0	0	1	0	1	0	1
Lattice Modes		8	6	8	10	4	11	7	9
Selectrion Rules		Raman	Inactive	Raman	IR	Raman	IR	Raman	IR

8.3 Infrared Spectra

Experimental IR reflectivity data for Gd_3NbO_7 was fitted with the generalized factorized four-parameter oscillator model in the following[162]:

$$R(\omega) = \left| \frac{\sqrt{\varepsilon^*(\omega)} - 1}{\sqrt{\varepsilon^*(\omega)} + 1} \right|^2 \tag{8-3}$$

$$\varepsilon^*(\omega) = \varepsilon(\infty) \prod_{j=1}^{n} \frac{\omega_{Lj}^2 - \omega^2 + i\omega\gamma_{Lj}}{\omega_{Tj}^2 - \omega^2 + i\omega\gamma_{Tj}} \tag{8-4}$$

where $\varepsilon(\infty)$ is the high frequency permittivity from electronic polarization, ω_{Tj} and ω_{Lj} are the eigenfrequencies of the transverse and longitudinal jth phonon mode and γ_{Tj} and γ_{Lj} are their corresponding damping constants. Dielectric contribution $\Delta\varepsilon_j$ of the jth mode to static permittivity can be calculated by

$$\Delta\varepsilon_j = \frac{\varepsilon(\infty)}{\omega_{Tj}^2} \frac{\prod_k (\omega_{Lk}^2 - \omega_{Lj}^2)}{\prod_{k \neq j} (\omega_{Tk}^2 - \omega_{Tj}^2)} \tag{8-5}$$

For the 600 K spectrum, 18 oscillators yielded a good fitting with mean square deviation 0.00634. Meanwhile, 24 oscillators were used to fit the 300 K spectrum, and 33 oscillators for the 10 K spectrum. It is expected that the number of oscillators used is less than the number of modes predicted by nuclear site group analysis (30 for the high temperature phase and 53 for the low temperature phase). One requirement for a successful fitting is that the number of oscillators used is the minimum number. Fitting routine of the experimental reflectivity followed least squares minimization techniques using the ASF program developed in Professor Kamba's lab. The complete lists of all the fitting parameters and calculated dielectric contribution $\Delta\varepsilon_j$ of each mode for different temperatures are in Table 8-3, Table 8-4, and Table 8-5. Figure 8-1 and Figure 8-2

show comparison between the experimental reflectivity and the fitting based on the parameters listed in Table 8-3 and Table 8-4 at 10 K and 600 K. The experimental reflectivity match well with the oscillator fit.

Table 8-3. List of fitting parameters for 33 oscillators at 10 K.

No.	ω_T(cm^{-1})	γ_T (cm^{-1})	ω_L (cm^{-1})	γ_L (cm^{-1})	$\Delta\varepsilon$
1	5.94	18.72	5.97	18.20	0.31
2	78.30	60.90	79.67	46.48	2.036
3	83.56	10.70	84.02	11.02	0.54
4	91.58	6.15	101.42	10.22	4.64
5	100.28	2.58	96.84	5.74	0.41
6	111.27	5.94	113.10	8.56	1.1
7	126.38	13.82	131.87	3.45	3.02
8	146.07	12.68	149.27	6.14	1.748
9	166.97	19.92	197.81	20.38	6.946
10	170.33	10.13	169.88	5.38	1.04
11	204.68	5.14	221.62	13.34	0.627
12	207.88	13.48	207.88	13.22	0.000
13	211.70	5.91	210.17	9.79	0.16
14	217.75	5.65	216.12	6.98	0.09
15	234.90	9.56	239.47	11.19	0.659
16	249.09	17.74	272.90	12.76	1.337
17	255.96	10.50	254.42	9.33	0.416
18	276.56	3.41	293.96	23.75	0.266
19	299.46	9.16	313.19	117.68	0.169
20	323.27	10.93	326.93	16.54	0.084
21	339.95	11.70	342.50	9.73	0.138
22	350.74	8.47	367.22	25.53	0.407
23	374.55	9.53	375.88	11.82	0.024
24	385.44	12.71	387.37	18.89	0.063
25	403.86	13.82	423.09	20.32	0.517
26	447.81	13.42	462.47	13.19	0.396
27	480.78	17.63	541.23	22.55	0.373
28	490.85	9.56	488.11	6.40	0.142
29	511.92	41.67	508.25	41.10	0.070
30	551.75	18.32	557.42	20.03	0.023
31	605.99	54.03	608.30	39.03	0.123
32	615.40	28.50	708.00	17.57	0.369
33	675.38	32.62	673.06	32.85	0.00855

Table 8-4. List of fitting parameters for 19 oscillators at 600 K.

No.	ω_T (cm^{-1})	γ_T (cm^{-1})	ω_L (cm^{-1})	γ_L (cm^{-1})	$\Delta\varepsilon$
1	61.021	30.5424	64.7379	20.7648	6.164
2	92.8806	31.1139	119.7191	30.3628	15.616
3	147.8207	14.0218	147.9071	13.9462	0.04
4	162.4217	40.587	184.8965	55.3917	5.387
5	202.1392	30.7635	214.6063	25.6496	1.476
6	230.2851	32.7406	239.3042	43.3296	0.99
7	259.9987	34.8091	291.3617	35.8644	2.31
8	296.2362	25.2799	311.3698	65.346	0.21
9	317.3912	38.8237	325.5188	81.6835	0.1058
10	349.1298	34.7643	366.5566	36.2629	0.5078
11	380.3553	24.5661	382.67	34.5537	0.07198
12	400.9602	41.4127	427.75	45.6446	0.61338
13	473.1506	64.9387	543.7183	36.4062	0.905
14	511.0153	33.849	508.846	30.623	0.038
15	550	22.3663	552.538	27.7063	0.00637
16	592.0126	50.7997	607.8256	49.9398	0.244
17	617.4507	48.0348	688.396	22.752	0.136
18	674.5646	59.5725	670.2173	53.3285	0.00589

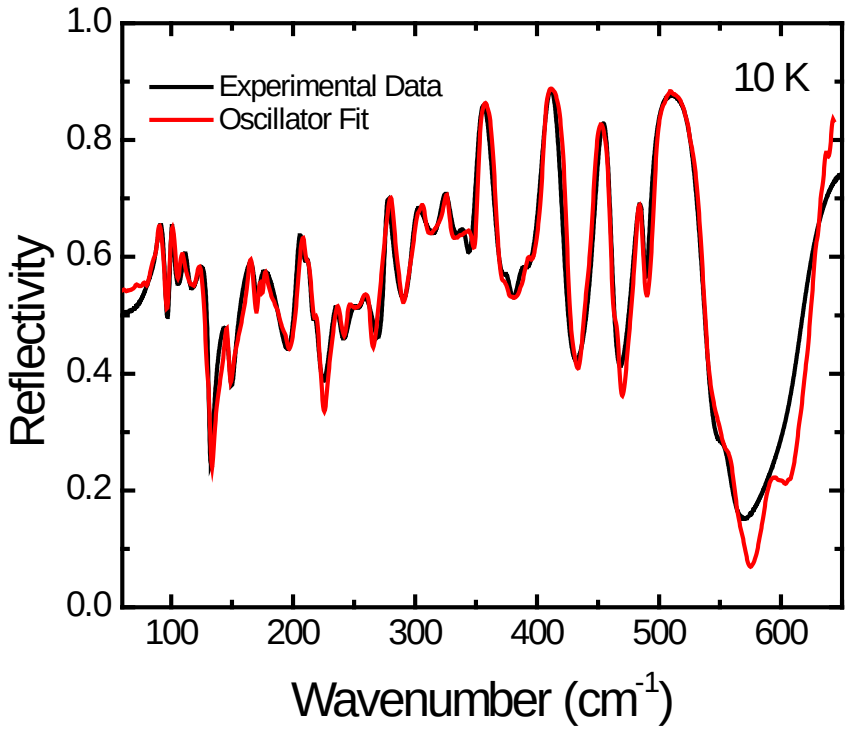

Figure 8-1. IR reflectivity of Gd_3NbO_7 at 10 K. Solid lines show experimental data. Dotted lines show fit curves to a sum of 33 oscillators.

Table 8-5. Fitting parameters for 24 oscillators at 300 K

No.	ω_T (cm^{-1})	γ_T (cm^{-1})	ω_L (cm^{-1})	γ_L (cm^{-1})	$\Delta\varepsilon$
1	61.58	35.71	65.24	24.94	5.66
2	92.23	9.97	109.00	13.19	5.63
3	98.30	15.18	94.60	8.60	6.12
4	113.91	13.70	119.41	13.26	1.23
5	125.00	11.46	128.00	11.28	0.56
6	146.29	12.25	147.03	9.87	0.34
7	163.64	25.95	182.72	35.13	4.85
8	167.11	10.52	166.70	9.87	0.56
9	204.69	21.83	218.57	15.68	2.57
10	230.14	26.24	239.39	34.55	1.06
11	260.21	25.01	291.43	26.45	2.82
12	296.56	15.21	312.25	55.37	0.30
13	316.97	26.09	324.67	58.55	0.11
14	348.10	26.17	372.38	29.56	0.83
15	380.08	22.55	382.39	34.98	0.05
16	400.14	26.09	429.05	34.40	0.66
17	452.18	24.94	460.27	20.24	0.27
18	476.00	34.55	545.85	25.59	0.63
19	487.00	10.66	486.87	10.63	0.0814
20	511.06	27.18	509.95	26.31	0.02
21	550.00	18.00	552.79	23.92	0.0459
22	592.11	44.52	608.00	46.84	0.23
23	622.18	35.13	708.00	17.85	0.2054
24	675.38	32.16	673.06	31.01	0.0076

During this type of fitting routines, it is good practice to use the combined data from THz and/or MW and/or low-frequency range if available to establish boudary conditions.[6,162] Therefore, the dielectric properties data at THz frequency range were used to normalize the reflectivity spectra. The room temperature real and imaginery parts of permittivity measured by time-domain terahertz transmission spectrometer and from the oscillateor fit are shown in Figure 8-3 and Figure 8-4. The real and imaginary parts of permittivity from the normalized reflectivity match well with the low frequency values measured by LCR as shown in Chapter 5: The real part of permittivity is 39 and

the imaginary part is 0.02 from IR at the wavenumber ~ 0, while the corresponding value is 45 and 0.04 at 1 MHz from LCR.

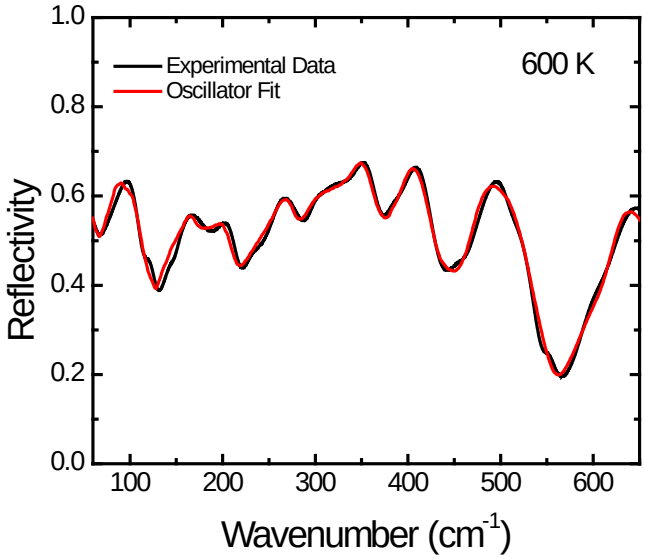

Figure 8-2. IR reflectivity of Gd_3NbO_7 at 600 K. Solid lines show experimental data. Dotted lines show fit curves to a sum of 19 oscillators.

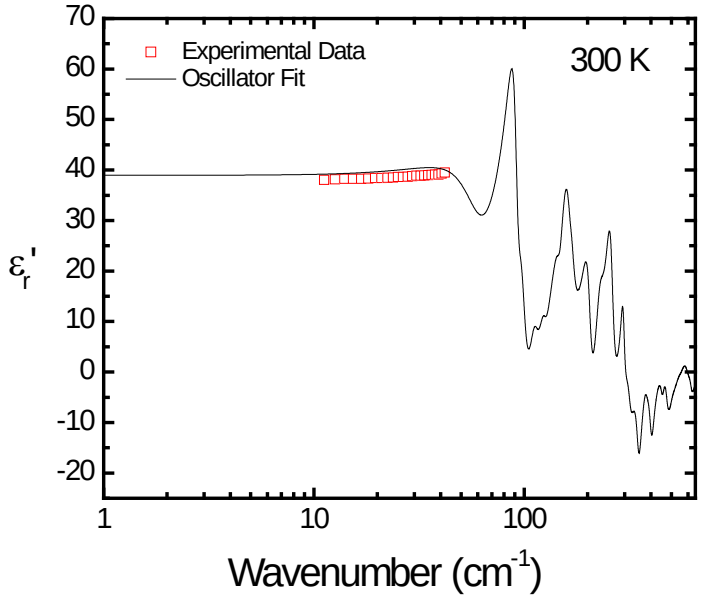

Figure 8-3. The real part of permittivity obtained from the time-domain THz spectrometer (dots) combined with the result of the IR reflectivity spectra.

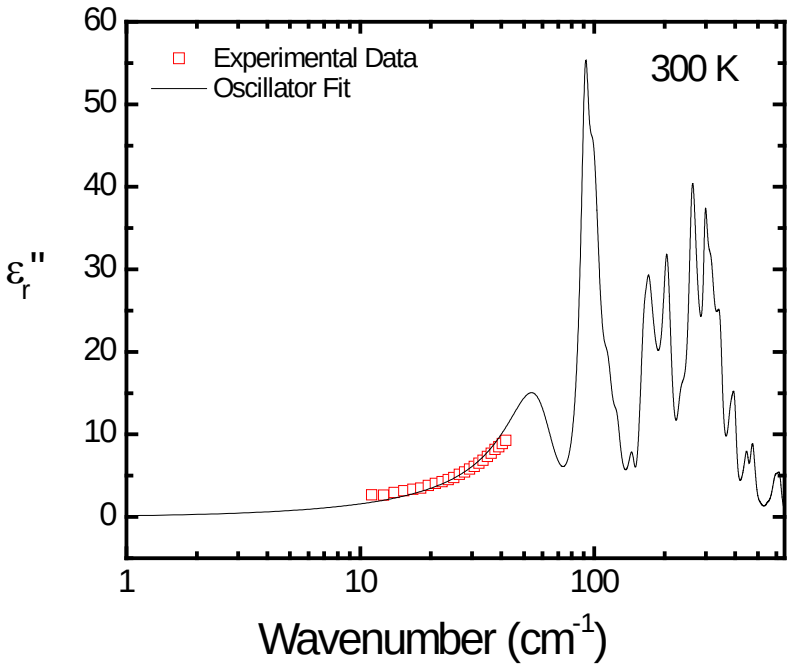

Figure 8-4. The imaginary part of permittivity obtained from the time-domain THz spectrometer (dots) combined with the result of the IR reflectivity spectra.

The real and imaginary parts of permittivity from the oscillator fit at 10 K and 600 K are presented in Figure 8-5 and Figure 8-6. The calculated real part of permittivity is 32.4 at the temperature of 10 K and wave number close to 0. The measured real part of permittivity is 32 at the temperature of 20 K and 1 MHz frequency. Considering the variation real part of permittivity is small below 100 K as shown in Chapter 5. It is expected the 10 K permittivity should near 32. Therefore, the lower limit of the real part of permittivity from IR is in a good match with the value by LCR.

The static permittivity can be calculated by the summation of each phonon contribution by

$$\varepsilon(0) = \sum \Delta\varepsilon_j + \varepsilon(\infty) \tag{8-6}$$

The fitted $\varepsilon(\infty)$ is 4.17 for all temperatures since the electronic polarization is temperature-insensitive as described in Chapter 2. The calculated static permittivity is shown in Figure 8-7. The experimental measured dielectric permittivity from 1 kHz to 1 MHz by LCR in Chapter 5 are also included in Figure 8-7 for comparison. The static permittivity maintain the same variation as function of temperature as that measured by LCR. The permittivity increases with increasing temperature until 340 K, then decreasing with a smaller slope with increasing temperature. The static permittivty is about 10% lower than the 1 MHz permittivity, which may be due to the errors created by different methods.

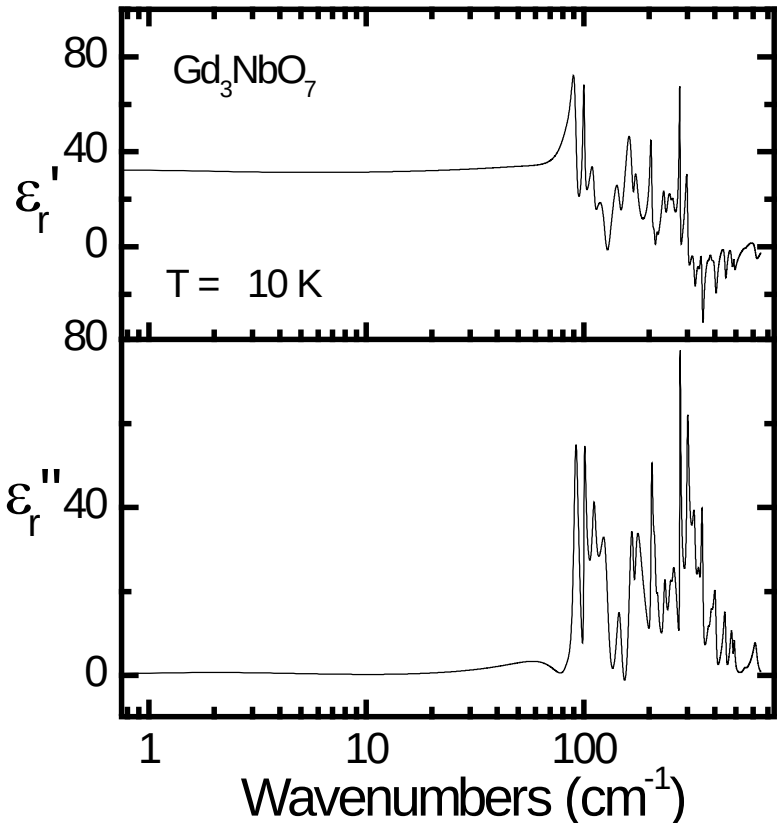

Figure 8-5. Calculations of the real and imaginary parts of the permittivity at 10 K.

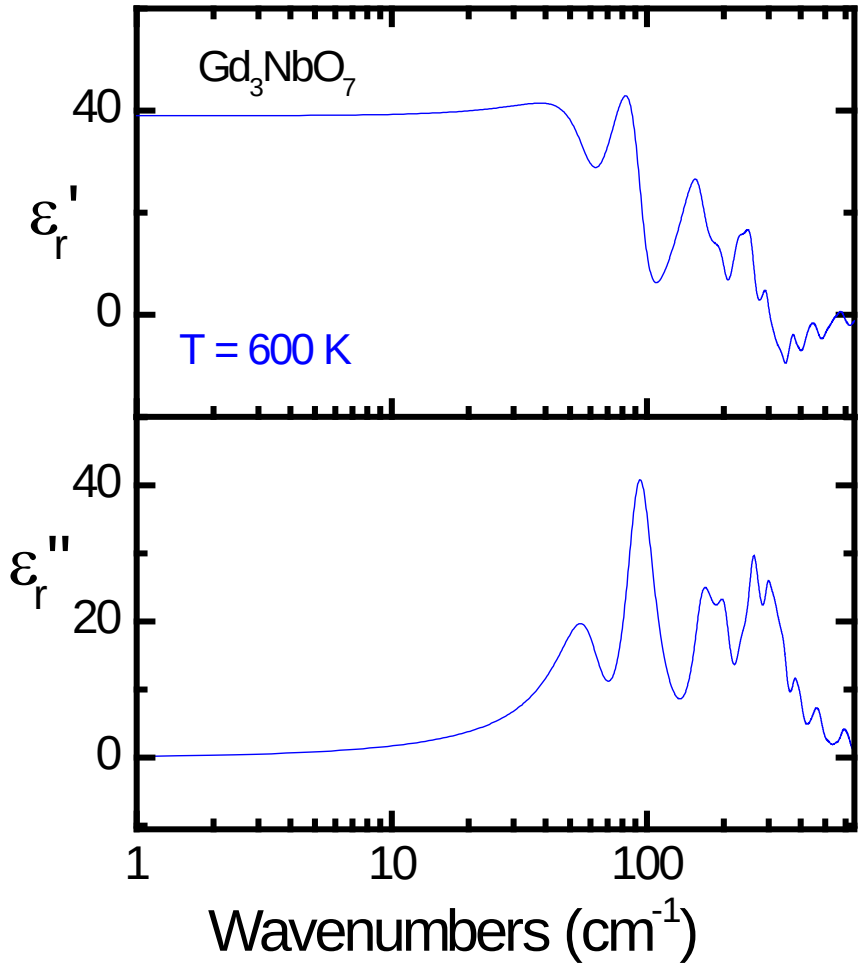

Figure 8-6. Calculations of the real and imaginary parts of the permittivity at 600 K.

There is not much change between the dielectric behavior at 300 K and that at 600 K (the phase transition temperature is 340 K). As discussed in Chapter 6 and also mentioned above, in reflectivity spectra, there is a mode at 450 cm^{-1} appearing below 340 K and disappearing above 340 K. However, there is not much difference in dielectric behavior at 450 cm^{-1} between 300 K and 600 K. As in Table 8-3 and Table 8-4, there is only a small dielectric contribution ($\Delta\varepsilon_j$) from the mode at 450 cm^{-1}. $\Delta\varepsilon_j$ is

0.396 at 10 K and 0.27 at 300 K, which are both less than 2% of the total dielectric permittivity. The major dielectric contribution is from the modes below 200 cm^{-1}.

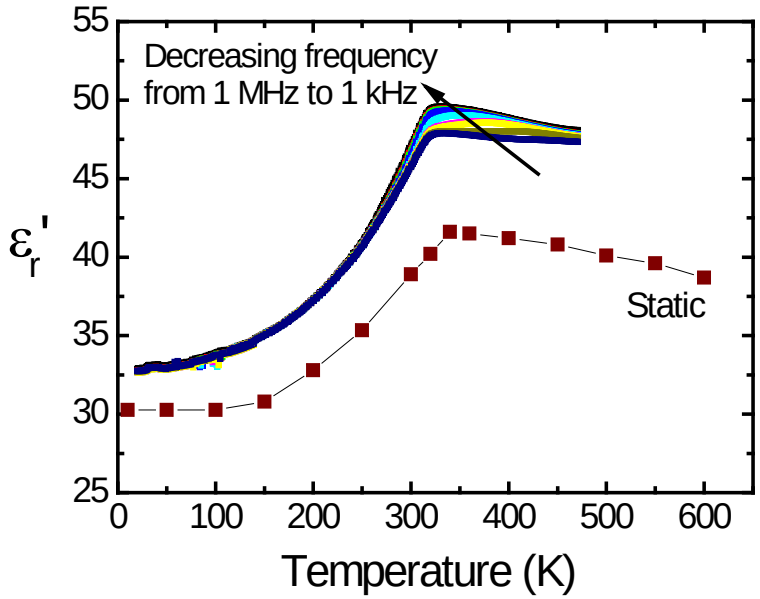

Figure 8-7. Dielectric permittivity of Gd_3NbO_7 from 1 kHz to 1 MHz by LCR meter and static permittivity.

8.4 Conclusion

Normal mode determination was used to calculate possible IR active modes below and above the phase transition temperature (340 K). The low temperature phase of Gd_3NbO_7 has 53 IR active modes and the high temperature phase has 30 IR active modes. A four-parameter oscillator model was used to fit the reflectivity. Total 33 oscillators were used to fit the 10 K spectrum, 24 oscillators were modeled for the 300 K spectrum, and only 19 oscillators were applied in the 600 K spectrum. The dielectric properties measured by terahertz transmission spectrometer were used to normalize the reflectivity. The dielectric properties at three temperatures were calculated from the fit up to 650 cm^{-1}. The calculated static permittivity as a function of temperature maintains the same shape as the 1 MHz permittivity and reaches the maximum at 340 K.

One mode at 450cm^{-1} disappears above the phase transition temperature (340 K), supporting the phase transiton. However, the dielectric contribution from the mode is small, less than 2% at both 10 K and 300 K. Therefore, comparing the dielectric behavior at 300 K and 600 K, there is not much change.

CHAPTER 9
STRUCTURE-DIELECTRIC PROPERTY RELATIONSHIPS IN FLUORITE-RELATED Ln_3NbO_7 AND $Ln_2Ln'NbO_7$

9.1 Introduction

The previous chapters presented a study on a series of fluorite-related Ln_3NbO_7 and $Ln_2Ln'NbO_7$ compounds based on crystallography as well as dielectric properties. The current chapter aims at establishing correlations between the crystal structure and the dielectric properties observed in these compounds. In order to accomplish this, two additional compounds (Sm_2YbNbO_7 and Gd_2YbNbO_7) are introduced. Despite the fact that the crystal structure of these two compounds is not completely resolved, it will be shown that their inclusion greatly helps in realizing general trends and correlations.

9.2 Summary of the Crystal Structure of Investigated Compounds

It is important to recall that one characteristic feature of the XRD patterns for the orthorhombic weberite-type structure is the peak splitting of the most intense fluorite peaks, for example, the (111) reflection of cubic fluorite split into (202) and (220) of orthorhombic weberite-type. The peak splitting decreases with decreasing ionic radius of Ln^{3+} for Ln_2YbNbO_7 compounds as shown in Figure 9-1. As for Gd_2YbNbO_7, the peak splitting is greatly depressed. The XRD pattern of Gd_2YbNbO_7 indicates a tetragonal lattice unlike the orthorhombic lattice observed in all other $Ln_2Ln'NbO_7$ in this study (Figure 9-2). The XRD pattern of Gd_2YbNbO_7 contains less minor reflections comparing to that Gd_3NbO_7. Therefore, though the peak splitting of Gd_3NbO_7 is depressed at 295 K and 100 K as discussed in Chapter 6, the lattice of Gd_3NbO_7 is orthorhombic.

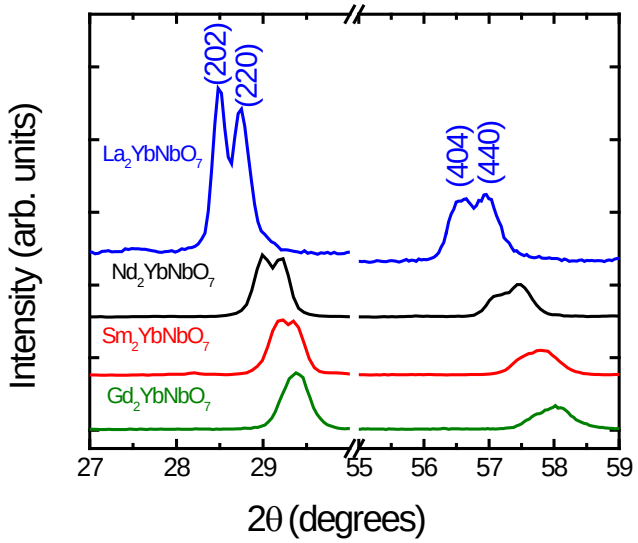

Figure 9-1. XRD of Ln_2YbNbO_7 (Ln^{3+} = La^{3+}, Nd^{3+}, Sm^{3+}, and Gd^{3+}) showing the peak splitting between (202) and (220), and between (404) and (440).

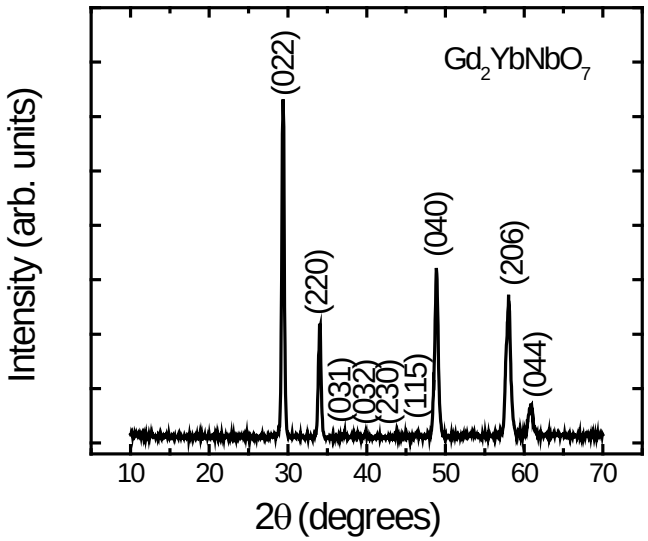

Figure 9-2. The XRD pattern of Gd_2YbNbO_7.

As discussed in Chapter 4, the crystal structure of Ln_3NbO_7 is mediated by the ionic radius of Ln^{3+}. Ln_3NbO_7 compounds with large Ln^{3+} ionic radius of such as La^{3+}, Nd^{3+}, and Gd^{3+} all crystallize with an orthorhombic weberite-type structure, whereas Dy_3NbO_7, Y_3NbO_7, Er_3NbO_7, and Yb_3NbO_7 all crystallize with a cubic fluorite structure.

The average ionic radius of Ln^{3+} ($2/3r_{Gd} + 1/3r_{Yb}$) for Gd_2YbNbO_7 is between the ionic radius of Dy^{3+} (1.027 Å) and Gd^{3+} (1.053 Å) as shown in Figure 9-3 (A), especially close to Dy_3NbO_7.[27] Therefore, the tetragonal lattice of Gd_2YbNbO_7 may be an intermediate between cubic fluorite and orthorhombic weberite-type.

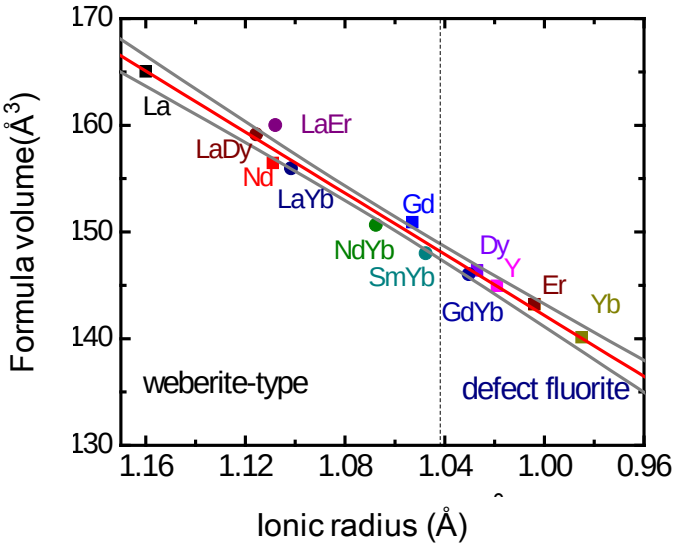

(A)

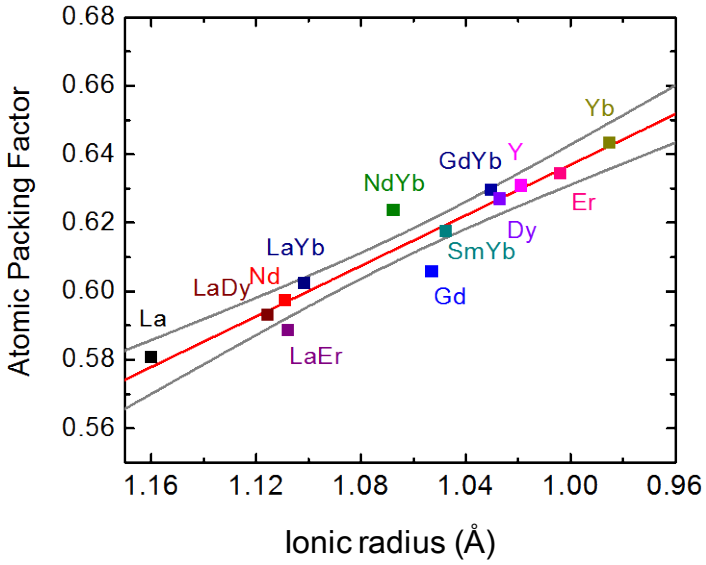

(B)

Figure 9-3. (A) The formula volume of Ln_3NbO_7 and $Ln_2Ln'NbO_7$ as a function of the (average) ionic radius of rare earth element.[27] (B) APF as a function of ionic radius. The red line is the linear fitting. The grey lines are the 95% confidence limit of the linear fitting. The formula volume is calculated by the unit cell volume divided by the formula number. For $Ln_2Ln'NbO_7$ compounds, $r_{average} = 2/3r_{Ln} + 1/3r_{Ln'}$.

A summary of lattice parameters, formula volume ($V_{unit\ cell}/Z$ as defined in Chapter 5), and atomic packing factor (APF) is listed in Table 9-1. The details of the lattice parameter calculation for Ln_3NbO_7 and $La_2Ln'NbO_7$ were discussed in Chapter 4. The lattice parameters for Nd_2YbNbO_7, Sm_2YbNbO_7, and Gd_2YbNbO_7 were calculated by the Checkcell program.[163] APF was calculated by the summation of the individual ion volume in a formula unit divided by the formula volume.

Table 9-1. Summary of the lattice parameters, formula volume, and atomic packing factor (APF) of Ln_3NbO_7 and $Ln_2Ln'NbO_7$.[86,120,159]

	a (Å)	b (Å)	c (Å)	Formula volume (Å^3)	APF (%)
La_3NbO_7	11.1593(4)	7.6309(3)	7.7522(2)	165.0356	58.08%
La_2DyNbO_7	10.921(2)	7.5646(12)	7.7060(13)	159.1539	59.32%
La_2ErNbO_7	10.9220(8)	7.5915(5)	7.7189(5)	160.0019	58.87%
Nd_3NbO_7*	10.8988(3)	7.5285(2)	7.6270(2)	156.4519	59.74%
La_2YbNbO_7	7.5623(13)	10.767(2)	7.6619(13)	155.9643	60.25%
Nd_2YbNbO_7	10.624(4)	7.482(4)	7.582(3)	150.671	62.37%
Gd_3NbO_7	7.5324(1)	10.6185(2)	7.5476(1)	150.9195	60.58%
Sm_2YbNbO_7	10.566(8)	7.443(5)	7.528(8)	148.0056	61.77%
Gd_2YbNbO_7	10.5440(11)	7.443(12)		146.0298	62.96%
Dy_3NbO_7	5.2701(6)			146.3715	62.70%
Y_3NbO_7	5.253(4)			144.9513	63.09%
Er_3NbO_7	5.232(2)			143.2198	63.45%
Yb_3NbO_7	5.194(5)			140.1218	64.35%

* The ionic radius of 7 coordinated Nd^{3+} is average of that of 6 coordinated and 8 coordinated Nd^{3+}.
The ionic radii are after Shannon.[27] The Nb^{5+} is 6 coordinated. For weberite-type Ln_3NbO_7 (Ln^{3+} = La^{3+}, Nd^{3+}, and Gd^{3+}), 1/3 of Ln^{3+} are 8 coordinated and 2/3 are 7 coordinated. For $Ln_2Ln'NbO_7$ (except Gd_2YbNbO_7), the Ln^{3+} ions are considered to be 8 coordinated and Ln'^{3+} are 6 coordinated. For Gd_2YbNbO_7 and defect fluorite Ln_3NbO_7, the Ln^{3+} ions are considered to be 8 coordinated.

It can be seen that the formula volume and APF of Ln_3NbO_7 and $Ln_2Ln'NbO_7$ has a nearly linear relationship with the (average) ionic radius of the rare earth element (Figure 9-3 (A) and (B)). The formula volume of Gd_3NbO_7 and La_2ErNbO_7 is slightly outside the upper 95% confidence limit, which may indicate structural openness. APF of Gd_3NbO_7 and La_2ErNbO_7 is outside the bottom limit of 95% confidence limit. It

confirms that Gd_3NbO_7 and La_2ErNbO_7 have more open structures. The openness of the structure may indicate easier movement of the ions (*i.e.* polarization) under the external field.

9.3 Weberite-type Ln_3NbO_7

The real part of the relative dielectric permittivity of Gd_3NbO_7 as a function of temperature and frequency is shown in Figure 9-4. The permittivity at 9 GHz was measured by composite dielectric resonator technique. The details of the setup and experiment can be found elsewhere.[164] The permittivity at 630 GHz was obtained by a custom made time-domain terahertz transmission spectrometer. The experimental setup and the measuring technique are described in Chapter 8. The static permittivity is calculated from IR fitting in Chapter 8. It is clear that the shape of the permittivity at different frequencies is well maintained. The transition temperature ($T(\varepsilon_m)$), where the slope of the permittivity curve changes from positive to negative, is almost the same at different frequencies. $T(\varepsilon_m)$ is also close to the phase transition temperature as discussed in Chapter 6.[159] The transition at 630 GHz is as sharp as that at frequencies in the kHz range. By contrast, in $Bi_{1.5}Zn_{0.92}Nb_{1.5}O_{6.92}$ pyrochlore, which has no phase transition near $T(\varepsilon_m)$, $T(\varepsilon_m)$ increases with increasing frequency and the transition is already greatly smoothed at 1.8 GHz.[6] Therefore, it is clear that the origin for the dielectric relaxation in Gd_3NbO_7 is the phase transition.

Since the static permittivity was calculated from IR, it only contains the permittivity contribution from the ionic polarization and electronic polarization. The difference between the measured permittivity at low frequency and the static permittivity indicates the permittivity contribution from the dipolar mechanism as shown in Figure 9-

4. On heating from 50 K, the dipolar contribution reaches a maximum near the phase transition (~ 340 K). In dipolar polarization, the average residence time (τ) of an atom or ion at any given site decreases with increasing temperature (Equation 2-13). Debye equations indicate that the dipolar contribution increases with decreasing τ as

$$\varepsilon_r'(\text{dipolar}) = \frac{\varepsilon_s - \varepsilon_\infty}{1+\omega^2\tau^2} \quad (9\text{-}1)$$

where ω is the frequency of an external field, ε_∞ is the sum of the ionic and electronic contribution, and ε_s is the sum of the dipolar, ionic and electronic contribution under the static field ($\varepsilon_s = \varepsilon_s(\text{dipolar}) + \varepsilon_s(\text{ionic}) + \varepsilon_s(\text{electronic})$). On the other hand, as in Equation 2-12, $\varepsilon_s(\text{dipolar})-1$ is proportional to 1/T. Therefore, at low temperature, the dipolar contribution increases with increasing temperature because of reduce in τ; at high temperature, thermal randomization begins to play a role.

The dielectric response of Gd_3NbO_7 is plotted as a function of frequency in Figure 9-5. The real part of the permittivity decreases slightly with increasing frequency from 1 kHz to 1 MHz. There is a sharp decrease in permittivity between 1 MHz and 9 GHz. There is an associated peak in the dielectric loss. The peak position at 380 K is at higher frequency than that at 293 K. The behavior of permittivity and dielectric loss respective to frequency confirms dielectric relaxation. The permittivity at 630 GHz is higher than that at 9 GHz. This may be due to the different measuring techniques used at these two frequencies. It may also be because that 630 GHz is approaching the resonating region for ionic polarization. As shown in Figure 2-23, the resonance process for ionic polarization occurs at about 10^{13} Hz.

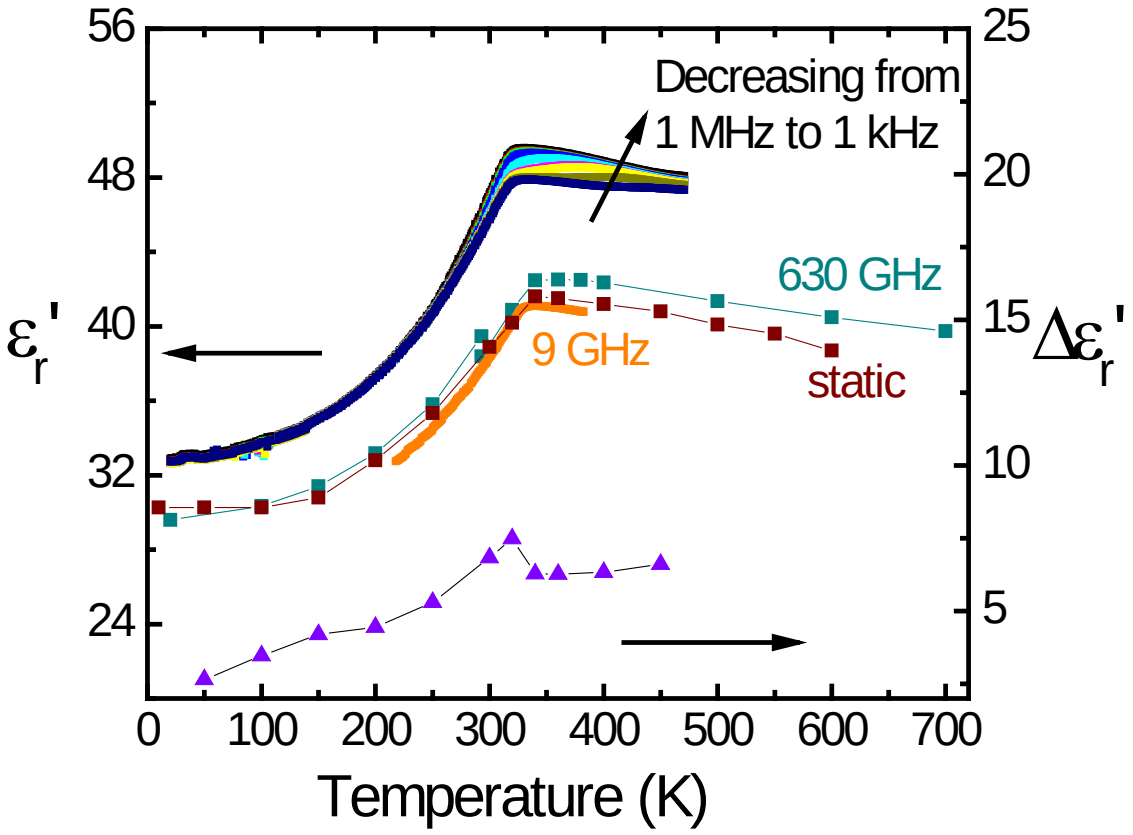

Figure 9-4. Dielectric properties of Gd_3NbO_7 at 1 kHz, 3 kHz, 8 kHz, 10 kHz, 30 kHz, 80 kHz, 100 kHz, 300 kHz, 800 kHz, 1 MHz, 9 GHz, and 630 GHz (left axis). Dielectric permittivity difference between dielectric permittivity at 1 MHz and the static permittivity (right axis).

The dielectric response does not exactly follow the Debye-type relaxation. Following Debye equations (Equation 9-2 and 9-3), when ω is at $1/\tau$, ε_r' is at an inflection point and ε_r" is at a peak position. There is a peak in tanδ below 1 MHz (1 MHz should be far below $1/\tau$) at both 295 K and 380 K. Since Debye-type relaxation does not take into consideration phase transition effects, it is expected that there would be discrepancies between the dielectric behavior of Gd_3NbO_7 and the Debye model. In order to better understand the dielectric relaxation as a function of frequency, more data points between 1 MHz and 9 GHz are needed.

$$\varepsilon_r^{'}(\omega) = \varepsilon_\infty + \frac{\varepsilon_s - \varepsilon_\infty}{1+\omega^2\tau^2} \quad (9\text{-}2)$$

$$\varepsilon_r^{''}(\omega) = \frac{\omega\tau}{1+\omega^2\tau^2}(\varepsilon_s - \varepsilon_\infty) \quad (9\text{-}3)$$

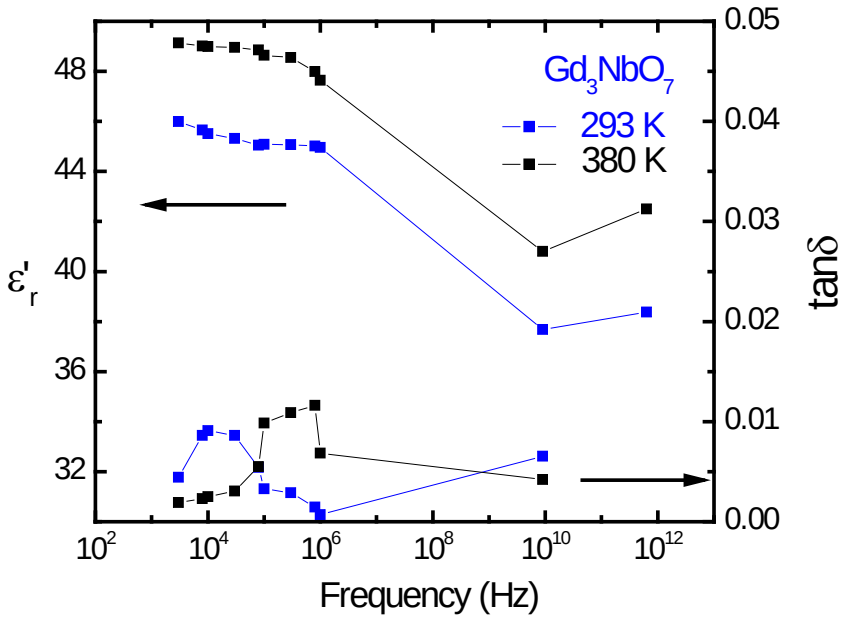

Figure 9-5. Dielectric response of Gd_3NbO_7 as a function of frequency at 293 K and 380 K.

A summary of the real part of permittivity for weberite-type Ln_3NbO_7 (Ln^{3+} = La^{3+}, Nd^{3+}, and Gd^{3+}) at 1 MHz is shown in Figure 9-6. As stated in Chapter 5, 6, and 7, the temperature ($T(\varepsilon_m)$) where the maximum permittivity occurs as well as the phase transition temperature is approximately 340 K for Gd_3NbO_7, 360 K for La_3NbO_7, and 450 K for Nd_3NbO_7. $T(\varepsilon_m)$ may be related to the openness of the structure. Gd_3NbO_7 has the most open structure among the three compounds as shown in Figure 9-3. It is proposed that the structural openness allows for an easier polarization of the material, which in turn results leads to lower temperatures needed to achieve maximum permittivity.[38]

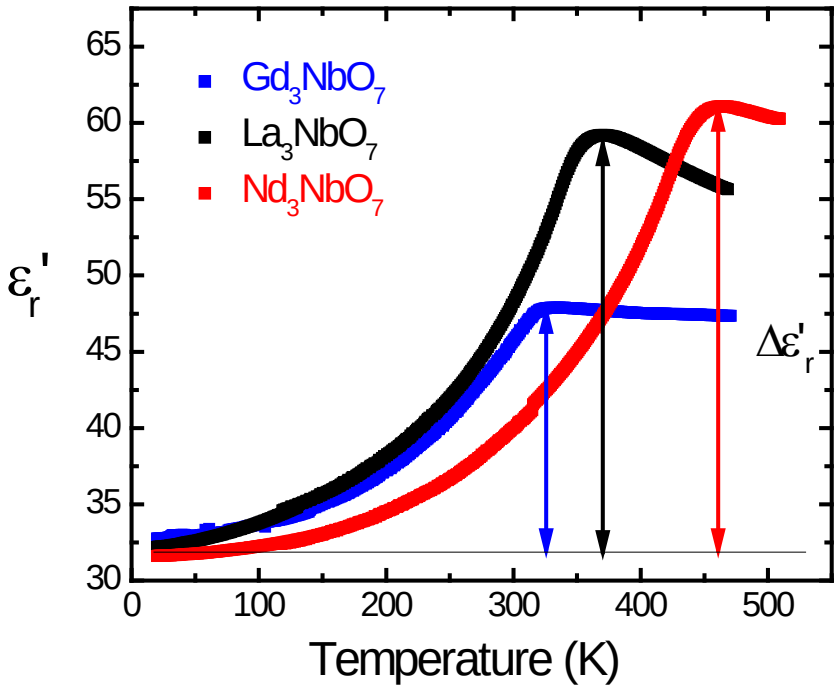

Figure 9-6. A summary of the real part of permittivity for weberite-type Ln_3NbO_7 at 1 MHz. The arrows show the difference ($\Delta\varepsilon'_r$) between the maximum permittivity and the minimum permittivity.

It is interesting to see that the off-center shift of 8-coordinated Ln^{3+} is largest in Nd_3NbO_7, intermediate in La_3NbO_7, and smallest in Gd_3NbO_7 (Figure 9-7). It can be inferred that it will take more thermal energy for Nd^{3+} to be able to move to the center of the corresponding polyhedra. Therefore, it makes sense that Nd_3NbO_7 has the highest phase transition temperature, La_3NbO_7 the second highest, and Gd_3NbO_7 the lowest (Figure 9-8). It is also important to notice that at 20 K the permittivity of these three compounds is almost the same, about 32. Nd_3NbO_7 has the highest difference in permittivity ($\Delta\varepsilon'_r$ in Figure 9-6) while Gd_3NbO_7 has the lowest difference. The normalized permittivity difference ($\Delta\varepsilon'_r/\alpha$, α is the polarizability of Ln^{3+}) is also presented in Figure 9-8. It also increases with increasing off-center shifts of $Ln1^{3+}$.

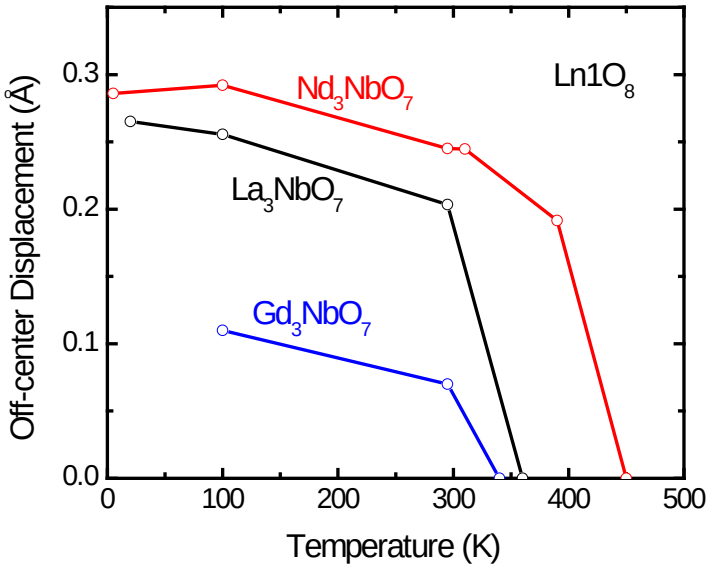

Figure 9-7. Off-center displacement of 8-cooridinated Ln^{3+} for Ln_3NbO_7 at different temperatures.

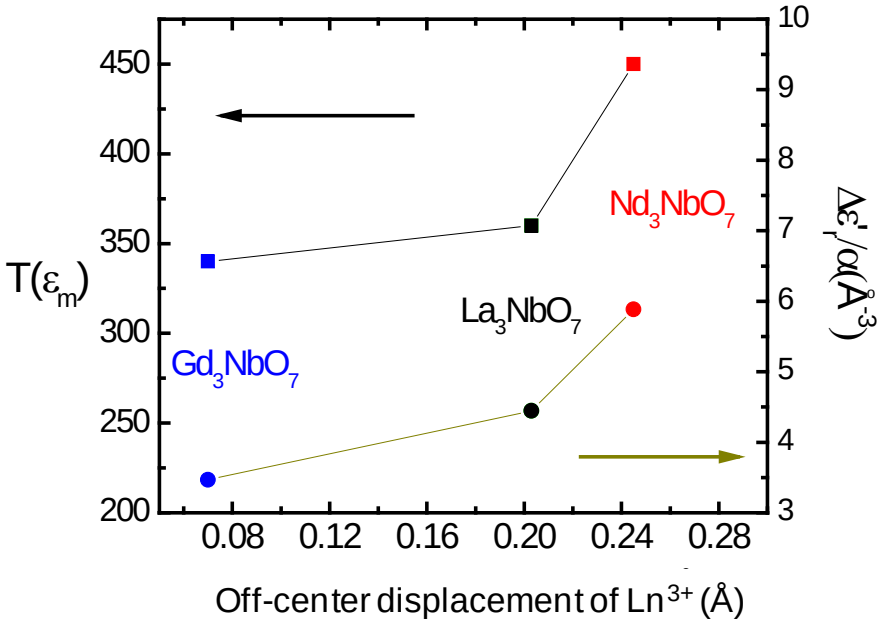

Figure 9-8. $T(\varepsilon_m)$ and normalized dielectric difference from the maximum to the minimum *vs.* off-center displacement of Ln^{3+} inside $Ln1O_8$ polyhedra. α (measured in $Å^3$) is the polarizability of Ln^{3+}.

Figure 9-9 shows the off-center shifts of Nb^{5+} within NbO_6 polyhedra. The off-center distances of Nb^{5+} in Gd_3NbO_7 are smaller than that of La_3NbO_7 at both 100 K and 295 K. Because of the shorter off-center displacements of both $Ln1^{3+}$ and Nb^{5+} ions in Gd_3NbO_7, it makes sense that Gd_3NbO_7 has lower $T(\varepsilon_m)$ than La_3NbO_7. As for Nd_3NbO_7 and La_3NbO_7, the off-center shifts of Nb^{5+} in Nd_3NbO_7 are smaller than that of La_3NbO_7 at or below RT. The off-center shifts of Nb^{5+} at all measured temperatures are below 0.17 Å for both compounds. They are smaller than the off-center distance of $Ln1^{3+}$ (above 0.19 Å, see Figure 9-10). Since the $Ln1^{3+}$ ions have to travel farther distance to reach the center of $Ln1O_8$ polyhedra at $T(\varepsilon_m)$, it is reasonable to conclude that the off-center shift of 8-coordinated $Ln1^{3+}$ plays a more important role in determining $T(\varepsilon_m)$ in La_3NbO_7 and Nd_3NbO_7.

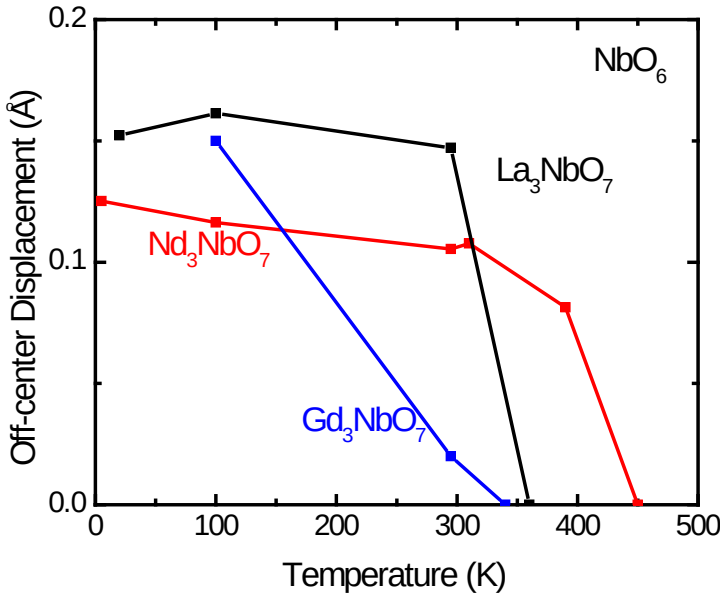

Figure 9-9. Off-center displacement of Nb^{5+} for Ln_3NbO_7 at different temperatures.

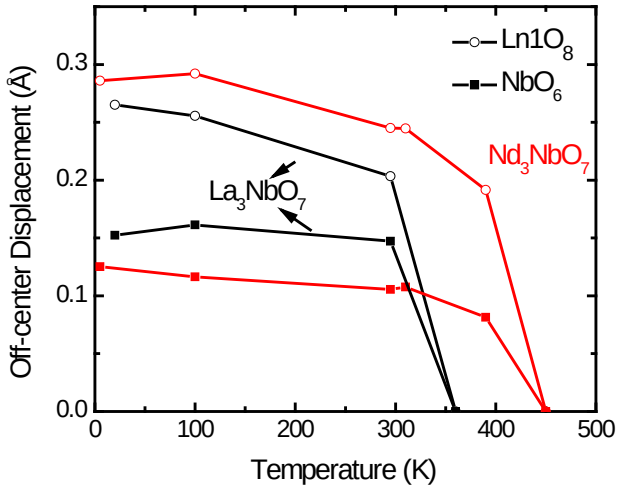

Figure 9-10. Comparison of off-center shifts of the Nb^{5+} and $Ln1^{3+}$ ions in La_3NbO_7 and Nd_3NbO_7.

9.4 $Ln_2Ln'NbO_7$

It can be expected that the more polarizable Ln^{3+} ions result in higher real part of permittivity, and indeed, the 1 MHz permittivity for the 6 investigated $Ln_2Ln'NbO_7$ compounds at all measured temperatures (from 20 K to 350 K) follow this trend. A summary of the 1 MHz real part of permittivity for the $Ln_2Ln'NbO_7$ compounds at 20 K and room temperature is shown in Figure 9-11 It is clear that the permittivity increases with ionic radius of Ln^{3+}. This is not too surprising since there is a nearly linear relationship between the average ionic radius of Ln^{3+} and the average polarizability of Ln^{3+} ($\alpha_{average} = 2/3\alpha_{Ln} + 1/3\alpha_{Ln'}$) across the rare earth element series.

As discussed above, Gd_2YbNbO_7 is an intermediate between cubic fluorite and orthorhombic weberite-type. The real part of permittivity of Gd_2YbNbO_7 increases with an increase in temperature from 20 K to 350 K (Figure 9-12). It is interesting to find out that the dielectric behavior of Gd_2YbNbO_7 resembles the dielectric response of defect fluorite Ln_3NbO_7, different from the other Ln_2YbNbO_7 investigated in this study.

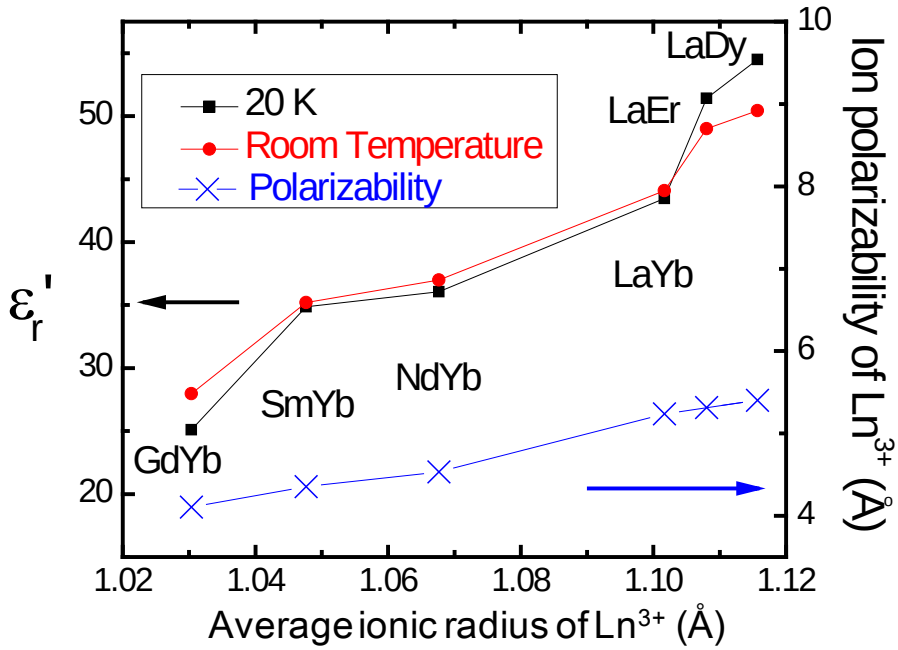

Figure 9-11. A summary of the real part of the permittivity for all investigated $Ln_2Ln'NbO_7$ compounds at the frequency of 1 MHz and the temperature of 20 K and room temperature. The average polarizability of Ln^{3+} is also included.

It suggests that the crystal structure of Gd_2YbNbO_7 is more closely related to the defect fluorite than the weberite-type, which is reasonable from the point of view of ionic radius. The average ionic radius of Ln^{3+} for Gd_2YbNbO_7 is close to the ionic radius of Dy^{3+} (Figure 9-3). A summary of the real part of permittivity at 20 K and RT as well as the (average) polarizability of Ln^{3+} for Gd_2YbNbO_7 and defect-fluorite Ln_3NbO_7 (Ln^{3+} = Dy^{3+}, Y^{3+}, Er^{3+}, and Yb^{3+}) is shown in Figure 9-13. It is clear that Gd_2YbNbO_7 has the highest ion polarizability and the average ionic radius of Ln^{3+} but the lowest permittivity. As presented in Chapter 5, the experimentally observed dielectric permittivity for defect-fluorite compounds is approximately 50% higher than the calculated values from Clausius-Mosotti equation at RT. A weak dipolar may be generated by the disorder of

the lanthanide and niobium ions. As for Gd_2YbNbO_7, it is expected that Gd^{3+} and Yb^{3+} are less disordered because of the difference in the ionic radius.

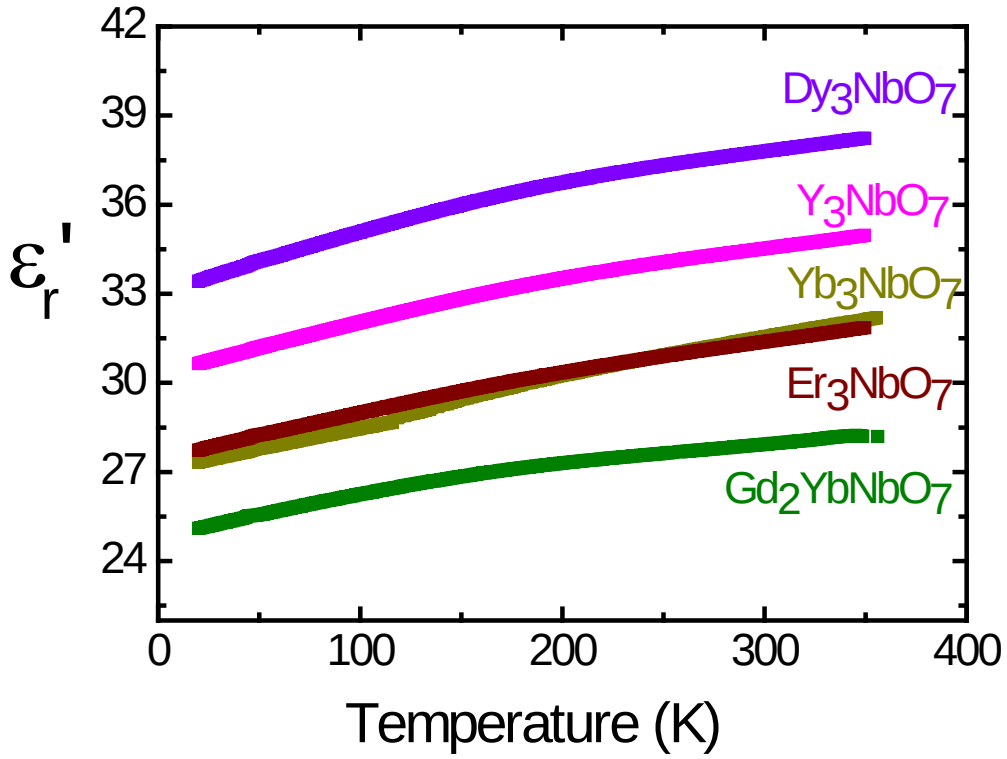

Figure 9-12. The real part of permittivity of Gd_2YbNbO_7 and defect fluorite Ln_3NbO_7 at 1 MHz.

It is interesting to find out that in Ln_2YbNbO_7 (except Gd_2YbNbO_7) the temperature ($T(\varepsilon_m)$), where the maximum permittivity occurs, decrease with decreasing the ionic radius of Ln^{3+} (Figure 9-14). The temperature (T_m), where the peak of the imaginary part of permittivity occurs, also decreases with decreasing the ionic radius of Ln^{3+}, following the same trend (Figure 9-15). It seems that the dielectric relaxation may be related to the ionic radius of Ln^{3+} or the ratio of the ionic radius of the Ln^{3+} cations (r_A) over the average ionic radius of Ln'^{3+} and Nb^{5+} (r_B).

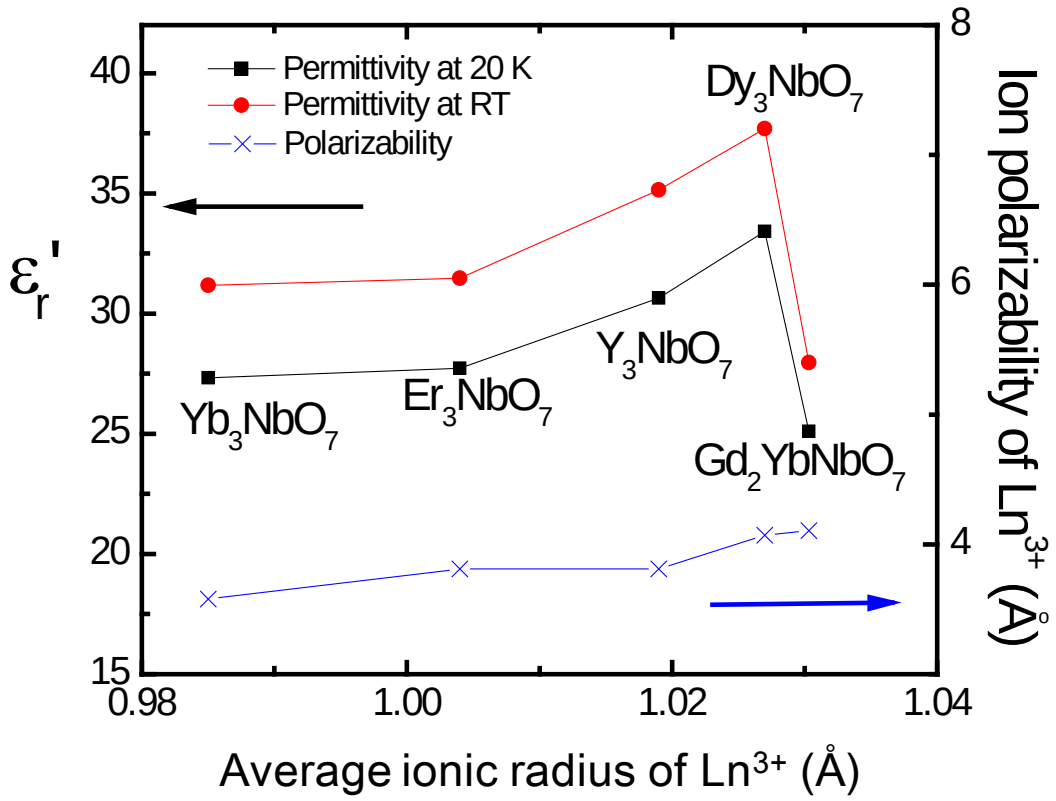

Figure 9-13. Summary of the real part of the permittivity for defect fluorite Ln_3NbO_7 and Gd_2YbNbO_7 compounds at the frequency of 1 MHz and the temperature of 20 K and room temperature. The average polarizability of Ln^{3+} is also included.

A series of $La_2Ln'NbO_7$ is also presented to show the effect of r_B. Figure 9-16 shows the real part of the permittivity of $La_2Ln'NbO_7$ (Ln'^{3+} = Yb^{3+}, Er^{3+}, and Dy^{3+}). The $T(\varepsilon_m)$ of La_2DyNbO_7 and La_2ErNbO_7 is comparable, at about 80 K. The $T(\varepsilon_m)$ of La_2YbNbO_7 is about 140 K. As for T_m, La_2YbNbO_7 has the highest value, La_2DyNbO_7 the second, and La_2ErNbO_7 the lowest (Figure 9-17). There is no obvious effect of r_B on either $T(\varepsilon_m)$ and T_m.

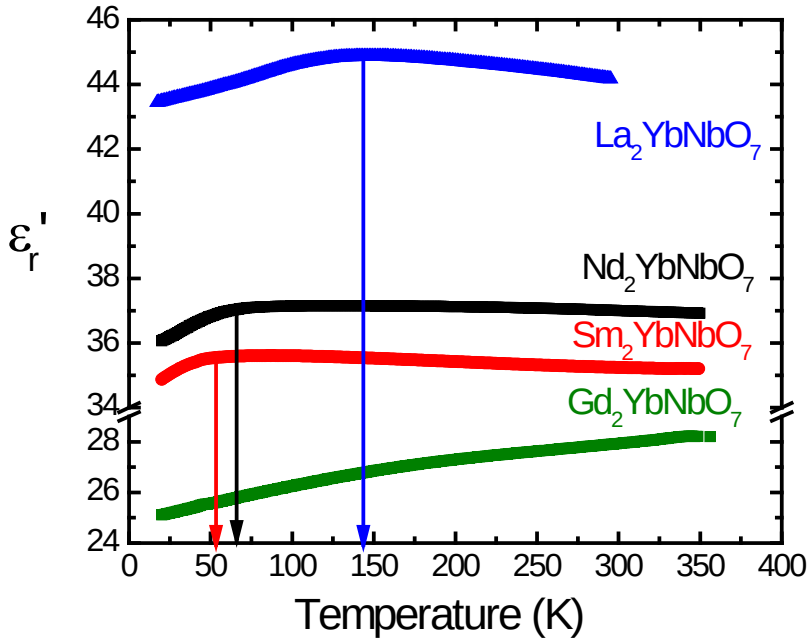

Figure 9-14. Summary of the real part of permittivity for Ln_2YbNbO_7 compounds. The arrows point to the temperature where the maximum permittivity occurs.

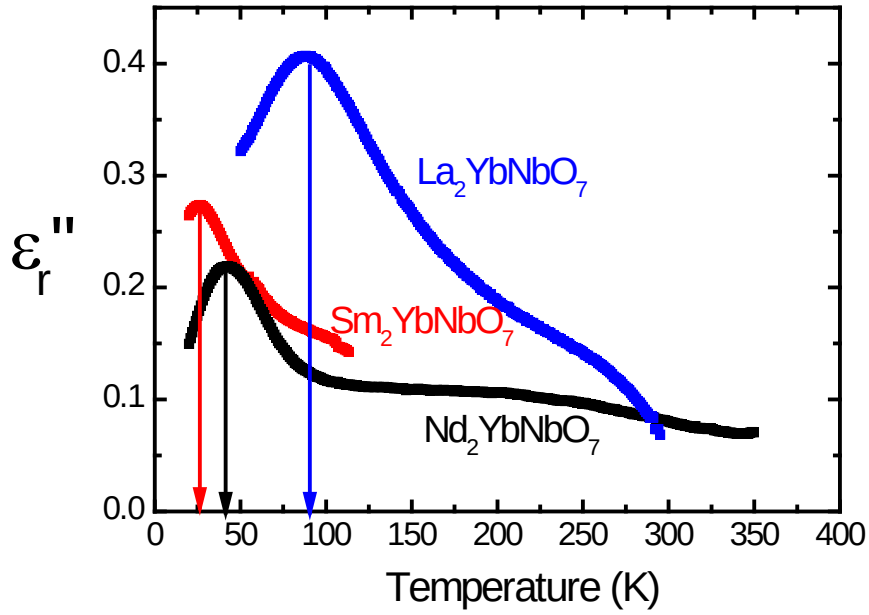

Figure 9-15. The imaginary part of permittivity for Ln_2YbNbO_7 at 1 MHz.

A summary of T_m for all five compounds is plotted in Figure 9-18 to see if there is any trend with respect to r_A/r_B. The T_m at 1 MHz for $Ln_2Ln'NbO_7$ generally increases with an increasing ratio of r_A over r_B but with one exception. La_2DyNbO_7 has a lower r_A/r_B value but higher T_m than La_2ErNbO_7. It is worth noting that La_2ErNbO_7 has a more open structure than La_2DyNbO_7 Figure 9-3). As discussed before, the structural openness in Gd_3NbO_7 may be one reason for the low $T(\varepsilon_m)$. The structural openness in La_2ErNbO_7 may also cause an easier polarization of the material, which in turn accounts for the lower T_m than that of La_2DyNbO_7. Therefore, the T_m generally increases with the increasing r_A/r_B. It is apparent that structural openness leads to lower T_m.

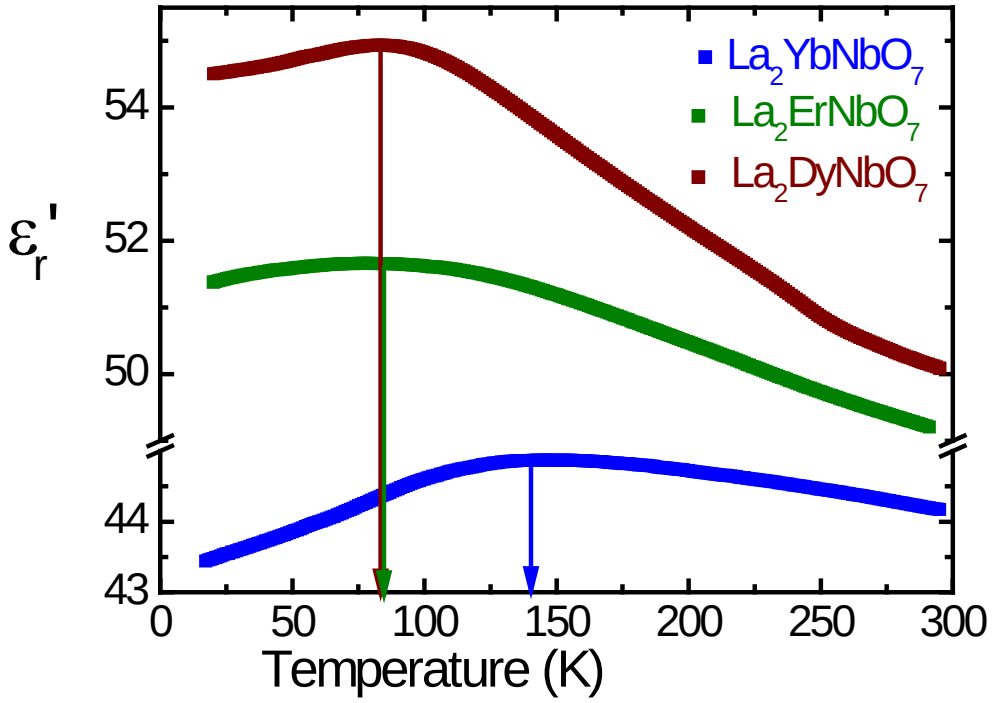

Figure 9-16. A summary of the real part of permittivity for $La_2Ln'NbO_7$ compounds.

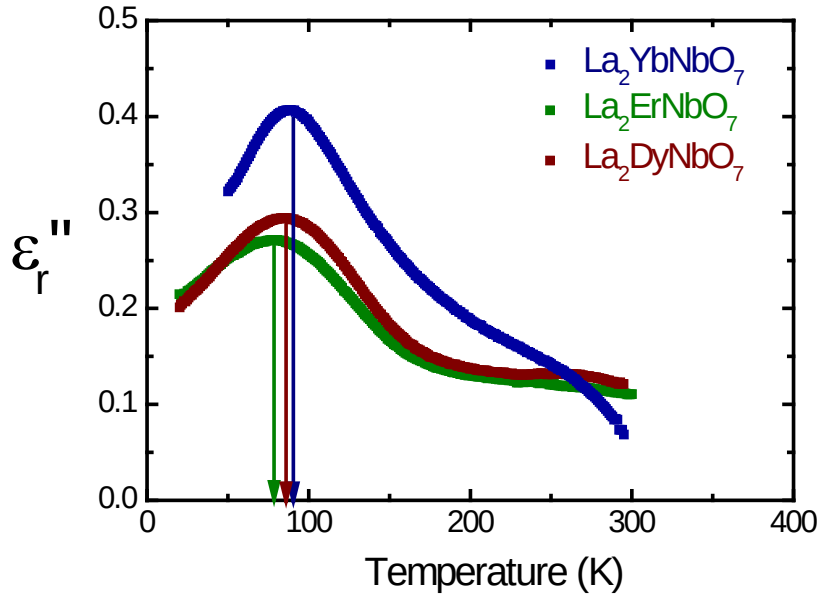

Figure 9-17 . The imaginary part of permittivity $La_2Ln'NbO_7$ at 1 MHz.

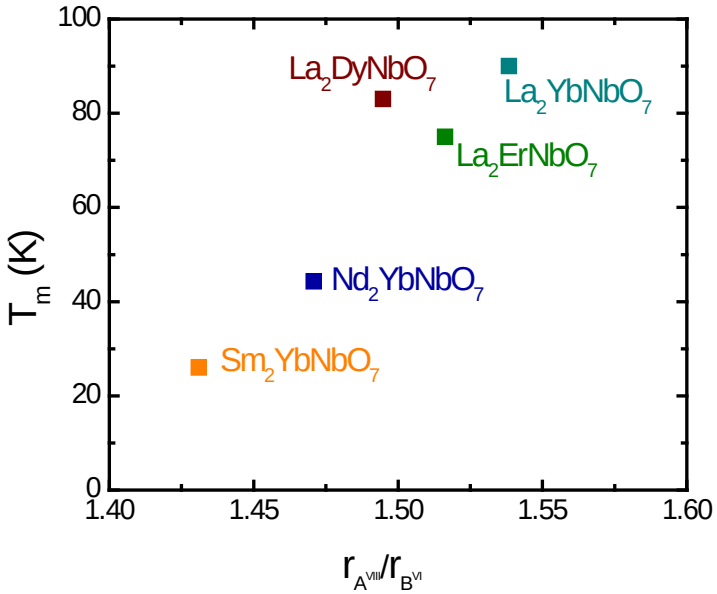

Figure 9-18. The temperature (T_m) where the peak of the 1 MHz imaginary occurs *vs.* the ratio of the ionic radius of *A* cations over that of *B* cations for $Ln_2Ln'NbO_7$. It is assumed that the Ln^{3+} ions with larger ionic radius are at *A* sites and Ln'^{3+} with smaller ionic radius are at *B* sites. The ionic radius are after Shannon.[27]

The real part of the permittivity has almost linear variation as a function of temperature above T(ε_m) for $Ln_2Ln'NbO_7$. As for Gd_2YbNbO_7, the variation of the real part of the permittivity against temperature is nearly linear from 150 K to 350 K. The temperature coefficient of permittivity (TCC) from 218 K to 350 K was calculated for all $Ln_2Ln'NbO_7$. The TCC increases with increasing average ionic radius of Ln^{3+}. The TCC varies from -137 MK^{-1} to 225 MK^{-1}. $Ln_2Ln'NbO_7$ has a negative TCC except Gd_2YbNbO_7. Nd_2YbNbO_7 and Sm_2YbNbO_7 have the most stable TCC (~ -40 MK^{-1}) in these compounds. As in Chapter 2, the 18mol% $Ca_2Nb_2O_7$ + 82mol% $Ca_2Ta_2O_7$ system is promising since the TCC is compensated to zero. It is also possible that a small amount of Gd_2YbNbO_7 secondary phase inside Sm_2YbNbO_7 and Nd_2YbNbO_7 can compensate TCC to zero, which may have potential applications.

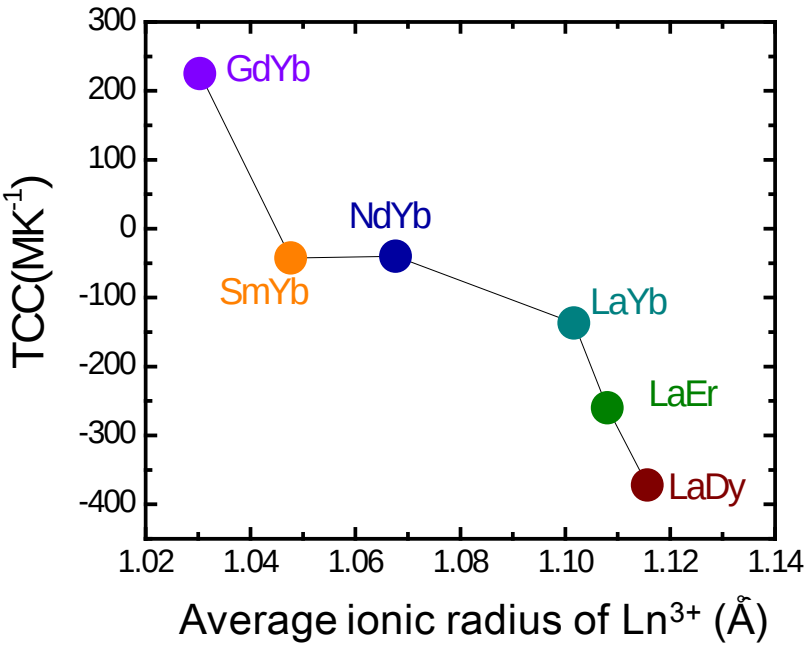

Figure 9-19. A summary of the temperature coefficient of permittivity for all $Ln_2Ln'NbO_7$.

A summary of the attempt frequencies, activation energy, the T_m (1 MHz), the $T(\varepsilon_m)$ (1MHz) and frequency dispersion between 10 kHz and 1 MHz is listed in Table 9-2. The corresponding thermal energy of the T_m and the $T(\varepsilon_m)$ is also listed. The thermal energy is much lower than the activation energy. It is clearly seen that the dielectric relaxation of Gd_3NbO_7 is different from the other $Ln_2Ln'NbO_7$. Gd_3NbO_7 has much higher T_m, activation energy and frequency dispersion.

Table 9-2. A summary of $T(\varepsilon_m)$, T_m and their corresponding energy at 1 MHz, and the attempt frequency, the activation energy, and frequency dispersion ($\Delta T_m/(\log f_1 - \log f_2)$, f_1 is 1 MHz, f_2 is 10 kHz) of dielectric relaxation.

	$T(\varepsilon_m)$ (K) at 1 MHz	E ($T(\varepsilon_m)$) (eV)	T_m (K) at 1 MHz	$E(T_m)$ (eV)	ν_0 (Hz)	E_a (eV)	$\Delta T_m/(\log f_1 - \log f_2)$ (K/Hz)
La_3NbO_7 [*1]	360	0.031	--	--	--	--	--
Nd_3NbO_7 [*1]	450	0.038	--	--	--	--	--
Gd_3NbO_7	340	0.029	442	0.038	1.5×10^{11}	0.45	60.32
La_2YbNbO_7 [*2]	--	--	90	0.0078	1.2×10^{14}	0.14	8.60
La_2DyNbO_7 [*2]	--	--	83	0.0072	1.9×10^{13}	0.12	8.78
La_2ErNbO_7 [*2]	--	--	75	0.0065	1.3×10^{12}	0.09	8.98
Nd_2YbNbO_7 [*2]	--	--	44	0.0038	2.5×10^{10}	0.04	7.03
Sm_2YbNbO_7 [*3]	--	--	26	0.0022	--	--	--

[*1] The imaginary part of the permittivity increases with increasing temperature due to conduction
[*2] $T(\varepsilon_m)$ is hard to determine due to the smooth transition of ε_r'.
[*3] The T_m at lower frequencies is expected beyond the limit of measured temperature range.

It is suggested in Chapter 5 that the origin of the dielectric relaxation in $Ln_2Ln'NbO_7$ is due to a phase transition, similar to weberite-type Ln_3NbO_7, or cation disorder, similar to pyrochlore (*e.g.* $Ca_{1.46}Ti_{1.38}Nb_{1.11}O_7$[28], also see APPENDIX A). Neutron diffraction was collected on Nd_2YbNbO_7, La_2YbNbO_7, and La_2ErNbO_7 below and above the temperature ($T(\varepsilon_m)$) where the maximum permittivity occurs. There are no extra reflections when comparing the patterns below and above $T(\varepsilon_m)$, which excludes the possibility of a phase transition. Figure 9-20 shows an example

(Nd_2YbNbO_7) of the neutron diffraction patterns below and above the $T(\varepsilon_m)$. Therefore, the origin of the dielectric relaxation of $Ln_2Ln'NbO_7$ compounds is different from weberite-type Ln_3NbO_7. Whether there is a cation disorder in $Ln_2Ln'NbO_7$ is worth further investigation.

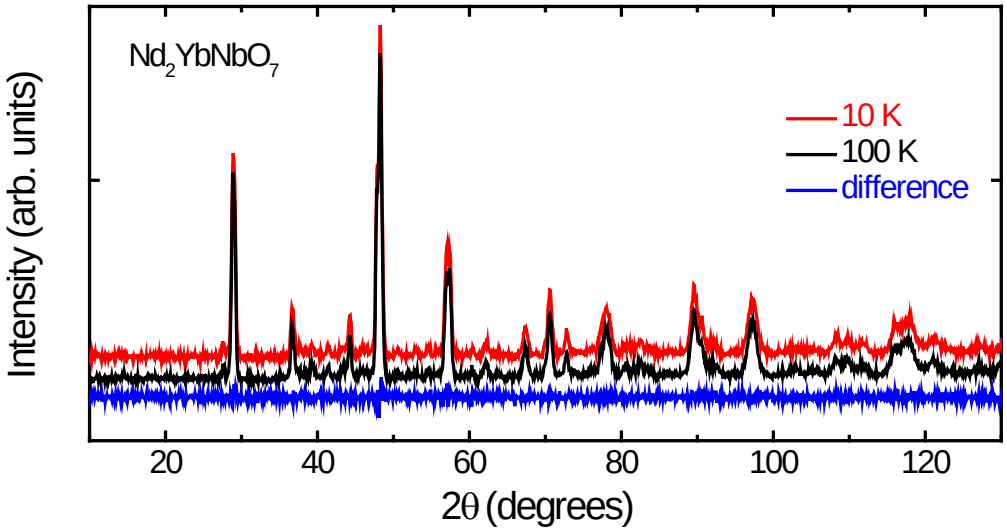

Figure 9-20. Neutron diffraction of Nd_2YbNbO_7 at 10 K an 100 K (λ = 1.5378 Å).

9.5 Conclusion

The crystal structure and dielectric property relationships were presented in this chapter. Weberite-type compounds exhibit dielectric relaxation. The real part of the permittivity of defect fluorite compounds just increases with increasing temperature. As shown in Figure 9-21, the dielectric relaxation is related to crystal structure.

For weberite-type Ln_3NbO_7, the origin of the dielectric relaxation is due to the phase transition. Gd_3NbO_7 has the most open structure while Nd_3NbO_7 has the most condensed. The structural openness may cause an easier polarization and a lower $T(\varepsilon_m)$. It is also found $T(\varepsilon_m)$ and $\Delta\varepsilon'_r/\alpha$ increases with increasing off-center distance of $Ln1^{3+}$ within their polyhedra.

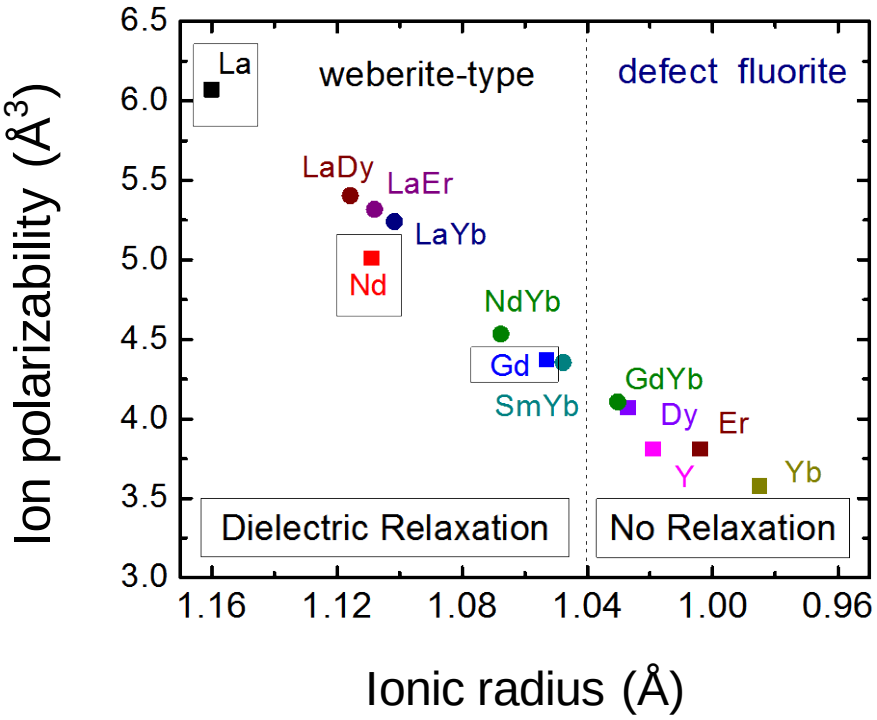

Figure 9-21. Average ion polarizability vs. average ionic radius of Ln^{3+} in Ln_3NbO_7 and $Ln_2Ln'NbO_7$. It shows that the dielectric relaxation is related to crystal structure. The rectangles on La, Nd, and Gd, identify the phases for which a phase transition was identified.

$Ln_2Ln'NbO_7$ with more polarizable Ln^{3+} ions has a higher real part of permittivity. The crystal structure of Gd_2YbNbO_7 is intermediate between orthorhombic weberite-type and cubic defect fluorite. The dielectric behaviors of Gd_2YbNbO_7 resemble that of the defect fluorite Ln_3NbO_7, other than $Ln_2Ln'NbO_7$. The TCC is negative for orthorhombic $Ln_2Ln'NbO_7$, but positive for Gd_2YbNbO_7 (~225 MK^{-1}). Nd_2YbNbO_7 and Sm_2YbNbO_7 have the most stable TCC, ~ -40 MK^{-1}. TCC increases with increasing the average ionic radius of Ln^{3+}. On the other hand, the T_m generally increases with an increasing ratio of r_A (Ln^{3+}) over r_B (average of Ln'^{3+} and Nb^{5+}). However, the structural openness also plays a role. As for the origin of dielectric relaxation, the possibility of phase transition has been ruled out by neutron diffraction at different temperatures.

Whether there is a cation disorder (like in $Ca_{1.46}Ti_{1.38}Nb_{1.11}O_7$) in $Ln_2Ln'NbO_7$ deserves further investigation.

CHAPTER 10
SUMMARY AND FUTURE WORK

10.1 SUMMARY

10.1.1 Phase Formation and Crystal Structure of Ln_3NbO_7 and $Ln_2Ln'NbO_7$

A series of Ln_3NbO_7 and $Ln_2Ln'NbO_7$ were successfully synthesized by conventional solid state processing. The phase formation was relatively easier for the defect fluorite compounds, Nd_3NbO_7, and Gd_3NbO_7 since the pure phase was formed after calcination at 1673 K for 8 h (the calcination temperature for Dy_3NbO_7 was even lower, 1573 K). As for La_3NbO_7, multiple calcinations with intermediate grinding were needed to eliminate the $LaNbO_4$ phase. La_3NbO_7 had to be calcined at 1773 K for at least 48 h in total. Multiple and long time calcinations with intermediate grinding were also necessary to reach the equilibrium phase for $Ln_2Ln'NbO_7$.

CuKα XRD, synchrotron x-ray diffraction, and neutron diffraction were used to characterize the crystal structure. The crystal structure of Ln_3NbO_7 at room temperature is defect fluorite if the ionic radius of Ln^{3+} is equal to or smaller than Dy^{3+} (1.027 Å), which is confirmed by XRD analysis. The lattice parameter of these compounds increases linearly with increasing ionic radius of Ln^{3+}.

La_3NbO_7 and Nd_3NbO_7 crystallize into a weberite-type structure. The correct space group between *Pmcn* (No. 62) and *Cmcm* (No. 63) cannot be discerned by room temperature CuKα XRD. Based on synchrotron XRD and neutron diffraction, the space group was found to be *Pmcn* at room temperature since a few minor reflections, which violate the reflection conditions for *Cmcm*, appeared in both synchrotron XRD and neutron diffraction patterns.

The crystal structure of Gd_3NbO_7 is another weberite-type. Like La_3NbO_7 and Nd_3NbO_7, the correct space group cannot be determined by CuKα XRD. The room temperature space group *Cm2m* was determined by synchrotron XRD.

As for $La_2Ln'NbO_7$, these compounds have an orthorhombic fluorite-related structure. $La_2(Yb_{0.5}Nb_{0.5})_2O_7$ is orthorhombic pyrochlore, and $La_2(Er_{0.5}Nb_{0.5})_2O_7$ and $La_2(Dy_{0.5}Nb_{0.5})_2O_7$ are weberite-type. Nd_2YbNbO_7 and Sm_2YbNbO_7 also have an orthorhombic lattice. However, Gd_2YbNbO_7 has a tetragonal lattice; it may be an intermediate structure between the cubic defect fluorite and orthorhombic weberite-type.

The formula volume, which is defined as the unit cell volume divided by the formula number, has a nearly linear relationship with the (average) ionic radius of Ln^{3+}. However, Gd_3NbO_7 and La_2ErNbO_7 have more open structure because these two compounds lie slightly outside the upper 95% confidence limit of the linear fitting. Therefore, there may be an easier ion movement or polarization in these two compounds.

10.1.2 Phase Transition in Weberite-type Ln_3NbO_7

There is a phase transition in Gd_3NbO_7 at 340 K, which is confirmed by second harmonic generation (SHG), heat capacity measurements, and IR. Based on the heat capacity curve and the dielectric susceptibility plot, the phase transition is likely to be a second order phase transition. High resolution x-ray diffraction was conducted at 100 K, 295 K, 345 K, and 400 K to study the crystal structure before and after the phase transition. The main difference in XRD patterns is the appearance of (201) reflection below the phase transition. Rietveld refinement was performed on the XRD patterns of the four mentioned temperatures which has resolved the controversy regarding the

space group of the low (*Cm2m*) and high temperature (*Cmcm*) phases. It was also concluded that the phase transition upon cooling is mainly due to the off-center shifts of Nb^{5+} and one third of the Gd^{3+} ions within their corresponding polyhedra. The off-center shift of the Nb^{5+} ions is in an antiparallel manner with their nearest Nb^{5+} neighbors along [001]. The same happens for the $Gd1^{3+}$ ions, antiparallel displacement with their nearest Gd^{3+} neighbors in [001]. The antiparallel shifts may cause antipolar displacements along [001]. The most interesting finding is that the off-center shifts cause net dipole along [010]. The calculated net dipole per unit cell is 0.0503 C/m^2 at 100 K and 0.0045 C/m^2 at 295 K. It indicates that Gd_3NbO_7 is an incipient ferroelectric with [010] being the polar axis. There are correlated antipolar displacements in [001].

Nd_3NbO_7 and La_3NbO_7 also exhibit phase transition above room temperature, which was proven by heat capacity measurement and neutron diffraction. However, unlike Gd_3NbO_7, SHG measurements indicate that Nd_3NbO_7 and La_3NbO_7 have a centrosymmetric structure both below and above the phase transition temperature. On the neutron diffraction patterns, the disappearance of (141) and (413) reflections above the phase transition temperature confirmed the phase transition from *Pmcn* to *Cmcm*. The Rietveld refinement method was performed on the diffraction patterns at different temperatures. It was concluded that the phase transition upon cooling is mainly due to the off-center shifts of Nb^{5+} and one third of the La^{3+} and Nd^{3+} ions within their corresponding polyhedra. As a result, two neighboring Nb^{5+} ions along [001] displace in an antiparallel manner parallel to [010]. The same thing also happens in the displacement of 8-coordinated Ln^{3+}. Because of the antiparallel manner, the net dipoles produced by the off-center displacements sum to zero. Therefore, these two materials

may be potential antiferroelectrics. The key difference of these two from Gd_3NbO_7 is that in the latter there is net dipole moment along [010].

10.1.3 Dielectric Properties

The different structures show different dielectric behavior as a function of temperature. The dielectric permittivity of defect fluorite Ln_3NbO_7 (Ln^{3+} = Dy^{3+}, Er^{3+}, Yb^{3+}, and Y^{3+}) increases with increasing temperature from 20 K to 475 K. The TCC increases with the decreasing ionic radius of Ln^{3+}. Weberite-type Ln_3NbO_7 (Ln^{3+} = La^{3+}, Nd^{3+}, and Gd^{3+}) exhibit dielectric relaxation. The temperature where the maximum permittivity occurs is close to the phase transition temperature. Above $T(\varepsilon_m)$, the TCC is negative with its value also increasing with decreasing Ln^{3+} in weberite-type Ln_3NbO_7. An Arrhenius-type function was used to model the relaxation behavior for Gd_3NbO_7. The resulting activation energy is 0.45 eV and the attempt frequency is 1.5×10^{11} Hz. $Ln_2Ln'NbO_7$ (except Gd_2YbNbO_7) demonstrate dielectric relaxation as well. However, the temperature where the maximum of permittivity occurs in $Ln_2Ln'NbO_7$ is a much lower than in the weberite-type Ln_3NbO_7. $Ln_2Ln'NbO_7$ has smaller variation of T_m as a function of frequency. The relaxation behavior was modeled by the Arrhenius function for $Ln_2(Ln'Nb)O_7$. The activation energy of all the $Ln_2(Ln'Nb)O_7$ compounds is lower than that of Gd_3NbO_7. $Nd_2(YbNb)O_7$ has the lowest activation energy, 0.04 eV.

The experimentally determined room temperature dielectric permittivity for Ln_3NbO_7 ranges between 29 and 45, at 1 MHz. Gd_3NbO_7 has a higher room temperature permittivity than Nd_3NbO_7, probably because the former has a more open structure. As for $Ln_2Ln'NbO_7$, the compounds with more polarizable Ln^{3+} ions have higher permittivity at all measured temperatures (from 20 K to 350 K).

10.1.4 IR

The low temperature phase of Gd_3NbO_7 has 53 IR active modes and the high temperature phase has 30 IR active modes based on the nuclear site group analysis. A four-parameter oscillator model was used to fit the reflectivity at different temperatures. A total of 33 oscillators were used to fit the 10 K spectrum, 24 oscillators were used for the 300 K spectrum, and only 18 oscillators were required to fit the 600 K spectrum. The dielectric properties measured by terahertz transmission spectrometer were used to normalize the reflectivity. The dielectric properties at three temperatures were calculated from the oscillator fit from 20 cm-1 up to 650 cm^{-1}. The calculated static permittivity as a function of temperature maintains the shape with 1 MHz permittivity. The dielectric contribution from the 450 cm^{-1} mode, which disappears above the phase transition temperature, is less than 2% from the total dielectric permittivity.

10.1.5 Structure-Dielectric Property Relationship

For weberite-type Ln_3NbO_7, the origin of dielectric relaxation is the phase transition. $T(\varepsilon_m)$, where the maximum permittivity occurs, increases with the increasing off-center shifts of the 8-coordinated $Ln1^{3+}$: Nd_3NbO_7 has the highest $T(\varepsilon_m)$ and largest off-center shift; La_3NbO_7 exhibits the intermediate $T(\varepsilon_m)$ and intermediate off-center displacement; Gd_3NbO_7 with the shortest off-center shift demonstrates the lowest $T(\varepsilon_m)$. In addition, $\Delta\varepsilon'_r/\alpha$ (the normalized permittivity by the polarizability) also increases with increasing off-center shifts of the $Ln1^{3+}$. On the other hand, Gd_3NbO_7 has the most open structure while Nd_3NbO_7 has the most dense among the three compounds. The structural openness may cause an easier polarization and result in a lower $T(\varepsilon_m)$.

The real part of the permittivity of $Ln_2Ln'NbO_7$ follows the trend of the average Ln^{3+} ion polarizability, *i.e.* more polarizable ions result in higher permittivity. The crystal structure of Gd_2YbNbO_7 is intermediate between orthorhombic weberite-type and cubic defect fluorite. The dielectric behaviors of Gd_2YbNbO_7 resemble that of defect fluorite Ln_3NbO_7, other than the other $Ln_2Ln'NbO_7$. However, the real part of the permittivity of Gd_2YbNbO_7 is lower than any other defect-fluorite Ln_3NbO_7 though the former has higher ion polarizability. For $Ln_2Ln'NbO_7$ (except Gd_2YbNbO_7), the T_m generally increases with an increasing ratio of r_A (Ln^{3+}) over r_B (average of Ln'^{3+} and Nb^{5+}). However, the structural openness can lower the T_m because La_2ErNbO_7, with a more open structure, has a lower r_A/r_B but lower T_m than La_2DyNbO_7. The TCC is negative for all investigated $Ln_2Ln'NbO_7$ except Gd_2YbNbO_7. The TCC also increases with the decreasing average ionic radius of Ln^{3+}. As for the origin of dielectric relaxation, the possibility of phase transition has been ruled out by neutron diffraction at different temperatures. The origin of dielectric relaxation may be due to a cation disorder like in pyrochlores.

10.2 Future Work

10.2.1 Crystallography

The phase refinements of weberite-type Ln_3NbO_7 at different temperatures were conducted. The relationships of the crystal structure and dielectric property as well as the origin of the dielectric relaxation have been studied in more depth. By contrast, the origin of the dielectric relaxation of $Ln_2Ln'NbO_7$ is still somewhat unclear. It would be appealing to perform phase refinements on neutron diffraction patterns of $Ln_2Ln'NbO_7$ to correlate the crystal structure with dielectric relaxation. It would be interesting to see if there is cation disorder (like in pyrochlores) in $Ln_2Ln'NbO_7$. In addition, TEM and high

resolution-TEM studies may provide additional structural information to help develop a better understanding of the crystal structure.

10.2.2 Thin films of Ln_3NbO_7 (Ln^{3+} = La^{3+}, Nd^{3+}, and Gd^{3+})

In Chapter 6, it indicates that Gd_3NbO_7 is an incipient ferroelectric with [010] polar axis. There are also correlated antipolar displacements perpendicular to the polar axis. However, some preliminary tests of bulk Gd_3NbO_7 (piezoelectric activity and polarization hysteresis) have not yielded significant insight in this respect. The d_{33} value measured using Piezoelectric Meter by KCF technologies shows almost zero. The polarization *vs.* the electric field indicates a linear dielectric, no hysteresis loop. It can be argued that the effect of the net dipole is too small to be detected for bulk Gd_3NbO_7. The net dipole is only in [010] direction. The fabrication of thin films especially epitaxial films will enable a better control of the domains.

It will also be interesting to study the thin films of Nd_3NbO_7 and La_3NbO_7. In Chapter 7, there are antiparallel displacements of the Nb^{5+} and $Ln1^{3+}$ ions. These two materials are potential antiferroelectrics. A typical hysteresis loop for an antiferroelectric material is shown in Figure 10-1. The polarization undergoes a double hysteresis loop if the applied field above the critical field. It is reasonable to expect that the critical (coercive) field for bulk materials is too high to be realized. Therefore, it will be interesting to grow Nd_3NbO_7 and La_3NbO_7 thin films to make the critical field achievable to see whether the antiparallel displacements result in antiferroelectric behavior.

10.2.3 Dielectric Properties

Recent developments in electronic technologies extensively demand ceramics with good dielectric properties. The good properties include high dielectric constant, low

dielectric loss and low temperature coefficient of capacitance (TCC). In general $Ln_2Ln'NbO_7$ has the smallest TCC and weberite-type Ln_3NbO_7 tends to have highest TCC among the investigated compounds. It will be interesting to delve on why TCC has such a trend, which may give an insight on how to predict or even control TCC.

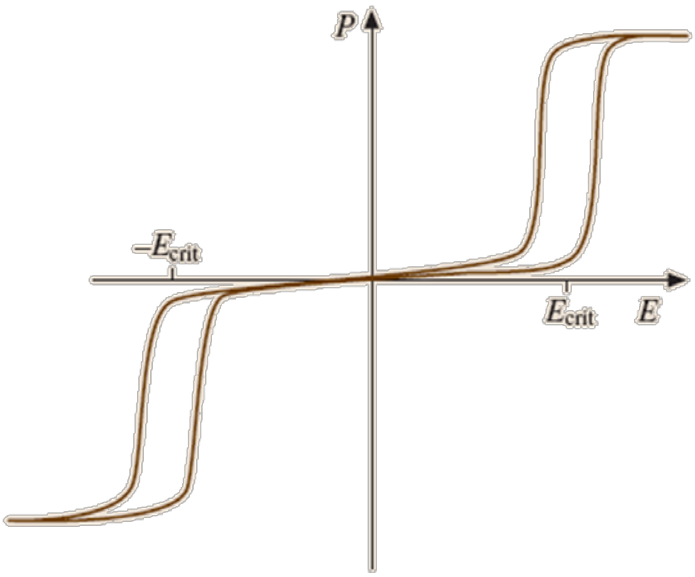

Figure 10-1. A typical hysteresis loop for an antiferroelectric material.[112] E_{crit} is the critical field.

There is an increasing need for the applications of dielectric materials at microwave frequencies. The dielectric properties investigated were focused on the frequency range 1 kHz to 1 MHz. Only the dielectric properties of Gd_3NbO_7 have been studied at GHz range. It would be compelling to investigate the dielectric properties at microwave frequency for the rest Ln_3NbO_7 and $Ln_2Ln'NbO_7$ to shed light on controlling dielectric properties at microwave frequencies through crystal structure. It will also be interesting to see how frequency will influence the dielectric relaxation.

APPENDIX A

DIELECTRIC RELAXATION IN THE $CaO\text{-}TiO_2\text{-}Nb_2O_5$ PYROCHLORE AND SYNTHESIS OF PYROCHLORE FILMS BY PULSED LASER DEPOSTION Deposition (PLD)

The core of the first section of the appendix is chiefly based on the journal article (Journal of the Solid State Chemistry ***181****(3) 406-414 (2008)) titled "Pyrochlore formation, phase relations, and properties in the* $CaO\text{-}TiO_2\text{-}(Nb,Ta)_2O_5$ *systems" by R.S. Roth, T.A. Vanderah, P.Bordet, I.E. Grey, W.G.Mumme, L.Cai, and J.C. Nino. It is reprinted with permission from* Elsevier*.*

Bi-based pyrochlores are among the most studied compounds in the family of fluorite-related structures due to their interesting dielectric properties. Generally, these compounds exhibit dielectric relaxation. Given that bismuth is the dominant element on the *A* site of Bi-based pyrochlores, it was speculated that the observed relaxor dielectric behavior was associated to the presence of Bi (with its lone electron pair). However, in collaboration with NIST, CNRS, and CSIRO, it was shown that a displacive cubic pyrochlore not containing bismuth, namely $Ca_{1.469}Ti_{1.469}Nb_{1.037}O_7$, also displays dielectric relaxation.

The first section of the appendix discusses dielectric properties of $Ca_{1.469}Ti_{1.469}Nb_{1.037}O_7$. The second section shows the continuing work on $Ca_{1.469}Ti_{1.469}Nb_{1.037}O_7$ pyrochlore; namely, the growth of $Ca_{1.469}Ti_{1.469}Nb_{1.037}O_7$ and $Bi_{1.657}Fe_{1.092}Nb_{1.15}O_7$ pyrochlore thin films by pulsed laser deposition (PLD).

A.1 Dielectric Relaxation in $CaO\text{-}TiO_2\text{-}Nb_2O_5$ pyrochlore

Preliminary capacitance measurements of Ca-Ti-Nb-O and Ca-Ti-Ta-O pyrochlores[165] suggested that both phases exhibited dielectric relaxation. resembling

that observed in bismuth pyrochlores (e.g. Bi-Zn-Nb-O[166-169] and Bi-Fe-Nb-O[170]). The real and imaginary parts of the relative permittivity for a pyrochlore specimen of composition 42.5:42.5:15.0 CaO : TiO_2 : Nb_2O_5 ($Ca_{1.469}Ti_{1.469}Nb_{1.037}O_7$) are shown in Figure A-1 as a function of temperature and frequency from 1 kHz to 1 MHz. This composition lies slightly outside the single-phase pyrochlore region. The sample contained a just-detectable amount of rutile (on the order of 1-2%). Remarkably, a dielectric relaxation characteristic of bismuth-based pyrochlores is clearly observed,[167] that is, with increasing measuring frequency the peak of the imaginary part of permittivity shifts towards higher temperatures and the width and maximum of the imaginary part of permittivity peak increases. At 1 MHz, the Ca-Ti-Nb-O pyrochlore exhibits a maximum relative dielectric permittivity of ≈ 107 at 200 K, and the peak of the imaginary part of permittivity occurs at $T_m \approx 150$ K. When compared with the bismuth niobate pyrochlores, the Ca-Ti-Nb-O analog exhibits a higher T_m but a lower dielectric constant. To better understand the phenomenon, the Arrhenius function was used to model the relaxation behavior. T_m was determined for each measuring frequency by fitting the peak of the imaginary part of the relative permittivity to a Gaussian function. The resulting Arrhenius plot is shown in Figure A-2. From the linear fit, $v_0 = 4.6 \times 10^{14}$ Hz and the activation energy E_a is 0.32 eV. Both the attempt-jump frequency and the activation energy are higher than those of Bi-based pyrochlores.[166-167] Previously, the attempt-jump frequency which drives the relaxation has been correlated with that of the O´–A–O´ bending phonon mode.[168] Since the A-site atoms in Ca-Ti-Nb-O pyrochlore (Ca and Ti) are lighter than those in Bi-based pyrochlores (primarily Bi), higher frequencies for the O´–A–O´ bending phonon mode and the attempt-jump frequency are

therefore expected. Although the activation energy for the Ca-Ti-Nb-O pyrochlore is higher than that observed for the bismuth pyrochlores (e.g. for Bi-Zn-Nb-O $E_a \approx 0.14$ eV), it is lower than that weberite-type Gd_3NbO_7 ($E_a \approx 0.45$ eV) as discussed in Chapter 5.[171]

The Ca-Ti-(Nb,Ta)-O pyrochlores, like the bismuth analogs, exhibit substantial displacive disorder in their A_2O' sub-networks. Observation of dielectric relaxation in these systems suggests, for the first time, that it arises from the displacive disorder and is not necessarily associated with the presence of polarizable lone-pair cations such as Bi^{3+}. This observation suggests that further investigations may result in a fundamental change in the understanding and analysis of dielectric relaxation in all fluorite-related materials.

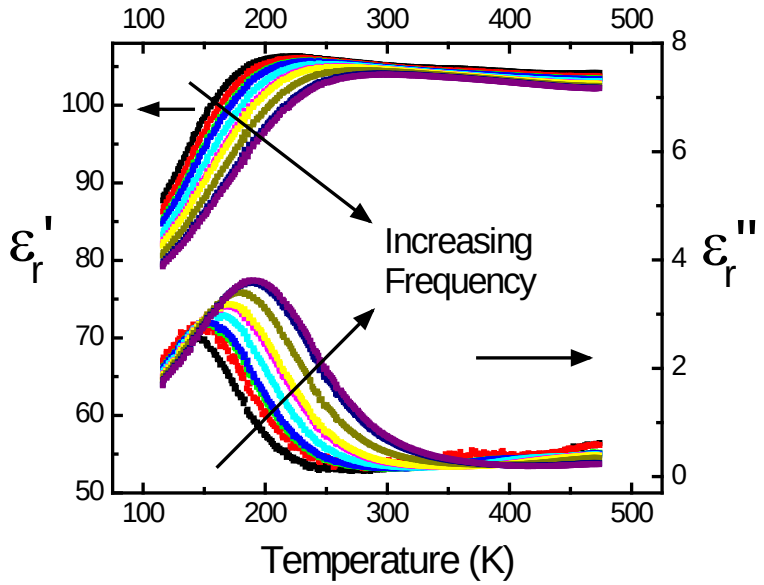

Figure A-1. The real part (ε_r') and imaginary parts of permittivity (ε_r") for a pyrochlore specimen 42.5:42.5:15.0 $CaO:TiO_2:Nb_2O_5$, measured at (from left to right) 1 kHz, 3 kHz, 8 kHz, 10 kHz, 30 kHz, 80 kHz, 100 kHz, 300 kHz, 800 kHz and 1 MHz.

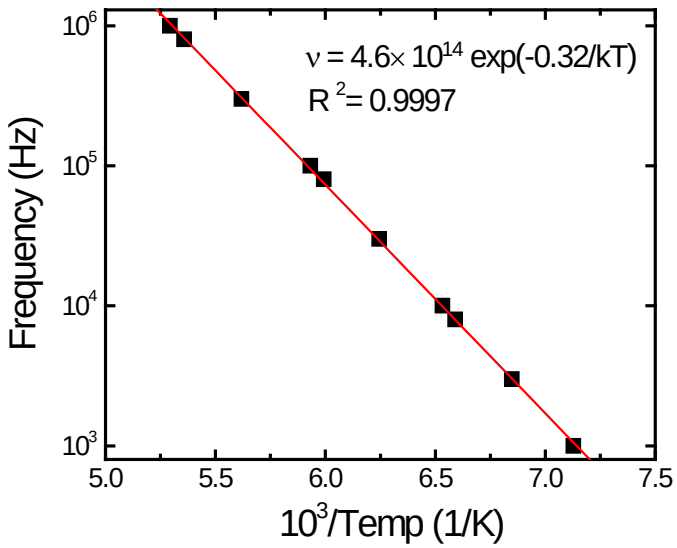

Figure A-2. Arrhenius plot of measuring frequency and T_m. The equation for the linear least squares fit is given along with the goodness of the fit.

A.2 $Ca_{1.469}Ti_{1.469}Nb_{1.037}O_7$ and $Bi_{1.657}Fe_{1.092}Nb_{1.15}O_7$ pyrochlore films

Due to the interesting dielectric properties of $Ca_{1.469}Ti_{1.469}Nb_{1.037}O_7$, deposition and growth of thin films of this material as well as another Bi-based pyrochlore, $Bi_{1.657}Fe_{1.092}Nb_{1.15}O_7$, were performed. This section is focused on the film growth using pulsed laser deposition (PLD) and phase formation.

Ceramic targets for laser ablation were synthesized by conventional solid state processing as discussed in Chapter 3. The calcination temperature for $Ca_{1.469}Ti_{1.469}Nb_{1.037}O_7$ was 1573 K. Multiple calcinations, each with an extended soaking time, were used but the secondary phases $CaTiO_3$, TiO_2, and $Ca_5Nb_4Ti_3O_{21}$ (CNT) were still present. Figure A-3 shows the XRD of the target which was calcined at 973 K for 4 h, followed by calcinations at 1273 K for 8 h, 1373 K for 8 h, 1473 K for 8 h, 1573 K for 4 h, 1573 K for 12 h, and 1573 K for 24 h. $Ca_{1.469}Ti_{1.469}Nb_{1.037}O_7$ thin films were grown on the <100> Si wafer under the growth conditions: 673 K – 723 K

substrate temperature, 10 Hz laser frequency, energy 600 mJ, and 100 mTorr oxygen pressure (Figure A-3). The phase formation was strongly dependent on the annealing temperature. The films were amorphous when the annealing temperature was below 973 K. Phase pure pyrochlore was formed when annealed at 973 K for 0.5 h. However, the pyrochlore phase decomposed if annealed for longer times. As shown in Figure A-4, after annealing at 973 K for 2 h, the CNT phase appears.

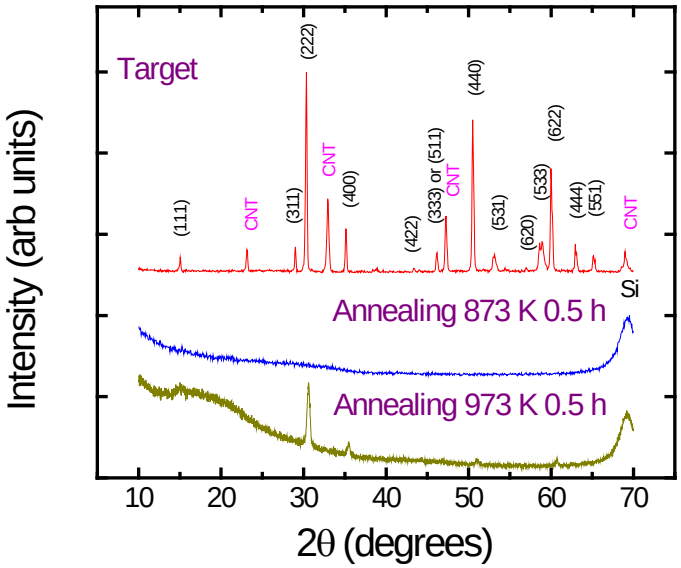

Figure A-3. XRD of the $Ca_{1.469}Ti_{1.469}Nb_{1.037}O_7$ target and the films annealed at 873 K and 973K, respectively. CNT stands for $Ca_5Nb_4Ti_3O_{21}$.

The $Bi_{1.657}Fe_{1.092}Nb_{1.15}O_7$ target was also synthesized by solid state processing with a calcination temperature of 1273 K for 12 h. The thin films of $Bi_{1.657}Fe_{1.092}Nb_{1.15}O_7$ with preferred orientations were successfully produced on the <100> Si wafer under growth conditions: 673 K – 723 K substrate temperature, 10 Hz laser frequency, energy 250 mJ, and 100 mTorr oxygen pressure. The annealing temperature was 973 K for 0.5 h. As shown in Figure A-5, the preferred orientation is (111).

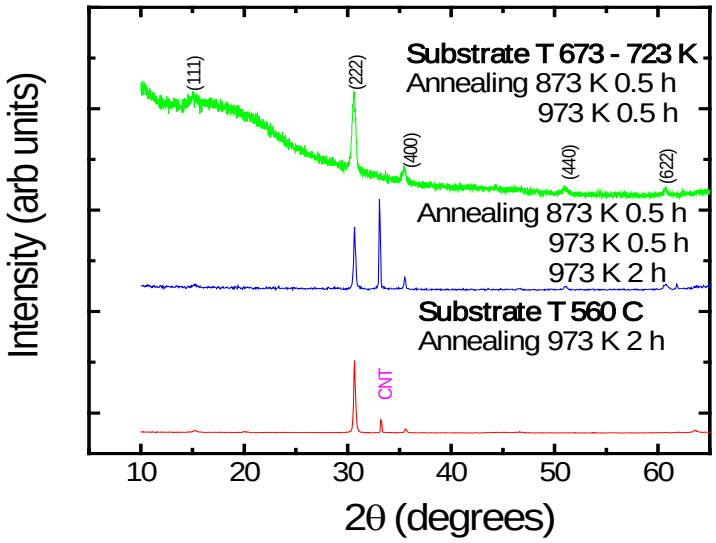

Figure A-4. XRD of the $Ca_{1.469}Ti_{1.469}Nb_{1.037}O_7$ films at different annealed temperature and time.

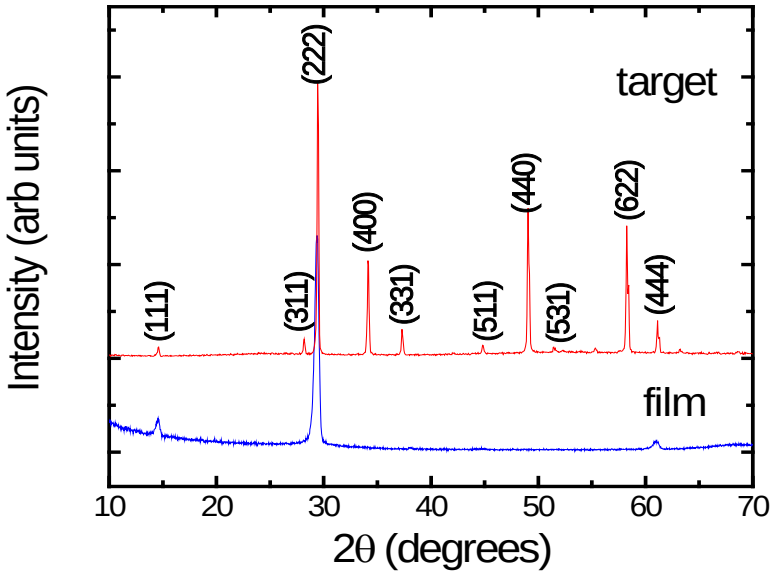

Figure A-5. XRD of the $Bi_{1.657}Fe_{1.092}Nb_{1.15}O_7$ target and film.

APPENDIX B

SUPPLEMENT INFORMATION FOR INFRARED SPECTROSCOPY

As stated in Chapter 6, two independent experiments were performed to measure the IR of Gd_3NbO_7 by Daniel Arenas in Professor Tanner's lab at University of Florida and Veronica Goian in Professor Kamba's lab at Institute of Physics of the AS CR, Republic. The first part of the appendix is to show the comparison between the two experiments. As shown in Figure B-1, Figure B-2, and Figure B-3, observable vibrational modes match well with each other at all three temperatures.

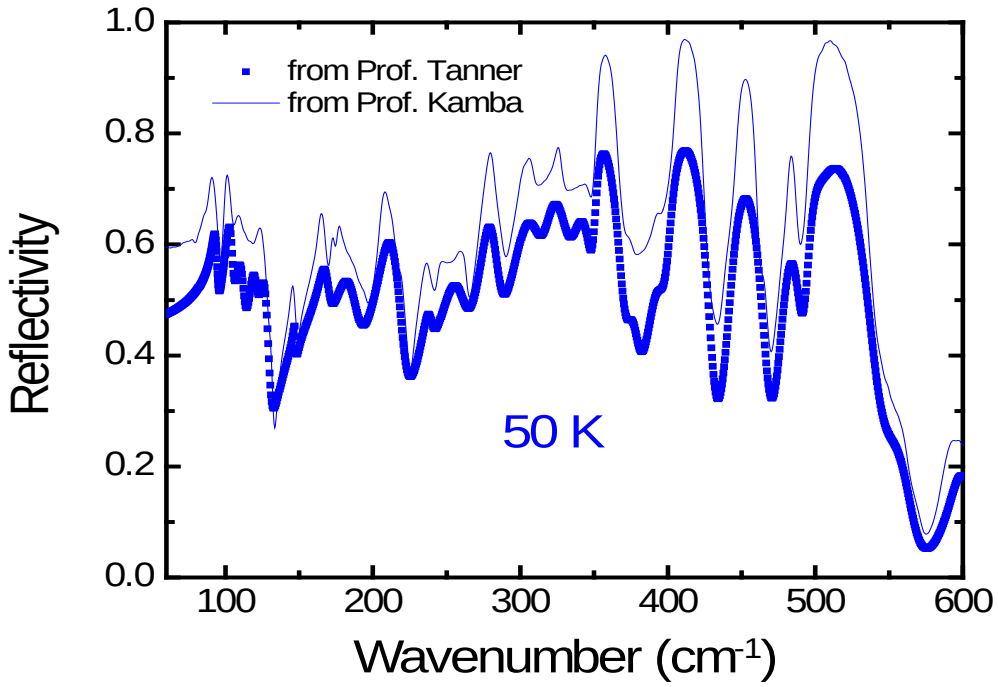

Figure B-1. Infrared reflectivity of Gd_3NbO_7 at 50 K.

The normal determination of the fluorite structure was shown in Chapter 2. The normal mode determination table for the RT Ln_3NbO_7 (Ln^{3+} = Nd^{3+} and La^{3+}) phase are presented in Table B-1.

Table B-1. Normal mode determination for RT La_3NbO_7 and Nd_3NbO_7 phase with space group *Pmcn*.

	Site Symmetry	A_g	A_u	B_{1g}	B_{1u}	B_{2g}	B_{2u}	B_{3g}	B_{3u}
Ln1	C_1 (8*d*)	3	3	3	3	3	3	3	3
Ln2	C_s^{xz} (4*c*)	2	1	1	2	2	1	1	2
Nb	C_s^{xz} (4*c*)	2	1	1	2	2	1	1	2
O1	C_1 (8*d*)	3	3	3	3	3	3	3	3
O2	C_s^{xz} (4*c*)	2	1	1	2	2	1	1	2
O3	C_1 (8*d*)	3	3	3	3	3	3	3	3
O4	C_1 (8*d*)	3	3	3	3	3	3	3	3
Acoustic Modes		0	0	0	1	0	1	0	1
Lattice Modes		18	15	15	17	18	14	15	17
Selectrion Rules		Raman	Inactive	Raman	IR	Raman	IR	Raman	IR

The irreducible representation for the RT La_3NbO_7 and Nd_3NbO_7 phase can be written as

$$\Gamma = 18A_g(R) + 15A_u(-) + 15B_{1g}(R) + 17B_{1u}(IR) + 18B_{2g}(R) + 14B_{2u}(IR) + 15B_{3g}(R) + 17B_{3u}(IR) \quad \text{B-1}$$

There are totally 66 Raman modes and 48 IR modes.

The infrared spectra of Nd_3NbO_7 and Sm_3NbO_7 are shown in Figure B-4 and Figure B-5. Classical damped harmonic oscillator model was used to fit the reflectivity:

$$\varepsilon(\omega) = \varepsilon_\infty + \sum_{j=1}^{n} \frac{\Delta\varepsilon_j \omega_j^2}{\omega_j^2 - \omega^2 + i\omega\gamma_j} \quad \text{B-2}$$

$$R(\omega) = \left| \frac{\sqrt{\varepsilon(\omega)} - 1}{\sqrt{\varepsilon(\omega)} + 1} \right|^2 \quad \text{B-3}$$

where ε_∞ is the permittivity at frequencies much higher than all oscillator eigenfrequencies, and ω_j, $\Delta\varepsilon_j$, and γ_j, is the frequency, dielectric strength, and damping constant of the jth phonon mode. The ASF program developed in Professor Kamba's lab was used for the fitting. The fitting parameters are listed in Table B-2and Table B-3.

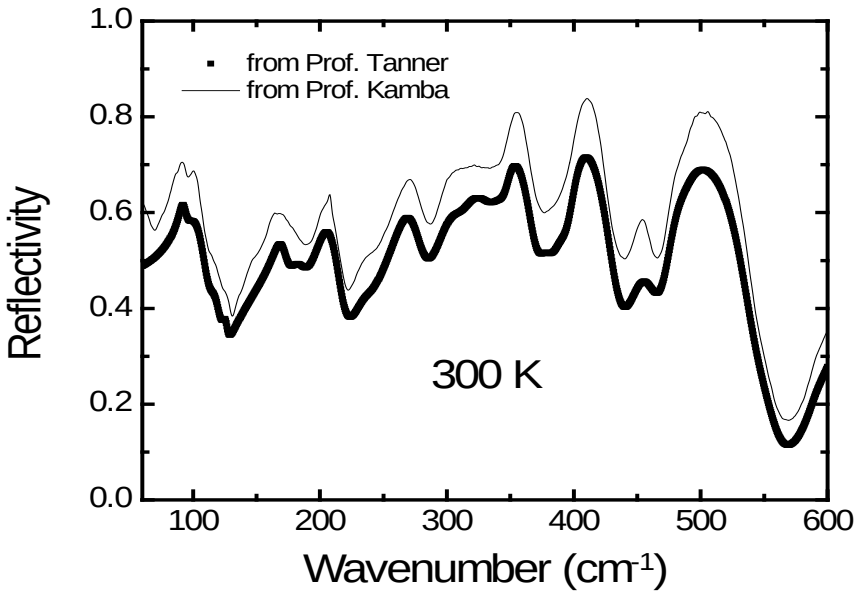

Figure B-2. Infrared reflectivity of Gd_3NbO_7 at 300 K.

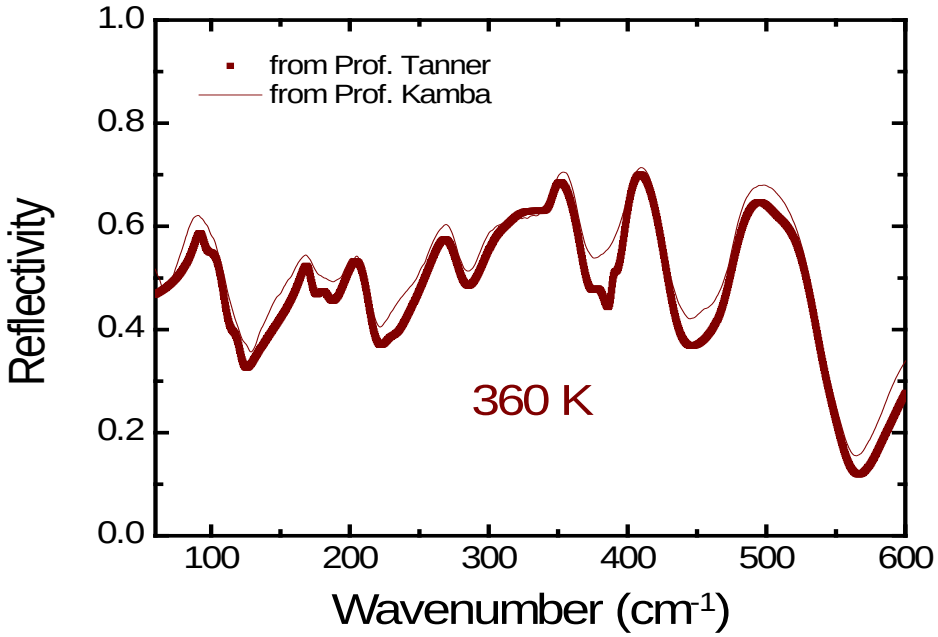

Figure B-3. Infrared reflectivity of Gd_3NbO_7 at 360 K.

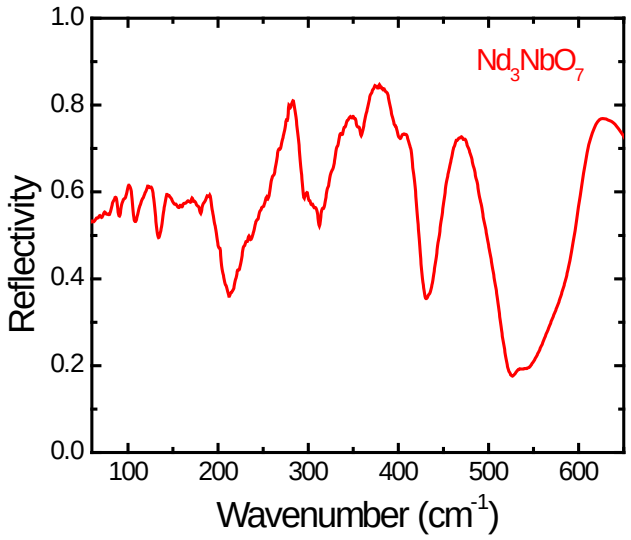

Figure B-4. Infrared reflectivity of Nd_3NbO_7 at room temperature.

Table B-2. Fitting Parameters for the reflectivity of Nd_3NbO_7

No.	ω (cm^{-1})	$\Delta\varepsilon$	γ (cm^{-1})
1	87.3629	1.1449	6.3491
2	102.6504	2.7107	8.5883
3	124.2524	4.2161	13.1363
4	145.4279	0.9907	7.1971
5	154.2582	1.8858	16.987
6	169.1808	2.676	20.5542
7	188.0656	3.0567	23.9089
8	265.7592	3.6556	19.3056
9	274.9751	2.3809	8.9648
10	300.8369	0.3052	12.6338
11	330.6909	1.6095	66.6918
12	330.9352	3.0274	27.5672
13	362.1505	0.2396	9.8237
14	447.9323	0.5565	22.7981
15	547.5186	0.2411	67.0734
16	577.5773	0.2742	29.2296
17	596.9123	0.2982	17.3937
18	770.0724	0.0555	85.305

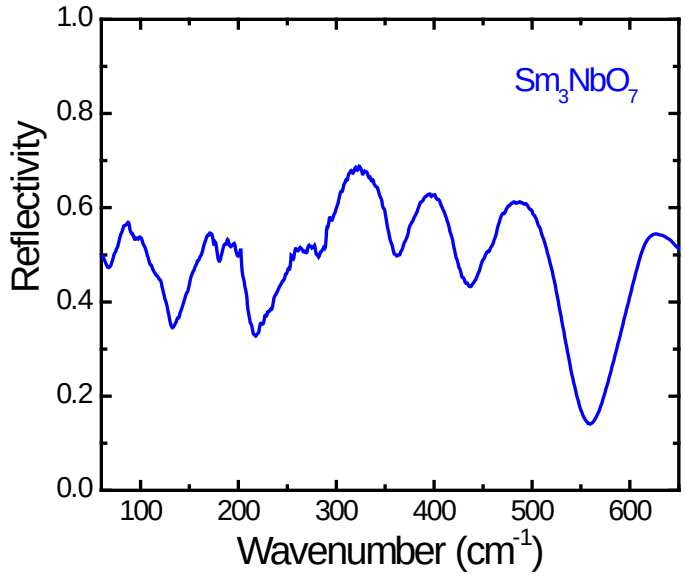

Figure B-5. Infrared reflectivity of Sm_3NbO_7 at room temperature.

Table B-3. Fitting Parameters for the reflectivity of Sm_3NbO_7

No.	ω (cm^{-1})	$\Delta\varepsilon$	γ (cm^{-1})
1	58.191	1.4608	13.3498
2	97.4834	7.2269	26.1808
3	119.395	1.1884	15.7315
4	172.7618	1.3772	11.7609
5	194.2726	2.7549	23.4876
6	267.5433	0.9934	20.7065
7	311.418	5.8778	38.4904
8	380.7177	1.618	40.7026
9	457.5484	1.094	53.3473
10	600.7356	0.59	43.3216
11	785.3206	0.0504	89.8245

APPENDIX C

THE TOLERANCE FACTORS OF PYROCHLORE

The tolerance factor (*t*) concept, widely used in crystallochemical analysis of perovskites ABO_3, is here applied to $A_2B_2O_7$ fluorite-derivative superstructure: pyrochlores. Based on geometrical considerations of the different cation coordination polyhedra two tolerance factors for pyrochlores are introduced in this appendix. The *t* values were calculated for 315 pyrochlores. A stability field is proposed to distinguish $A^{2+}{}_2B^{5+}{}_2O_7$ pyrochlores from $A^{2+}{}_2B^{5+}{}_2O_7$ weberites. A relationship between the tolerance factors and dielectric properties is also discussed.

C.1. Introduction

The tolerance factor (*t*) concept was first introduced by Goldschmidt[172] in 1926 and it is routinely used analyze structure-property relations of ceramics with the perovskite crystal structure (ABO_3). The tolerance factor is a geometrical parameter that provides a measure of how well the *A*-site cation fits the twelve-fold coordinated space within the corner-shared octahedral network formed by the *B*-site cation. Based on the ionic radii and assuming a sphere model where anions and cations are touching, *t* for perovskites can be expressed as:

$$t = \frac{1}{\sqrt{2}} \frac{r_A + r_O}{r_B + r_O} \qquad \text{C - 1}$$

where r_A, r_B, r_O are ionic radii of *A*, *B*, and oxygen ions, respectively. The constant $1/\sqrt{2}$ is a geometric factor, which is the ratio of the *B*-O bond length (half of the lattice parameter) over the *A*-O bond length (1/2 of the face diagonal). The tolerance factor is 1.0 for the ideal perovskite structure. The closer *t* is to unity, the greater is the stability of the structure. The application of the *t* is not only limited to providing an indication of the

structural stability but also to providing key information about the physical properties. For example, Reaney *et al.*[173] determined there is a relationship between the *t* and the temperature coefficient of the dielectric permittivity (τ_ε) in Ba- and Sr-based perovskites. Suarez *et al.*[174] concluded that the temperature T_c (paraelectric-to-ferrroelectric phase transition temperature) decreases as the *t* increases in Aurivillius phases (perovskite-related).

There have been very few attempts to extend the tolerance factor concept (*t*) to other crystal structures. Perhaps more notable, is the attempt at introducing it for the pyrochlore structure ($A^{VIII}{}_2B^{VI}{}_2O_7$) by Isupov[175] in 1958. On the assumption that the BO_6 were perfect octahedra, he determined the tolerance factor to be:

$$t = 0.866\frac{r_A + r_O}{r_B + r_O} \qquad \text{C - 2}$$

However, BO_6 octahedra are almost never regular in real pyrochlores. For an ideal pyrochlore, when placing the *B* site at the origin (space group $Fd\bar{3}m$, origin 2), 6/7 of the oxygen ions are located at Wyckoff position 48*f* (*x*, 1/8, 1/8). The *x* parameter can vary from 0.3125, leading to perfect BO_6 octahedra and distorted AO_8 cube, to 0.375, leading to distorted BO_6 octahedra and regular AO_8 cube (see Figure C-1). The disregard of the *x* parameter in Isupov's tolerance factor diminishes important structural features. Therefore, in this appendix, a new tolerance factor for pyrochlores is proposed and correlated with physical properties.

C.2. Derivation of the Tolerance Factor

Following the logic of the tolerance factor for perovskites, the *t* for pyrochlores is proposed to have a similar format as below:

$$t = g\frac{r_A + r_O}{r_B + r_O} \qquad \text{C - 3}$$

where g is a geometric factor. In cubic perovskites, it is evident that the g is a constant $(1/\sqrt{2})$.

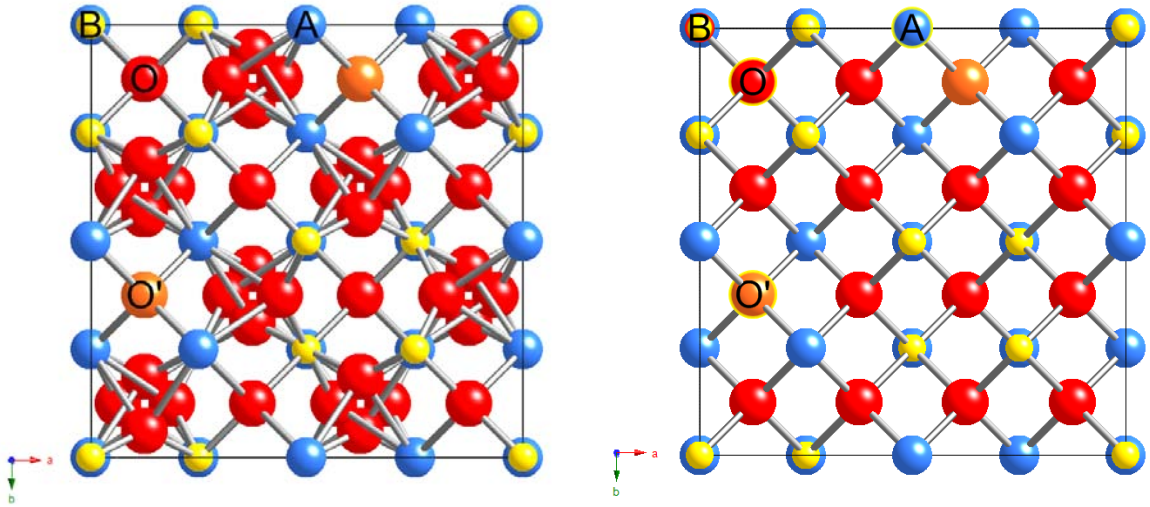

(A) (B)

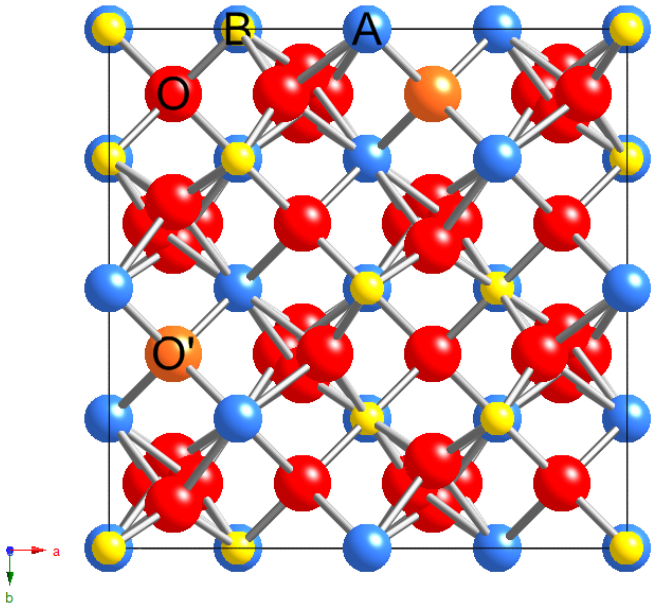

(C)

Figure C-1. [001] view of pyrochlores when (A) x = 0.3125 (perfect BO_6 octahedra) (B) x = 0.375 (perfect AO_8 cube) (C) x is between 0.3125 and 0.375 (both BO_6 octahedra and AO_8 cube distorted).

The pyrochlore structure is more complicated than the perovskite structure since the former contains more ions per unit cell. Therefore, it is easier to relate r_A+r_O and r_B+r_O in a cationic polyhedra where the oxygen ions lie inside rather than in a unit cell as in perovskites. In ideal pyrochlores, A_2B_2 tetrahedra are regular, which means the tetrahedral edges have the same length:

$$l_{A-A} = l_{B-B} = l_{A-B} = \frac{\sqrt{2}}{4}a \qquad \text{C - 4}$$

where l is the distance between the two subscripted ions and a is the lattice parameter.

$$l_{A-A} = 2l_{A-O}\sin\frac{\angle AOA}{2} \qquad \text{C - 5}$$

$$l_{B-B} = 2l_{B-O}\sin\frac{\angle BOB}{2} \qquad \text{C - 6}$$

$$2l_{A-O}\sin\frac{\angle AOA}{2} = 2l_{B-O}\sin\frac{\angle BOB}{2} \qquad \text{C - 7}$$

In a stable ionic compound, cations should contact anions, *i.e.* the distance between nearest neighboring cation and anion should be close to the summation of the two ionic radii. The tolerance factor t_1 is introduced in the following equation based on the equation C - 7:

$$(r_A + r_O)\sin\frac{\angle AOA}{2} = t_1(r_B + r_o)\sin\frac{\angle BOB}{2} \qquad \text{C - 8}$$

where r indicates the ionic radius of the subscripted ion. It is evident that $\sin(\angle AOA/2)$ and $\sin(\angle BOB/2)$ are functions of x:

$$l_{A-O} = a\sqrt{\left(x-\frac{1}{2}\right)^2 + \frac{1}{32}} \qquad \text{C - 9}$$

$$l_{B-O} = a\sqrt{\left(x-\frac{1}{4}\right)^2 + \frac{1}{32}} \qquad \text{C - 10}$$

$$\sin\frac{\angle AOA}{2} = \frac{\frac{1}{2}l_{A-A}}{l_{A-O}} = \frac{\sqrt{2}}{8\sqrt{\left(x-\frac{1}{2}\right)^2 + \frac{1}{32}}} \qquad \text{C - 11}$$

$$\sin\frac{\angle BOB}{2}=\frac{\frac{1}{2}l_{B-B}}{l_{B-O}}=\frac{\sqrt{2}}{8\sqrt{\left(x-\frac{1}{4}\right)^2+\frac{1}{32}}} \qquad \text{C - 12}$$

Therefore, the t_1 is defined as:

$$t_1=\frac{\sin\frac{\angle AOA}{2}}{\sin\frac{\angle BOB}{2}}\frac{r_A+r_O}{r_B+r_O}=\frac{\sqrt{\left(x-\frac{1}{4}\right)^2+\frac{1}{32}}}{\sqrt{\left(x-\frac{1}{2}\right)^2+\frac{1}{32}}}\frac{r_A+r_O}{r_B+r_O} \qquad \text{C - 13}$$

It is important to recall that there are two Wyckoff positions for oxygen ions in ideal cubic pyrochlores (*B* cations at the origin): O at 48*f* (*x,* 1/8, 1/8) inside A_2B_2 tetrahedra and O' 8*b* (3/8, 3/8, 3/8) inside A_4 tetrahedra (Figure C-2(A)). The discussion above has considered the tolerance factor based on A_2B_2 tetrahedra (Figure C-2(B)). It is reasonable to consider the other tolerance factor corresponding to A_4 tetrahedra. In A_4 tetrahedra, the edge length ($l_{A\text{-}O'}$) is only related to the lattice parameter (Figure C-2 (C)):

$$l_{A-O'}=a\frac{3\sqrt{3}}{8} \qquad \text{C - 14}$$

The second tolerance factor (t_2) is defined as

$$t_2=\frac{l_{A-o'}}{r_A+r_o}=a\frac{3\sqrt{3}}{8(r_A+r_O)} \qquad \text{C - 15}$$

In Isupov's tolerance factor(t_i), the *g* is 0.866, which is the ratio of $l_{A\text{-}O'}$ to $l_{B\text{-}O}$ when BO_6 is perfect octahedra (x = 0.3125).[175] The t_i ignores the importance of the *x* and the introduction of 0.866 as geometric factor is rather misleading since $l_{A\text{-}O'}$ and $l_{B\text{-}O}$ are not directly related to each other.

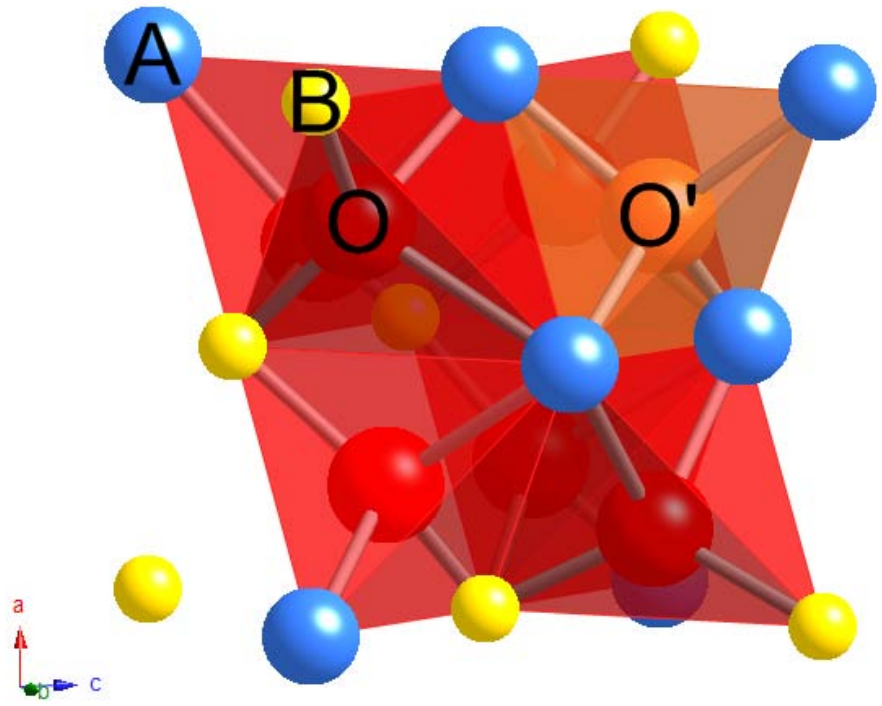

(A)

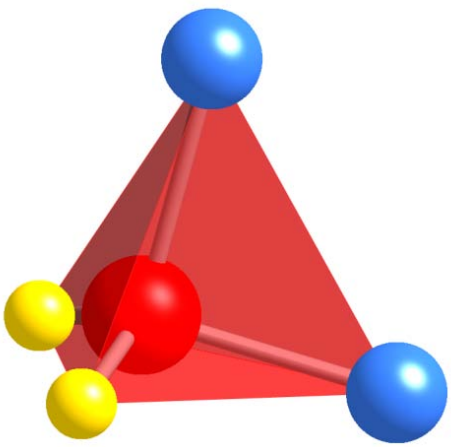

(B)

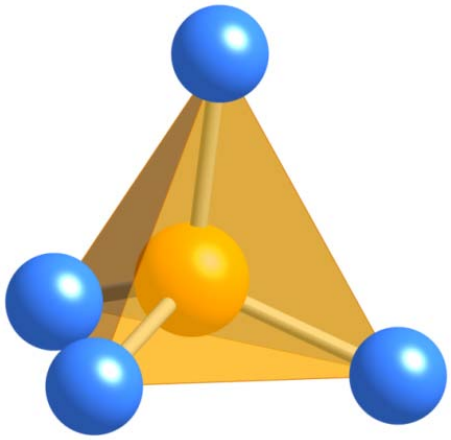

(C)

Figure C-2. (A) 1/8 pyrochlore unit cell showing cation tetrahedra (B) A_2B_2 tetrahedra with O inside (C) A_4 tetrahedra with O' in the center.

The involvement of the *x* makes the *t* more precise. However, the disadvantage is the limited availability of the *x*. Nikiforov[176] developed a mathematical relationship to

calculate the range of the unknown oxygen positional parameter *x* (O' at the origin) based on the ionic radius of *A*, *B*, and O ions.

$$\frac{1}{2} - r_o \frac{\sqrt{2}}{a} \geq x \geq \frac{2r_o}{a} \qquad \text{C - 16}$$

$$\frac{3}{8} - \frac{1}{8}\left\{3\left[\frac{(r_B + r_O)}{(r_A + r_O)}\right]^2 - 2\right\}^{\frac{1}{2}} \geq x \geq \frac{3}{8} - \left\{\left[\frac{(r_B + r_O)}{a}\right]^2 - \frac{1}{32}\right\}^{\frac{1}{2}} \qquad \text{C - 17}$$

McCauley[177] obtained the *x* by averaging the smaller of the two larger values and the larger of the two smaller values from the inequalities C - 16 and C - 17. The *x* value in above inequalities are for an origin at the O' site. The following equation can convert *x* into *B* origin lattice.

$$x(B) = \frac{5}{8} - x(O') \qquad \text{C - 18}$$

To test Nikiforov's method, in this study, the reported *x* of 76 pyrochlore compounds not satisfying the inequality C - 19 were compared with the calculated *x*.[14,39,58,71,178-211] The ionic radii used in the calculation were after Shannon.[27] The calculated *x* and the reported *x* are in good agreement (71 compounds have less than 4% difference). However, the calculated *x* of $Tl_2Pt_2O_7$ (high pressure phase)[178] and $Pr_2Te_2O_7$[179] pyrochlores have a 7%~8% difference, possibly because the ratio, Tl^{3+}/Pt^{4+}, is small (one of the smallest in pyrochlores) and Te^{4+} is large. The calculated *x* of Zr^{4+}-based pyrochlores, like $Gd_2Zr_2O_7$[39,182] (some publications refer this as defect fluorite[211-212]), $Am_2Zr_2O_7$[181], and $Sm_2Zr_2O_7$[180,184], differ by 4%-5% from the report values due to relative large ionic radius of Zr^{4+}. Table C-1. Table 10-4. lists selected pyrochlores comparing the calculated and reported *x*. It clearly shows that the reported and the calculated values match better for Ti^{4+}-based pyrochlores than Sn^{4+}-based pyrochlores,

probably due to the smaller ionic radius of Ti^{4+}.[27] It is apparent that when the ratio of r_A over r_B is small or the ionic radius of r_B is large, the discrepancy becomes larger.

Table C-1. Comparison of the *x* value from literature with calculated after Nikiforov[176]

Compound	Lattice constant (Å)	Reported x	Calculated x	difference%
Tb_2Ti_2O7[197]	10.1589	0.3281	0.3252	0.89
$Dy_2Ti_2O_7$[14]	10.1237	0.323	0.3263	1.02
$Y_2Ti_2O_7$[208]	10.0949	0.3282	0.3272	0.30
$Er_2T_{i2}O_7$[14]	10.0869	0.3293	0.3274	0.55
$Tm_2Ti_2O_7$[197]	10.0638	0.3292	0.3282	0.30
$Yb_2Ti_2O_7$[197]	10.0325	0.3309	0.3292	0.51
$Lu_2Ti_2O_7$[14]	10.0172	0.3297	0.3297	0.005
$Ho_2Ti_2O_7$[208]	10.1041	0.3285	0.3269	0.48
$Pr_2Sn_2O_7$[191]	10.6004	0.33148	0.3210	3.15
$Nd_2Sn_2O_7$[194]	10.5671	0.3322	0.3220	3.06
$Sm_2Sn_2O_7$[191]	10.5099	0.333	0.3238	2.77
$Eu_2Sn_2O_7$[191]	10.47526	0.3338	0.3248	2.69
$Tb_2Sn_2O_7$[194]	10.4235	0.3356	0.3264	2.75
$Dy_2Sn_2O_7$[194]	10.3979	0.3372	0.3271	2.99
$Y_2Sn_2O_7$[191]	10.3725	0.338	0.3279	2.99
$Ho_2Sn_2O_7$[194]	10.3726	0.3366	0.3279	2.59
$Er_2Sn_2O_7$[194]	10.3504	0.3375	0.3287	2.60
$Tm_2Sn_2O_7$[194]	10.3262	0.3382	0.3304	2.31
$Yb_2Sn_2O_7$[194]	10.3046	0.33908	0.3318	2.14
$Lu_2Sn_2O_7$[194]	10.2917	0.3397	0.3330	1.98
$Gd_2Sn_2O_7$[194]	10.45438	0.3348	0.3254	2.80
$Gd_2Ru_2O_7$[209]	10.2281	0.332	0.3247	2.20
Gd_2ScNbO_7[210]	10.4429	0.334	0.3260	2.38
Gd_2TiZrO_7[211]	10.3772	0.3281	0.3248	1.00
$Gd_2Ti_{0.5}Zr_{1.5}O_7$[211]	10.4594	0.3348	0.3254	2.80
$Gd_2Zr_2O_7$[39,182]	10.523	0.3411	0.3266	4.25

It is worth noting that Nikiforov's method does not work for some compounds. The inequalities C - 19 and C - 20 are derived from the assumption that the bond length was equal to the sum of the ionic radii. However, the bond length is less than the sum of the ionic radii for many cases. For example, all 315 of pyrochlores investigated in this work have shorter *A*-O' bond length than the sum of r_A and r_O (*i.e.* all the t_2 are smaller

than 1). For some compounds, the difference between the bond length and the sum of the ionic radii is not negligible, like $BaLaHfNbO_7$ and $PbBiSnTaO_7$ ($l_{A\text{-}O'}$ is below 0.86 of $r_A + r_O$).[39] In these cases, the following inequality results and Nikiforov's method should not be applied[177]:

$$3\left(\frac{r_B + r_O}{r_A + r_O}\right)^2 \leq 2 \qquad \text{C - 19}$$

There is however, another way to predict x which is based on the bond valence sum concept:

$$V_B = 6 \times \exp\left(\frac{l_{B-O} - R_{B-O}}{0.37}\right) \qquad \text{C - 20}$$

where $l_{B\text{-}O}$ is B-O bond length and $R_{B\text{-}O}$ is the bond-valence parameter.[52,57] For $A_2(B_yB'_{1-y})_2O_7$ ($0<y<1$) compounds,

$$V_B = 6y \times \exp\left(\frac{l_{B-O} - R_{B-O}}{0.37}\right) + 6(1-y) \times \exp\left(\frac{l_{B-O} - R_{B'-O}}{0.37}\right) \qquad \text{C - 21}$$

In this method, the bond valence sum is used on B ions to obtain the B-O bond length ($l_{B\text{-}O}$), and then x from equation C - 21.[200,213-215] In this study, a valence sum prediction method is used to calculate x for those compounds which do not have a reported x (based on crystallographic characterization), and cannot be resolved by Nikiforov's method.

C.3. Results and Discussions

Figure C-3 (A) shows the distribution of compounds from the total 315 pyrochlores investigated based on t_1 with a grouping range of 0.01.[6,8,14,28,39,58,71,139,178-207,210,216-247] t_1 values based on the reported and calculated x values are also distinguished. t_1 values vary from 0.83 to 1.07. The majority of the t_1 values are between 0.90 and 0.99. Figure C-3 (B) indicates the distribution of the t_2. It clearly

shows that all t_2 are less than 1. This is expected because the actual bond length is less than the sum of the ionic radii. The number of compounds generally increases with increasing t_2 from 0.83 to 0.92. The distribution has a peak when the t_2 value is between 0.91 and 0.92 and decreases with increasing t_2 afterward. The t_2 values of the majority of the compounds lie between 0.89 and 0.93, which is a narrower distribution than the t_1. It is interesting to note that t_2 shows a clearer trend in its values as a function of r_A/r_B when compared with the t_1. The t_2 weakly decreases with increasing r_A/r_B, especially between t_2 values of 0.91 and 0.92. By contrast, the t_1 is rather scattered against r_A/r_B (Figure C-4).

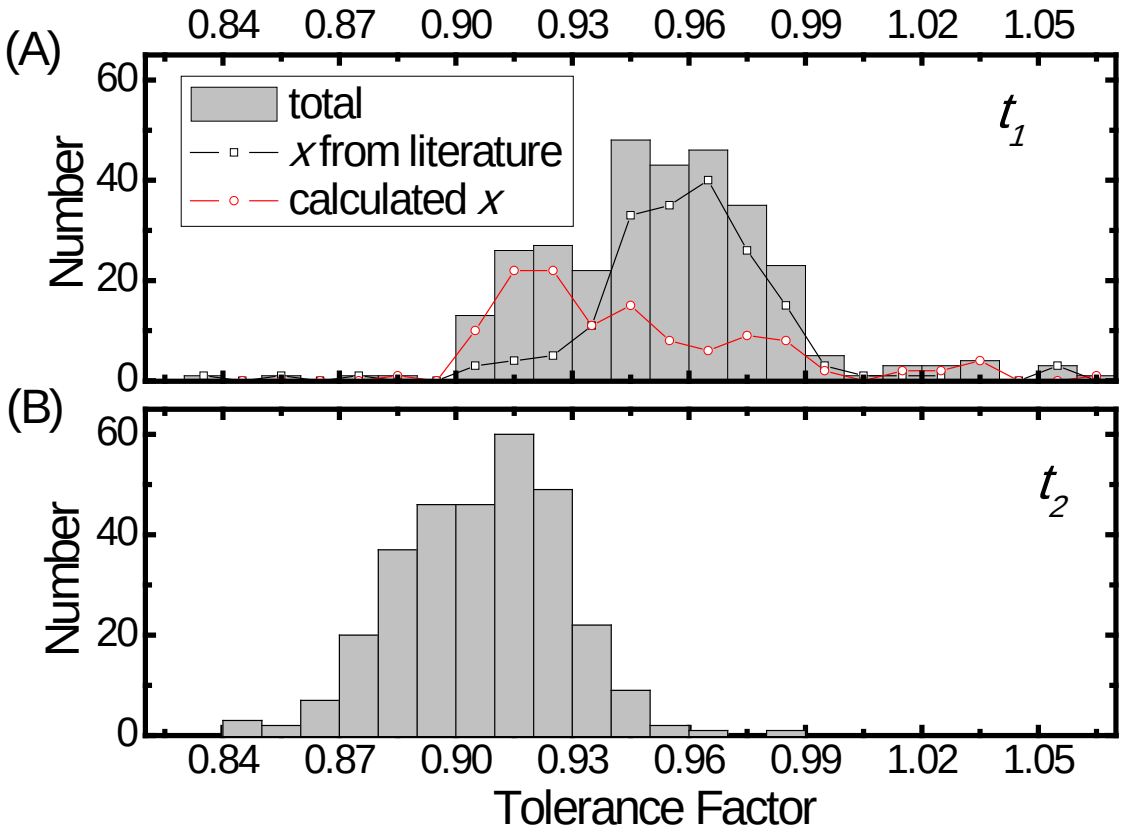

Figure C-3. The distribution of pyrochlore compounds with a grouping range of 0.01 based on (a) t_1 (distinguishing the x from literature and calculated x from the total) and (b) t_2.

One important function for tolerance factors is to determine the stability field. It is important to recall previous work on the stability field of pyrochlores: Subramanian[14] used r_A *vs.* r_B to define the stability region; Lopatin *et al.*[73,76] successfully utilized electronegativity (χ_A) and r_A/r_B to distinguish pyrochlores and weberites, another anion-deficient fluorite-related structure; Sych *et al.*[72] and Cai *et al.*[248] (as stated in Chapter 2) introduced r_A/r_B vs. relative ionicity of *A-O* bond, which is a ratio of the ionicity of *A-O* bond to the sum of ionicity of *A-O* and *B-O* bonds. Here, t_1 and r_A/r_B are used to determine the pyrochlore stability region against the weberite. t_1 has been chosen rather than t_2 for the stability field because its calculations contain more structural information. As another anion-deficient fluorite-related structure, the lattice parameters of orthorhombic weberites are approximately $\sqrt{2}/2a_p$, a_p, and $\sqrt{2}/2a_p$ (a_p is the lattice parameter of pyrochlores). The converted a_p from weberites is $(4V_w)^{0.5}$ (V_w is the unit cell volume of weberites). The x is calculated by the bond valence approach. Based on 25 orthorhombic weberite oxides, only 16 have the calculated x in the required pyrochlore range (0.3125 - 0.375).[13,54,58,72,75,100,249-252] Since there are very few, if any, $A_2^{3+}B_2^{4+}O_7$ weberites reported, the stability field is only for $A^{2+}{}_2B^{5+}{}_2O_7$ pyrochlores and weberites. As seen in Figure C-5., there is a clear separation between weberites and pyrochlores. The dashed line is for visual effect; the weberite region is found above the line. It is interesting to note that $Cd_2Sb_2O_7$ pyrochlore is close to the weberite region. Actually, $Cd_2Sb_2O_7$ can form a metastable phase of weberite, which can be fully converted to pyrochlore under high pressure.[54] In summary, weberites prefer higher t_1 and higher ratio of r_A/r_B than pyrochlores.

Due to the meaningless value of x for weberites, t_1 may not be the best way to distinguish pyrochlores and weberites. Bond ionicity is a more meaningful way to define the stability field for weberites due to the covalent nature of their bonds when compared to pyrochlores.[72-75] Nevertheless, t_1 may serve as a supplement for the calculation of the stability field.

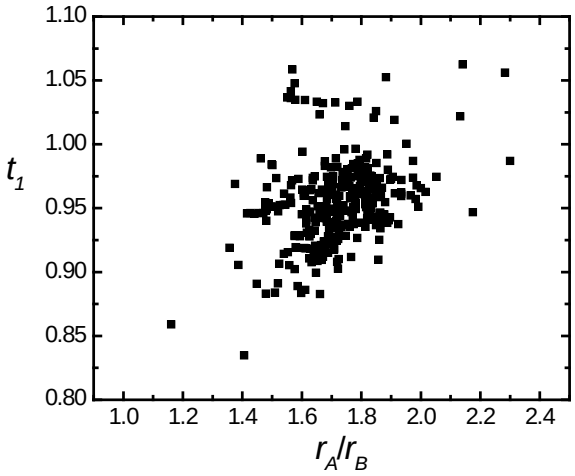

(A)

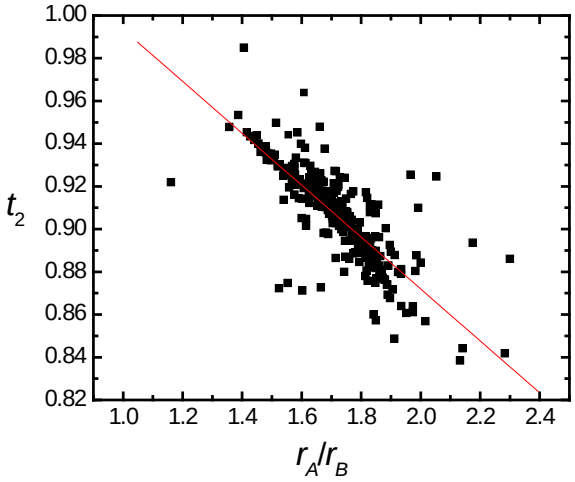

(B)

Figure C-4. (A) t_1 as a function of r_A/r_B, the ratio of the ionic radius of A over the ionic radius of B (B) t_2 as a function of r_A/r_B, with a linear regression for observation of the trend.

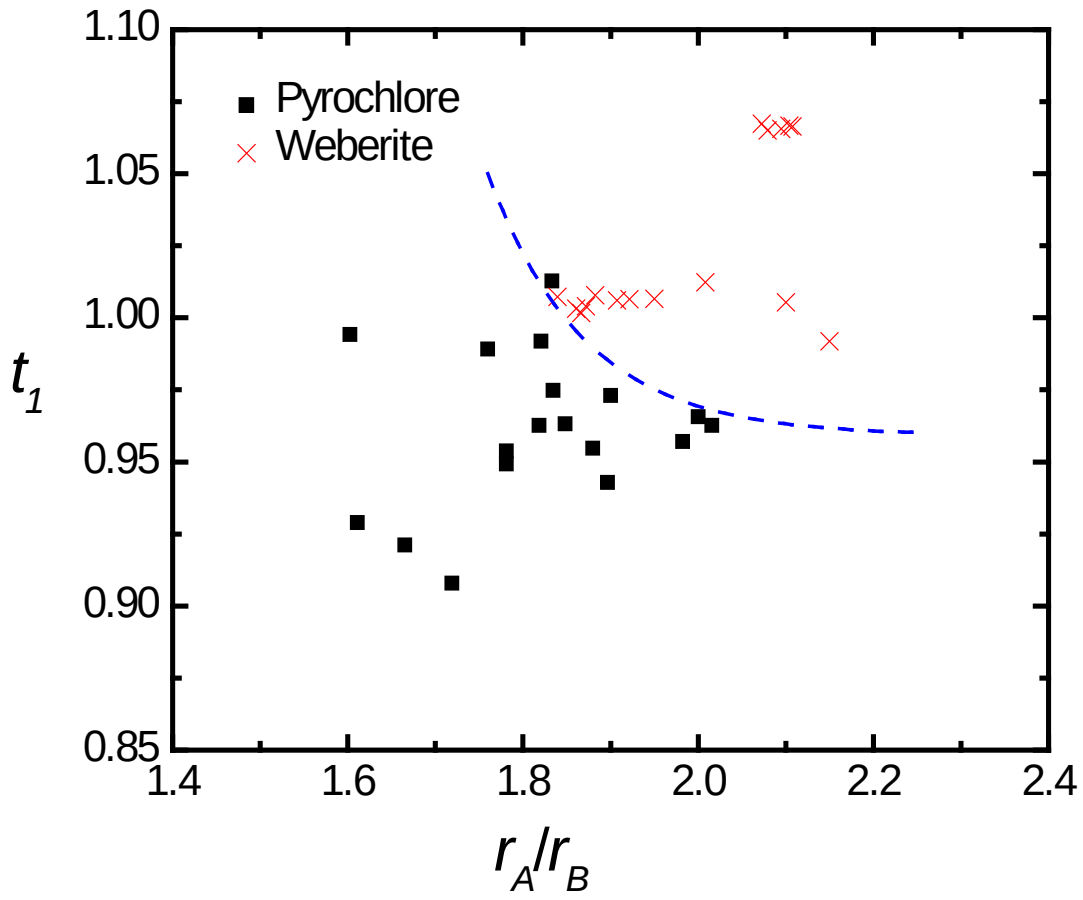

Figure C-5. t_1 as a function of r_A/r_B. The dashed line is for visual separation between pyrochlore and weberite range.

The significance of the tolerance factor in the perovskite or related structures is that *t* is related to dielectric properties, *i.e.* τ_ε and T_c.[173-174] It will be interesting to see if the *t* of pyrochlores can also have such indication. Previous work has shown that more than 60% of the total dielectric permittivity is contributed by the O'-*A*-O' bending modes in $Bi_{1.5}Zn_{0.92}NbO_{6.92}$ pyrochlore.[6,139,160] As the t_2 is closely related to *A*-O' bond length, it is reasonable to classify dielectric permittivity as a function of the t_2. The normalized difference in dielectric permittivity ($\Delta\varepsilon_n$, define below) is proposed here to correlate the t_2.

In Clausius-Mossotti relation, the macroscopic relative dielectric permittivity (ε_r) is related to microscopic polarizability (α) as follows:

$$\frac{\varepsilon_r - 1}{\varepsilon_r + 2} = \frac{4\pi N \alpha_{cgs}}{3} \qquad \text{C - 22}$$

α_{cgs} is polarizability measured in Å^3, N is the number of "molecules" per Å^3.[109] For $A_2B_2O_7$ pyrochlore,

$$\alpha_{cgs} = 2\alpha_A + 2\alpha_B + 7\alpha_o \qquad \text{C - 23}$$

α_A, α_B, and α_O can be found from Shannon's ion polarizabilities.[26] Then, the $\Delta\varepsilon_n$ is defined as

$$\Delta\varepsilon_n = \frac{\varepsilon_m - \varepsilon_r}{\alpha_{cgs}} \qquad \text{C - 24}$$

ε_m is measured permittivity (obtained from literature), ε_r is calculated permittivity based on Clausius-Mossotti relation. Figure C-6. (A) shows $\Delta\varepsilon_n$ *vs.* t_2 of the 16 pyrochlores containing Bi^{3+}, Zn^{2+}, and Nb^{5+} ions.[6,8,234,253-256] It indicates that $\Delta\varepsilon_n$ has a clear correlation to t_2, increasing with decreasing the t_2. The $\Delta\varepsilon_n$ as a function of x is also plotted in Figure C-6. (B) and there is no observable trend. It shows that dielectric permittivity may have a closer relationship with t_2 than with x, which corresponds to the experimental results that O'-*A*-O' bending modes contribute more to dielectric permittivity in $Bi_{1.5}Zn_{0.92}NbO_{6.92}$. It demonstrates the importance of the tolerance factors, not only in the geometric aspect but also in establishing a trend that will allow for the tailoring of dielectric materials based on the predicted properties.

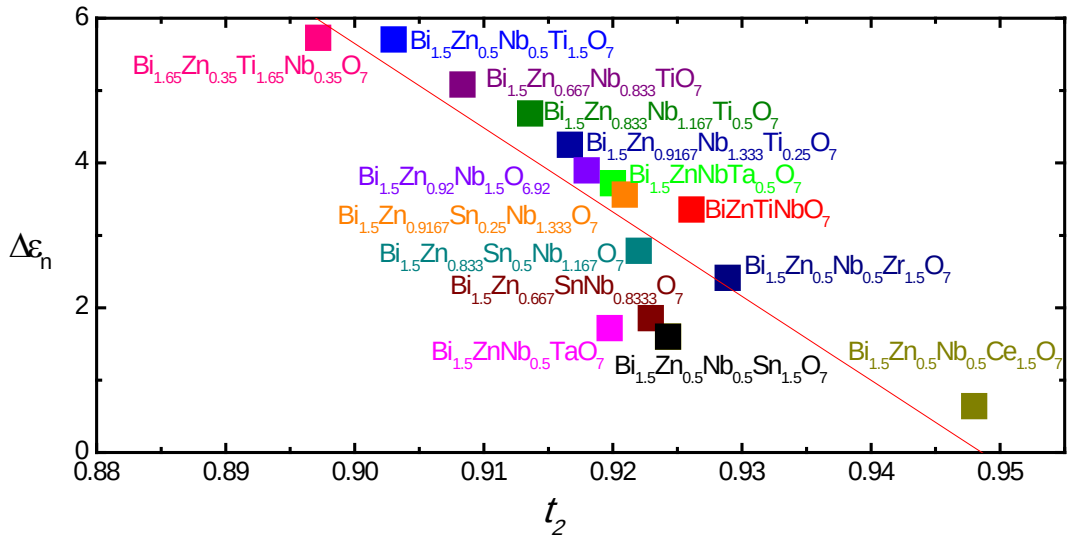

(A)

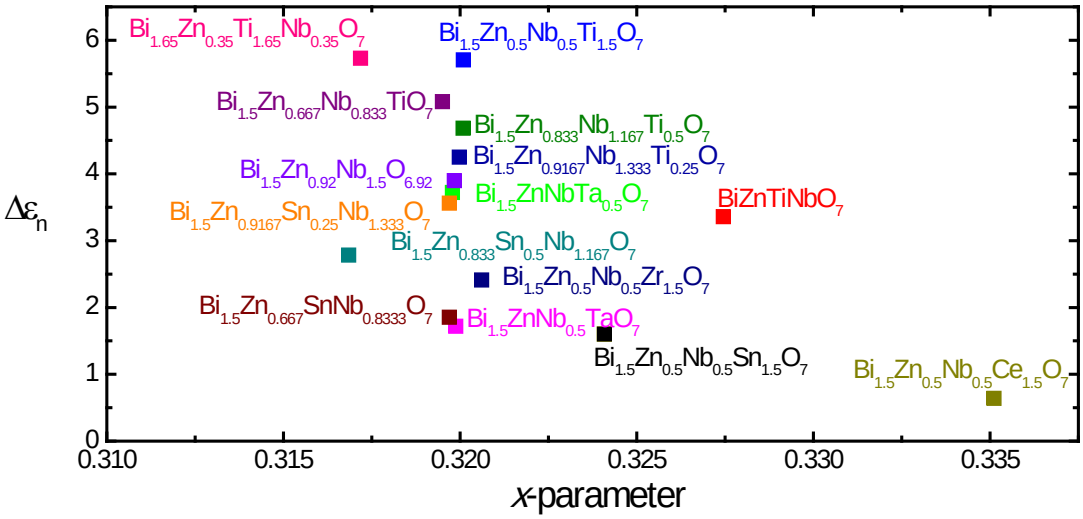

(B)

Figure C-6. (A) The normalized permittivity difference vs. t_2 with a linear regression for the observation of the trend for (Bi,Zn,Nb)-based pyrochlore. (B) The normalized permittivity difference vs. the *x*-parameter showing no observable correlation.

C.4. Conclusion

The concept of the tolerance factor has been re-introduced into the pyrochlore structure. Two tolerance factors (*t*) for pyrochlores were derived from the geometrical aspects and the positional parameter *x* has been incorporated into the calculation. The

tolerance factors were calculated for 315 pyrochlore compounds. t_1, based on the A_2B_2 cation tetrahedra (O inside), ranges from 0.83 to 1.07 with the majority of compounds lying between 0.9 and 0.99. Together with r_A/r_B, it can define the stability field for $A^{2+}{}_2B^{5+}{}_2O_7$ pyrochlores versus weberites, another fluorite-related structure. However, t_2 values, based on the lattice parameter and the ionic radius of the *A* and O' ions, are between 0.83 and 0.99, with the majority between 0.88 and 0.93. t_2 seems to have clearer trend against r_A/r_B than t_1. It is now established that the normalized dielectric difference ($\Delta\varepsilon_n$) decreases with increasing t_2 and does not have a clear trend with *x*. This provides another way from the structural point of view to predict dielectric properties, thus, increasing the fundamental understanding of structure-dielectric-property relationships and a creating a more complete picture for the behavior of dielectric materials with the pyrochlore structure.

APPENDIX D

RAMAN OF Ln_3NbO_7

This appendix introduces collaborative and independent work on Raman spectroscopy of Ln_3NbO_7. Some of issues and problems, which haven't been solved or understood, are also presented here.

The normal mode determination table for the RT Ln_3NbO_7 (Ln^{3+} = Nd^{3+} and La^{3+}) phase are presented in Appendix B. There are totally 66 Raman modes and 48 IR modes.

The Raman spectroscopy of Ln_3NbO_7 is puzzling. One interesting finding of Gd_3NbO_7 by Kovyazina *et. al.*[121] was that there was one peak at 944 cm^{-1} in Raman spectroscopy at room temperature, which disappears at the spectrum above 373 K. It was claimed to be a proof of phase transition. However, it is not repeatable in this study (Figure D-1). A laser with the same wavelength (λ = 514.5 nm) was utilized but the peak at about 944 cm^{-1} exists even at 400 K.

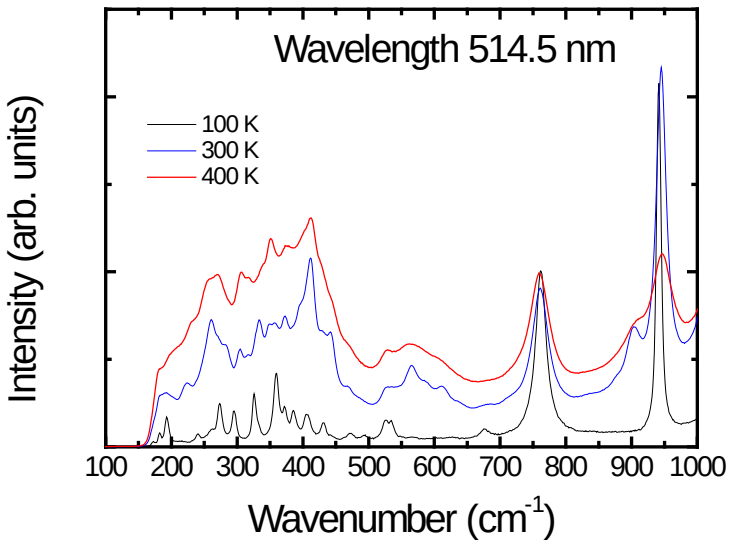

Figure D-1. Raman spectroscopy (wavelength 514.5 nm) of Gd_3NbO_7 at 100 K, 300 K, and 400 K.

Three independent experiments of Gd_3NbO_7 with green laser were performed by Daniel Arenas, in Professor Reaney's lab, and in Professor Kamba's lab. The Raman spectra match well with each other. However, red lasers (632 nm, 785 nm, and 1036 nm) were also used to collect the Raman spectra of Gd_3NbO_7; oddly, different laser wavelengths result in significantly different spectra (Figure D-2). The same thing also happened in Nd_3NbO_7. The Raman spectra by the green laser and the red laser are different (Figure D-3). Different Raman spectra with different lasers are probably due to electronic transitions in rare earth. In the case of resonant Raman (i.e. energy of laser is close to band gap) the intensity is completely different. It is worth noting that the Raman spectra of Sm_3NbO_7 are the same at different laser wavelengths, different from Gd_3NbO_7 and Nd_3NbO_7 (Figure D-4).

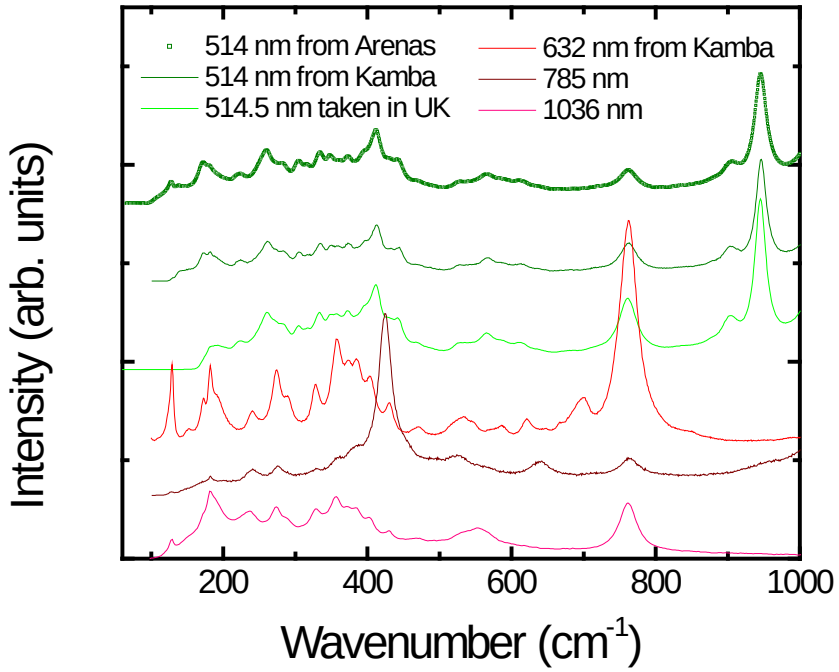

Figure D-2. Raman spectroscopy of Gd_3NbO_7 by different laser wavelengths at room temperature.

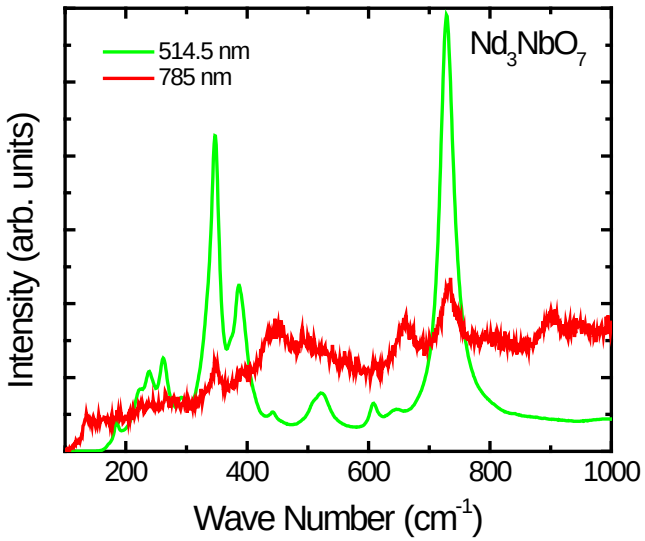

Figure D-3. Raman spectroscopy of Nd_3NbO_7 at room temperature (λ = 514.5 nm or 785 nm).

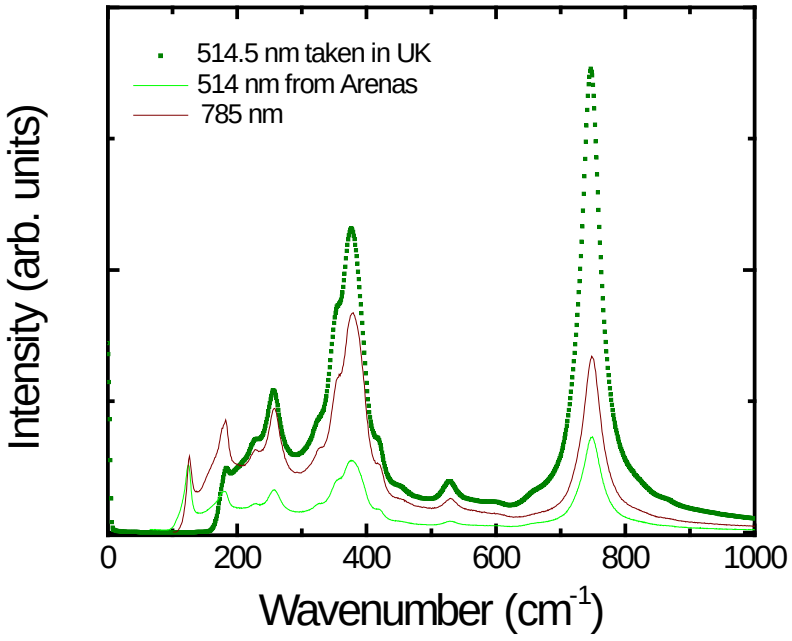

Figure D-4. The Raman spectroscopy of Sm_3NbO_7 at room temperature.

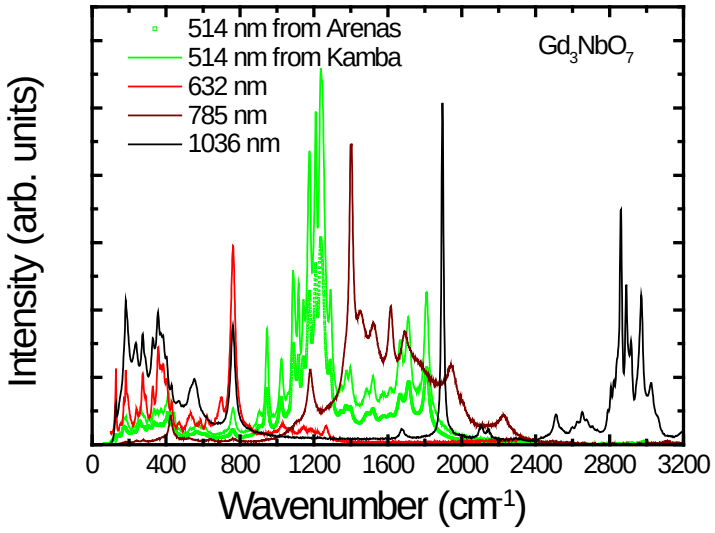

Figure D-5. Raman spectroscopy of Gd_3NbO_7 by different laser wavelengths up to 3200 cm^{-1} at room temperature.

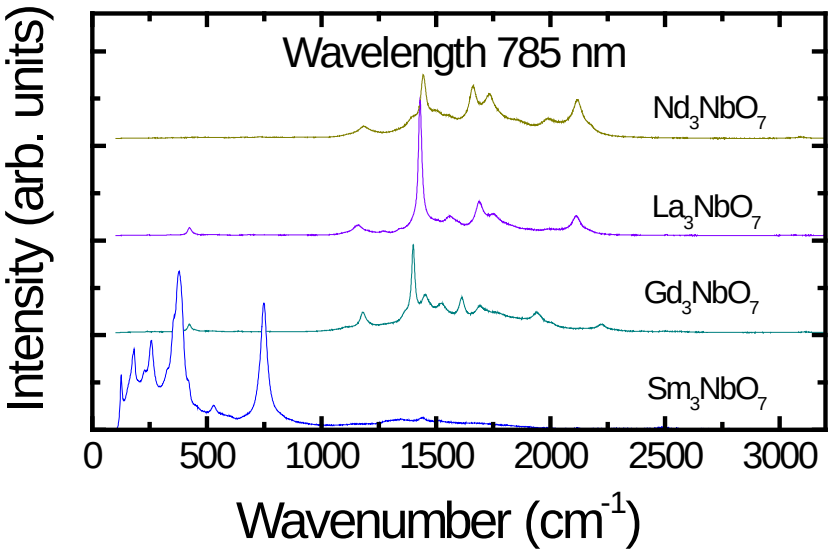

Figure D-6. The Raman spectra of Ln_3NbO_7 (Ln^{3+} = La^{3+}, Nd^{3+}, Sm^{3+}, and Gd^{3+}).

Another confusing phenomena is that there are strong peaks above 900 cm^{-1} at all laser wavelength measured for Gd_3NbO_7 (Figure D-5), Nd_3NbO_7, La_3NbO_7 (Figure D-6), and Y_3NbO_7 (Figure D-7). Given that these are ceramics materials (primarily ionic bonding), their composition, and their crystal structure, it is safe to assume that the

peaks above 900 cm^{-1} should not be related to phonons. Among the four orthorhombic Ln_3NbO_7 compounds, only Sm_3NbO_7 does not have strong peaks above 900 cm^{-1} (Figure D-4). Also, defect-fluorite Er_3NbO_7, Yb_3NbO_7, and Dy_3NbO_7 are shown in Figure D-8. The spectrum of Er_3NbO_7 is different from Yb_3NbO_7 and Dy_3NbO_7, which may indicate the presence of local structure in Er_3NbO_7.

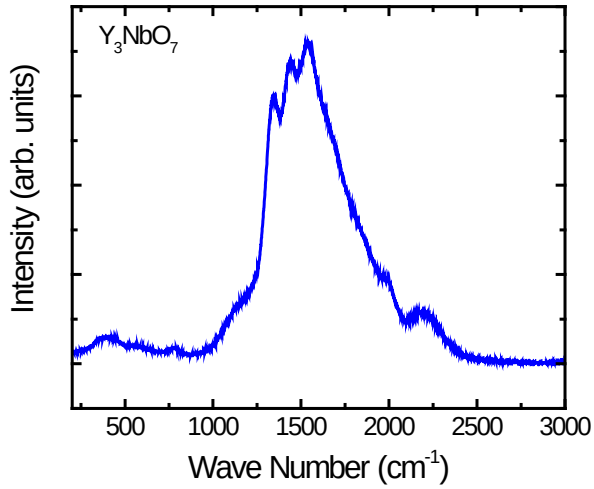

Figure D-7. The Raman spectroscopy of Y_3NbO_7 at room temperature.

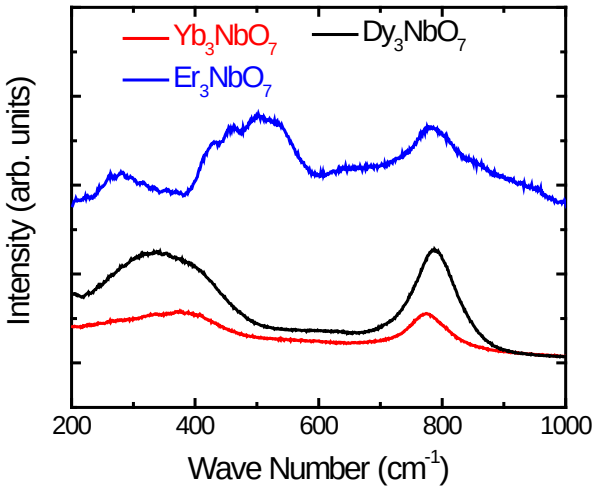

Figure D-8. Spectroscopy of defect fluorite Yb_3NbO_7, Er_3NbO_7, and Dy_3NbO_7.

APPENDIX E

Sm_3NbO_7

The Sm_3NbO_7 samples were also synthesized by solid state processing as discussed in Chapter 3. The calcination temperature was 1723 K. Multiple calcinations were needed to reduce $SmNbO_4$. After calcined at 1723 K for totally 48 h, the amount of the secondary phase of $SmNbO_4$ was below than 1%, measured by comparing the XRD pattern of Sm_3NbO_7 with the simulated XRD pattern of Sm_3NbO_7 and $SmNbO_4$ mixtures using CrystalDiffract software. Figure E-1 shows high resolution XRD pattern of powder Sm_3NbO_7, the simulated XRD pattern of Sm_3NbO_7 based on the space group $C222_1$[36], and the simulated XRD pattern of $SmNbO_4$.[257] The highest intensity peak of $SmNbO_4$ is about 0.9% relative intensity.

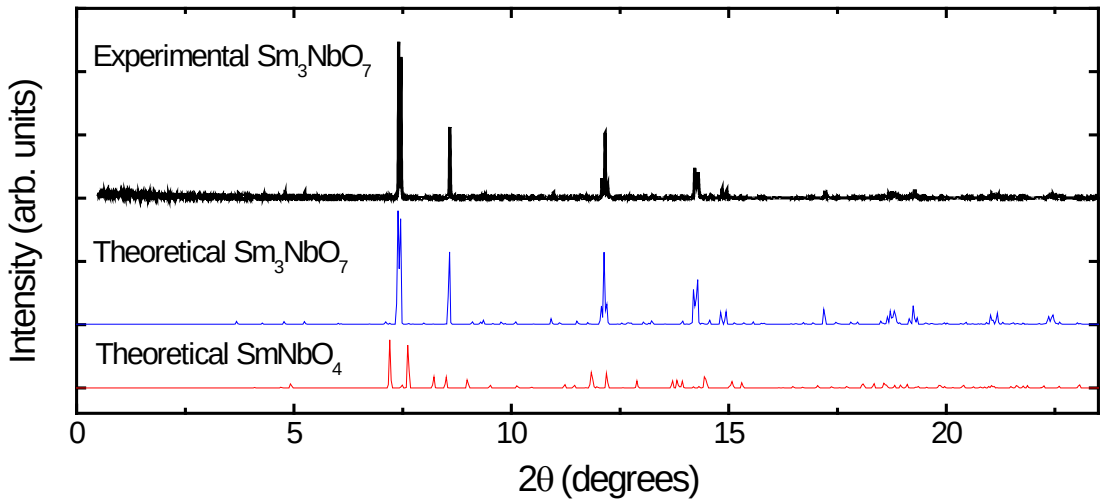

Figure E-1. Comparison of High resolution XRD pattern of Sm_3NbO_7 at RT (λ = 0.400919 Å), simulated XRD pattern of Sm_3NbO_7, and simulated XRD pattern of $SmNbO_4$ from CrystalDiffract software.

After sintered at 1873 K for 4 h, the Sm_3NbO_7 pellet was polished and thermal etching for SEM as described in Chapter 3. A secondary phase in the form of particles

was observed (Figure E-2). Chemical analysis was performed using energy dispersive spectroscopy (EDS). The secondary phase was found to be a Nb – deficient phase with the presence of Al element. The Al element was most likely from the alumina rectangle tray. The Sm_3NbO_7 powders were used as the sacrificing powders to separate the pellet from direct contacting the Al_2O_3 tray. The Nb – deficient phase was still present.

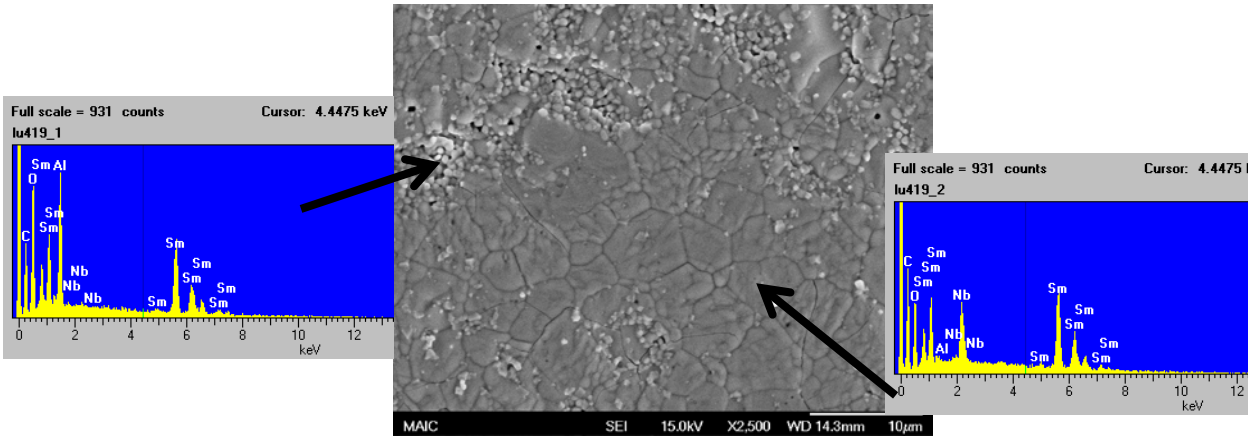

Figure E-2. The SEM picture and the EDS pattern of Sm_3NbO_7 pellet.

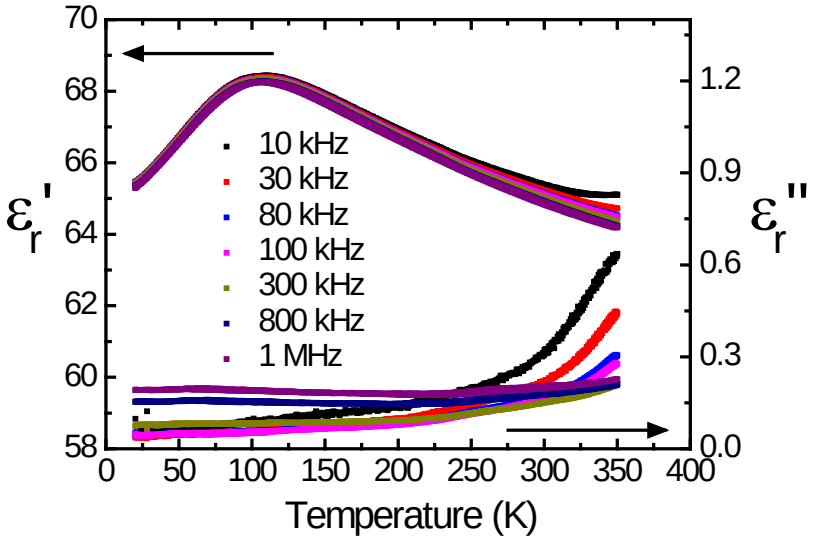

Figure E-3. Dielectric properties of Sm_3NbO_7 from 10 kHz to 1 MHz.

The Sm_3NbO_7 compound also exhibits dielectric relaxation as shown in Figure E-3. Unlike other Ln_3NbO_7 (Ln^{3+} = La^{3+}, Nd^{3+}, and Gd^{3+}), T(ε_m) is below RT, at about 120 K. Figure E-4 is the reproduction of Figure 9-22 and includes the Sm_3NbO_7 point. It is clear that dielectric relaxation is related to the crystal structure.

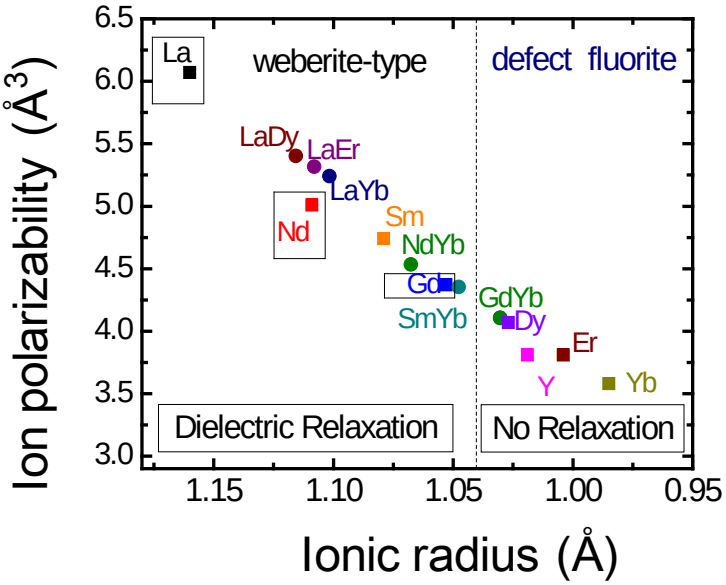

Figure E-4. Average ion polarizability vs. average ionic radius of Ln^{3+} in Ln_3NbO_7 and $Ln_2Ln'NbO_7$ including Sm_3NbO_7. The dielectric relaxation occurs only in weberite-type.

LIST OF REFERENCES

1. O. Yakubovich, V. Urusov, W. Massa, G. Frenzen, and D. Babel, "Structure of $Na_2Fe_2F_7$ and Structural Relations in the Family of Weberites $Na_2M^{II}M^{III}F_7$," *Zeitschrift Fur Anorganische Und Allgemeine Chemie*, **619** [11] 1909-1919 (1993).

2. A. Jaiswal and E.D. Wachsman, "Bismuth-ruthenate-based Cathodes for IT-SOFCs," *Journal of the Electrochemical Society*, **152** [4] A787-A790 (2005).

3. M. Camaratta and E. Wachsman, "High-performance Composite $Bi_2Ru_2O_7$-$Bi_{1.6}Er_{0.4}O_3$ Cathodes for Intermediate-temperature Solid Oxide Fuel Cells," *Journal of the Electrochemical Society*, **155** [2] B135-B142 (2008).

4. V. Esposito, B.H. Luong, E. Di Bartolomeo, E.D. Wachsman, and E. Traversa, "Applicability of $Bi_2Ru_2O_7$ Pyrochlore Electrodes for ESB and BIMEVOX Electrolytes," *Journal of the Electrochemical Society*, **153** [12] A2232-A2238 (2006).

5. A. Jaiswal, C.T. Hu, and E.D. Wachsman, "Bismuth Ruthenate-stabilized Bismuth Oxide Composite Cathodes for IT-SOFC," *Journal of the Electrochemical Society*, **154** [10] B1088-B1094 (2007).

6. J.C. Nino, Ph.D dissertation, The Pennsylvania State University, 2002.

7. H. Wang, R. Elsebrock, R. Waser, and X. Yao, "Low Temperature Microwave Properties of Bismuth Based Dielectric Ceramics," *Ferroelectrics*, **327** 33-37 (2005).

8. Q.A. Wang, H. Wang, and X. Yao, "Structure, Dielectric and Optical Properties of $Bi_{1.5}ZnNb_{1.5-x}Ta_xO_7$ Cubic Pyrochlores," *Journal of Applied Physics*, **101** [10] - (2007).

9. C.H. Gao, T.Q. Yang, and X. Yao, "Structure and Dielectric Properties of Bi-Zn-Ti-Nb-O Ceramics," *Ferroelectrics*, **388** 109-113 (2009).

10. W.H. Liu, H. Wang, K.C. Li, M.H. Zhang, and X. Yao, "$Bi_{1.5}ZnNb_{1.5}O_7$ Cubic Pyrochlore Ceramics Prepared by Aqueous Solution-gel Method," *J Sol-Gel Sci Techn*, **52** [1] 153-157 (2009).

11. A.V. Astafev, A.A. Bush, S.Y. Stefanovich, and Y.N. Venevtsev, "Preparation and Polar Properties of $Pb_2Sb_2O_7$ with the Weberite Structure," *Inorganic Materials*, **21** [4] 560-563 (1985).

12. S. Ivanov, R. Tellgren, and H. Rundlof, "Structural Aspects of Ferroelectric Phase Transitions in the Complex Metal Oxides $A_2Sb_2O_7$ (A=Pb, Sr, Ca) with Weberite Structure," *Epdic 5, Pts 1 and 2*, **278-2** 768-772 (1998).

13. S.A. Ivanov and V.E. Zavodnik, "Crystal-Structure of Lead Antimonate $Pb_2Sb_2O_7$," *Kristallografiya*, **35** [4] 842-846 (1990).

14. M.A. Subramanian, G. Aravamudan, and G.V.S. Rao, "Oxide Pyrochlores - a Review," *Progress in Solid State Chemistry*, **15** [2] 55-143 (1983).

15. J.F. Vente, R.B. Helmholdt, and D.J.W. Ijdo, "The Structure and Magnetic-Properties of Pr_3MO_7 with M=Nb, Ta, and Sb," *J Solid State Chem*, **108** [1] 18-23 (1994).

16. F. Wiss, N.P. Raju, A.S. Wills, and J.E. Greedan, "Structure and Magnetism in Pr_3RuO_7," *International Journal of Inorganic Materials*, **2** [1] 53-59 (2000).

17. G. Wltschek, H. Paulus, I. Svoboda, H. Ehrenberg, and H. Fuess, "Crystal Structure and Magnetic Properties of Sm_3ReO_7," *Journal of Solid State Chemistry*, **125** [1] 1-4 (1996).

18. H. Nishimine, M. Wakeshima, and Y. Hinatsu, "Crystal Structures, Magnetic and Thermal Properties of Ln_3IrO_7 (Ln = Pr, Nd, Sm, and Eu)," *Journal of Solid State Chemistry*, **177** [3] 739-744 (2004).

19. H. Nishimine, M. Wakeshima, and Y. Hinatsu, "Structures,Magnetic, and Thermal Properties of Ln_3MoO_7 (Ln = La, Pr, Nd, Sm, and Eu)," *Journal of Solid State Chemistry*, **178** [4] 1221-1229 (2005).

20. J.R. Plaisier, R.J. Drost, and D.J.W. IJdo, "Structures and Magnetic Properties of Ln_3OsO_7 (Ln = Pr, Nd, Sm)," *Journal of Solid State Chemistry*, **169** [2] 189-198 (2002).

21. M. Wakeshima and Y. Hinatsu, "Magnetic Properties of Lanthanide Rhenium Oxides Ln_3ReO_7 (Ln = Sm, Eu, Ho)," *Journal of Solid State Chemistry*, **179** [11] 3575-3581 (2006).

22. R. Abe, M. Higashi, K. Sayama, Y. Abe, and H. Sugihara, "Photocatalytic activity of R_3MO_7 and $R_2Ti_2O_7$ (R = Y, Gd, La; M = Nb, Ta) for water splitting into H_2 and O_2," *J Phys Chem B*, **110** [5] 2219-2226 (2006).

23. R. Abe, M. Higashi, Z.G. Zou, K. Sayama, Y. Abe, and H. Arakawa, "Photocatalytic Water Splitting into H_2 and O_2 over R_3TaO_7 and R_3NbO_7 (R = Y, Yb, Gd, La): Effect of Crystal Structure on Photocatalytic Activity," *Journal of Physical Chemistry B*, **108** [3] 811-814 (2004).

24. X.P. Lin, F.Q. Huang, W.D. Wang, Y.M. Wang, Y.J. Xia, and J.L. Shi, "Photocatalytic Activities of $M_2Sb_2O_7$ (M = Ca, Sr) for Degrading Methyl Orange," *Applied Catalysis a-General*, **313** [2] 218-223 (2006).

25. J. Sato, N. Saito, H. Nishiyama, and Y. Inoue, "Photocatalytic Water Decomposition by RuO_2-loaded Antimonates, $M_2Sb_2O_7$ (M = Ca, Sr), $CaSb_2O_6$

and $NaSbO_3$, with d^{10} Configuration," *Journal of Photochemistry and Photobiology a-Chemistry*, **148** [1-3] 85-89 (2002).

26. R.D. Shannon, "Dielectric Polarizabilities of Ions in Oxides and Fluorides," *Journal of Applied Physics*, **73** [1] 348-366 (1993).

27. R.D. Shannon, "Revised Effective Ionic-Radii and Systematic Studies of Interatomic Distances in Halides and Chalcogenides," *Acta Crystallographica Section A*, **32** [Sep1] 751-767 (1976).

28. R.S. Roth, T.A. Vanderah, P. Bordet, I.E. Grey, W.G. Mumme, L. Cai, and J.C. Nino, "Pyrochlore formation, phase relations, and properties in the CaO-TiO_2-$(Nb,Ta)_2O_5$ systems," *J Solid State Chem*, **181** [3] 406-414 (2008).

29. H.P. Rooksby and E.A.D. White, "Rare-Earth Niobates and Tantalates of Defect Fluorite-Type and Weberite-Type Structures," *Journal of the American Ceramic Society*, **47** [2] 94-96 (1964).

30. V.P. Sirotinkin, A.A. Evdokimov, and V.K. Trunov, "Parameter Improvement of Nucleus of Ln_3NbO_7 and Ln_3TaO_7 Compounds," *Zhurnal Neorganicheskoi Khimii*, **27** 1648-1652 (1982).

31. H.J. Rossell, "Fluorite-Related Phases Ln_3MO_7, Ln = Rare-Earth, Y or Sc, M = Nb, Sb, or Ta .2. Structure Determination," *Journal of Solid State Chemistry*, **27** 115-122 (1979).

32. J.G. Allpress and H.J. Rossell, "Fluorite-Related Phases Ln_3MO_7,Ln= Rare-Earth, Y, or Sc, M = Nb, Sb, or Ta .1. Crystal-Chemistry," *Journal of Solid State Chemistry*, **27** 105-114 (1979).

33. H.P. Rooksby and E.A.D. White, "Rare-Earth Niobates and Tantalates of Defect Fluorite-Type and Weberite-Type Structures," *Journal of the American Ceramic Society,*, **47** 94-96 (1964).

34. O.B. Thakre, P.V. Patil, and Chinchol.Vs, "Crystallographic Studies in System (1-X)La_3NbO_7+X Sm_3NbO_7," *Current Science*, **40** 62 (1971).

35. R. Abe, M. Higashi, Z. G. Zou, K. Sayama, Y. Abe, and H. Arakawa, "Photocatalytic water splitting into H-2 and O-2 over R_3TaO_7 and R_3NbO_7 (R = Y, Yb, Gd, La): Effect of crystal structure on photocatalytic activity," *Journal of Physical Chemistry B*, **108** 811-814 (2004).

36. H.J. Rossell, "Fluorite-Related Phases Ln_3MO_7, Ln = Rare-Earth, Y or Sc, M = Nb, Sb, or Ta .2. Structure Determination," *J Solid State Chem*, **27** [1] 115-122 (1979).

37. A. Kahnharari, L. Mazerolles, D. Michel, and F. Robert, "Structural Description of La_3NbO_7," *J Solid State Chem*, **116** [1] 103-106 (1995).

38. A.V. Astafyev, V.P. Sirotinkin, and S.Y. Stefanovich, "Phase-Transitions in the Compounds Sm_3NbO_7 and Gd_3NbO_7 with a Fluorite-Like Structure," *Kristallografiya*, **30** [3] 603-604 (1985).

39. V.A. Isupov, "Oxide Pyrochlores and Their Phase Transitions," *Ferroelectrics Review* **2**115-168 (2000).

40. L. Cai and J.C. Nino, "Complex Ceramic Structures. I. Weberites," *Acta Crystallographica Section B-Structural Science*, **65** 269-290 (2009).

41. R. Bogvad, "Webertie, A New Mineral from Ivigtut," *Meddelelser om Grønland*, **119** [7] 1-11 (1938).

42. A. Byström, "The structure of weberite, Na_2MgAlF_7," *Arkiv Kemi,mineralogi och geologi*, **B18** [10] 1-7 (1944).

43. R.E. Schmidt, W. Massa, and D. Babel, "The Crystal-Structure of Na_2NiAlF_7 - a Contribution to the Problem of the True Space Group of Orthorhombic Weberites," *Zeitschrift Fur Anorganische Und Allgemeine Chemie*, **615** [9] 11-15 (1992).

44. Y. Laligant, Y. Calage, G. Heger, J. Pannetier, and G. Ferey, "Ordered Magnetic Frustration .7. Na_2NiFeF_7 - Reexamination of Its Crystal-Structure in the True Space Group after Corrections from Renninger Effect and Refinement of Its Frustrated Magnetic-Structure at 4.2 and 55 K," *Journal of Solid State Chemistry*, **78** [1] 66-77 (1989).

45. I.E. Grey, W.G. Mumme, T.J. Ness, R.S. Roth, and K.L. Smith, "Structural Relations between Weberite and Zirconolite Polytypes-refinements of Doped 3T and 4M $Ca_2Ta_2O_7$ and 3T $CaZrTi_2O_7$," *Journal of Solid State Chemistry*, **174** [2] 285-295 (2003).

46. M. Mekata, "Kagome: The story of the Basketweave Lattice," *Physics Today*, **56** [2] 12-13 (2003).

47. I. Syozi, "Statistics of Kagome Lattice," *Progress of Theoretical Physics*, **6** [3] 306-308 (1951).

48. T.J. White, "The Microstructure and Microchemistry of Synthetic Zirconolite, Zirkelite and Related Phases," *American Mineralogist*, **69** [11-1] 1156-1172 (1984).

49. A.A. Coelho, R.W. Cheary, and K.L. Smith, "Analysis and Structural Determination of Nd-substituted Zirconolite-4M," *Journal of Solid State Chemistry*, **129** [2] 346-359 (1997).

50. J. Renaudin, M. Leblanc, G. Ferey, A. Dekozak, and M. Samouel, "Complex Copper(Ii) Fluorides .9. Weberite-Related $NaCu_3F_7$ - the 1st Fluoride with Copper Both in Square-Planar and Octahedraal Coordination," *Journal of Solid State Chemistry*, **73** [2] 603-609 (1988).

51. T. Hahn and International Union of Crystallography., International Tables for Crystallography. Brief Teaching Edition of Volume A, Space-group Symmetry, Published for the International Union of Crystallography by Kluwer Academic Publishers, Dordrecht ; Boston, 2002.

52. N.E. Brese and M. Okeeffe, "Bond-Valence Parameters for Solids," *Acta Crystallographica Section B-Structural Science*, **47** 192-197 (1991).

53. O. Knop, T.S. Cameron, and K. Jochem, "What Is the True Space Group of Weberite," *Journal of Solid State Chemistry*, **43** [2] 213-221 (1982).

54. O. Knop, G. Demazeau, and P. Hagenmuller, "Pyrochlores .11. High-Pressure Studies of the Antimonates $A_2Sb_2O_7$ (a=Ca, Sr, Cd) and Preparation of the Weberite $Sr_2Bi_2O_7$," *Canadian Journal of Chemistry-Revue Canadienne De Chimie*, **58** [21] 2221-2224 (1980).

55. W.A. Groen and D.J.W. Ijdo, "Distrontium Diantimonate(V) - a Rietveld Refinement of Neutron Powder Diffraction Data," *Acta Crystallographica Section C-Crystal Structure Communications*, **44** 782-784 (1988).

56. W. Klein, J. Curda, E.M. Peters, and M. Jansen, "$Ag_2Te_2O_7$, a Novel Silver Tellurate of Weberite Structure Type," *Zeitschrift Fur Anorganische Und Allgemeine Chemie*, **632** [8-9] 1508-1513 (2006).

57. D.I. Brown, "The Chemical Bond in Inorganic Chemistry : The Bond Valence Model," (2002).

58. J. Reading, C.S. Knee, and M.T. Weller, "Syntheses, structures and properties of some osmates(iv,v) adopting the pyrochlore and weberite structures," *J Mater Chem*, **12** [8] 2376-2382 (2002).

59. E. Aleshin and R. Roy, "Crystal Chemistry of Pyrochlore," *Journal of the American Ceramic Society*, **45** [1] 18-25 (1962).

60. M.A. Aia, R.W. Mooney, and C.W.W. Hoffman, "An X-Ray Study of Pyrochlore Fluoantimonates of Calcium, Cadmium, and Manganese," *Journal of the Electrochemical Society*, **110** [10] 1048-1054 (1963).

61. P. Bayliss, F. Mazzi, R. Munno, and T.J. White, "Mineral Nomenclature - Zirconolite," *Mineralogical Magazine*, **53** [373] 565-569 (1989).

62. I.E. Grey and R.S. Roth, "New Calcium Tantalate Polytypes in the System $Ca_2Ta_2O_7$-$Sm_2Ti_2O_7$," *Journal of Solid State Chemistry*, **150** [1] 167-177 (2000).

63. I.E. Grey, R.S. Roth, G. Mumme, L. Bendersky, and D. Minor, "Crystal Chemistry of new calcium tantalate dielectric materials," *Solid-State Chemistry of Inorganic Materials II (Materials Research Society Symposium Proceedings)*, **547** 127-138 (1999).

64. I.E. Grey, R.S. Roth, W.G. Mumme, J. Planes, L. Bendersky, C. Li, and J. Chenavas, "Characterization of New 5M and 7M Polytypes of Niobia-doped $Ca_2Ta_2O_7$," *Journal of Solid State Chemistry*, **161** [2] 274-287 (2001).

65. S.G. Ebbinghaus, A. Kalytta, J. Kopf, A. Weidenkaff, and A. Reller, "Crystal Structure and Optical Properties of the New 8O Polytype of $Ca_2Ta_2O_7$," *Zeitschrift Fur Kristallographie*, **220** [2-3] 269-276 (2005).

66. S. Kummer, W. Massa, and D. Babel, "Concerning the Structures of the Copper Weberites Na_2CuCrF_7 and Na_2CuFeF_7," *Zeitschrift Fur Naturforschung Section B-a Journal of Chemical Sciences*, **43** [6] 694-701 (1988).

67. N. Ruchaud, J. Grannec, P. Gravereau, P. Nunez, A. Tressaud, W. Massa, G. Frenzen, and D. Babel, "Copper Weberites - Crystal-Structure and Magnetic Investigation of Na_2CuGaF_7 and Na_2CuInF_7," *Zeitschrift Fur Anorganische Und Allgemeine Chemie*, **610** [4] 67-74 (1992).

68. G. Frenzen, W. Massa, D. Babel, N. Ruchaud, J. Grannec, A. Tressaud, and P. Hagenmuller, "Structure and Magnetic-Behavior of the Na_2NiInF_7 Weberite," *Journal of Solid State Chemistry*, **98** [1] 121-127 (1992).

69. R.W.G. Wyckoff, Crystal Structures, New York, Interscience Publishers, 1963.

70. E.H.P. Cordfunke and D.J.W. Ijdo, "$Ba_2U_2O_7$ - Crystal-Structure and Phase-Relationships," *Journal of Physics and Chemistry of Solids*, **49** [5] 551-554 (1988).

71. F. Brisse, D.J. Stewart, V. Seidl, and O. Knop, "Pyrochlores .8. Studies of Some 2-5 Pyrochlores and Related Compounds and Minerals," *Canadian Journal of Chemistry*, **50** [22] 3648-& (1972).

72. A.M. Sych, M.I. Kabanova, V.V. Garbuz, and E.N. Kovalenko, "Synthesis of the Compound $KLnSb_2O_7$ and Region of Existence of the $A_2B_2O_7$ Phase with a Weberite Structure," *Inorganic Materials*, **24** [9] 1316-1320 (1988).

73. S.S. Lopatin, L.N. Averyanova, and I.N. Belyaev, "Effect of Ion Radii and the Atom Electronegativity on the Type of Crystal-Structure of $A_2B_2O_7$ Combination Compounds," *Zhurnal Neorganicheskoi Khimii*, **30** [4] 867-872 (1985).

74. M.T. Weller, J. Reading, and C.S. Knee, "Structure and Electronic Properties of the Heavy Transition Metal Pyrochlores and Weberitet $A_2B_2O_7$, A=Ca, Cd, Hg, Tl, Pb; B=Os, Ru, Re," *Solid State Chemistry V*, **90-91** 201-205 (2003).

75. G. Burchard and W. Rudorff, "New Oxides with Weberite Structure," *Zeitschrift Fur Anorganische Und Allgemeine Chemie*, **454** [7] 107-112 (1979).

76. S.S. Lopatin, L.N. Averyanova, I.N. Belyaev, B.I. Zvyagintsev, and E.V. Dyatlov, "$AgLnSb_2O_7$ Compounds with Weber Structures," *Zhurnal Neorganicheskoi Khimii*, **27** [11] 2751-2755 (1982).

77. A.L. Allred and E.G. Rochow, "A Scale of Electronegativity Based on Electrostatic Force," *Journal of Inorganic & Nuclear Chemistry*, **5** [4] 264-268 (1958).

78. E.J. Little and M.M. Jones, "Complete Table of Electronegativities," *Journal of Chemical Education*, **37** 231-233 (1960).

79. S.S. Batanov, "System of Electronegativities and Effective Atomic Charge in Crystalline Compounds," *Zhurnal Neorganicheskoi Khimii*, **20** [10] 2595-2600 (1975).

80. J.G. Allpress and H.J. Rossell, "Fluorite-Related Phases Ln_3MO_7,Ln= Rare-Earth, Y, or Sc, M = Nb, Sb, or Ta .1. Crystal-Chemistry," *J Solid State Chem*, **27** [1] 105-114 (1979).

81. N. Barrier, P. Gall, and P. Gougeon, "Rare-earth site splitting in Sm3MoO7," *Acta Crystallographica Section C-Crystal Structure Communications*, **63** I102-I104 (2007).

82. N. Barrier and P. Gougeon, "Pr3MoO7," *Acta Crystallographica Section E-Structure Reports Online*, **59** I22-I24 (2003).

83. R.P. Bontchev, A.J. Jacobson, M.M. Gospodinov, V. Skumryev, V.N. Popov, B. Lorenz, R.L. Meng, A.P. Litvinchuk, and M.N. Iliev, "Crystal Structure, Electric and Magnetic Properties, and Raman Spectroscopy of Gd_3RuO_7," *Physical Review B*, **62** [18] 12235-12240 (2000).

84. W.T. Fu and D.J.W. Ijdo, "On the Crystal Structures of Ln_3MO_7 (Ln = Nd, Sm, Y and M = Sb, Ta)—Rietveld Refinement using X-raypowder Diffraction Data," *Journal of Solid State Chemistry*, **182** 2451-2455 (2009).

85. L. Cai, J. Guzman, L. Perez, and J.C. Nino, "Phase Formation and Dielectric Properties of Ln_3NbO_7 (Ln = Rare Earth Elements)," *Solid-State Chemistry of Inorganic Materials VI (Materials Research Society Symposium Proceeding)*, **998E** 0988-qq01-04 (2007).

86. L. Cai and J.C. Nino, "Structure and Dielectric Properties of Ln_3NbO_7 (Ln = Nd, Gd, Dy, Er, Yb and Y)," *Journal of the European Ceramic Society*, **27** [13-15] 3971-3976 (2007).

87. J.E. Greedan, N.P. Raju, A. Wegner, P. Gougeon, and J. Padiou, "A study of the structure and electronic and thermal properties of quasi-one-dimensional La_3MoO_7," *J Solid State Chem*, **129** [2] 320-327 (1997).

88. M. Wakeshima, H. Nishimine, and Y. Hinatsu, "Crystal Structures and Magnetic Properties of Rare Earth Tantalates RE_3TaO_7 (RE = rare earths)," *Journal of Physics Condensed Matter*, **16** [23] 4103-4120 (2004).

89. J.F. Vente and D.J.W. Ijdo, "The Orthorhombic Fluorite Related-Compounds Ln_3IrO_7," *Materials Research Bulletin*, **26** [12] 1255-1262 (1991).

90. F.P.F. Vanberkel and D.J.W. Ijdo, "The Orthorhombic Fluorite Related-Compounds Ln_3RuO_7, Ln=Nd, Sm and Eu," *Materials Research Bulletin*, **21** [9] 1103-1106 (1986).

91. H. Nishimine, Y. Doi, Y. Hinatsu, and M. Sato, "Phase transition of Ln_3IrO_7 (Ln = Pr, Nd, Sm, Eu) and its low-temperature structure," *Journal of the Ceramic Society of Japan*, **115** [1346] 577-581 (2007).

92. R. Lam, F. Wiss, and J.E. Greedan, "Magnetic Properties of the Fluorite-related La_3MO_7 Phases, M=Ru and Os - Local Moment Magnetism, Short- and Long-range Order in 4d and 5d Transition Metal Oxides," *Journal of Solid State Chemistry*, **167** [1] 182-187 (2002).

93. R. Lam, T. Langet, and J.E. Greedan, "Structure and Magnetism in Pr_3ReO_7 and Nd_3ReO_7 - Materials with an Ordered, Defect Fluorite Structure," *Journal of Solid State Chemistry*, **171** [1-2] 317-323 (2003).

94. P. Khalifah, Q. Huang, J.W. Lynn, R.W. Erwin, and R.J. Cava, "Synthesis and Crystal Structure of La_3RuO_7," *Materials Research Bulletin*, **35** [1] 1-7 (2000).

95. P. Khalifah, R.W. Erwin, J.W. Lynn, Q. Huang, B. Batlogg, and R.J. Cava, "Magnetic and Electronic Characterization of Quasi-one-dimensional La_3RuO_7," *Physical Review B*, **60** [13] 9573-9578 (1999).

96. Y. Hinatsu, M. Wakeshima, N. Kawabuchi, and N. Taira, "Structures and Magnetic Properties of Rare Earth Rhenium Oxides Ln_3ReO_7 (Ln = Gd, Tb, and Dy)," *Journal of Alloys and Compounds*, **374** [1-2] 79-83 (2004).

97. D. Harada, Y. Hinatsu, and Y. Ishii, "Studies on the Magnetic and Structural Phase Transitions of Nd_3RuO_7," *Journal of Physics Condensed Matter*, **13** [48] 10825-10836 (2001).

98. D. Harada and Y. Hinatsu, "Magnetic and Calorimetric Studies on One-Dimensional Ln_3RuO_7 (Ln=Pr, Gd) " *Journal of Solid State Chemistry*, **164** [1] 163-168 (2002).

99. D. Harada and Y. Hinatsu, "A study of the Magnetic and Thermal Properties of Ln_3RuO_7 (Ln = Sm, Eu)," *Journal of Solid State Chemistry*, **158** [2] 245-253 (2001).

100. W.A. Groen, F.P.F. Vanberkel, and D.J.W. Ijdo, "Trineodymium Ruthenate .5. A Rietveld Refinement of Neutron Powder Diffraction Data," *Acta Crystallographica Section C-Crystal Structure Communications*, **43** 2262-2264 (1987).

101. W.T. Fu and D.J. Ijdo, "On the Crystal Structures of Ln_3MO_7 (Ln=Nd, Sm, Y and M=Sb, Ta)—Rietveld Refinement Using X-ray Powder Diffraction Data," *Journal of Solid State Chemistry*, **182** [9] 2451-2455 (2009).

102. G. Heger, "Magnetic Properties of the Ferrimagnet Na_2NiFeF_7 and the Linear Antiferromagnet Na_2NiAlF_7," *International Journal of Magnetism*, **5** [1-3] 119-124 (1973).

103. G.R. Thompson, Q.A. Pankhurst, and C.E. Johnson, "Investigation of the Curie-Point in Ferrimagnetic Na_2NiFeF_7," *Journal of Magnetism and Magnetic Materials*, **104** 893-894 (1992).

104. Q.A. Pankhurst, C.E. Johnson, and B.M. Wanklyn, "A Mossbauer Study of Paramagnetic Na_2MgFeF_7," *Journal of Magnetism and Magnetic Materials*, **97** [1-3] 126-130 (1991).

105. R.J. Cava, J.J. Krajewski, and R.S. Roth, "Low Temperature Coefficient Bulk Dielectrics in the $Ca_2Nb_2O_7$-$Ca_2Ta_2O_7$ System," *Materials Research Bulletin*, **33** [4] 527-532 (1998).

106. P.M. Milyan and E.E. Semrad, "Preparation and Properties of Compounds of the PbO-Sb_2O_5 System," *Russian Journal of Inorganic Chemistry*, **50** [10] 1599-1604 (2005).

107. I.M. Reaney and D. Iddles, "Microwave Dielectric Ceramics for Resonators and Filters in Mobile Phone Networks," *Journal of the American Ceramic Society*, **89** [7] 2063-2072 (2006).

108. V.P. Sirotinkin, A.A. Evdokimov, and V.K. Trunov, "Parameter Improvement of Nucleus of Ln_3NbO_7 and Ln_3TaO_7 Compounds," *Zhurnal Neorganicheskoi Khimii*, **27** [7] 1648-1651 (1982).

109. A.J. Moulson and J.M. Herbert, Electroceramics : Materials, Properties, Applications, Wiley, Chichester ; Hoboken, NJ, 2003.

110. M.W. Barsoum, Fundamentals of Ceramics, IoP, Bristol ; Philadelphia, 2003.

111. K. Uchino, Ferroelectric Devices, Marcel Dekker, New York, 2000.

112. W. Martienssen and H. Warlimont, Springer Handbook of Condensed Matter and Materials Data, Springer, 2005.

113. M.E. Lines and A.M. Glass, Principles and Applications of Ferroelectrics and Related Materials, Clarendon Press, Oxford 1977.

114. U. Müller, Inorganic Structural Chemistry, Wiley, Chichester, England ; Hoboken, NJ, 2007.

115. P.A. Franken, G. Weinreich, C.W. Peters, and A.E. Hill, "Generation of Optical Harmonics," *Phys Rev Lett*, **7** [4] 118-& (1961).

116. R. Paschotta, Encyclopedia of Laser Physics and Technology, Wiley-Vch, 2008.

117. D.L. Rousseau, R.P. Bauman, and S.P.S. Porto, "Normal Mode Determination in Crystals," *J Raman Spectrosc*, **10** [Jan] 253-290 (1981).

118. J. Wang, B.H. Toby, P.L. Lee, L. Ribaud, S.M. Antao, C. Kurtz, M. Ramanathan, R.B. Von Dreele, and M.A. Beno, "A Dedicated Powder Diffraction Beamline at the Advanced Photon Source: Commissioning and Early Operational Results," *Rev Sci Instrum*, **79** [8] - (2008).

119. ASTM E1269-05, Standard Test Method for Determining Specific Heat Capacity by Differential Scanning Calorimetry, ASTM International, 2005.

120. L. Cai and J.C. Nino, "Phase Formation and Dielectric Properties of $Ln_2(Ln_{0.5}'Nb_{0.5})_2O_7$ (Ln = Rare Earth Element)," *Journal of the European Ceramic Society*, **30** [2] 307-313 (2010).

121. S.A. Kovyazina, L.A. Perelyaeva, I.A. Leonidov, and Y.A. Bakhteeva, "High-temperature Structural Disorder in R_3NbO_7," *Journal of Structural Chemistry*, **44** [6] 975-979 (2003).

122. O.B. Thakre, P.V. Patil, and Chinchol.Vs, "Crystallographic Studies in System (1-X)La_3NbO_7+X Sm_3NbO_7," *Curr Sci India*, **40** [3] 62-& (1971).

123. N.V. Gundobin, K.I. Petrov, and S.S. Plotkin, "Vibration-Spectra and Structure Ln_3MO_7-Type Niobates and Tantalates," *Zhurnal Neorganicheskoi Khimii*, **22** [11] 2973-2977 (1977).

124. W.W. Barker, "The Systems Y_2O_3-Nb_2O_5 and Ho_2O_3-Nb_2O_5 - the Cubic Solid-Solution Region," *J Mater Sci Lett*, **3** [6] 492-494 (1984).

125. V.A. Isupov, "Oxide pyrochlores and their phase transitions," *Ferroelectrics Review*, **2** 115-168 (2000).

126. W. Kraus and G. Nolze, "Powdercell for Windows Version 2.4," (2000).

127. Y. Yamasaki and Y. Sugitani, "Flux Growth of Double Oxides of Niobium and Rare-Earth Elements (Ln_3NbO_7)," *B Chem Soc Jpn*, **51** [10] 3077-3078 (1978).

128. G. Tilloca, "Formation of Compounds between Niobium Pentoxide and Some Divalent and Trivalents Elements among Which Lanthanide Oxides," *Rev Int Hautes Temp*, **10** [3] 183-196 (1973).

129. Y. Yokogawa, N. Ishizawa, S. Somiya, and M. Yoshimura, "High-Temperature Phase-Relations in the System Gd_2O_3-Ta_2O_5," *Journal of the American Ceramic Society*, **74** [9] 2073-2076 (1991).

130. R. Shirley, "The CRYSFIRE System for Automatic Powder Indexing,"

131. L. Lutterotti, "Maud-Materials Analysis Using Diffraction,"

132. M. Fischer, T. Malcherek, U. Bismayer, P. Blaha, and K. Schwarz, "Structure and stability of $Cd_2Nb_2O_7$ and $Cd_2Ta_2O_7$ explored by ab initio calculations," *Physical Review B*, **78** [1] - (2008).

133. G. Nolze and W. Kraus, "BAM Berlin PowderCell,"

134. Chinchol.Vs, "Dielectric Constants of System x Sm_3NbO_7 + (1-x) La_3NbO_7," *Curr Sci India*, **40** [15] 400-& (1971).

135. S. Roberts, "Dielectric Constants and Polarizabilities of Ions in Simple Crystals and Barium Titanate," *Phys Rev*, **76** [8] 1215-1220 (1949).

136. H.B. Johnson, N.J. Tolar, G.R. Miller, and I.B. Cutler, "Electrical and Mechanical Relaxation in CaF_2 Doped with NaF," *J Phys Chem Solids*, **30** [1] 31-42 (1969).

137. B.L. Cheng, C. Wang, S.Y. Wang, T.W. Button, H.B. Lu, Y.L. Zhou, Z.H. Chen, and G.Z. Yang, "Temperature stability of permittivity and dielectric relaxation in multilayered thin films of $(Ba_{0.80}Sr_{0.20})(Ti_{1-x}Zr_x)O_3$ with a compositionally graded layer," *Applied Physics Letters*, **84** [26] 5431-5433 (2004).

138. J.C. Nino, M.T. Lanagan, and C.A. Randall, "Dielectric relaxation in Bi_2O_3-ZnO-Nb_2O_5 cubic pyrochlore," *J Appl Phys*, **89** [8] 4512-4516 (2001).

139. J.C. Nino, M.T. Lanagan, C.A. Randall, and S. Kamba, "Correlation between infrared phonon modes and dielectric relaxation in Bi2O3-ZnO-Nb2O5 cubic pyrochlore," *Applied Physics Letters*, **81** [23] 4404-4406 (2002).

140. G.A. Samara, "The relaxational properties of compositionally disordered ABO(3) perovskites," *Journal of Physics-Condensed Matter*, **15** [9] R367-R411 (2003).

141. V.K. Wadhawan, P. Pandit, and S.M. Gupta, "PMN-PT Based Relaxor Ferroelectrics as Very Smart Materials," *Materials Science and Engineering B*, **120** [1-3] 199-205 (2005).

142. D. Jeong,Ph.D Thesis, Pennsylvania State Univeristy, 2004.

143. S. Kamba, V. Bovtun, J. Petzelt, I. Rychetsky, R. Mizaras, A. Brilingas, J. Banys, J. Grigas, and M. Kosec, "Dielectric dispersion of the relaxer PLZT ceramics in the frequency range 20 Hz-100 THz," *Journal of Physics-Condensed Matter*, **12** [4] 497-519 (2000).

144. K. Binder and A.P. Young, "Spin glasses: Experimental facts, theoretical concepts, and open questions," *Reviews of Modern Physics*, **58** [4] 801 (1986).

145. S. Bhattacharya, S.R. Nagel, L. Fleishman, and S. Susman, "Dielectric Susceptibility of $(KBr)_{0.50}(KCN)_{0.50}$ - Is It a Dipole Glass," *Physical Review Letters*, **48** [18] 1267-1270 (1982).

146. L. Cai, D. Sava, V. Gopolan, and J.C. Nino, "Phase Transition in Webeirte-type Gd_3NbO_7," *Journal of the American Ceramic Society*, **93** [3] 875-880 (2010).

147. A.N. Klimenko, V.M. Ionov, N.A. Tomilin, V.S. Sergeev, V.P. Sirotinkin, A.E. Prozorovskii, V.B. Rybakov, and S.G. Zhukov, "Phase-Transformations in Rare-Earth-Metals of R_3NbO_7 Niobates at High-Temperatures," *Zhurnal Neorganicheskoi Khimii*, **35** [3] 599-603 (1990).

148. H. Nishimine, M. Wakeshima, and Y. Hinatsu, "Structures, magnetic, and thermal properties of Ln_3MoO_7 (Ln=La, Pr, Nd, Sm, and Eu) " *J Solid State Chem*, **178** [4] 1221-1229 (2005).

149. W.R. Gemmill, M.D. Smith, Y.A. Mozharivsky, G.J. Miller, and H.C. zur Loye, "Crystal Growth, Structural Transitions, and Magnetic Properties of the Fluorite-related Osmates: Sm_3OsO_7, Eu_3OsO_7, and Gd_3OsO_7," *Inorganic Chemistry*, **44** [20] 7047-7055 (2005).

150. D. Harada, Y. Hinatsu, and Y. Ishii, "Studies on the magnetic and structural phase transitions of Nd_3RuO_7," *J Phys-Condens Mat*, **13** [48] 10825-10836 (2001).

151. N. Ishizawa, K. Tateishi, S. Kondo, and T. Suwa, "Structural phase transition of Gd_3RuO_7," *Inorganic Chemistry*, **47** [2] 560-566 (2008).

152. A.A. Levchenko, L. Marchin, Y. Moriya, H. Kawaji, T. Atake, S. Guillemet-Fritsch, B. Durand, and A. Navrotsky, "Calorimetric Study of $CaCu_3Ti_4O_{12}$, a Ceramic With Giant Permittivity," *J Mater Res*, **23** [6] 1522-1531 (2008).

153. B.F. Woodfield, J. Boerio-Goates, J.L. Shapiro, R.L. Putnam, and A. Navrotsky, "Molar Heat Capacity and Thermodynamic Functions of Zirconolite $CaZrTi_2O_7$," *J Chem Thermodyn*, **31** [2] 245-253 (1999).

154. R. Shirley, "The CRYSFIRE System for Automatic Powder Indexing," (2004).

155. A.C. Larson and R.B. Von Dreele, "General Structure Analysis System (GSAS)," *Los Alamos National Laboratory Report*, LAUR 86-748 (1994).

156. B.H. Toby, "EXPGUI, a Graphical User Interface for GSAS," *Journal of Applied Crystallography*, **34** 210-213 (2001).

157. W.R. Gemmill, M.D. Smith, and H.C. zur Loye, "Crystal Growth, Observation, and Characterization of the Low-temperature Structure of the Fluorite-related Ruthenates: Sm_3RuO_7 and Eu_3RuO_7," *Inorganic Chemistry*, **43** [14] 4254-4261 (2004).

158. Y. Yokogawa and M. Yoshimura, "Formation and Stability Regions of the High-temperature Fluorite-related Phase in the R_2O_3-Ta_2O_5 System (R=La, Nd, Sm, Ho, Er, and Yb)," *Journal of the American Ceramic Society*, **80** [8] 1965-1974 (1997).

159. L. Cai, D. Sava, V. Gopolan, and J.C. Nino, "Phase Transition in Webeirte-type Gd_3NbO_7," *Journal of the American Ceramic Society*, **In press** (2009).

160. S. Kamba, V. Porokhonskyy, A. Pashkin, V. Bovtun, J. Petzelt, J.C. Nino, S. Trolier-McKinstry, M.T. Lanagan, and C.A. Randall, "Anomalous broad dielectric relaxation in $Bi_{1.5}Zn_{1.0}Nb_{1.5}O_7$ pyrochlore," *Physical Review B*, **66** [5] - (2002).

161. P. Kuzel and J. Petzelt, "Time-resolved Terahertz Transmission Spectroscopy of Dielectrics," *Ferroelectrics*, **239** [1-4] 949-956 (2000).

162. E. Buixaderas, S. Kamba, and J. Petzelt, "Lattice dynamics and central-mode phenomena in the dielectric response of ferroelectrics and related materials," *Ferroelectrics*, **308** 131-192 (2004).

163. J. Laugier and B. Bochu, "LMGP-Suite Suite of Programs for the interpretation of X-ray Experiments,"

164. J. Krupka, T. Zychowicz, V. Bovtun, and S. Veljko, "Complex permittivity measurements of ferroelectrics employing composite dielectric resonator technique," *Ieee T Ultrason Ferr*, **53** [10] 1883-1888 (2006).

165. P.K. Davies, *unpublished data,*, (2002).

166. D.P. Cann, C.A. Randall, and T.R. Shrout, "Investigation of the dielectric properties of bismuth pyrochlores," *Solid State Commun.*, **100** [7] 529-534 (1996).

167. J.C. Nino, M.T. Lanagan, and C.A. Randall, "Dielectric relaxation in Bi2O3-ZnO-Nb2O5 cubic pyrochlore," *J. Appl. Phys.*, **89** [8] 4512 (2001).

168. J.C. Nino, M.T. Lanagan, C.A. Randall, and S. Kamba, "Correlation between infrared phonon modes and dielectric relaxation of Bi2O3-ZnO-Nb2O5 cubic pyrochlore," *Appl. Phys. Lett.*, **81** [23] 4404-4406 (2002).

169. S. Kamba, V. Porokhonskyy, A. Pashkin, V. Bovtun, J. Petzelt, J.D. Nino, S. Trolier-McKinstry, M.T. Lanagan, and C.A. Randall, "Anomalous broad dielectric relaxation in Bi1.5Zn1.0Nb1.5O7 pyrochlore," *Phys. Rev. B*, **66** 054106 (2002).

170. M.W. Lufaso, T.A. Vanderah, I.P. Pazos, I. Levin, R.S. Roth, J.C. Nino, V. Provenzano, and P.K. Schenck, "Phase formation, crystal chemistry, and properties in the system Bi2O3-Fe2O3-Nb2O5," *J. Solid State Chemistry*, **170** 3900-3910 (2006).

171. L. Cai and J.C. Nino, "Structure and Dielectric Properties of Ln3NbO7 (Ln = Nd, Gd, Dy, Er, Yb, and Y)," *Journal of the European Ceramic Society*, **27** 3971-3976 (2007).

172. V.M. Goldschmidt, "The laws of crystal chemistry," *Naturwissenschaften*, **14** 477-485 (1926).

173. I.M. Reaney, E.L. Colla, and N. Setter, "Dielectric and Structural Characteristics of Ba-Based and Sr-Based Complex Perovskites as a Function of Tolerance Factor," *Jpn J Appl Phys 1*, **33** [7A] 3984-3990 (1994).

174. D.Y. Suarez, I.M. Reaney, and W.E. Lee, "Relation between tolerance factor and T-c in Aurivillius compounds," *J Mater Res*, **16** [11] 3139-3149 (2001).

175. V.A. Isupov, "Geometric Criteria of Structures of the Pyrochlore Type," *Kristallografiya*, **3** 96-97 (1958).

176. L.G. Nikiforov, "Possible Method for Estimating the Parameter x in Compounds of the Pyrochlore Type with General Formula $A_2B_2O_7$," *Soviet Physics-Crystallography*, **17** [2] 347 (1971).

177. R.A. Mccauley, "Structural Characteristics of Pyrochlore Formation," *J Appl Phys*, **51** [1] 290-294 (1980).

178. H.R. Hoekstra and Gallaghe.F, "Synthesis of Some Pyrochlore-Type Oxides of Platinum(4) at High Pressure," *Inorg Chem*, **7** [12] 2553-& (1968).

179. F.A. Weber and T. Schleid, "$Pr_2Te_2O_7$: A praseodymium(III) oxide oxotellurate(IV) according to $Pr2O(TeO_3)_2$ with pyrochlore-type crystal structure," *Z Anorg Allg Chem*, **626** [6] 1285-1287 (2000).

180. Y. Tabira, R.L. Withers, L. Minervini, and R.W. Grimes, "Systematic structural change in selected rare earth oxide pyrochlores as determined by wide-angle CBED and a comparison with the results of atomistic computer simulation," *J Solid State Chem*, **153** [1] 16-25 (2000).

181. R.C. Belin, P.J. Valenza, P.E. Raison, and M. Tillard, "Synthesis and Rietveld structure refinement of americium pyrochlore AM(2)Zr(2)O(7)," *J Alloy Compd*, **448** [1-2] 321-324 (2008).

182. T. Moriga, A. Yoshiasa, F. Kanamaru, K. Koto, M. Yoshimura, and S. Somiya, "Crystal-Structure Analyses of the Pyrochlore-Type and Fluorite-Type Zr2gd2o7 and Anti-Phase Domain-Structure," *Solid State Ionics*, **31** [4] 319-328 (1989).

183. M.P. Vandijk, J.H.H. Termaat, G. Roelofs, H. Bosch, G.M.H. Vandevelde, P.J. Gellings, and A.J. Burggraaf, "Electrical and Catalytic Properties of Some Oxides with the Fluorite or Pyrochlore Structure .1. Synthesis, Characterization and Conductivity," *Mater Res Bull*, **19** [9] 1149-1156 (1984).

184. Y. Tabira and R.L. Withers, "The determination of an unknown oxygen atom position in rare-earth zirconate pyrochlores by a 111 systematic-row convergent-beam electron diffraction technique," *Philos Mag A*, **79** [6] 1335-1346 (1999).

185. Y. Tabira, R.L. Withers, T. Yamada, and N. Ishizawa, "Annular dynamical disorder of the rare earth ions in a La2Zr2O7 pyrochlore via single crystal synchrotron X-ray diffraction," *Z Kristallogr*, **216** [2] 92-98 (2001).

186. C.H. Lu, B.K. Fang, and C.Y. Wen, "Structure identification and electrical properties of the new pyrochlore phase in the Sr-Bi-Ta-Ti-O system," *Jpn J Appl Phys 1*, **39** [9B] 5573-5576 (2000).

187. G. Nalini, R. Somashekar, and T.N.G. Row, "X-ray structure refinements and strain analysis of substituted cubic lead pyrochlores Pb-2(M2-yPby)O7-delta(0.0 < y < 0.8; M = Nb or Ta)," *J Solid State Chem*, **156** [1] 207-212 (2001).

188. R. Ubic, I. Abrahams, and Y. Hu, "Oxide ion disorder in $Nd_2Hf_2O_7$," *J Am Ceram Soc*, **91** [1] 235-239 (2008).

189. M. Avdeev, M.K. Haas, J.D. Jorgenson, and R.J. Cava, "Static disorder from lone-pair electrons in Bi2-xMxRu2O7-y (M=Cu, Co; x=0, 0.4) pyrochlores," *J Solid State Chem*, **169** [1] 24-34 (2002).

190. F. Beech, W.M. Jordan, C.R.A. Catlow, A. Santoro, and B.C.H. Steele, "NEUTRON POWDER DIFFRACTION STRUCTURE AND ELECTRICAL-PROPERTIES OF THE DEFECT PYROCHLORES PB1.5NB2O6.5, PB1.5TA2O6.5," *J Solid State Chem*, **77** [2] 322-335 (1988).

191. F. Brisse and O. Knop, "Pyrochlores .3. X-Ray Neutron Infrared and Dielectric Studies of A2sn2o7 Stannates," *Can J Chemistry*, **46** [6] 859-& (1968).

192. J.E. Greedan, D. Gout, A.D. Lozano-Gorrin, S. Derahkshan, T. Proffen, H.J. Kim, E. Bozin, and S.J.L. Billinge, "Local and average structures of the spin-glass pyrochlore Y2Mo2O7 from neutron diffraction and neutron pair distribution function analysis," *Phys Rev B*, **79** [1] - (2009).

193. B.J. Kennedy, "Structure Refinement of Y2ru2o7 by Neutron Powder Diffraction," *Acta Crystallogr C*, **51** 790-792 (1995).

194. B.J. Kennedy, B.A. Hunter, and C.J. Howard, "Structural and bonding trends in tin pyrochlore oxides," *J Solid State Chem*, **130** [1] 58-65 (1997).

195. B.J. Kennedy and T. Vogt, "Structural and bonding trends in ruthenium pyrochlores," *J Solid State Chem*, **126** [2] 261-270 (1996).

196. H. Kobayashi, R. Kanno, Y. Kawamoto, T. Kamiyama, F. Izumi, and A.W. Sleight, "Synthesis, Crystal-Structure, and Electrical-Properties of the Pyrochlores Pb(2-X)Ln(X)Ru(2)O(7-Y)(Ln=Nd, Gd)," *J Solid State Chem*, **114** [1] 15-23 (1995).

197. J. Lian, J. Chen, L.M. Wang, R.C. Ewing, J.M. Farmer, L.A. Boatner, and K.B. Helean, "Radiation-induced amorphization of rare-earth titanate pyrochlores," *Phys Rev B*, **68** [13] - (2003).

198. F. Matteucci, G. Cruciani, M. Dondi, G. Baldi, and A. Barzanti, "Crystal structural and optical properties of Cr-doped Y2Ti2O7 and Y2Sn2O7 pyrochlores," *Acta Mater*, **55** [7] 2229-2238 (2007).

199. B. Nguyen, Y. Liu, and R.L. Withers, "Relaxor dielectric properties of a (Ca1.5Ti0.5)(NbTi)O-7 misplaced-displacive' cubic pyrochlore synthesised via metallorganic decomposition," *Solid State Commun*, **145** [1-2] 72-76 (2008).

200. B. Nguyen, Y.R. Liu, and R.L. Withers, "The local crystal chemistry and dielectric properties of the cubic pyrochlore phase in the Bi2O3-M2+ O-Nb2O5 (M2+ = Ni2+ and Mg2+) systems," *J Solid State Chem*, **180** [2] 549-557 (2007).

201. H.B. Nguyen, L. Noren, Y. Liu, R.L. Withers, X.Y. Wei, and M.M. Elcombe, "The disordered structures and low temperature dielectric relaxation properties of two misplaced-displacive cubic pyrochlores found in the Bi2O3-(MO)-O-II-Nb2O5 (M = Mg, Ni) systems," *J Solid State Chem*, **180** [9] 2558-2565 (2007).

202. L. Soderholm and J.E. Greedan, "Relationship between Crystal-Structure and Magnetic-Properties of (Re)2v2o7 - Re=Lu,Yb,Tm," *Mater Res Bull*, **17** [6] 707-713 (1982).

203. W. Somphon, V. Ting, Y. Liu, R.L. Withers, Q. Zhou, and B.J. Kennedy, "Local crystal chemistry, structured diffuse scattering and the dielectric properties of (Bi1-xYx)(2)((MNbV)-Nb-III)O-7 (M=Fe3+, In3+) Bi-pyrochlores," *J Solid State Chem*, **179** [8] 2495-2505 (2006).

204. T. Takeda, R. Kanno, Y. Kawamoto, M. Takano, F. Izumi, A.W. Sleight, and A.W. Hewat, "Structure-property relationships in pyrochlores: low-temperature structures of Tl2Ru2O7-delta (delta = 0.00 and 0.05)," *Journal of Materials Chemistry*, **9** [1] 215-222 (1999).

205. D.V. West, T.M. McQueen, Q. Huang, and R.J. Cava, "Structural and magnetic properties of pyrochlore solid solutions (Y,Lu)(2)Ti2-x(Nb,Ta)(x)O-7 +/- y," *J Solid State Chem*, **181** [8] 1753-1758 (2008).

206. T. Yamamoto, R. Kanno, Y. Takeda, O. Yamamoto, Y. Kawamoto, and M. Takano, "Crystal-Structure and Metal-Semiconductor Transition of the Bi2-Xlnxru2o7 Pyrochlores (Ln=Pr-Lu)," *J Solid State Chem*, **109** [2] 372-383 (1994).

207. S. Zouari, R. Ballou, A. Cheikh-Rouhou, and P. Strobel, "Synthesis and structure of new pyrochlore-type oxides Ln(2)ScNbO(7) (Ln = Pr, Nd, Eu, Gd, Dy)," *Mater Lett*, **62** [21-22] 3767-3769 (2008).

208. O. Knop and F. Brisse, "Pyrochlores .V. Thermoanalytic X-Ray Neutron Infrared and Dielectric Studies of $A_2Ti_2O_7$ Titanates," *Can J Chemistry*, **47** [6] 971-& (1969).

209. H. Kobayashi, R. Kanno, Y. Kawamoto, T. Kamiyama, F. Izumi, and A.W. Sleight, "Synthesis, Crystal-Structure, and Electrical-Properties of the Pyrochlores $Pb_{2-X}Ln_XRu_2O_{7-Y}$(Ln=Nd, Gd)," *J Solid State Chem*, **114** [1] 15-23 (1995).

210. S. Zouari, R. Ballou, A. Cheikh-Rouhou, and P. Strobel, "Synthesis and structure of new pyrochlore-type oxides Ln_2ScNbO_7 (Ln = Pr, Nd, Eu, Gd, Dy)," *Mater Lett*, **62** [21-22] 3767-3769 (2008).

211. N.J. Hess, B.D. Begg, S.D. Conradson, D.E. McCready, P.L. Gassman, and W.J. Weber, "Spectroscopic investigations of the structural phase transition in $Gd_2(Ti_{1-y}Zr_y)_2O_7$ pyrochlores," *J Phys Chem B*, **106** [18] 4663-4677 (2002).

212. J. Lian, X.T. Zu, K.V.G. Kutty, J. Chen, L.M. Wang, and R.C. Ewing, "Ion-irradiation-induced amorphization of La2Zr2O7 pyrochlore," *Phys Rev B*, **66** [5] - (2002).

213. R.L. Withers, T.R. Welberry, A.K. Larsson, Y. Liu, L. Noren, H. Rundlof, and F.J. Brink, "Local crystal chemistry, induced strain and short range order in the cubic pyrochlore (Bi1.5-alpha Zn0.5-beta)(Zn0.5-gamma Nb1.5-delta)O(7-1.5 alpha-beta-gamma-2.5-delta) (BZN)," *J Solid State Chem*, **177** [1] 231-244 (2004).

214. W. Somphon, V. Ting, Y. Liu, R.L. Withers, Q. Zhou, and B.J. Kennedy, "Local crystal chemistry, structured diffuse scattering and the dielectric properties of $(Bi_{1-x}Y_x)_2((MNb^{V})Nb^{III})O_7$ ($M=Fe^{3+}$, In^{3+}) Bi-pyrochlores," *J Solid State Chem*, **179** [8] 2495-2505 (2006).

215. Y. Liu, R.L. Withers, T.R. Welberry, H. Wang, and H.L. Du, "Crystal chemistry on a lattice: The case of BZN and BZN-related pyrochlores," *J Solid State Chem*, **179** [7] 2141-2149 (2006).

216. P.Y. Piffard, M. Dion, and M. Tournoux, "Crystal-Structure of Pyrochlore, K0,51sb0(Iii)67sb2(V)O6,26," *Acta Crystallogr B*, **34** [Feb] 366-368 (1978).

217. I. Radosavljevic, J.S.O. Evans, and A.W. Sleight, "Synthesis and structure of pyrochlore-type bismuth titanate," *J Solid State Chem*, **136** [1] 63-66 (1998).

218. K. Ramesha, L. Sebastian, B. Eichhorn, and J. Gopalakrishnan, "Pb2FeReO6: new defect pyrochlore oxide with a geometrically frustrated Fe/Re sublattice," *J Mater Chem*, **13** [8] 2011-2014 (2003).

219. P.P. Rao, K.R. Nair, P. Koshy, and V.K. Vaidyan, "New dielectric materials based on pyrochlore-type oxides-Ca3RE3Ti7Ta2O26.5 (RE = Pr, Sm, Gd, Dy or Y): Structure, FT-IR spectra, microstructure and dielectric properties," *J Mater Sci-Mater El*, **17** [7] 497-502 (2006).

220. P.P. Rao, K.R. Nair, P. Koshy, and V.K. Vaidyan, "Microwave dielectric properties of novel lithium containing pyrochlore type oxides: Li3Sm3-xBixTi7Nb2O25 (x=0, 1, 2 or 3)," *Mater Lett*, **61** [19-20] 4188-4191 (2007).

221. P.P. Rao, D.N. Rajendran, K.R. Nair, P. Koshy, and V.K. Vaidyan, "Microwave dielectric properties of new pyrochlore type oxides: Pb3R3Ti7Nb2O26.5 (R = Y, Pr, Nd, Gd or Dy)," *Mat Sci Eng B-Solid*, **128** [1-3] 184-187 (2006).

222. J.N. Reimers, J.E. Greedan, and M. Sato, "The Crystal-Structure of the Spin-Glass Pyrochlore, $Y_2Mo_2O_7$," *J Solid State Chem*, **72** [2] 390-394 (1988).

223. N. Sekido, H. Murakami, and Y. Yamabe-Mitarai, "Phase equilibria and oxidation behavior of Ir-rich Ir-Y binary alloys," *J Alloy Compd*, **476** [1-2] 107-112 (2009).

224. M. Sellami, A. Bekka, N. Bettahar, V. Caignaert, and N. Ninh, "Crystallographic, magnetic and electric studies of a new pyrochlore-like structure (Bi1.56Co0.44)(Sb1.48Co0.52)O-7 compound," *C. R. Chim.*, **12** [1-2] 276-283 (2009).

225. Shaplygi.Is and V.B. Lazarev, "$Ln_2Os_2O_7$ - New Family of Pyrochlores," *Mater Res Bull*, **8** [7] 761-765 (1973).

226. Y. Shimakawa, Y. Kubo, T. Manako, Y.V. Sushko, D.N. Argyriou, and J.D. Jorgensen, "Structural and magnetotransport properties of the colossal magnetoresistance material $Tl_2Mn_2O_7$," *Phys Rev B*, **55** [10] 6399-6404 (1997).

227. A.V. Shlyakhtina, A.V. Knotko, M.V. Boguslavskii, S.Y. Stefanovich, D.V. Peryshkov, I.V. Kolbanev, and L.G. Shcherbakova, "Effects of the synthesis procedure, doping and non-stoichiometry on the order-disorder transformation in Ln(2)Ti(2)O(7) (Ln=Tm-Lu) oxygen-ion conductors," *Solid State Ionics*, **176** [29-30] 2297-2304 (2005).

228. V.I. Sidey, P.M. Milyan, O.O. Semrad, and A.M. Solomon, "X-ray powder diffraction studies and bond-valence analysis of Hg2Sb2O7," *J Alloy Compd*, **457** [1-2] 480-484 (2008).

229. V.P. Sirotinkin and A.A. Bush, "Preparation and dielectric properties of Bi1.5MNb1.5O7 (M = Cu, Mg, Mn, Ni, Zn) pyrochlore oxides," *Inorg Mater+*, **39** [9] 974-977 (2003).

230. A.W. Sleight, "New Ternary Oxides of Mercury with Pyrochlore Structure," *Inorg Chem*, **7** [9] 1704-& (1968).

231. M.A. Subramanian, A.K. Ganguli, and A.W. Sleight, "High-Pressure Synthesis of New Plumbates of Bismuth and Thallium," *Mater Res Bull*, **27** [7] 799-803 (1992).

232. G.J. Thorogood, B.J. Kennedy, M. Avdeev, and T. Kamiyama, "The stability of Na-doped $Bi_2(NbCr)O_{7-x}$ pyrochlores: The non-existence of "$(BiNa)(NbCr)O_6$"," *J Phys Chem Solids*, **69** [4] 918-922 (2008).

233. J. Ting, B.J. Kennedy, R.L. Withers, and M. Avdeev, "Synthesis and structural studies of lanthanide substituted bismuth-titanium pyrochlores," *J Solid State Chem*, **182** [4] 836-840 (2009).

234. M. Valant and P.K. Davies, "Synthesis and dielectric properties of pyrochlore solid solutions in the Bi_2O_3-ZnO-Nb_2O_5-TiO_2 system," *J Mater Sci*, **34** [22] 5437-5442 (1999).

235. M. Valant and P.K. Davies, "Crystal chemistry and dielectric properties of chemically substituted $(Bi_{1.5}Zn_{1.0}Nb_{1.5})O_7$ and $Bi_2(Zn_{2/3}Nb_{4/3})O_7$ pyrochlores," *J Am Ceram Soc*, **83** [1] 147-153 (2000).

236. T.A. Vanderah, J. Guzman, J.C. Nino, and R.S. Roth, "Stability Phase-Fields and Pyrochlore Formation in Sections of the Bi_2O_3-Al_2O_3-Fe_2O_3-Nb_2O_5 System," *J Am Ceram Soc*, **91** [11] 3659-3662 (2008).

237. T.A. Vanderah, M.W. Lufaso, A.U. Adler, I. Levin, J.C. Nino, V. Provenzano, and P.K. Schenck, "Subsolidus phase equilibria and properties in the system Bi_2O_3 : $Mn_2O_{3\ +/-\ x}$: Nb_2O_5," *J Solid State Chem*, **179** [11] 3467-3477 (2006).

238. T.A. Vanderah, T. Siegrist, M.W. Lufaso, M.C. Yeager, R.S. Roth, J.C. Nino, and S. Yates, "Phase formation and properties in the system Bi_2O_3 : $2CoO_{1+x}$: Nb_2O_5," *Eur J Inorg Chem*, [23] 4908-4914 (2006).

239. R. Wang and A.W. Sleight, "Synthesis and characterization of $Cd_2Ru_2O_7$," *Mater Res Bull*, **33** [7] 1005-1007 (1998).

240. D.V. West, T.M. McQueen, Q. Huang, and R.J. Cava, "Structural and magnetic properties of pyrochlore solid solutions $(Y,Lu)_2Ti_{2-x}(Nb,Ta)_xO_{7\ +/-\ y}$," *J Solid State Chem*, **181** [8] 1753-1758 (2008).

241. T. Yamamoto, R. Kanno, Y. Takeda, O. Yamamoto, Y. Kawamoto, and M. Takano, "Crystal-Structure and Metal-Semiconductor Transition of the $Bi_{2-x}In_xRu_2O_7$ Pyrochlores (Ln=Pr-Lu)," *J Solid State Chem*, **109** [2] 372-383 (1994).

242. H.J. Youn, C. Randall, A. Chen, T. Shrout, and M.T. Lanagan, "Dielectric relaxation and microwave dielectric properties of Bi_2O_3-ZnO-Ta_2O_5 ceramics," *J Mater Res*, **17** [6] 1502-1506 (2002).

243. H.J. Youn, T. Sogabe, C.A. Randall, T.R. Shrout, and M.T. Lanagan, "Phase relations and dielectric properties in the Bi_2O_3-ZnO-Ta_2O_5 system," *J Am Ceram Soc*, **84** [11] 2557-2562 (2001).

244. Z.G. Zou, J.H. Ye, and H. Arakawa, "Synthesis, magnetic and electrical transport properties of the Bi_2InNbO_7 compound," *Solid State Commun*, **116** [5] 259-263 (2000).

245. Z.G. Zou, J.H. Ye, and H. Arakawa, "Growth, photophysical and structural properties of Bi_2InNbO_7," *J Cryst Growth*, **229** [1] 462-466 (2001).

246. Z.G. Zou, J.H. Ye, and H. Arakawa, "Photocatalytic and photophysical properties of a novel series of solid photocatalysts, Bi_2MNbO_7 (M = Al^{3+}, Ga^{3+} and In^{3+})," *Chem Phys Lett*, **333** [1-2] 57-62 (2001).

247. Z.G. Zou, J.H. Ye, and H. Arakawa, "Optical and structural properties of solid oxide photocatalyst Bi_2FeNbO_7," *J Mater Res*, **16** [1] 35-37 (2001).

248. L. Cai and J.C. Nino, "Complex Ceramic Structures. 1.Weberites," *Acta Crystallographica Section B-Structural Science*, **B65** 269-290 (2009).

249. Y.S. Au, W.T. Fu, and D.J.W. Ijdo, "Crystal Structure of $Ca_2Ln_3Sb_3O_{14}$ (Ln = La, Pr, Nd and Y): A Novel Variant of Weberite," *Journal of Solid State Chemistry*, **180** [11] 3166-3171 (2007).

250. G. Desgardin, C. Robert, and B. Raveau, "New Weberite Type Oxides, $LnNaSb_2O_2$," *Journal of Inorganic & Nuclear Chemistry*, **39** [5] 907-908 (1977).

251. A.M. Sych, M.I. Kabanova, and S.G. Andreeva, "Structural Characteristics and Oscillating Spectra of $A_2B_2O_7$ Crystals with the Weberite Structure," *Zhurnal Neorganicheskoi Khimii*, **33** [11] 2756-2760 (1988).

252. K. Gade and V.S. Chincholkar, "Some New Weberites," *Journal of the Chemical Society-Dalton Transactions*, [12] 1959-1959 (1979).

253. H.L. Du and X. Yao, "Dielectric relaxation characteristics of bismuth zinc niobate pyrochlores containing titanium," *Physica B*, **324** [1-4] 121-126 (2002).

254. H.L. Du and X. Yao, "Investigations on structural evolution and dielectric characteristics of high performance Bi-based dielectrics," *Mater Res Bull*, **40** [9] 1527-1535 (2005).

255. H.L. Du, X. Yao, and H. Wang, "Dielectric properties of pyrochlore $(Bi_{1.5}Zn_{0.5})(Nb_{0.5}M_{1.5})O_7$ (M=Ti, Sn, Zr, and Ce) dielectrics," *Appl Phys Lett*, **88** [21] - (2006).

256. H.L. Du, X. Yao, and L.Y. Zhang, "Structure, IR spectra and dielectric properties of Bi2O3-ZnO-SnO2-Nb2O5 quarternary pyrochlore," *Ceram Int*, **28** [3] 231-234 (2002).

257. L.N. Kinzhibalo, V.K. Trunov, A.A. Evdokimov, and V.G. Krongauz, "Refinement of the Crystal-Structure of Fergusonite," *Kristallografiya*, **27** [1] 43-48 (1982).

BIOGRAPHICAL SKETCH

Lu Cai was born in 1982 in Chengdu, China. She attended Sichuan University, obtaining her B.S. degree in Materials Science and Engineering. She spent one year studying in the Department of Materials Science and Engineering at University of Washington (UW), from 2003 to 2004, as an exchange student. While in UW, she joined Dr. Younan Xia's research group. In 2005, she began her Ph.D. study in Dr. Juan C. Nino's research group. After spending almost 5 years at UF in Gainesville, she received her Ph.D. in Spring of 2010.